THE UNIVERSITY *of* EDINBURGH

Search for $VH \rightarrow$ leptons $+ b\bar{b}$ with the ATLAS experiment at the LHC

Chiara Debenedetti

A thesis submitted in fulfilment of the requirements
for the degree of Doctor of Philosophy
to the
University of Edinburgh

2014

Abstract

The search for a Higgs boson decaying to a $b\bar{b}$ pair is one of the key analyses ongoing at the ATLAS experiment. Despite being the largest branching ratio decay for a Standard Model Higgs boson, a large dataset is necessary to perform this analysis because of the very large backgrounds affecting the measurement. To discriminate the electroweak $H \to b\bar{b}$ signal from the large QCD backgrounds, the associated production of the Higgs with a W or a Z boson decaying leptonically is used.

Different techniques have been proposed to enhance the signal over background ratio in the $VH(b\bar{b})$ channel, from dedicated kinematic cuts, to a single large radius jet to identify the two collimated b's in the Higgs high transverse momentum regime, to multivariate techniques. The high-p_{T} approach, using a large radius jet to identify the b's coming from the Higgs decay, has been tested against an analysis based on kinematic cuts for a dataset of 4.7 fb^{-1} luminosity at $\sqrt{s} = 7$ TeV, and compatible results were found for the same transverse momentum range.

Using a kinematic cut based approach the $VH(b\bar{b})$ signal search has been performed for the full LHC Run 1 dataset: 4.7 fb^{-1} at $\sqrt{s} = 7$ TeV and 20.7 fb^{-1} at $\sqrt{s} = 8$ TeV. Several backgrounds to this analysis, such as $Wb\bar{b}$ have not been measured in data yet, and an accurate study of the theoretical description has been performed, comparing the predictions of various Monte Carlo generators at different orders.

The complexity of the analysis requires a profile likelihood fit with several categories and almost 200 parameters, taking into account all the systematics coming from experimental or modelling limitations, to extract the result. To validate the fit model, a test of the ability to extract the signal is performed on the resonant $VZ(b\bar{b})$ background. A

4.8σ excess compatible with the Standard Model rate expectation has been measured, with a best fit value $\mu_{VZ} = 0.93^{+0.22}_{-0.21}$.

The full LHC Run1 dataset result for the $VH(b\bar{b})$ process is a limit of (1.3)1.4 $\times$ SM (expected) observed, with a best fit value of $0.2 \pm 0.5(\text{stat}) \pm 0.4(\text{sys})$ for a Higgs boson of 125 GeV mass.

Declaration

This dissertation is the result of my own work, except where explicit reference is made to the work of others, and has not been submitted for another qualification to this or any other university.

Chiara Debenedetti

Acknowledgements

I would like to thank my supervisor, Phil Clark, for supporting me through my PhD, believing in me and giving me the opportunity to experience life at CERN. I am very grateful to the University of Edinburgh and SUPA for making my doctoral studies possible. I have enjoyed my time in the Edinburgh PPE and ATLAS groups, and I want to thank everybody for the precious discussions and time spent together, and our ATLAS group leader Victoria Martin for her help and advice. I would also like to thank a lot Jane Patterson, for being always there when needed, kind and extremely helpful.

In my two years at CERN I had the possibility to work with many great people, on interesting and challenging projects. I want to especially thank Gabriel Facini, Paolo Francavilla and Andy Buckley for the help, the chats and the fun times. A special mention goes to the HSG5 group, and the VH analysis group, especially to Heather, Christian, Yuji and Tim for their precious support. Thanks Inês, for being a great (distant) PhD colleague, and a friend.

I would like to thank all my friends in Edinburgh and Geneva, you helped in making this period a great one! And thanks also to my "old" friends, spread everywhere, it would be too long to list you all! Thanks for always being there, despite the distance.
I want to dedicate this to the newborns: Alessandro, Teo and Elsa. You are our future.

Above all, there are four people I am grateful to.
Attilio, for being my shoulder, my nightmare, my friend, my counsellor, my source of information, and for being there for me and with me when it was really important. I am looking forward to our new adventure.
Mum, dad and Cecilia, without whom nothing would be possible, with whom everything is wonderful. Vi voglio bene.

Contents

"O frati, dissi, che per cento milia
perigli siete giunti a l'occidente,
a questa tanto picciola vigilia

d'i nostri sensi ch'è del rimanente
non vogliate negar l'esperïenza,
di retro al sol, del mondo sanza gente.

Considerate la vostra semenza:
fatti non foste a viver come bruti,
ma per seguir virtute e canoscenza."

— Dante Alighieri, Divina Commedia
Canto XXVI, vv. 112-120

Chapter 1.

Introduction

The evidence of a $\sim$125 GeV mass resonance in the search for the Standard Model (SM) Higgs boson by the ATLAS [1] and CMS [2] collaborations is one of the most outstanding physics results obtained recently at the LHC. Studying the characteristics of this new particle is crucial to confirm its nature, and demonstrate whether or not it is the missing brick in the SM wall.

The Higgs boson can be produced via various processes and it can decay to several final states, at different rates. The searches for a Higgs boson decaying to vector boson pairs, $\gamma\gamma$, WW^* and ZZ^*, present an excess at $\sim$125 GeV. These channels have also been used by the ATLAS collaboration to study the spin and parity of the observed particle, and to obtain constraints on the couplings of the new particle to the SM fermions and vector boson [3, 4]. More precisely, a 5σ indirect evidence of the coupling to fermions has been extracted, assuming that the $gg \to H$ production mode proceeds via a top quark loop, as predicted by the SM. The first hint of direct coupling to fermions was reported by the TeVatron experiments [5]. An excess in the $b\bar{b}$ channel with a 2.8σ significance is observed when combining the results from the CDF and D$\emptyset$ experiment. Recently, the ATLAS collaboration has reported an excess of 4σ significance for a 125 GeV mass boson in the search for a SM Higgs boson decaying to a τ lepton pair [6]. To corroborate this result, and be able to claim a 5σ evidence of the direct coupling to fermions, the $H \to b\bar{b}$ search is very important.

The $H \to b\bar{b}$ signal is dominated by large backgrounds, produced via strong interactions. To be able to discriminate the $H \to b\bar{b}$ signal from the backgrounds, the associated production process, $VH \to \text{leptons} + b\bar{b}$, is used, instead of the gluon fusion production mode. This significantly reduces the cross section of the signal searched for, but allows to trigger on a cleaner signature in the detector, reducing therefore the backgrounds. This

thesis presents the ATLAS preliminary results from the search for $VH \to \text{leptons} + b\bar{b}$ using the full LHC Run 1 dataset: 4.7 fb^{-1} collected at $\sqrt{s} = 7$ TeV and 20.3 fb^{-1} at $\sqrt{s} = 8$ TeV. It also discusses generator level studies of the modelling of the $Wb\bar{b}$ process, one of the most important backgrounds to the $VH \to \text{leptons} + b\bar{b}$ search, and a feasibility study using an alternative technique based on jet substructure, performed on the $\sqrt{s} = 7$ TeV dataset.

In chapt. 2, the Standard Model of particle physics is presented, starting from the basic concepts of quantum field theory, and including the spontaneous symmetry breaking mechanism, predicting the existence of the Higgs boson. The theoretical limits on the Higgs boson mass are also described, and an overview of the different Higgs production and decay modes is given. This is followed by the description of the $H \to b\bar{b}$ backgrounds, providing details on the $VH \to \text{leptons} + b\bar{b}$ case, which is the main topic of this dissertation.

Chapt. 3 is an overview of the LHC accelerator and the ATLAS detector, discussing the design parameters of both and their activity from 2009 to 2012. The different ATLAS sub-detectors and their role in particle identification are described in detail. In chapt. 4, an overview of the statistics used to test the existence of a signal in a typical Higgs analysis is given. This serves as an introduction to the fit employed in the $VH \to \text{leptons} + b\bar{b}$ analysis.

Chapt. 5 describes the main ingredients of the $VH \to \text{leptons} + b\bar{b}$ analysis. Here the main Monte Carlo generators used to model the signal and the backgrounds are described, as well as the techniques used to identify the objects forming the process final states. Chapt. 6 concentrates on the description of the strategy adopted by ATLAS in the analysis of the full LHC Run 1 dataset to search for $VH \to \text{leptons} + b\bar{b}$, providing an outline of the kinematic selection adopted. A detailed description of the background modelling and the systematic uncertainties affecting the result is provided, together with an in-depth explanation of the Monte Carlo generator-based extraction of the systematic uncertainties on the modelling of the irreducible $Wb\bar{b}$ background.

Chapt. 7 is a description of a feasibility study, using the $\sqrt{s} = 7$ TeV dataset, of an alternative technique to search for $VH \to \text{leptons} + b\bar{b}$ events. It concentrates on Higgs bosons produced at high transverse momenta, causing the b quarks from their decay to be collimated in the laboratory frame. They are identified as a single object, a jet of large radius and decomposed to find a hard substructure compatible with two collimated b quarks.

Chapt. 8 presents the result of a preliminary version of the $VH \to \text{leptons} + b\bar{b}$ analysis, based on a smaller dataset, of 4.7 fb^{-1} at $\sqrt{s} = 7$ TeV and 13 fb^{-1} at $\sqrt{s} = 8$ TeV. To validate the background estimate and the complex fit model, used to extract from the data both the signal and the main background normalisations, a cross-check on a known process, $VZ \to \text{leptons} + b\bar{b}$, is studied, and first observed in the ATLAS data. It presents a very similar signature to $VH \to \text{leptons} + b\bar{b}$, but has a higher cross section. The statistical analysis and the results of the full Run 1 analysis are shown in chapt. 9. The treatment of the systematic uncertainties in the fit is also outlined.

Lastly, in chapt. 10, the ATLAS results on the search for the SM Higgs boson and the characterisation of the newly discovered particle are presented. A discussion of the results, compared to other $H \to b\bar{b}$ searches carried out by ATLAS, CMS and the TeVatron [7] experiments, CDF [8] and D$\emptyset$ [9], can be found in the same chapter. Also the possible future developments to be employed during the LHC Run 2 data taking period, aimed at observing the $VH \to \text{leptons} + b\bar{b}$ channel, are discussed. Chapt. 11 is a summary of the results presented in the thesis.

Chapter 2.

The Standard Model and the Higgs boson

In this chapter, the Standard Model (SM) of particle physics will be presented, from quantum electrodynamics (QED) to the description of the spontaneous symmetry breaking mechanism (SSB) in the electroweak (EW) sector of the theory and the Higgs boson. Natural units will be adopted: $\hbar = c = 1$. After the theoretical formulation of the SM, details of the production mechanisms at the LHC, and of the decay modes of the SM Higgs boson will be given in sec. 2.4. The final part of this chapter describes in detail the $H \to b\bar{b}$ decay channel, with a particular focus on the WH and ZH production modes and their backgrounds.

2.1. Introductory phenomenology

The Standard Model of particle physics is the theory that best describes matter and its interactions at a subnuclear level. It is expressed using the language of quantum field theory (QFT) and it classifies all the particles discovered to date and predicts their interactions with high precision.

The model groups the elementary matter constituents into two categories, leptons and quarks. Both are subdivided in three doublets of spin 1/2 particles.

- The three lepton doublets contain a neutral and a charged lepton. Each family is characterised by a lepton quantum number, L_ℓ. Neutral leptons only interact via the weak force, while charged ones can in addition interact electromagnetically.

Three corresponding doublets of antileptons with opposite quantum numbers exist:

$$\begin{pmatrix} \nu_e \\ e^- \end{pmatrix} \quad \begin{pmatrix} \nu_\mu \\ \mu^- \end{pmatrix} \quad \begin{pmatrix} \nu_\tau \\ \tau^- \end{pmatrix} . \tag{2.1}$$

All leptons are massive, and the presence of neutrino masses has been demonstrated through the measurement of their oscillations.

- The three families of quarks, carrying non-integer electric charge are composed by an up-type quark, with charge $+2/3e$ and a down-type quark, with charge $-1/3e$:

$$\begin{pmatrix} u \\ d \end{pmatrix} \quad \begin{pmatrix} c \\ s \end{pmatrix} \quad \begin{pmatrix} t \\ b \end{pmatrix} . \tag{2.2}$$

They also interact strongly and they cannot be observed as free particles. They exist in nature as meson ($q\bar{q}$) or baryon (qqq) bound states, because of the confinement property of the strong force [10]. To each quark corresponds an antiquark, with opposite quantum numbers.

The other particles constituting the SM are bosons, with integer spin. There are three types of vector bosons, mediating the fundamental interactions: electromagnetic, strong and weak force.

- The photon, γ, which is massless and carries the electromagnetic force.
- The eight massless gluons, g, which are the strong interaction mediators.
- The three gauge bosons, $W^\pm$ and Z, which are responsible for the weak interactions.

Moreover, the SM postulates the existence of a scalar boson, the Higgs boson, whose field allows the other particles to be massive.

2.1.1. General principles of QFT

Quantum field theory [11] is the link between quantum mechanics and special relativity. It describes particles as local fields ($\varphi(x)$), functions of the space-time coordinates. The dynamics of the field $\varphi(x)$ are described by its Lagrangian density $\mathcal{L}$, which is a function of its first derivatives in the space-time coordinate ($\partial_\mu \varphi(x)$) as well:

$$\mathcal{L}(\varphi(x), \partial_\mu \varphi(x)) . \tag{2.3}$$

As in classical mechanics, requiring the action to be stationary, according to the Hamilton principle ($\delta S = 0$), allows the derivation of the Euler-Lagrange equations of motion for the field. The corresponding gauge symmetry group is the continuous group of transformations of the fields that leave δS unchanged. Noether's theorem postulate the existence of a conserved current, and thus a conserved charge, in the presence of a continuous symmetry.

The Lagrangian density associated with the Standard Model is:

$$\mathcal{L}_{SM} = \mathcal{L}_{QCD} + \mathcal{L}_{EW} \ , \tag{2.4}$$

where the QCD component can be treated separately from the electroweak one. $\mathcal{L}_{SM}$ is invariant under the gauge group $SU(3)_C \otimes SU(2)_L \otimes U(1)_Y$, where $SU(3)_C$ represents the QCD colour charge symmetry, described in sec. 2.1.3 and $SU(2)_L \otimes U(1)_Y$ is the electroweak symmetry. $SU(2)_L$ refers to the weak isospin charge symmetry group, while $U(1)_Y$ to the hypercharge.

2.1.2. Quantum electrodynamics

The simplest example of a gauge theory, introducing the fundamental concept of local gauge invariance, is quantum electrodynamics [12]. It is an abelian gauge theory describing the interactions of particles carrying an electric charge e, with mass m and spin 1/2, under the $U(1)$ symmetry group. Its Lagrangian density, in the case of one fermion of charge e, is expressed as follows:

$$\mathcal{L}_{QED} = \bar{\psi}(i\gamma^\mu D_\mu - m)\psi - \frac{1}{4}F^{\mu\nu}F_{\mu\nu} \ , \tag{2.5}$$

where ψ is the spinor field representing the charged particles, γ^μ are the 4×4 Dirac matrices, for which $\{\gamma^\mu, \gamma^\nu\} = 2g^{\mu\nu}$ holds, with $g^{\mu\nu}$ the Minkowski metric tensor. Generally, the full Lagrangian is expressed as the sum over all fermions. $F_{\mu\nu}$ is the gauge invariant electromagnetic field strength tensor, defined as:

$$F_{\mu\nu} = \partial_\nu A_\mu(x) - \partial_\mu A_\nu(x) \ , \tag{2.6}$$

with A_μ being the gauge field, representing the electromagnetic charge carrier: the massless vector boson known as photon. Finally, the covariant derivative D_μ is defined

as:

$$D_\mu = \partial_\mu + ieA_\mu(x) \ . \tag{2.7}$$

This theory is invariant under the following local unitary transformations:

$$\psi(x) \to U(x)\psi(x) = e^{i\alpha(x)}\psi(x) \tag{2.8a}$$

$$A_\mu(x) \to U(x)A_\mu(x) = A_\mu(x) + \frac{1}{e}\partial_\mu\alpha(x) \ , \tag{2.8b}$$

with $\alpha(x)$ an arbitrary function of the coordinate x.

The form of the photon coupling to matter can be seen explicitly by expanding the Lagrangian:

$$\mathcal{L}_{QED} = \bar{\psi}(i\gamma^\mu\partial_\mu - m)\psi - e\bar{\psi}\gamma^\mu\psi A_\mu - \frac{1}{4}F^{\mu\nu}F_{\mu\nu} \ , \tag{2.9}$$

where $e\bar{\psi}\gamma^\mu\psi A_\mu$ is the interaction term, showing that the strength of the coupling between the spin 1/2 charged particles and the photon is the electric charge e.

The invariance of $\mathcal{L}_{QED}$ under $U(1)$ implies the conservation of the current $J^\mu = \bar{\psi}\gamma^\mu\psi$ and of the electric charge, as from Noether's theorem.

2.1.3. Quantum chromodynamics: the description of strong interactions

Quantum chromodynamics is the gauge theory, invariant under $SU(3)_C$ transformations, that describes the interactions between quarks, spin 1/2 particles carrying a colour charge, C [13–15]. These interactions are mediated by massless vector bosons, the gluons. Quarks can carry six different colours: blue, green red, and their three corresponding anticolours.

The QCD Lagrangian density is built the same way as the QED one, and can be written as follows:

$$\mathcal{L}_{QCD} = \sum_f \bar{q}_f(i\gamma^\mu D_\mu - m_f)q_f - \frac{1}{4}F^a_{\mu\nu}F^{a,\mu\nu} \ . \tag{2.10}$$

In this expression, $a = 0, \cdots, 7$ is the colour index, $f = 0, \cdots, 5$ is the quark flavour index, and the strength tensor, invariant under gauge transformations, $F^a_{\mu\nu}$ is expressed as:

$$F^a_{\mu\nu} = \partial_\mu G^a_\nu - \partial_\nu G^a_\mu - g f^{abc} G^b_\mu G^c_\nu \ . \tag{2.11}$$

G_μ is the gluon vector field, $g = 4\pi\alpha_S$ is the strength of the interaction, and f^{abc} is the $SU(3)_C$ structure constant. The covariant derivative is expressed as:

$$D_\mu = \partial_\mu + igT^a G^a_\mu \ , \tag{2.12}$$

where T^a are the $SU(3)_C$ group generators, satisfying the commutation rule $[T^a, T^b] = if^{abc}T^c$.

The Lagrangian is invariant under the transformations:

$$q(x) \to U(x)q(x) = e^{-ig\alpha^a(x)}T^a q(x) \tag{2.13a}$$

$$G^a_\mu \to G^a_\mu - \frac{1}{g}\partial_\mu \alpha^a - f^{abc}\alpha^b G^c_\mu \ . \tag{2.13b}$$

The Lagrangian can be expanded, to show explicitly the interactions it describes. The following three terms arise from the expansion: a kinetic term

$$\mathcal{L}^{\text{kinetic}}_{QCD} = -\frac{1}{4}(\partial_\mu G^a_\nu - \partial_\nu G^a_\mu)(\partial^\mu G^{a,\nu} - \partial^\nu G^{a,\mu}) \ , \tag{2.14}$$

an interaction term between quarks and gluons

$$\mathcal{L}^{q-g}_{QCD} = -g \sum_f G^a_\mu \bar{q}_f \gamma^\mu G^a_\mu T^a q_f \ , \tag{2.15}$$

and a gluon self interaction term, arising from the fact that gluons carry the colour charge, as opposed to the neutral photons in the case of QED:

$$\mathcal{L}^{g-\text{self}}_{QCD} = \frac{g}{2} f^{abc}(\partial_\mu G^a_\nu - \partial_\nu G^a_\mu)(G^{b,\mu}G^{c,\nu}) - \frac{g}{2} f^{abc} f_{ade} G^{b,\mu} G^{c,\nu} G_{d,\mu} G_{e,\nu} \ . \tag{2.16}$$

According to Noether's theorem, the colour charge is conserved, and this has been proven experimentally.

QCD has the property of asymptotic freedom, determining the strength of the force to be high at low energy, binding hadrons together, and low at high energy, allowing for a perturbative treatment of the interaction. Quarks and gluons produced in collisions are coloured states, and a colour field exists among them. When the distance between the collision originated coloured particles increases, non-coloured $q\bar{q}$ or qqq hadrons are created, preserving the colour neutrality of the final state. This process is called fragmentation and hadronisation, and is used to identify quarks at hadron colliders. The identified object is a colourless jet formed along the momentum axis of the originating quark or gluon, creating a shower of particles of decreasing momentum. Jet clustering algorithms are employed to group this shower according to an angular or momentum-dependent hierarchy, and to measure momentum, energy and direction of the originating particle.

2.1.4. The electroweak theory

The electroweak theory [16–20] describes both electromagnetic and weak interactions, arising from the same force at high energies ($\sim$100 GeV). The weak force was first described by E. Fermi in 1934 [21], as a theoretical formulation of the radioactive β decay of the neutron: $n \to p + e^- + \bar{\nu}_e$. The Lagrangian proposed by Fermi,

$$\mathcal{L}_W = -G_F(\bar{\psi}_p\gamma^\mu\psi_n)(\bar{\psi}_e\gamma_\mu\psi_\nu) + \text{h.c.}\ , \tag{2.17}$$

describes a contact interaction, which violates unitarity and is not renormalisable. It is though a valid effective description of low energy weak interactions ($E \ll m_W$).

The electroweak force can be mediated by both charged and neutral gauge bosons, allowing for different interaction types. Charged currents, in fact, cause lepton flavour transitions, while flavour is conserved in neutral current mediated interactions. The electroweak theory is invariant under the $SU(2)_L \otimes U(1)_Y$ gauge group, representing the weak isospin I and hypercharge Y spaces respectively. This representation describes the flavour changing interactions, that take place between left-handed fermion fields. Fermion fields are described via their left- and right-handed helicity projections, defined as follows:

$$\psi_L = P_L\psi = \frac{1}{2}(1-\gamma^5)\psi \tag{2.18a}$$

$$\psi_R = P_R\psi = \frac{1}{2}(1+\gamma^5)\psi \ , \tag{2.18b}$$

with $\gamma^5 = i\gamma^0\gamma^1\gamma^2\gamma^3$, and $P_{L,R}$ the left and right handed projection operators. The components ψ and $\gamma^5\psi$ transform differently, respectively as a vector and an axial vector, showing the $V-A$ nature of the EW interactions, violating the parity symmetry.

The left and right lepton and quark fields are thus defined in multiplets:

$$Q_L(x) = \begin{pmatrix} u_L(x) \\ d_L(x) \end{pmatrix} \quad u_R(x) \quad d_R(x) \ , \tag{2.19}$$

for quarks, and:

$$\psi_L(x) = \begin{pmatrix} \nu_L(x) \\ l_L(x) \end{pmatrix} \quad \nu_R(x) \quad l_R(x) \ , \tag{2.20}$$

for leptons. The following relation holds among the weak hypercharge Y, the third component of the isospin I_3 and the electric charge Q:

$$Q = I_3 + \frac{Y}{2} \ . \tag{2.21}$$

Considering f as any of the fermion fields previously described, the electroweak Lagrangian can be expressed as follows:

$$\mathcal{L}_{EW} = i\sum_f \bar{f}\gamma^\mu D_\mu f - \frac{1}{4}B_{\mu\nu}B^{\mu\nu} - \frac{1}{4}W^a_{\mu\nu}W^{\mu\nu}_a \ , \tag{2.22}$$

where the covariant derivative has the form:

$$D_\mu = \partial_\mu + igI^aW^a_\mu - ig'YB_\mu \ , \tag{2.23}$$

where g and g' are the coupling constants associated respectively to the gauge fields W_μ and B_μ, corresponding to the two gauge groups $SU(2)_L$ and $U(1)_Y$. The I^a, $a = 1,2,3$, are the isospin operators that can be re-written in terms of the Pauli matrices σ_a ($I_a = \sigma_a/2$). The kinetic terms of the Lagrangian contain the strength tensors of the two fields:

$$W^a_{\mu\nu} = \partial\nu W^a_\mu - \partial_\mu W^a_\nu - g\epsilon^{abc}W^b_\mu W^c_\nu \tag{2.24a}$$

$$B_{\mu\nu} = \partial_\nu B_\mu - \partial_\mu B_\nu \ , \tag{2.24b}$$

the first being the gauge field of a non-abelian group, with ϵ^{abc} its structure constant, and coupling only to left-handed fermions. The B_μ field, instead, couples to both chiralities.

This Lagrangian is invariant under the transformations of the $U(1)$ group, involving both left- and right-handed fermions:

$$f(x) \to e^{i\alpha(x)\frac{Y}{2}} f(x) \ , \tag{2.25}$$

and under the $SU(2)_L$ transformations, involving only left-handed fermion fields f_L:

$$f_L(x) \to e^{i\beta^a(x)I^a} f_L(x) \ . \tag{2.26}$$

The physical fields of the gauge bosons of the electroweak theory, Z^0, γ and $W^\pm$ can be defined in terms of the gauge fields W^a_μ and B_μ, introducing the weak mixing angle θ_W:

$$Z^\mu = \cos\theta_W W^\mu_3 - \sin\theta_W B^\mu \tag{2.27a}$$

$$A^\mu = \sin\theta_W W^\mu_3 + \cos\theta_W B^\mu \tag{2.27b}$$

$$W^\mu_\pm = -\frac{W^\mu_1 \pm i W^\mu_2}{\sqrt{2}} \ . \tag{2.27c}$$

The weak mixing angle is defined as follows:

$$\frac{g}{\sin\theta_W} = \frac{g'}{\cos\theta_W} = e \ . \tag{2.28}$$

The interaction part of the Lagrangian can be rewritten in terms of the conserved electric, charged and neutral weak currents associated to the physical vector bosons:

$$\begin{aligned} L^{\text{int}}_{EW} &= L^{\text{int}}_{QED} + L^{\text{int}}_{CC} + L^{\text{int}}_{NC} \\ &= eJ^{EM}_\mu A^\mu + \frac{g}{\sqrt{2}}(J^+_\mu W^{+\mu} + J^-_\mu W^{-\mu}) + \frac{g}{\cos\theta_W} J^0_\mu Z^\mu \ , \end{aligned} \tag{2.29}$$

with the currents defined as follows:

$$J_\mu^{EM} = \sum_f \bar{f}\gamma_\mu Q f \tag{2.30a}$$

$$J_\mu^{+} = \sum_{u_L,d_L} \bar{u}_L\gamma_\mu \left(\frac{1-\gamma_5}{2}\right) d_L + \sum_{\nu_L,l_L} \bar{\nu}_L\gamma_\mu \left(\frac{1-\gamma_5}{2}\right) l_L \tag{2.30b}$$

$$J_\mu^{-} = \sum_{u_L,d_L} \bar{d}_L\gamma_\mu \left(\frac{1-\gamma_5}{2}\right) u_L + \sum_{\nu_L,l_L} \bar{l}_L\gamma_\mu \left(\frac{1-\gamma_5}{2}\right) \nu_L \tag{2.30c}$$

$$J_\mu^{0} = \sum_f \bar{f}\gamma_\mu \frac{1}{2}(c_V - c_A\gamma_5) f \ , \tag{2.30d}$$

where $c_V = \sigma_3 - 2Q\sin^2\theta_W$ and $c_A = \sigma_3$.

2.2. Spontaneous symmetry breaking and the Brout-Englert-Higgs mechanism

The Standard Model Lagrangian $\mathcal{L}_{SM} = \mathcal{L}_{EW} + \mathcal{L}_{QCD}$ as presented so far, describes a theory for massless particles, which does not match the experimental evidence. $\mathcal{L}_{SM}$ is also renormalisable, and to preserve this, the particle masses have to be introduced via the Brout-Englert-Higgs (BEH) mechanism [22–27], describing the spontaneous symmetry breaking $SU(3)_C \otimes SU(2)_L \otimes U(1)_Y \rightarrow SU(3)_C \otimes U(1)_Q$. This justifies the presence of the massive $W^\pm$ and Z bosons, as well as the massless photon, associated with the residual symmetry group $U(1)_Q$.

A scalar isospin doublet, the Higgs field ϕ, is introduced:

$$\phi(x) = \begin{pmatrix} \varphi^+(x) \\ \varphi^0(x) \end{pmatrix} \quad \phi^c(x) = (i\sigma_2)\phi^*(x) = \begin{pmatrix} \varphi^{0*}(x) \\ -\varphi^-(x) \end{pmatrix} , \tag{2.31}$$

with φ being complex scalar fields. Imposing gauge invariance, the following Lagrangian density form holds for this field:

$$\mathcal{L}_H = (D_\mu \phi)^\dagger (D_\mu \phi) - V(\phi) \ , \tag{2.32}$$

where the potential $V(\phi)$ can be expressed as:

$$V(\phi) = \mu^2 \phi^\dagger \phi + \lambda (\phi^\dagger \phi)^2 \quad \text{with } \mu, \lambda \in \Re \ . \tag{2.33}$$

The vacuum state $|0\rangle$ of the potential in eq. 2.33 is defined by the lower bound $\lambda > 0$. This state can be either unique or degenerate, depending on the sign of μ^2. If $\mu^2 > 0$, the minimum of the potential is $\phi = 0$, the particle mass is given by μ and λ represents the strength of the interaction. If $\mu^2 < 0$, instead, $V(\phi)$ has a local maximum at $\phi = 0$ and its minimum lies on a circumference, as pointed out in fig. 2.1.

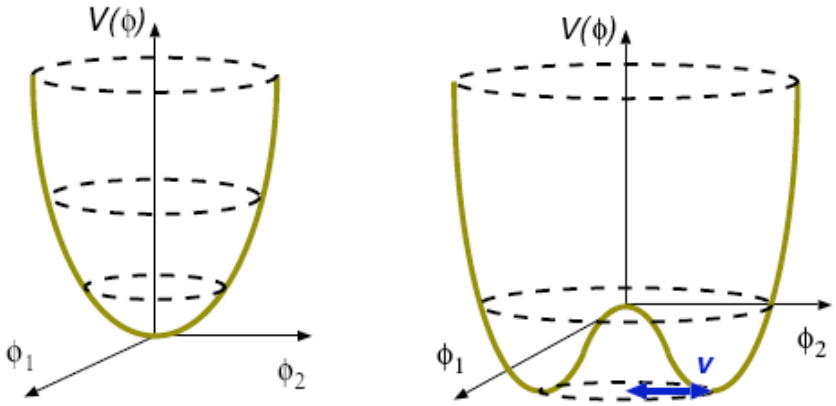

Figure 2.1.: The Higgs potential $V(\phi)$ in case of different sign of μ^2, positive (left) and negative (right).

The choice of a precise value on the circumference around which to expand the Lagrangian spontaneously breaks the symmetry in the ground state. The following choice is made for the vacuum expectation value:

$$\langle |\phi| \rangle = \begin{pmatrix} 0 \\ \eta \end{pmatrix} \quad \text{with } \eta = \frac{v}{\sqrt{2}} = \left(-\frac{\mu^2}{4\lambda} \right)^{1/2} \ . \tag{2.34}$$

The perturbative expansion around this minimum leads to two particles associated to the complex field ϕ: a massless one, known as Goldstone boson, and one of mass $4\lambda\eta^2$. This does still not correspond to reality, where no scalar massless boson is observed. The choice of a unitary gauge, possible because of the invariance of $\mathcal{L}_{SM}$ under local gauge

transformations, leads to the following expression for the Higgs field:

$$\phi(x) = \frac{1}{\sqrt{2}} \begin{pmatrix} 0 \\ v + h(x) \end{pmatrix} . \tag{2.35}$$

This causes the replacement of the scalar massive and massless bosons with a massive scalar boson H, and a massive vector boson A, with masses $m_H^2 = -2\mu^2 = 4\lambda\eta^2$ and $m_A^2 = 2e^2\eta^2$.

Expanding the kinetic term of $\mathcal{L}_H$, using the expression for the covariant derivative defined in eq. 2.23, the mass terms for the weak vector bosons [28] arise:

$$\begin{aligned} (D_\mu\phi)^\dagger(D^\mu\phi) = \frac{1}{2}\partial^\mu h \partial_\mu h + \frac{1}{8}g^2(v+h)^2|W_1^\mu + iW_2^\mu|^2 \\ + \frac{1}{8}(v+h)^2|gW_3^\mu - g'B_\mu|^2 . \end{aligned} \tag{2.36}$$

Using the inverse formulae for W_μ^a and B_μ presented in eqs. 2.27a, 2.27b and 2.27c, the masses for the weak vector bosons are found to be:

$$m_W = \frac{gv}{2} , \quad m_Z = \frac{\sqrt{g^2 + g'^2}v}{2} \text{ and } \quad m_\gamma = 0 , \tag{2.37}$$

and the following relation holds:

$$\frac{m_W}{m_Z} = \cos\theta_W . \tag{2.38}$$

From the Fermi constant, the value of the vacuum expectation value of the Higgs field can be obtained as follows:

$$G_F = \frac{\sqrt{2}g^2}{8m_W^2} = \frac{1}{\sqrt{2}v^2} \Rightarrow v = 246 \text{ GeV} . \tag{2.39}$$

2.2.1. The case of fermion masses

Fermion masses are introduced in the SM Lagrangian density via a Yukawa term, that preserves the $SU(2)_L \otimes U(1)_Y$ symmetry. For example, for the case of electrons:

$$\mathcal{L}_{m_e} = -y_e(\bar{l}_L\phi e_R + \bar{e}_R\phi^\dagger l_L) , \tag{2.40}$$

in the case of the electron, with l_L referring only to the first family of left-handed lepton spinors, and y_e the strength of the electron Yukawa coupling. For ϕ of the form:

$$\phi = \frac{1}{\sqrt{2}} \begin{pmatrix} 0 \\ v + h(x) \end{pmatrix} , \tag{2.41}$$

the Lagrangian density takes the form:

$$\mathcal{L}_{m_e} = -\frac{y_e v}{\sqrt{2}}(\bar{e}_L e_R + \bar{e}_R e_L) - \frac{y_e h}{\sqrt{2}}(\bar{e}_L e_R + \bar{e}_R e_L) , \tag{2.42}$$

from which the value of the electron mass is clear:

$$m_e = \frac{y_e v}{\sqrt{2}} . \tag{2.43}$$

The coupling to the Higgs boson is thus proportional to the mass of the fermions. It has a similar expression for all of them.

2.3. The Higgs mass

The observation of a scalar boson of mass $\sim$125 GeV, consistent with the one described by the BEH mechanism by the ATLAS and CMS experiments in July 2012 [29, 30], has shed light on the unknown mass of this particle. The BEH mechanism in the SM Lagrangian does not predict a precise value for the mass of the scalar boson. Some constraints [31] on it can be derived from the theory, and will be described here.

Three bounds, one lower, and two upper, on the Higgs boson mass value are derived from theoretical considerations.

- The stability bound sets a lower limit on m_H, requiring the stability of the vacuum state.
- The unitarity bound sets an upper limit on m_H, requiring the unitarity of the scattering amplitudes of W bosons.
- The triviality bound sets again an upper limit on m_H, asking for the Higgs self coupling at high energies not to diverge.

The stability bound [32–35] originates from the renormalisation group equations (RGE) at one loop, describing the dependence of λ on the energy scale Q at which it

is evaluated. At low energies, λ is strongly dependent on the Yukawa coupling to the massive top quark, via a quartic term. The potential at one loop has the form:

$$V_{\text{eff}} = \mu^2\phi^\dagger\phi + \lambda(Q)(\phi^\dagger\phi)^2 \ . \tag{2.44}$$

Imposing the Higgs quartic coupling λ to be positive ($\lambda(Q) > 0$) avoids the case of an unstable ground state of the potential, and gives a lower bound on $m_H > 2\lambda v^2$.

The unitarity bound [36–39] arises from the study of scattering amplitudes in case of longitudinally polarised vector bosons. In the high energy limit ($s \gg m_V^2$), it is possible to express the scattering amplitude as follows:

$$A(W_L^+W_L^- \to W_L^+W_L^-) = -2\sqrt{G_F}m_H^2\left(\frac{s}{s-m_H^2} + \frac{t}{t-m_H^2}\right) \ . \tag{2.45}$$

Such amplitude grows as a function of s and t for $m_H \to \infty$. Large values of m_H lead therefore to unitarity violation. Considering the decomposition of the amplitudes in partial waves of spin l, in the case of $l = 0$ and in the high energy limit $s \gg m_H^2$, the following expression holds:

$$a_0 = -\frac{G_F m_H^2}{4\pi\sqrt{2}} \ . \tag{2.46}$$

The unitarity condition $|a_0|^2 \leq |\text{Im}\, a_0|$ leads to:

$$|\text{Re}\, a_0| < \frac{1}{2} \quad \Rightarrow \quad m_H < \frac{C}{\sqrt{G_F}} \ , \tag{2.47}$$

where C is a constant multiplicative factor. This calculation leads to an upper limit on m_H of the order of 850 GeV.

The triviality bound [32] is related again to the RGE for the Higgs quartic coupling $\lambda(\mu)$:

$$\frac{d\lambda}{d\log\mu^2} = \frac{3}{8\pi}(\lambda^2 + \lambda y_t^2 - y_t^4) + \mathcal{O}(e^2) + \mathcal{O}(y_f^2) \ . \tag{2.48}$$

This equation has a Landau pole, leading to the need of defining a cutoff scale, Λ, below which the theory is valid. This sets as a consequence an upper limit on the Higgs mass, illustrated, together with the stability lower bound, in fig. 2.2, as a function of the cutoff scale Λ, at which new physics is expected.

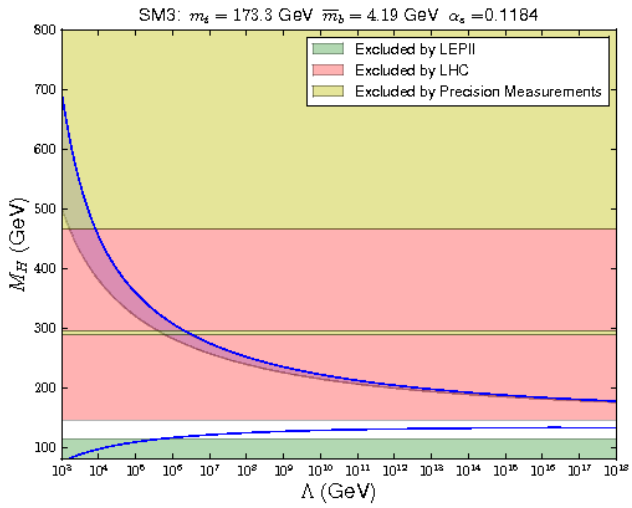

Figure 2.2.: Illustration of the stability lower bound and the triviality upper bound on the Higgs mass, from [40]. The horizontal lines indicate exclusions from LEP and LHC before the July 2012 observation [29, 30], and electroweak precision measurements of the other parameters of the SM theory.

2.4. Production mechanisms and decays of the SM Higgs boson

The Standard Model Higgs boson can be produced and decay through different channels, that can be evaluated directly from the Lagrangian of the theory. These production and decay modes will be described in detail in the following.

2.4.1. Higgs production mechanisms

Fig. 2.3 illustrates the SM Higgs production mechanisms at the LHC for centre of mass energies of 7 and 8 TeV [41–43]. The dominant production mechanism of the SM Higgs boson at the LHC is via gluon fusion: $pp \to gg \to H$. Gluons do not couple directly to the Higgs boson, and at the lowest order the production is mediated by a fermion loop, as illustrated in fig. 2.4a. The greatest contribution comes from the top quark, as the ffH coupling is proportional to the fermion mass. The cross section of this process is know at the next-to-next-to leading order (NNLO) in QCD, with a $\sim 10\%$ uncertainty.

The second production mode, in order of decreasing rate, is the Vector Boson Fusion (VBF) process $pp \to qq \to qqV^*V^* \to qqH$. This process has a very distinct signature

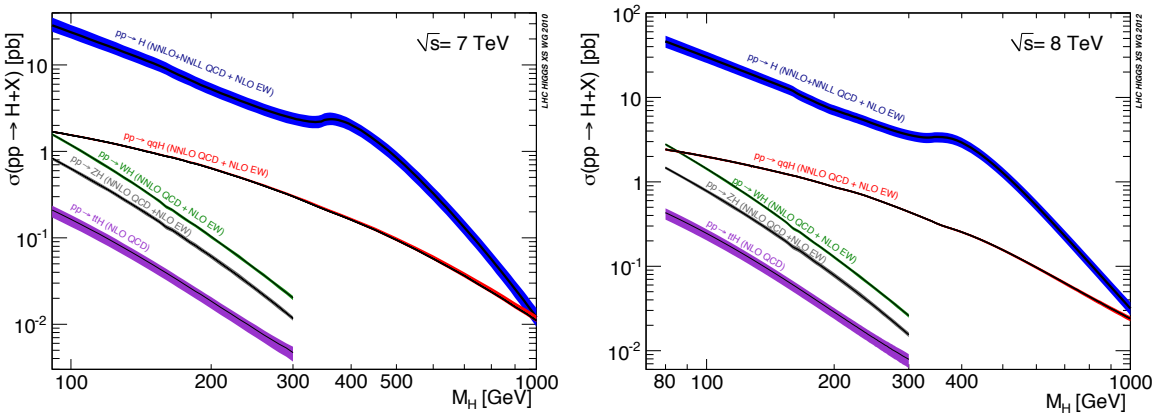

(a) $\sqrt{s} = 7$ TeV **(b)** $\sqrt{s} = 8$ TeV

Figure 2.3.: Standard model Higgs boson production cross sections versus the mass of the Higgs boson M_H for the different production modes for LHC energies of $\sqrt{s} = 7$ TeV 2.3a and $\sqrt{s} = 8$ TeV 2.3b, taken from [41].

the ATLAS detector. The two quarks from the initial state result in two highly energetic jets almost collinear to the proton beams. The Feynman diagram of this process is shown in fig. 2.4b. The cross section is known at next-to-leading order (NLO) with a $\sim 10\%$ uncertainty.

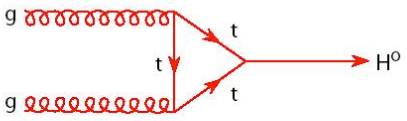

(a) Gluon fusion (ggF) Higgs production

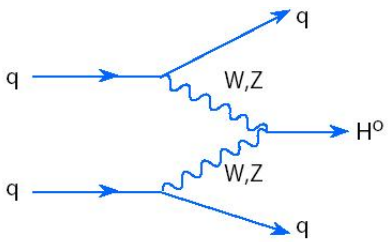

(b) Vector boson fusion (VBF) Higgs production

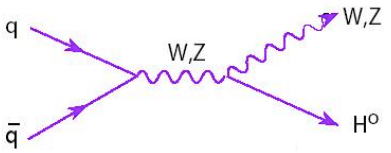

(c) Vector boson associated Higgs production (VH)

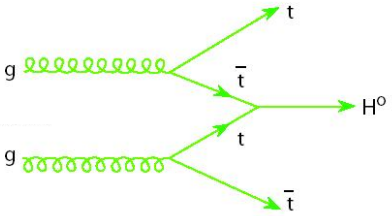

(d) $t\bar{t}$ associated Higgs production

Figure 2.4.: The Feynman diagrams of the main SM Higgs boson production modes: gluon fusion (2.4a), VBF (2.4b), vector boson associated production (2.4c) and $t\bar{t}H$ (2.4d).

The Higgsstrahlung process, i.e. the associated production of a vector boson and a Higgs ($pp \to q\bar{q} \to V \to VH$), illustrated in fig. 2.4c, has a lower cross section than VBF production, and presents again a clean signature in the detector, with two massive particles, that can be identified through their decay products. The cross section of this process is known at NNLO with a 5% accuracy.

An interesting production mechanism, although with a much lower cross section, is the associated production of a Higgs boson with a top quark pair: $pp \to gg \to t\bar{t}t\bar{t} \to t\bar{t}H$, shown in fig. 2.4d. This process is a direct probe of the coupling of the Higgs with fermions. It presents a difficult signature in the detector, with two W bosons, two b quarks and a Higgs boson, making it an extremely challenging mode from the experimental point of view.

2.4.2. Higgs decay modes

The Standard Model Higgs boson has several decay channels, at rates determined by the couplings. The various modes and their branching ratios (BR) are illustrated in fig. 2.5.

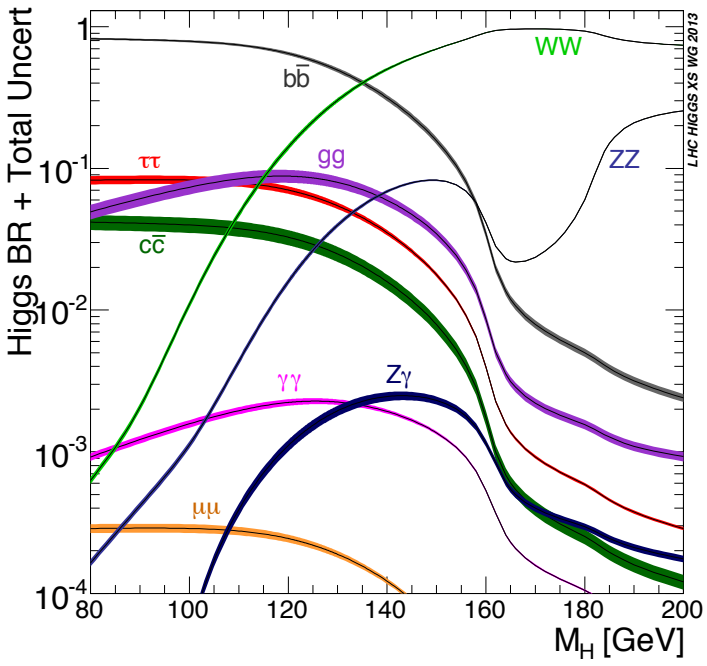

Figure 2.5.: The Standard Model Higgs boson decay branching ratios versus the mass of the Higgs boson M_H, for Higgs masses between 80 and 200 GeV [41].

For a 125 GeV mass Higgs boson, the dominant decay mode is to b quark pairs. This mode is not easily detectable at hadron colliders using all the production mechanisms. More details on this process will be given in sec. 2.5.

The second highest decay rate is that of W boson pair production, where one of the bosons is off-shell. This decay channel can be exploited in all the production modes, but is experimentally challenging. As in the $b\bar{b}$ case, it can present large hadronic activity in the detector in case of W decaying to quarks, or high missing transverse energy values in the case of leptonic decays, because of the presence of neutrinos in the final state. The m_H peak is expected to be broad, because of the large experimental resolution of the missing transverse energy.

The gluon pair decay, the third largest, is not distinguishable from the backgrounds, therefore will not be treated. The next largest mode is the τ lepton pair production. Experimentally difficult, because of the presence of final state neutrinos ($E_{\mathrm{T}}^{\mathrm{miss}}$), and the difficulty in discriminating hadronically decaying τ leptons from light-quark jets, it can be exploited in all the production modes.

The charm quark pair production has an extremely low rate and a hardly detectable signal, dominated by $g \to c\bar{c}$ production and the difficulty in tagging charm jets. This channel will therefore not be treated. The ZZ^* production, instead, with a very similar rate to $c\bar{c}$, has a very clean signature in the detector, when considering the charged leptonic Z decays. This choice causes a further reduction in the production rate, but represents an almost background-free process. All the production modes and decay channels can be exploited in this analysis, and the $H \to Z^*Z \to 4\ell$ is known as the "golden channel".

The $\gamma\gamma$ production is a very low-rate but relatively clean process. It is mediated by a top quark or W boson loop, as shown in fig. 2.6, and can be identified against a smooth background of photon pair production. A similar process, but at an even lower rate, is $Z\gamma$ production. The $\mu\mu$ decay process has a very low rate and is the best decay channel to probe the coupling of the Higgs boson with fermions of the second family.

2.5. H $\to$ b$\bar{\text{b}}$ phenomenology

The $H \to b\bar{b}$ channel is one of the most important for the search of a SM Higgs boson. For a Higgs boson with a mass of around 125 GeV, the highest decay rate predicted by the

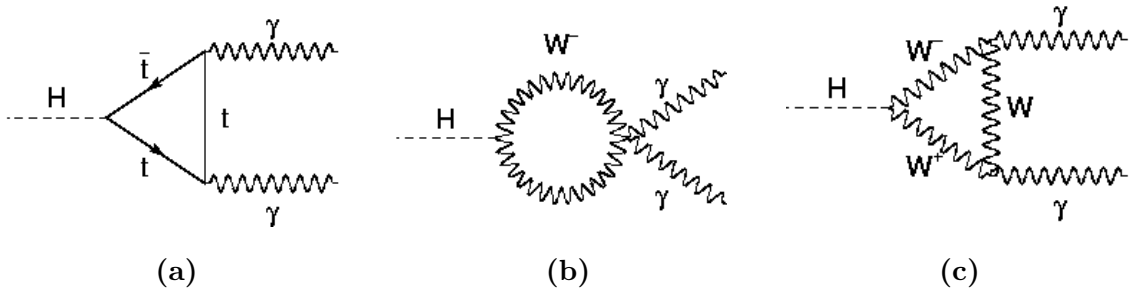

(a) (b) (c)

Figure 2.6.: Feynman diagrams of the Higgs decay to a pair of photons, showing the t and W mediating loops.

Standard Model is to b quark pairs ($BR \approx 58\%$ [41]). The gluon fusion production mode cannot be exploited, given the large $b\bar{b}$ pair production which constitutes an irreducible background with several orders of magnitude higher cross section, as can be seen in fig. 2.7.

It is thus necessary to exploit the other production modes, which take place at a lower rate, but have additional particles in the final states, providing more distinct signatures to trigger, identify and discriminate. Searches in the VBF, VH and $t\bar{t}H$ modes are being and have been carried out with $b\bar{b}$ final states. The most significant results can be obtained via the VH mode, when the vector boson V decays to leptons. This allows to efficiently trigger on the events, using the leptons, and reduces the background from strong interactions. The VBF $H \to b\bar{b}$ process presents a rather complex final state, with four jets, and a large background from QCD events. The $t\bar{t}H(H \to b\bar{b})$ mode has a challenging final state, with up to eight jets and four b-jets, and a lower production rate.

2.5.1. VH →leptons +bb̄ phenomenology

The $VH \to \text{leptons} + b\bar{b}$ process, that from now on will be referred to as $VH(b\bar{b})$, has three possible final states, where the W decays to $\ell\nu$, and the Z decays either to $\ell^+\ell^-$ or to $\nu\bar{\nu}$, as shown in fig. 2.8. The typical signature in the detector consists of a pair of b-jets produced together with charged electron(s) or muon(s) and/or large missing transverse energy coming from the undetected neutrinos. Despite the lepton final states, these processes still have large backgrounds, overwhelming the signal. Such backgrounds are largely common across the three channels, but they contribute in different proportions in each. Details of the background treatment and their fractions in each channel will be

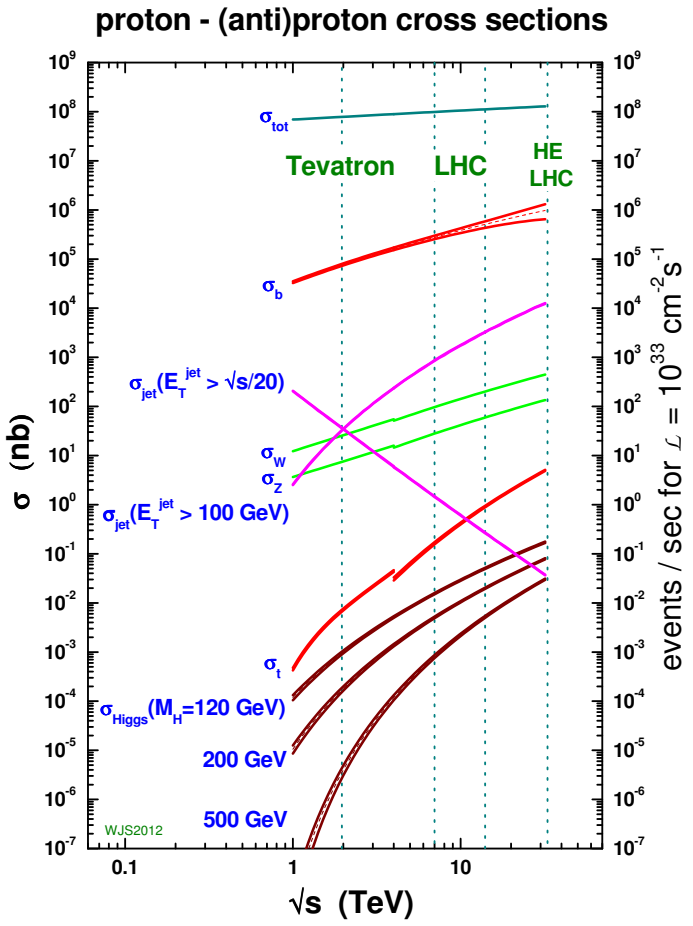

Figure 2.7.: Production rates for signal and background processes at hadron colliders, as a function of the centre of mass energy of the collisions [44].

given in the following chapters, while here only a general description of the backgrounds and how they appear in the detector is presented.

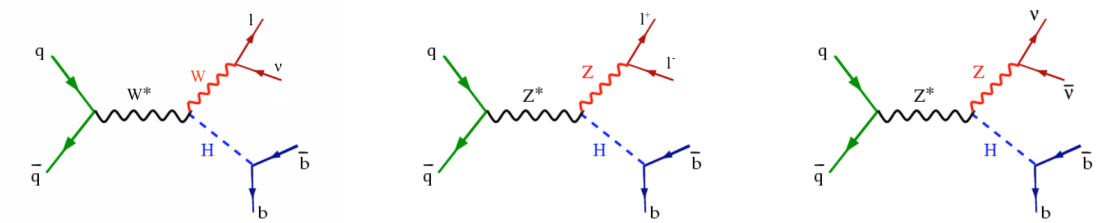

(a) $WH \to \ell\nu b\bar{b}$ **(b)** $ZH \to \ell^+\ell^- b\bar{b}$ **(c)** $ZH \to \nu\bar{\nu} b\bar{b}$

Figure 2.8.: Feynman diagrams for the three possible decay channels of the $VH(b\bar{b})$ process.

The main backgrounds to this search are the production of a vector boson in association with jets (particularly b-jets) and $t\bar{t}$. Other backgrounds come from resonant VV production, single top production and QCD events with high jet multiplicity in the final state. In the following, details on how they can be misidentified as the signal will be given.

The V+jet background, when the final state includes exactly two b-jets, is an irreducible background for the $VH(b\bar{b})$ search. The $Wb\bar{b}$ and $Zb\bar{b}$ production diagrams at tree level are shown in fig. 2.9, corresponding to the three processes: $q\bar{q}' \to Wb\bar{b}$, $q\bar{q} \to Zb\bar{b}$ and $gg \to Zb\bar{b}$. Other combination of jet flavours in the final state can constitute a background to the VH search: bl, $c\bar{c}$, cl and two light-quark jets (l refers to light-quark jets). In these cases, the background comes from the misidentification of the light and c-jets as b-jets. Therefore, the rejection of such backgrounds is strongly influenced by the purity achieved by the employed b-tagging algorithms.

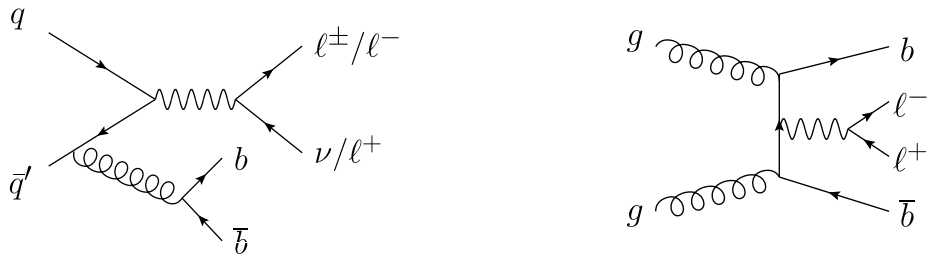

(a) $q\bar{q}$ initial state **(b)** gg initial state

Figure 2.9.: Feynman diagrams of $Wb\bar{b}$ and $Zb\bar{b}$ production. As shown in 2.9b, only the latter can be produced with initial gluon states [45].

Top pair production is a very large background, as can be seen in fig. 2.7. It is reducible though, and different techniques can be employed to minimise its contribution. A typical $t\bar{t}$ event has a very rich final state in terms of number of jets and missing transverse energy. The top quark decays to Wb, as shown in fig. 2.10, therefore the $t\bar{t}$ decay signatures can be:

- di-leptonic: both W bosons decay to $\ell\nu$, giving a final state with two b-jets, large $E_{\mathrm{T}}^{\mathrm{miss}}$ and two oppositely charged leptons;
- semi-leptonic: one of the W bosons decays to leptons, and the second to hadrons, resulting in a final state with one charged lepton, significant $E_{\mathrm{T}}^{\mathrm{miss}}$ and four jets, of which two are b-jets;

- hadronic: both W bosons decay to hadrons, producing a final state with six jets, two of which are b-jets.

The first two cases are the main background to the $VH(b\bar{b})$ search. An effective cut to suppress $t\bar{t}$ background is the veto on the presence of extra-jets, additional to the two b-tagged ones, in the selected events. Also, at high vector boson transverse momenta, when the production energy is high and the laboratory and rest frames almost coincide, the $t\bar{t}$ background is strongly suppressed. This happens because the two b-jets are produced from two recoiling top quarks, while in the $VH(b\bar{b})$ case they are more collimated. Therefore, an angular cut on the b-jet pair distance is effective in rejecting this background. In the high momentum case, the main background comes from a misidentified c-jet from the W decay, very close to the b-jet from the same top decay, therefore a b-tagging algorithm with high purity can further reduce this background.

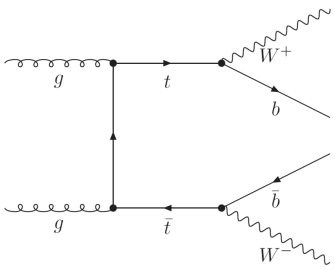

Figure 2.10.: Feynman diagram of $t\bar{t}$ production and decay.

WW, ZZ and WZ events, often referred to as diboson, are an important background to this search. WW acts as a background in the case of its $l\nu qq$ decay, but it is a small contributing background, strongly dependent on the purity reached by the b-jet identification algorithm. In fact, real b-jets are typically not produced in W hadronic decays, and most of the background comes from $W \to sc$ decays, mis-identified as b quarks. VZ (WZ and ZZ) production has the same signature as the $VH(b\bar{b})$ process: leptons + $b\bar{b}$, but with a production cross section ~ 5 times larger. The invariant mass of the two b-jets coming from the Z peaks at lower values than the expected Higgs mass. There is a region where the tails of the two peaks overlap, and the amount of contamination is dependent on the mass resolution achieved. This is generally rather poor, if compared to the $H \to \gamma\gamma$ or $H \to Z^{(*)}Z \to 4\ell$ channels, as it is determined by the jet energy resolution. Typical values and techniques used in ATLAS to improve and reduce the mass resolution are described in chapt. 6.

Single top production can take place in three different ways at tree level:

- s-channel: a top and a bottom quark are produced together via a virtual W, fig. 2.11a;
- t-channel: a top is produced in association to a bottom and a light quark, fig. 2.11b;
- Wt: where a top quark is produced in association with a W boson via an s- or t-channel, fig. 2.11c and 2.11d.

All these cases present final states with at least one W boson and at least one b-jet, producing often a fake $VH(b\bar{b})$ signal topology. In these cases, analogously to what mentioned for $t\bar{t}$ production, an angular cut between the b-jets at high p_{T} can reduce the contributions.

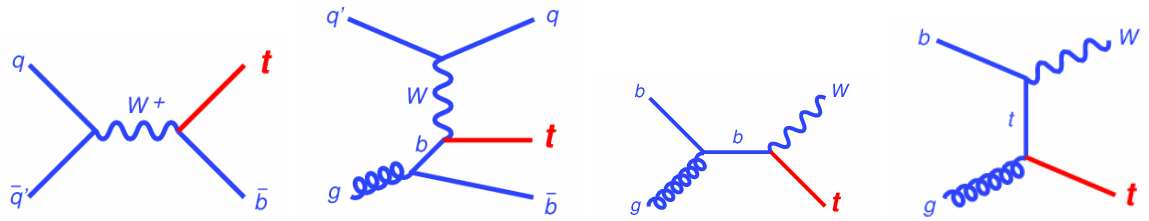

(a) s-channel **(b)** t-channel **(c)** Wt s-channel **(d)** Wt t-channel

Figure 2.11.: Feynman diagrams illustrating the different production modes of single top quarks [46].

The QCD multijet background can partially affect this search, mostly because of the large production rate. Light quark jets can, for example, fake electrons, and b-jets produce both $E_{\mathrm{T}}^{\mathrm{miss}}$ and muons in their decays. It is therefore important to identify leptons isolated from additional activity on the detector, to discriminate between the V decay products and the QCD background. All these cases are relevant mostly for the $WH \to \ell\nu b\bar{b}$ decay mode, and become negligible when raising the W boson p_{T} threshold.

Chapter 3.

The LHC and the ATLAS experiment

The LHC (Large Hadron Collider) [47] is the largest particle accelerator ever built. The main goal of the LHC was the Higgs boson discovery and the search for new physics. It hosts four large experiments: ATLAS (A Toroidal LHC ApparatuS) [1] and CMS (Central Muon Solenoid) [2], both multipurpose experiments; ALICE (A Large Ion Collider Experiment) [48] dedicated to the study of Pb-ion and p-Pb collisions to understand quark-gluon plasma physics, and LHCb [49] designed to study heavy flavour physics, with particular attention to CP violation in B meson decays. It also hosts two additional smaller experiments, dedicated to forward physics and high energy cosmic ray studies: LHCf [50] and TOTEM [51]. A general overview of the LHC, and a more detailed one at the ATLAS experiment, will be given in this chapter.

3.1. The large hadron collider

The Large Hadron Collider (LHC) is a superconducting proton synchrotron hosted in the 27 km long tunnel previously occupied by the LEP (Large Electron-Positron collider) at CERN. It is designed to accelerate two beams of protons (or heavy ions) travelling in opposite directions up to 7 TeV (2.76 TeV per nucleon). The design instantaneous luminosity, indicating the rate of the collisions per unit area, is 10^{34} cm^{-2}s^{-1}.

The acceleration chain begins with a LINAC, bringing protons to 50 MeV and injecting them into the Proton Synchrotron Booster (PSB). This increases the proton energy up to 1.8 GeV, feeding them into the Proton Synchrotron (PS), reaching 26 GeV. The last ring of the injection chain is the Super Proton Synchrotron (SPS), which provides acceleration for protons up to 450 GeV and injects them into LHC. The LHC accelerated

the proton beams to 1.18 TeV, 3.5 TeV and 4 TeV during the Run 1 data taking period, which started in November 2009, and ended in February 2013. The accelerating chain layout is shown in figure 3.1.

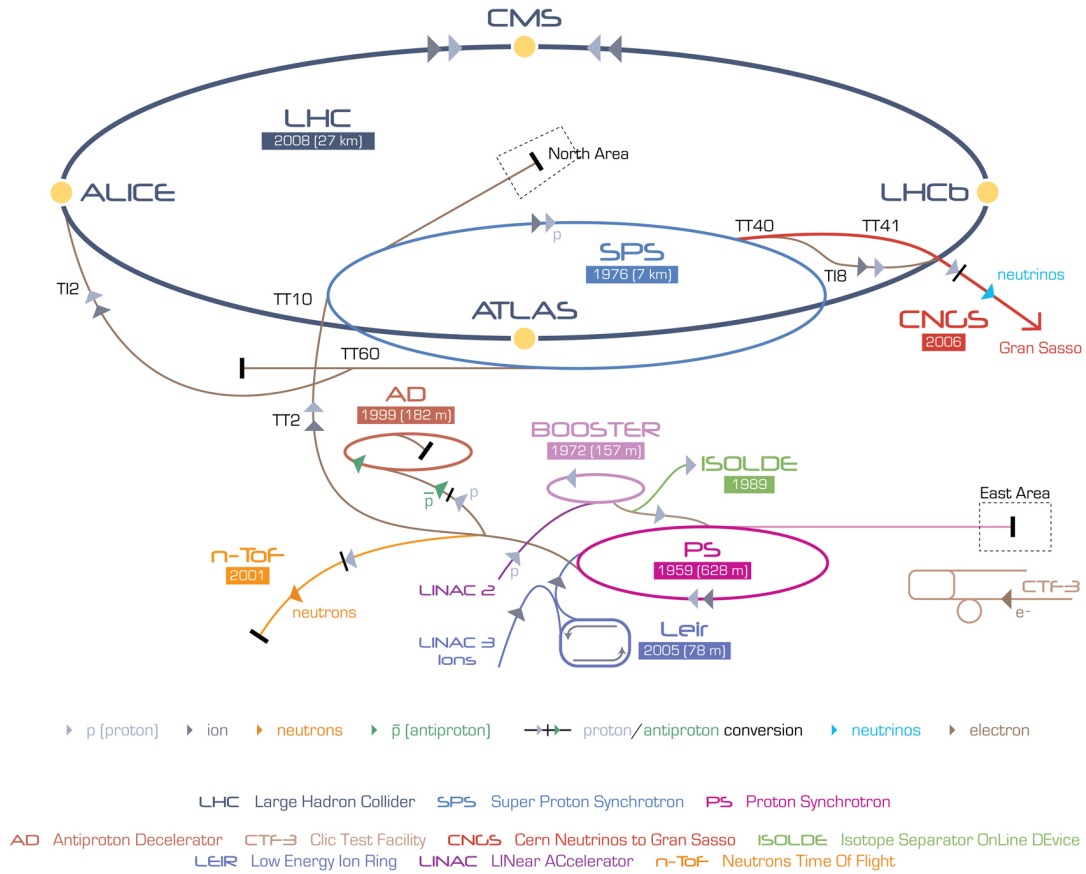

Figure 3.1.: Overview of the CERN accelerator complex.

The LHC dipole magnets have two different magnetic channels, housed in one single twin bore magnet with the same cryostat and yoke. The magnetic field provided is 8.33 T, necessary for the design centre of mass energy of 14 TeV. The LHC design luminosity can be reached with 2808 bunches made up of 10^{11} protons each, crossing every 25 ns, corresponding to a spatial separation of 7.5 m.

The integrated luminosity in a scattering process is defined as the ratio between the observed number of produced events, N, and the production cross section of the process, σ: $L = N/\sigma$. It corresponds to the integral over a time period T of the instantaneous luminosity $\mathcal{L}$:

$$L = \int_0^T \mathcal{L} \mathrm{d}t \ . \tag{3.1}$$

It can also be expressed as a function of the characteristic parameters of the collider considered:

$$L = \frac{F n_b N_b^2 f_{\text{rev}} \gamma_r}{4\pi\beta^* \epsilon_n} \ . \tag{3.2}$$

Here, F is a geometric factor determined by the crossing angle between the two beams, n_b corresponds to the number of bunches circulating in the machine, f_{rev} is the frequency of revolution, N_b the number of protons in a bunch, γ_r the relativistic gamma factor, ϵ_n the normalised transverse beam emittance, and β^* the beta function at the collision point. The factor F can be expressed as a function of the crossing angle θ_c:

$$F \approx \frac{1}{\sqrt{1 + \left(\frac{\theta_c \sigma_z}{2\sigma^*}\right)^2}} \ , \tag{3.3}$$

with $\theta_c \lesssim 300$ µrad, σ_z the RMS length of the bunch and σ^* the RMS beam width at the interaction point. The LHC design parameters are shown in table 3.1.

Parameter	Value
n_b	2808
N_b	1.15×10^{11}
ϵ_n	3.57 µm
f_{rev}	11245 kHz
σ^*	16.7 µm
θ_c	285 µrad
σ_z	7.55 cm
F	0.84

Table 3.1.: LHC design parameters [47].

On November 20$^{\text{th}}$ 2009, the first proton beam was injected into the LHC with an energy of 450 GeV. Subsequently, on the 23$^{\text{rd}}$, the first collision at $\sqrt{s} = 900$ GeV took place. After a very short running period, the LHC registered the centre of mass energy world record, reaching 2.36 TeV. Between November 10$^{\text{th}}$ and December 16$^{\text{th}}$ 2009, the first data at 900 GeV were collected and analysed by the LHC experiments. After the winter shutdown, on the 31$^{\text{st}}$ of March 2010, the LHC began p-p collisions at $\sqrt{s} = 7$ TeV, which lasted until the end of 2011. The total delivered integrated luminosity to ATLAS in the $\sqrt{s} = 7$ TeV data taking period is 5.6 fb^{-1}, as shown in fig. 3.2a, with a peak instantaneous luminosity of 3.65×10^{33} cm^{-2}s^{-1}, illustrated in fig. 3.2c. During 2012, LHC collided protons at $\sqrt{s} = 8$ TeV, delivering to ATLAS an integrated luminosity

of 23.3 fb^{-1}, shown in fig. 3.2b. The maximum instantaneous luminosity reached was 7.73×10^{33} cm^{-2}s^{-1}, as can be seen in fig. 3.2d.

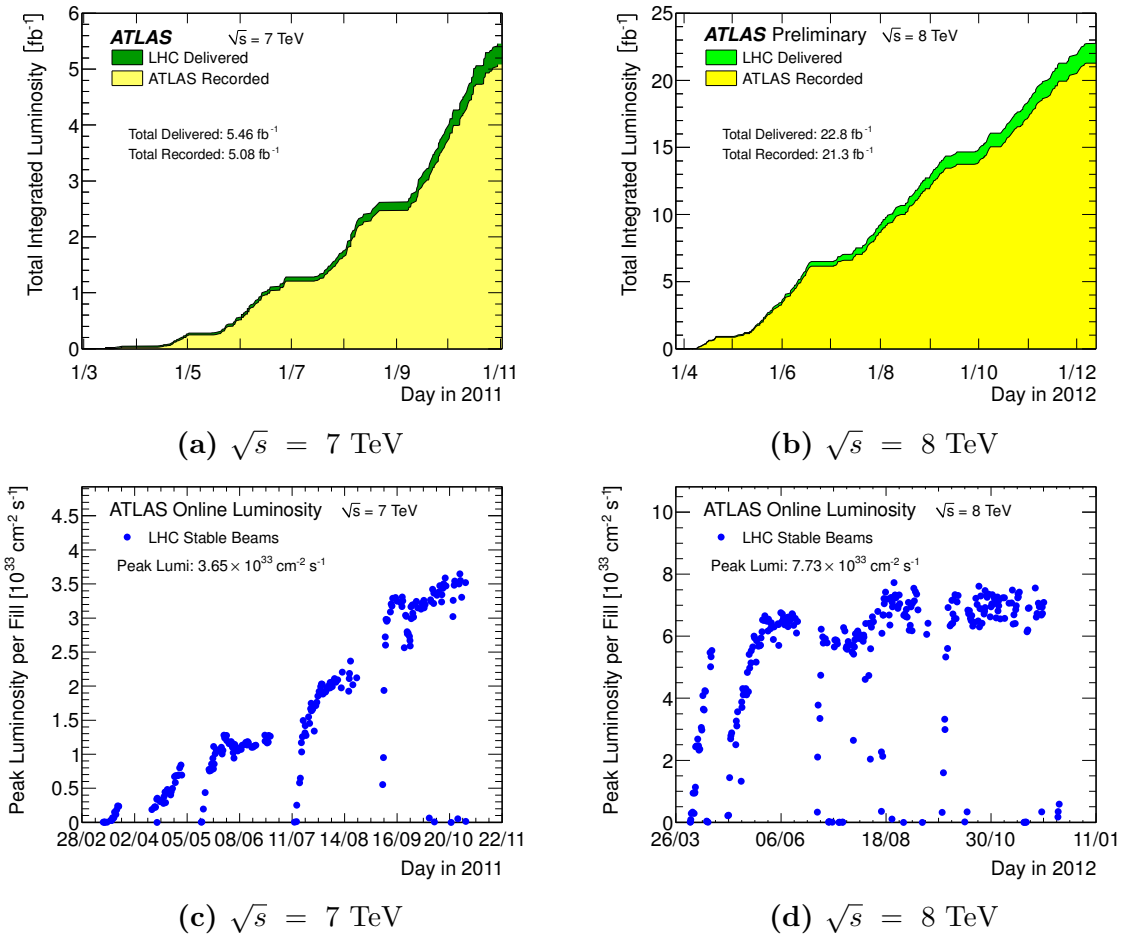

(a) $\sqrt{s} = 7$ TeV **(b)** $\sqrt{s} = 8$ TeV

(c) $\sqrt{s} = 7$ TeV **(d)** $\sqrt{s} = 8$ TeV

Figure 3.2.: Integrated (3.2a,3.2b) and instantaneous (3.2c,3.2d) luminosity for the $\sqrt{s} = 7$ TeV and $\sqrt{s} = 8$ TeV ATLAS data taking period, as a function of time.

The LHC is planned to restart beam circulation in 2015, for the new data taking run: Run 2. The foreseen centre of mass energy is 13 TeV, and bunches are expected to be injected with 25 ns spacing.

3.2. The ATLAS detector

The ATLAS [1] detector is installed at Point 1 of the LHC. The origin of the right-handed coordinate system is centred on the nominal interaction point and the z axis corresponds to the beam direction. The transverse $x - y$ plane is defined with the

positive x axis pointing from the origin to the centre of the LHC ring. The azimuthal (φ) and polar (θ) angles are defined with respect to the z axis as conventional cylindrical coordinates. The polar angle is generally substituted by the pseudorapidity, η, defined as $\eta = -\ln(\tan(\theta/2))$, for which a convenient property holds. The $\Delta\eta$, defined as $\eta_1 - \eta_2$ for two detected objects 1 and 2, is invariant under Lorentz boost along the z axis.

The ATLAS subdetectors are arranged radially (tracker, calorimeters, muon chambers) from the interaction point up to a radius of about 25 m. The ATLAS detector is 44 m long and weighs 7 kt, and it is illustrated in fig. 3.3.

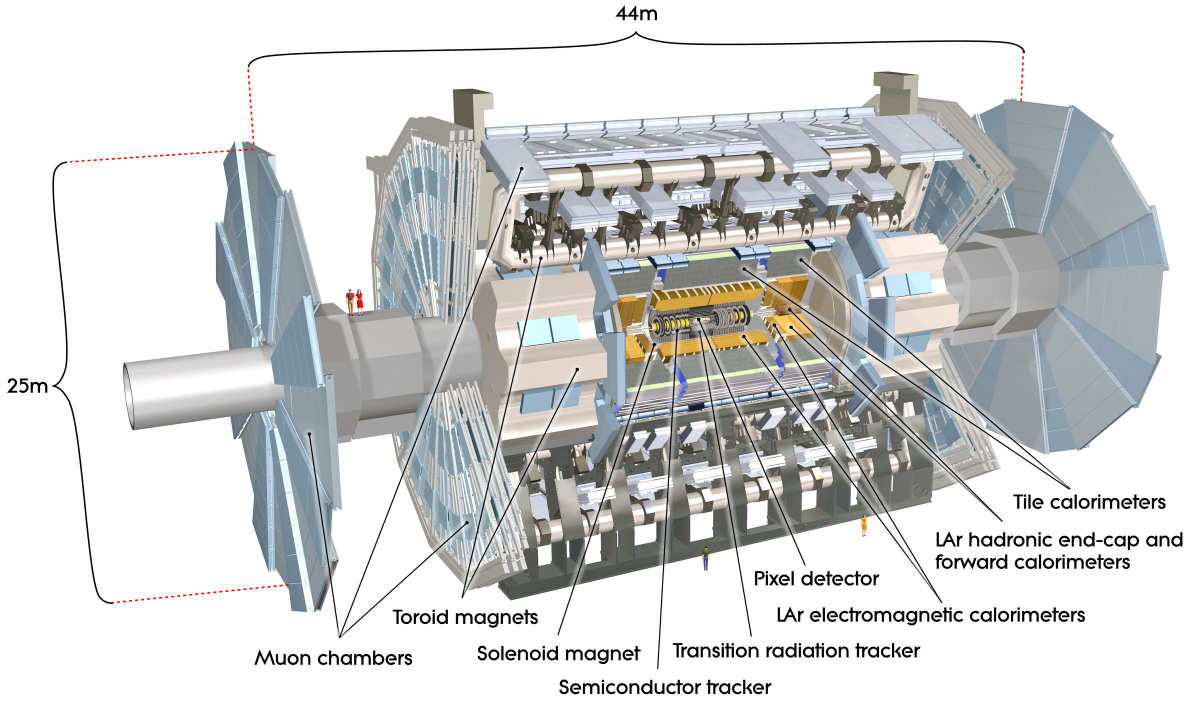

Figure 3.3.: Schematic view of the ATLAS detector [1].

3.2.1. Physics requirements

In the LHC high-energy environment, it is possible to study a large number of physics processes. High precision tests of QCD, flavour physics and electroweak processes can be performed, such as dedicated studies of the top quark coupling. The Higgs boson can be studied in several production and decay channels, and its Standard Model nature can be tested against new physics hypotheses. A wide spectrum of new physics phenomena, from SUSY to heavy gauge bosons, to quark compositeness, can be tested. All these

phenomena can be identified via their decay modes, and the subdetectors are designed to resolve them as well as possible. Fig. 3.4 shows the interactions of particles within the various ATLAS detector volumes, described in detail below.

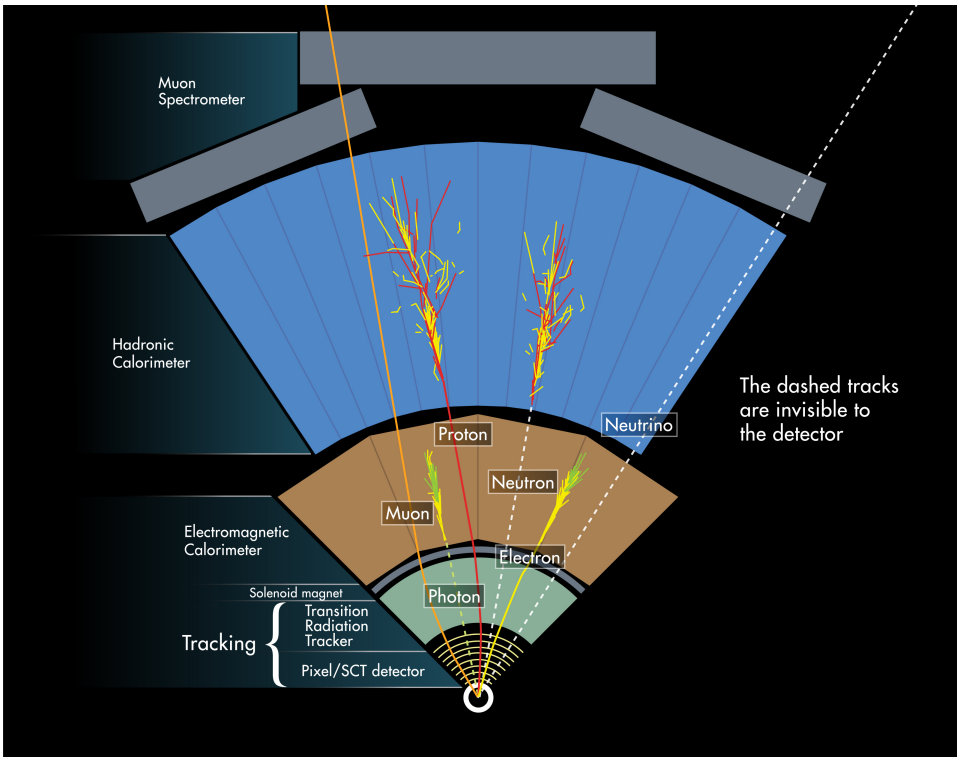

Figure 3.4.: Interaction of the different particles with the ATLAS detector active volumes.

To detect electrically charged particles, the Lorentz force is used, and magnetic fields are employed to bend their trajectories. This way, their electrical charge and momentum can be measured. To detect such trajectories, silicon or gaseous detectors can be employed, using the signal from material ionisation caused by the particle travelling through them. This signal is generally referred to as hit and indicates the spatial coordinate of the particle interaction. An energetic charged particle produced in a collision travels enough to leave several hits in the tracking detectors, from which the particle trajectory can be reconstructed. The high luminosity at the LHC implies the production of many particles, therefore a precise spatial resolution for hits is needed for the tracking detector, which are generally placed close to the interaction point. The tracking detectors also reconstruct the originating collision vertex, or primary vertex (PV), and possible secondary interactions (via the secondary vertices, SV) coming either from long-lived particle decays, like the case of heavy flavour hadrons or τ leptons, or from interactions taking place in the proton bunch (pileup).

Charged particles also undergo electromagnetic (EM) interactions and can radiate photons via the bremsstrahlung process. This process has a higher rate in the case of electrons, and photons above the energy threshold $2m_e$ can produce electron pairs, giving rise to electromagnetic showers. Electromagnetic calorimeters are designed to detect these showers using scintillating material. Electromagnetic shower longitudinal development is described in units of the radiation length X_0, and the calorimeters are designed to contain showers from highly energetic photons and electrons.

Strongly interacting particles, hadrons, undergo inelastic nuclear processes when encountering heavy nuclei, producing hadronic showers in heavy materials. These showers are characterised in units of the interaction length λ, and the hadronic calorimeters are designed to contain highly energetic hadron showers. Charged hadrons undergo electromagnetic interactions in the electromagnetic calorimeter, too, therefore a good detector needs to achieve a ratio between electron and hadron detection efficiency, e/h, close to unity. The energy deposits in the calorimeters, coming from a gluon, τ lepton or quark-initiated shower, are clustered to form jets, introduced in sec. 2.1.3.

Muons only interact electromagnetically and weakly with matter, releasing minimum ionisation energy in the calorimeters. Therefore, they can penetrate the calorimeters, retaining most of their energy. They are detected by muon chambers, placed outside the calorimeters. These are tracking chambers, and the information from them is combined with that from the inner tracker.

The neutrino interaction cross section with the typical material of a detector in a collider experiment is extremely low. Therefore, neutrinos are generally identified exploiting the momentum conservation in the transverse plane: ${p_{\mathrm{T}}}^{\nu} = -\sum_i \overrightarrow{p_{\mathrm{T}}}^i$, where i are all the reconstructed particles in the event. p_{T}^{ν} is generally referred to as $p_{\mathrm{T}}^{\mathrm{miss}}$, the missing transverse momentum.

The different particle signatures and the methods used for particle identification provide the main requirements for a multi-purpose detector like ATLAS. They are:

- fast, radiation hard electronics and sensors, and high granularity detectors to handle high particle rate and overlapping events (pileup);
- need for the largest possible pseudorapidity acceptance and full azimuthal coverage;
- good resolution and reconstruction efficiency for charged particles in the tracker;

- precise impact parameter resolution in the high radiation dose environment close to the interaction point for secondary vertex reconstruction, aimed at identifying b-jets and τ leptons;
- efficient identification and measurement of photons and electrons in the electromagnetic calorimeter;
- maximal hadronic calorimeter coverage for precise measurements of jets and missing transverse energy;
- good muon identification and momentum resolution for the widest possible range of momenta;
- fast and flexible trigger, to identify interesting events in wide transverse momentum ranges.

The expected performance parameters for each subdetector are listed in table 3.2. In the following sections, the detector components will be described in detail.

Detector component	Required resolution	η coverage	
		Measurement	Trigger
Tracking	$\sigma p_{\mathrm{T}}/p_{\mathrm{T}} = 0.05\%\ p_{\mathrm{T}} \oplus 1\%$	± 2.5	
EM calorimeter	$\sigma_E/E = 10\%/\sqrt{E} \oplus 0.7\%$	± 3.2	± 2.5
Hadronic calorimeter			
barrel and endcap	$\sigma_E/E = 50\%/\sqrt{E} \oplus 3\%$	± 3.2	± 3.2
forward	$\sigma_E/E = 100\%/\sqrt{E} \oplus 10\%$	$3.1 < \lvert\eta\rvert < 4.9$	$3.1 < \lvert\eta\rvert < 4.9$
Muon spectrometer	$\sigma p_{\mathrm{T}}/p_{\mathrm{T}} = 10\%$ at $p_{\mathrm{T}} = 1\,\mathrm{TeV}$	± 2.7	± 2.4

Table 3.2.: Design performance parameters of the ATLAS detector. E and p_T are expressed in units of GeV.

3.2.2. Magnet systems

The ATLAS superconducting magnet system is composed in two parts: a central solenoid and external toroids. The structure of the system is shown in fig. 3.5.

The central superconducting solenoid provides a magnetic field of 2 T along the beam axis. It is designed to minimise the amount of the material in front of the calorimeter, achieving $\sim 0.66 X_0$ for normally incident particles. For this reason, it is housed in the

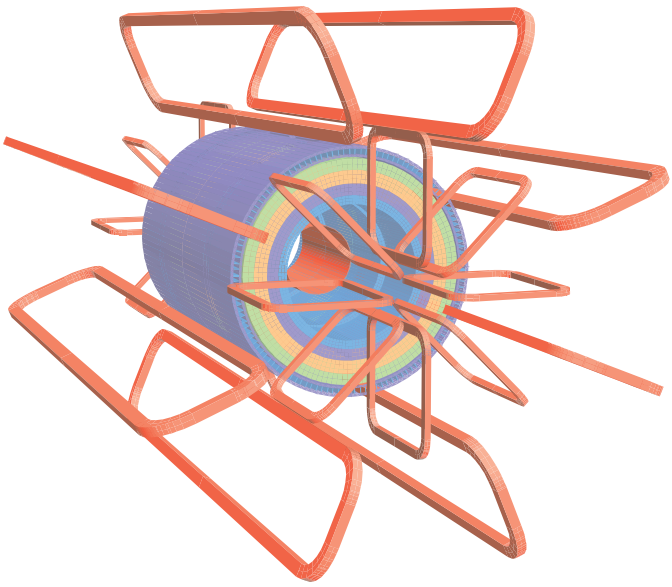

Figure 3.5.: The geometry of the magnet system and the hadronic calorimeter steel [1]. The eight barrel toroid coils, with the end-cap coils interleaved are visible. The solenoid lies inside the calorimeter volume. The tile calorimeter is modelled by four layers with different magnetic properties, plus an outside return yoke.

same vacuum vessel of the LAr calorimeter, to minimise the material due to the presence of the solenoid and the cryostat. The solenoid is 5.8 m long, with 2.46 m inner diameter.

The toroidal magnetic field for the muon spectrometer (see sec. 3.2.5) has average values of 0.5 T and 1 T in the barrel and end cap regions respectively. It is composed of a system of 8 coils assembled radially with an eight fold symmetry. In the barrel region, each coil is 25 m long and 4.5 m tall and has its own cryostat. Coils in the end-cap are housed all in the same cryostat and are shorter (5 m) than those in the central region. End-cap coils are rotated, with respect to the barrel ones, by 22.5°, providing radial overlap and optimising the bending power in the intersection regions of the two parts of the external magnet system.

3.2.3. Inner detector

The main goal of a tracker is to provide precise charged particle reconstruction in terms of momentum and impact parameter, to allow for precise momentum measurements and the identification of primary and secondary vertices. To achieve this, the ATLAS tracker strategy is to combine a small number of high precision measurements close to the interaction point, with a higher number of measurements in the outer zone. Therefore the

information from the hits collected in the pixel (PIXEL) and microstrip silicon detectors (SCT) is combined with that of the straw-tube tracker (TRT). The latter is also designed to detect transition radiation, to aid in particle identification. The Inner Detector (ID) is placed inside the superconducting solenoid described in sec. 3.2.2. A view of the ID is given in fig. 3.6, and its geometrical parameters are listed in table 3.3.

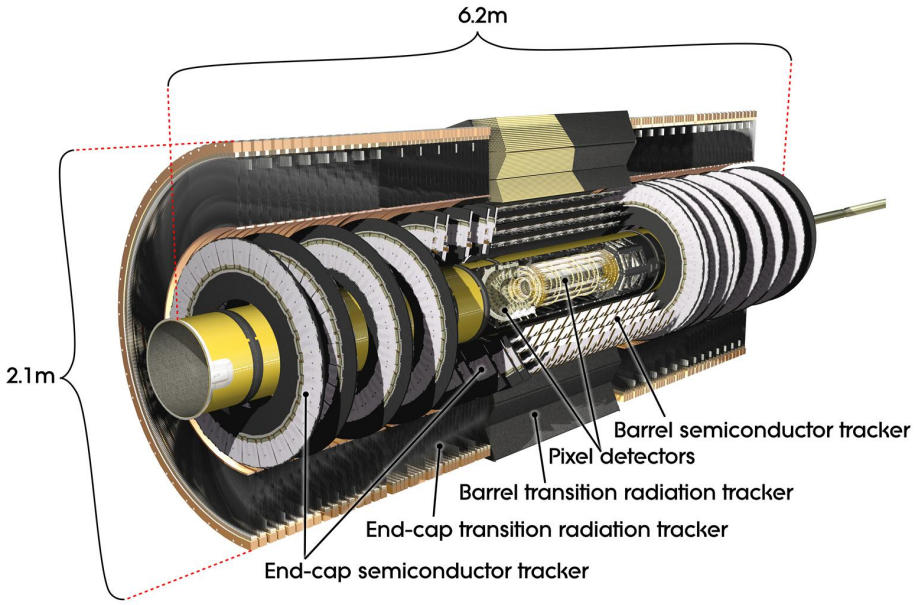

Figure 3.6.: Overview of the ATLAS Inner Detector [1].

As anticipated in sec. 3.2.1, the ID is designed to reconstruct charged particles, bent by the magnetic field of the superconducting solenoid, described in sec. 3.2.2. The Lorentz force :

$$\mathbf{F} = \frac{q}{m}\mathbf{p} \times \mathbf{B} \ , \tag{3.4}$$

describing the motion of a particle of charge q and mass m in a magnetic field $\mathbf{B}$, gives the relation between the particle bending and its momentum $\mathbf{p}$. The important parameters that can be measured in a tracker, and which characterise the helix motion of a charged particle in a uniform field, are:

- the transverse momentum of the particle, p_{T};
- the track azimuthal angle, φ, related to the particle momentum by the relation $\tan\varphi = p_y/p_x$;

Item		Radial extension (mm)	Length (mm)
Overall ID envelope		$0 < R < 1150$	$0 < \|z\| < 3512$
Beam pipe		$29 < R < 36$	
Pixel	Overall envelope	$45.5 < R < 242$	$0 < \|z\| < 3092$
3 cylindrical layers	Sensitive barrel	$50.5 < R < 122.5$	$0 < \|z\| < 400.5$
2×3 disks	Sensitive endcap	$88.8 < R < 149.6$	$495 < \|z\| < 650$
SCT	Overall envelope	$255 < R < 549$ (barrel)	$0 < \|z\| < 805$
		$251 < R < 610$ (endcap)	$810 < \|z\| < 2797$
4 cylindrical layers	Sensitive barrel	$299 < R < 514$	$0 < \|z\| < 749$
2×9 disks	Sensitive endcap	$275 < R < 560$	$839 < \|z\| < 2735$
TRT	Overall envelope	$554 < R < 1082$ (barrel)	$0 < \|z\| < 780$
		$617 < R < 1106$ (endcap)	$827 < \|z\| < 2744$
73 straw planes	Sensitive barrel	$563 < R < 1066$	$0 < \|z\| < 712$
160 straw planes	Sensitive endcap	$644 < R < 1004$	$848 < \|z\| < 2710$

Table 3.3.: Geometry parameters of the Inner Detector [1].

- the polar angle θ, related to the particle momentum by the relation $\cot\theta = p_z/p_\mathrm{T}$;
- the transverse impact parameter d_0, the distance in the xy plane between the track closest point to the z axis and the z axis itself;
- the longitudinal impact parameter z_0, describing the z coordinate of the closest approach point to the z axis.

The high granularity necessary for precision measurements, together with the readout and cooling, results in a rather large amount of material in the inner detector. This is mapped in ATLAS simulation and shown in fig. 3.7.

The next paragraphs describe in more detail the three sub-detectors forming the ID. The overall ID momentum resolution, summarised in table 3.2, is

$$\frac{\sigma_{p_\mathrm{T}}}{p_\mathrm{T}} = 0.05\% \cdot p_\mathrm{T} \oplus 1\% \ . \tag{3.5}$$

The pixel detector

The pixel detector is the closest sub-detector to the interaction point. It consists of three cylinders of silicon pixels centred around the z axis in the barrel region ($|\eta| < 2$), and

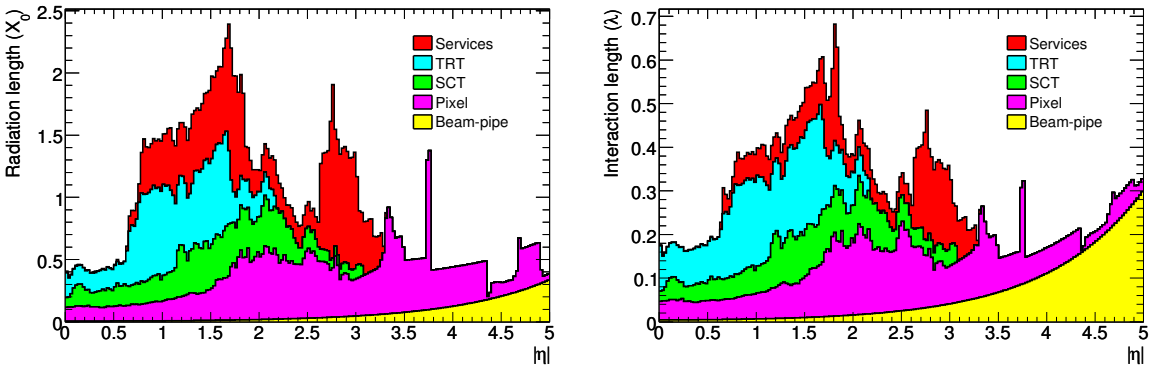

(a) (b)

Figure 3.7.: The material distribution of the inner detector [1], including services and beampipe, expressed in terms of radiation length (X_0) in 3.7a and interaction length (λ) in 3.7b.

three end-cap ($|\eta| < 2.5$) disks on each side perpendicular to the beam axis. A more detailed picture of the pixel detector, also including its scale, is given in fig 3.8.

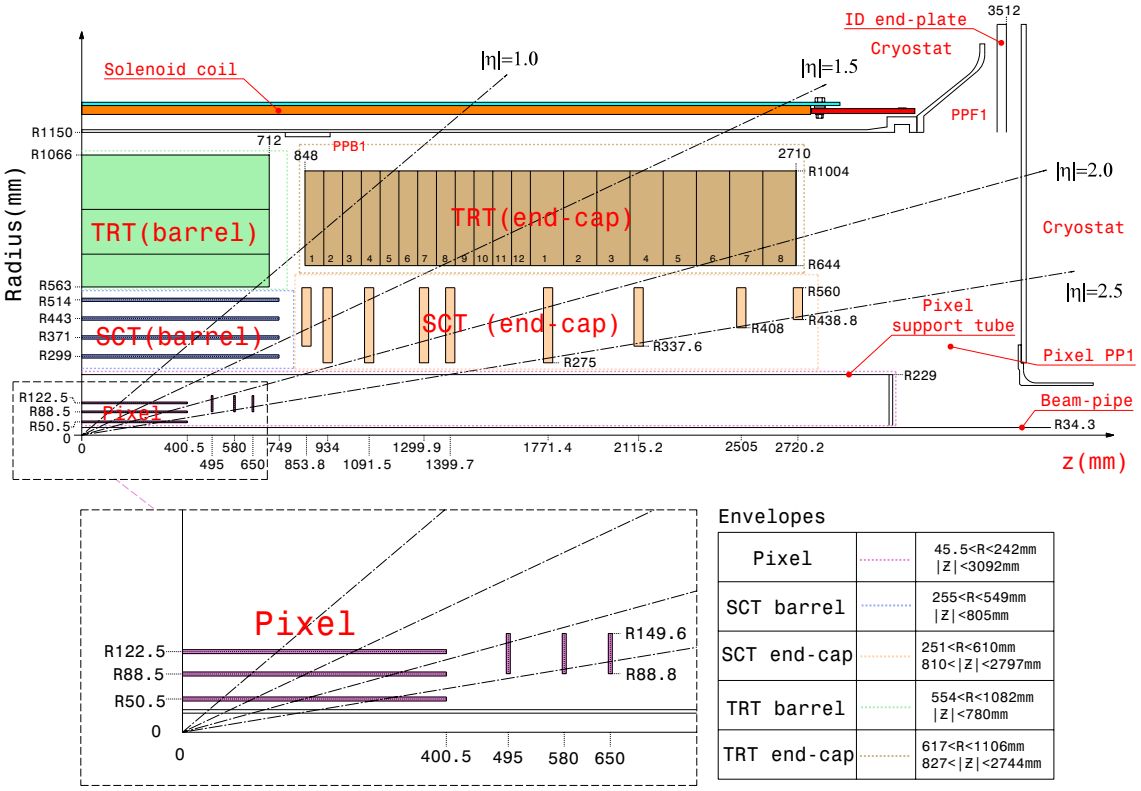

Figure 3.8.: Detailed scheme of the Inner Detector, with a zoom on the pixel layers [1].

To achieve a robust pattern recognition, to discriminate between close-by charged particles in a high-luminosity and high pileup environment, very high granularity is

needed. The ATLAS pixel detector is segmented in $R-\varphi$ and z down to a minimum pixel size of 50 µm in $R-\varphi$ and 400 µm in z. Its intrinsic accuracy is 10 µm in the $R-\varphi$ plane and 115 µm in the z plane in the barrel and end-cap. The pixel layers provide on average three tracking points per track. The total number of readout channels is 80.4 M.

The closest layer to the interaction point is often referred to as B-layer, as it is crucial in secondary vertex reconstruction for b-jet tagging, providing the best d_0 and z vertex resolution. During the current LHC shutdown, before the start of Run 2 data taking, mentioned in sec. 3.1, an additional pixel layer will be installed. It is called Insertable B-layer (IBL) [52], and it is designed to aid the current B-layer vertex resolution and achieve better identification of b-jets.

The silicon strip detector

The silicon strip detector (SCT) has four double-sided layers of strips, providing four tracking space points, both in the barrel and endcap regions. The strip sides are rotated with respect to each other of a stereo angle of 40 mrad to obtain a measurement in both $R-\varphi$ and R or z planes, depending whether placed in the endcap or in the barrel.

The mean strip pitch is 80 µm, allowing for an intrinsic accuracy of 17 µm in $R-\varphi$ and 580 µm in $z(R)$ in the barrel (endcap) region. The SCT has 6.3 M readout channels. A diagram of the strip detector within the ID is shown in fig 3.8. On average, the SCT provides four space points for a track in the barrel region.

The transition radiation tracker

The transition radiation tracker (TRT) is composed of 2 mm radius straw tubes, providing on average 36 hits for a track. It also distinguishes between charged pions and electrons by detecting photons from transition radiation. It is composed of 73 layers of straws disposed axially at ≈ 7 mm distance, alternated to polypropylene fibres (in the barrel), and 160 straw planes arranged in wheels, interleaved with polypropylene foils (in the end cap).

It provides coverage up to $|\eta| = 2.0$ and only measures $R-\varphi$ of the track. Its intrinsic accuracy is 130 µm per straw. The barrel structure consists of 144 cm long straws parallel to the beam axis, split into two halves at $\eta = 0$. In the endcap, the 37 cm long tubes are arranged radially in wheels.

The TRT plays an important role in the momentum resolution, because of the high number of measurements provided, and the higher lever arm. Its low granularity is compensated by its large radius and it is designed to have the possibility to perform a standalone pattern recognition up to the design luminosity ($10^{34}\,\mathrm{cm}^{-2}\mathrm{s}^{-1}$).

3.2.4. The calorimeter system

The ATLAS calorimeter system consists of two separate subsystems: the electromagnetic and the hadronic calorimeters. The system is designed to meet precise physics requirements, mainly to provide the best possible resolution for high-energy photons, electrons, jets and missing transverse energy.

To obtain a good missing transverse energy resolution, the main requirement for a calorimeter is hermeticity. Good containment for jets and missing transverse energy is also important, and it is achieved because of the calorimeter thickness, allowed by the large radius toroidal magnet muon system. The total thickness of the electromagnetic calorimetry is larger than $22X_0$ in the barrel region and larger than $24X_0$ in the endcap region. The total interaction length of the entire system is approximately 10λ, with a peak value of 11λ at $\eta = 0$.

These characteristics allow for electromagnetic and hadronic showers coming from particles produced with energies of the TeV scale to be resolved and contained in the calorimeter, for jets with a momentum of up to ~ 1.5 TeV.

The ATLAS calorimeter system consists of an electromagnetic calorimeter, using liquid argon (LAr) as active material and lead as absorber, and a hadronic calorimeter, using LAr technology and a copper absorber in the forward region (HEC) and active scintillating tiles with absorbing steel in the barrel (TileCal). The forward calorimeter (FCAL) uses LAr and copper in the EM part and tungsten in the hadronic part. The main characteristics of these subdetectors are described in the following paragraphs, and the overall scheme of the calorimeter system is shown in fig. 3.9.

Electromagnetic calorimeter

The EM calorimeter is divided into a barrel $|\eta| < 1.475$ and an end cap region ($1.375 < |\eta| < 3.2$). An additional pre-sampler detector, consisting of an active layer of LAr of 1.1 cm thickness, is installed in front of the cryostat wall. It provides a

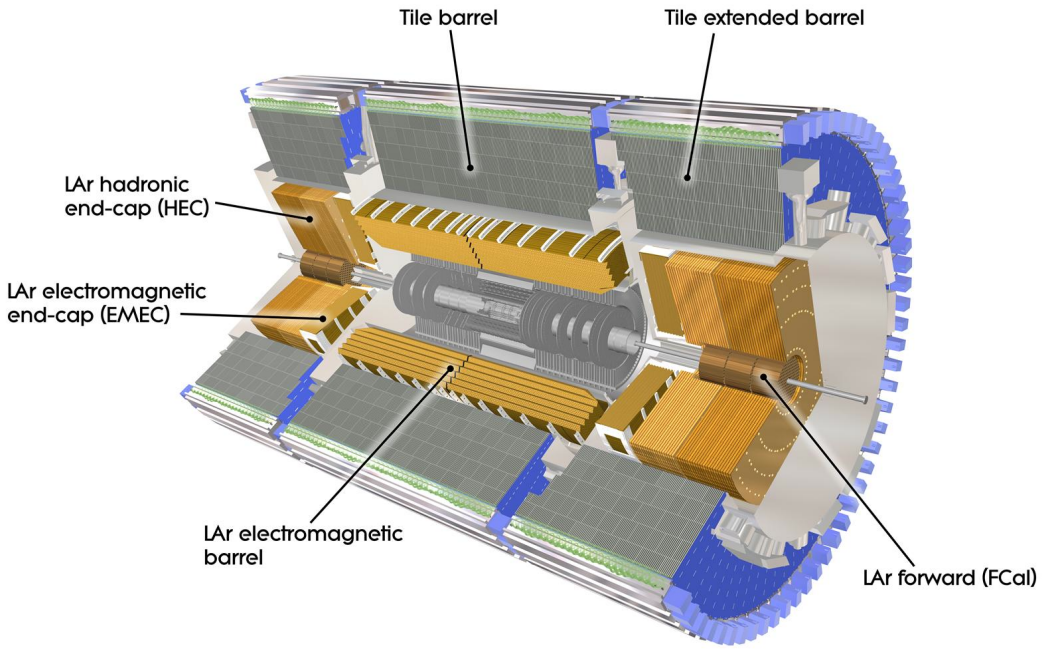

Figure 3.9.: Overall view of the calorimetric system [1].

correction to the energy loss caused by the material in front of the calorimeter in the $|\eta| < 1.8$ region.

The barrel calorimeter is composed by two half-barrels with a 6 mm gap at $z = 0$. A module is shown in fig. 3.10. The end-caps (EMEC), instead, are divided into two coaxial wheels covering up to $|\eta| < 2.5$ and 3.2 respectively. The accordion shape of the electrodes, in both the barrel and endcap regions, guarantees complete azimuthal coverage.

The calorimeter sampling is fine and subdivided in three layers, as can be seen in fig. 3.10:

- the first layer, $4.3X_0$ thick, consists of strips with $\Delta\eta = 0.0031$, allowing for charged and neutral pion separation;
- the second layer, $16X_0$ thick, is segmented in squared towers of $\Delta\eta \times \Delta\varphi = 0.025 \times 0.025$;
- the third layer has $\Delta\eta \times \Delta\varphi = 0.050 \times 0.025$ towers, specifically for electrons and photons with $E > 50$ GeV producing larger showers.

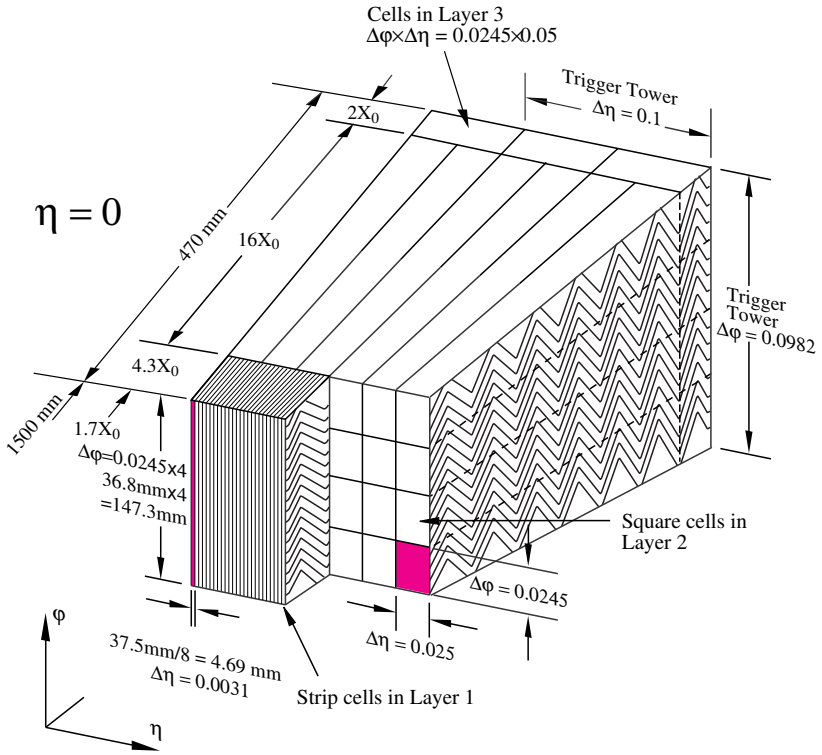

Figure 3.10.: Sketch of the EM calorimeter structure [1].

The segmentation allows for high precision spatial measurements, providing a pointing geometry that helps in identifying photons coming from a primary vertex, crucial for example in the $H \to \gamma\gamma$ search.

The lead thickness in the barrel is optimised as a function of η, providing the best possible resolution in energy measurements. The energy resolution, summarised in table 3.2, is:

$$\frac{\sigma_E}{E} = \frac{10\%}{\sqrt{E[\text{GeV}]}} \oplus 0.3\% \ , \tag{3.6}$$

and the pseudorapidity resolution is:

$$\Delta\eta = \frac{40 \text{ mrad}}{\sqrt{E[\text{GeV}]}} \ . \tag{3.7}$$

The hadronic calorimeter

The barrel region (TileCal) is divided into a central ($|\eta| < 1$) and two extended barrels ($1 < |\eta| < 1.7$). Gap scintillators are placed along the internal edge of the extended

barrel to partially recover the energy loss in the gap between the two barrel regions, where the readout of the EM calorimeter is located. The hadronic endcap (HEC) covers the $1.5 < |\eta| < 3.2$ region, and is placed in the same cryostat as the EMEC and the forward calorimeter (FCAL). Its absorbing material is copper.

TileCal is composed by a sampling structure of 14 mm iron plates alternated with 3 mm scintillating tiles. Its granularity is $\Delta\eta \times \Delta\varphi = 0.1 \times 0.1$. Each hadronic endcap is composed of two independent wheels with ~ 2 m outer radius. Each wheel is segmented longitudinally in two parts.

The overall energy resolution of the TileCal and HEC systems is:

$$\frac{\sigma_E}{E} = \frac{50\%}{\sqrt{E[\text{GeV}]}} \oplus 3\% \ . \tag{3.8}$$

FCAL

The forward calorimeter is built using an intrinsic radiation-hard technology, due to the large amount of radiation it is exposed to. It is housed in the same cryostat of both the EM and hadronic end-caps. Its front face is 4.7 m from the interaction point. It is made of thin gap LAr (2 mm), centred in tubes parallel to the z axis. The electromagnetic and hadronic parts use different absorbers, respectively copper and tungsten.

It has a high-density design, because of the reduced available longitudinal space and the need to avoid energy leakage from it to its neighbours. Its energy resolution is:

$$\frac{\sigma_E}{E} = \frac{100\%}{\sqrt{E}} \oplus 10\% \ . \tag{3.9}$$

3.2.5. The muon system

The ATLAS muon system is located within the toroidal magnetic field described in sec. 3.2.2. It is designed as an independent subdetector, exploiting the clean signature of muons, the only charged particles that are not stopped by the calorimeters. The direction of the magnetic field causes the muons to bend in the $R - z$ plane, orthogonal to the solenoidal field in the inner detector. An illustration of the muon spectrometer layout can be found in fig 3.11, and its design parameters in table 3.4.

The muon spectrometer is composed of two types of subdetectors:

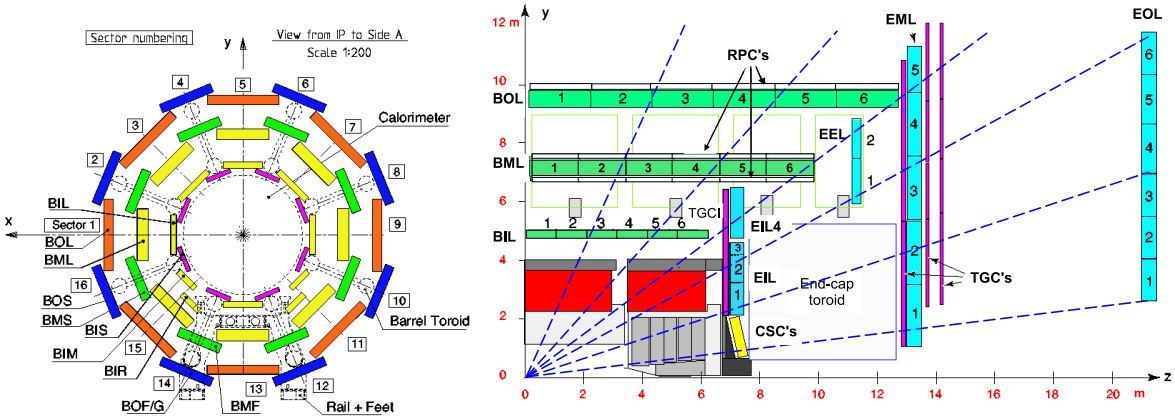

(a) (b)

Figure 3.11.: In 3.11a, a section of the barrel muon system perpendicular to the beam axis, showing the three concentric cylindrical layers with eight large and eight small chambers is shown. In 3.11b, a section of the muon system along the beam axis is shown [1].

(a) chambers providing precision measurements for the particle momentum;

(b) chambers with coarser granularity and fast response for online triggering.

The type (a) subdetectors are: the MDT (Monitored Drift Tube) chambers, and the CSC (Cathode Strip Chambers). The MDTs are composed by several layers of drift tubes (three to eight), operated with Ar/CO_2 gas at 3 bar pressure. The MDT layout is projective, increasing the lever dimensions and chamber sizes as a function of the distance from the interaction point. This sub-system covers up to $|\eta| < 2.7$, apart from the innermost endcap layer, stopping at $|\eta| = 2.0$. It is complemented by CSCs, which have a better time resolution. The relevant parameters are shown in table 3.4. The CSCs are multi-wire proportional chambers containing cathode planes segmented in strips along the orthogonal direction, allowing for measurements both in the bending and transverse planes. The sub-system is composed of two disks, containing eight chambers each.

The subdetectors of type (b) complement the MDTs, giving a φ coordinate measurement. They also provide online event selection (trigger) identifying the bunch crossing originating an event with 99% accuracy. For this reason, they need to have very fast response. In the barrel region ($|\eta| < 1.05$), they consist of resistive plate chambers (RPC) and in the endcap ($1.05 < |\eta| < 2.4$) of thin gap chambers (TGC). The relevant parameters are outlined in table 3.4. The RPC sub-system does not have wires, but planes, arranged in three cylindrical layers around the z axis. Each plane is further composed of

Subdetector	Chamber resolution			Measurements/track		Number of	
	z/R	φ	time	barrel	endcap	chambers	channels
MDT	35 µm (z)	–	–	20	20	1088	339k
CSC	40 µm (R)	5 mm	7 ns	–	4	32	30.7k
RPC	10 mm (z)	10 mm	1.5 ns	6	–	544	359k
TGC	$2-6$ mm (R)	$3-7$ mm	4 ns	–	9	3588	318k

Table 3.4.: Main parameters of the four subdetectors forming the muon spectrometer [1].

two layers, measuring the η and φ coordinates. The TGC sub-system complements the MDTs, measuring the azimuthal coordinate. The TGCs are segmented radially into one endcap and forward region. The TGC wire groups measure the bending plane coordinate, and the radial strips provide the φ measurement. Details on the parameters of the RPC and TGC sub-systems are shown in table 3.4.

In general, the precision of the momentum measurement for a high-p_{T} muon track depends mainly on the resolution of the determination of the sagitta (deviation in $R-z$ plane with respect to a straight line). For a high-momentum track ($p_T \approx 1$ TeV) the sagitta is typically around 500 µm. The MDTs provide a momentum measurement with $\sigma_{p_{\mathrm{T}}}/p_{\mathrm{T}} \approx 10\%$ resolution for 1 TeV muons, and $2-3\%$ for lower momenta. In case of low-momentum muons, it is necessary to complement the measurement in the muon system with the information from the inner detector.

3.2.6. ATLAS forward detectors

Additional smaller detectors are built to provide coverage in the very forward region to detect inelastic p-p scattering at small angles. These detectors are, in order of increasing distance form the interaction point (IP): LUCID (Luminosity measurement Using Čerenkov Integrating Detectors), ZDC (Zero-Degree Calorimeter) and ALFA (Absolute Luminosity For ATLAS). A scheme showing their position along the beam line is shown in fig. 3.12. These detectors and their functionalities will be described in detail in the following.

LUCID

This detector is placed at ± 17 m from the IP, close to the TAS (Target Absorber Secondaries) collimator. It is dedicated primarily to online luminosity monitoring.

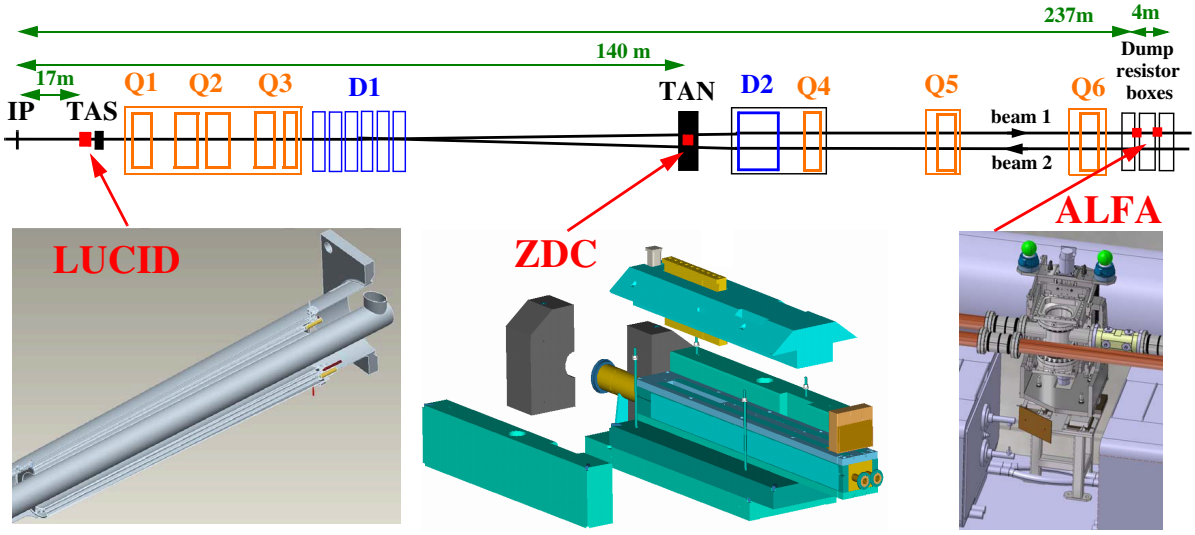

Figure 3.12.: Placement of the forward detectors along the beam line with respect to the ATLAS interaction point (IP) [1].

Through the measurement of *p*-*p* inelastic collisions, it can measure the integrated luminosity and monitor the beam conditions and the instantaneous luminosity. The goal of LUCID is the absolute luminosity measurement with a $\lesssim 5\%$ uncertainty.

LUCID is based on the principle that the number of interactions per bunch crossing is proportional to that of the particles it detects. The LUCID main requirements are:

- sufficient time resolution to measure individual bunch crossings at the design rate of one every 25 ns;
- resistance to large radiation doses;
- good acceptance for minimum bias events;
- possibility of counting charged particles;
- pointing features to suppress extra tracks not coming from the IP.

It is composed by an array of Cerenkov tubes, used for counting particles. There are twenty tubes made of aluminium, 1.5 m long and with 15 mm diameter, surrounding the beam pipe. They are filled with C_4F_{10} at a constant pressure of $1.2 - 1.4$ bar, with a 2.8 GeV Cerenkov threshold for pions and 10 MeV for electrons. The two detectors are approximately at 10 cm radial distance from the beam pipe, at $|\eta| \approx 5.8$. The light is read out by photomultipliers (PMT) with the same diameter as the Cerenkov tubes. These

PMTs have quartz windows, but strongly suffer from the high radiation environment they are exposed to.

ZDC

It is located at ± 140 m from the interaction point, where the beam pipe is divided into two separate pipes. It is embedded in the TAN (Target Absorber Neutral), which is located between the two pipes after the split, as can be seen in fig. 3.12. It is designed to detect neutrons from heavy-ion collisions with $|\eta| > 8.3$. It is used to determine the centrality of heavy-ion collisions, correlated to the number of spectator (forward) neutrons. It is also used to reduce beam-halo and -gas effects, by requiring a tight coincidence (9% of the total inelastic rate) between the two ZDC detectors.

Its time resolution is approximately 100 ps, allowing the location of the IP with a 3 cm precision in z. There are four ZCD modules per arm, an EM module ($\sim 29 X_0$ deep) and three hadronic ones (each of $\approx 1.4\lambda$). Each EM module has eleven tungsten plates, normal to the beam axis, each of which is vertically extended by 290 mm steel plates. Quartz rods of 1 mm diameter enter the plates parallel to the z direction, forming a 8×12 matrix. They are viewed by phototubes, to capture the Čerenkov light from incident particle decays. The hadronic modules have a similar layout, but with fewer readout channels.

ALFA

ALFA is the furthest detector from the interaction point, located at ± 240 m. It is composed by scintillating fibre trackers and is placed inside Roman pots. It is designed to detect elastic scatterings at small angles, as their amplitude is related to the total cross section by the optical theorem. The scattering angle needed to perform such measurements, typically of the order of 3 µrad, is smaller than the beam divergence. Therefore, special beam conditions are required, specifically high-β^* optics, combined with small beam emittance.

The Roman pots allow the detectors to be the closest possible to the beampipe (≈ 1 mm). There are two Roman pots on each side at 4 m distance from each other. The required spatial resolution for ALFA is ≈ 30 µm. This detector is operated only at high-β^*, implying low instantaneous luminosity, allowing for the use of non-radiation hard technologies. The detector has ten modules of 64 fibres each, with stereo geometry.

Each fibre has a 0.5 mm width, and has a 70 µm pitch. ALFA spatial resolution is 25 ± 3 µm.

3.2.7. ATLAS trigger and data acquisition

The ATLAS trigger and data-acquisition (DAQ) consists of three levels of online event selection. Each level refines the selection made by the previous one by adding additional information and selection criteria.

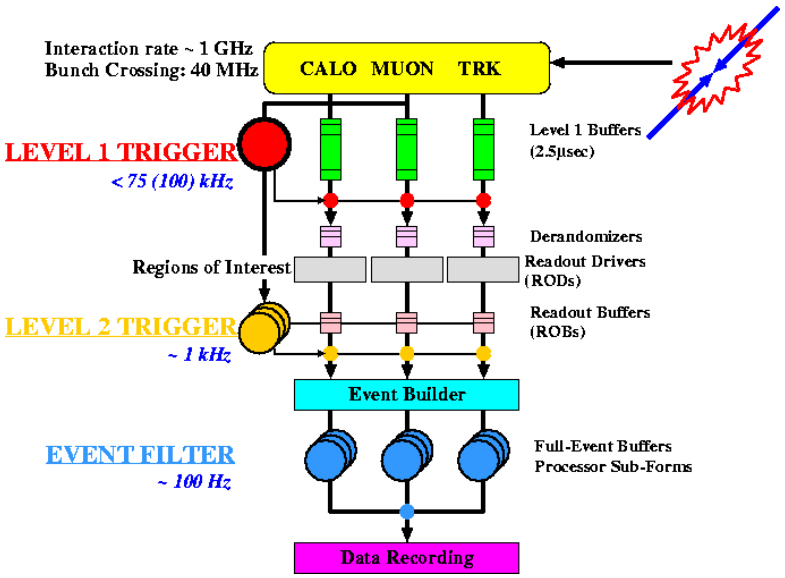

Figure 3.13.: Scheme of the ATLAS trigger system.

Considering an initial bunch-crossing rate of 40 MHz, it is necessary to reduce the rate of the selected events to about 100 Hz, for permanent storage. The event rate is about 10^9 Hz at the nominal luminosity, determined by the p-p cross section. A strict requirement of rejection against minimum bias events (a factor of 10^7) is necessary to match the desired efficiency for the rare physics processes investigated by ATLAS. Hence, the main requirement for Level-1 (LVL1) trigger is to identify the interesting events, strongly reducing the total rate.

The initial selection made by the LVL1 trigger is based on reduced granularity information. Calorimeter trigger looks for: high p_{T} electrons and photons, jets, hadronically decaying τ leptons and large missing transverse energy. The muon trigger identifies high and low p_{T} muons. The EM and hadronic calorimeters contribute separately to e/γ and hadron/τ triggers, with the possibility to apply isolation cuts too. Missing and total

scalar transverse energy are calculated by summing over trigger towers. Due to the need for the LVL1 trigger to be very fast, and the lower resolution at high p_{T}, it does not use information on the tracks coming from the inner detector. The expected final LVL1 rate is < 100 kHz

An essential requirement for the LVL1 trigger is to identify with no ambiguity the interesting bunch-crossing, given the very short 25 ns interval. In the muon trigger case, the time-of-flight in the spectrometer is of the same order of magnitude of the bunch-crossing. On the other hand, for the calorimeter trigger case, the calorimeter signal pulse shape extends over many bunch-crossings. During this latency time (~ 2.5 µs), the information coming from the detector is stored into pipeline memories and then passed to the trigger decision system, consisting of purpose-built hardware processors. The LVL1 trigger system has a very important feature, which is particular to ATLAS: it allows the identification of the Regions of Interest (ROIs), which represent the position of the trigger objects in the $\eta - \varphi$ plane. ROI information is used to reduce the computation time at LVL2 and the size of the data to be recorded.

The Level-2 (LVL2) trigger runs offline-like algorithms optimised for the on-line processing, using information also from the inner detector. It processes only data coming from the ROIs selected by LVL1. Therefore, it works only on roughly $2 - 5\%$ of the whole ATLAS data size. After the maximum latency time of 10 ms, an event can be either selected and moved to the Event Filter system, or discarded and removed from the data flow chain. The expected final rate for LVL2 is about $1 - 2$ kHz.

The last trigger stage in ATLAS is represented by the Event Filter (EF). It performs a full event reconstruction using offline selection algorithms adapted to online decisions and the most up-to-date calibrations for the calorimeters. The EF performs the final physics selection to be written to mass storage for the following offline analysis. The expected time available for this last level to make a decision on the event is 1 s. It is expected to reduce the output from LVL2 by an order of magnitude, getting a final output of 100 Hz. The expected final event size is 1 Mbyte. Hence, the output data rate is expected to be of about 100 Mbytes/s, with 10^{15} bytes of data collected per year.

3.2.8. Computing facilities

Due to the event rate, size and high number of physicists involved in the physics analysis, the data distribution, processing and analysis require a well-structured system. ATLAS

uses a multi-tier schema, very well-suited to distribute both storage and computing among the participating institutes. To reach the final goal, new performant tools were developed.

The EF output data are first transferred to the CERN computing centre, the Tier-0, which represents the first step of ATLAS offline analysis system. After copying the raw data, reconstruction is applied, leading to the production of ESD (Event Summary Data) and AOD (Analysis Object Data). These two data formats contain different information about the events. The ESDs contain the reconstructed quantities measured in the detector, together with the reconstructed physics objects. The ESD event size is about 500 kbytes. The AOD is a smaller size format, with only 100 kbytes per event. It records only the physics objects. A reduced format of them is represented by D3PDs, which are the data format generally used for the final physics analyses.

Data are distributed by of the Tier-1 centres, in which raw data, AODs, ESDs and D3PDs are copied. Tier-1 centres are distributed in different countries and have the requirement to be able to reprocess raw data, in order to get more accurate updated versions of smaller-sized data formats.

The physics analyses are mainly performed at the Tier-2 and -3 centres. In average there are five Tier-2 connected to a Tier-1. Tier-1 and -2 implement the Monte Carlo production and the simulated data are stored in the Tier-1. The multi-tier structure relies on the presence of GRID technology and middle-ware software, hiding the complex structure to the user.

Chapter 4.

Statistical introduction

One of the most important aspects of a Higgs boson analysis is the statistical interpretation of the results. After applying the selection cuts, the analysis leads to two sets of events, one for the simulated and one for the measured data. These are compared in two hypotheses: when the simulation contains only background events or when the simulation takes into account both signal and background. The comparison is performed for a set of variables, which have high discriminant power between the signal searched for and the backgrounds. A statistical test is then carried out, as a function of the discriminant variables, to find the possible presence of a signal, or to exclude it. The formulation of the statistical methods applied to the analysis presented in this thesis is described in this chapter. The technique described is implemented via the RooStats and RooFit packages [53, 54], which are part of the ROOT program [55].

4.1. General concepts

In a Higgs analysis, if a signal is observed, it is quantified by a p-value. This can be seen as the level of agreement of the data with a hypothesis H. It indicates the probability under H to find data that are equally or more inconsistent with the hypothesis predictions. In the case of presence of a signal, the p-value is generally converted to the corresponding Gaussian significance, Z, defined as follows: a Gaussian distributed variable with upper-tail probability equal to the p-value will be Z standard deviations (σ) above its mean. A discovery can be claimed when the background hypothesis can be rejected, and the typical threshold corresponds to $Z \geq 5$. A signal hypothesis can also be excluded in case of an absence of signal in the data, always by means of the p-value.

The exclusion limits on a signal cross section are generally set at 95% confidence level (CL), corresponding to a threshold p-value of 0.05.

To characterise the sensitivity of a specific analysis, the expected significance is generally quoted. It is obtained testing an hypothesis H_0 under another assumption H_1. The median Z and p-value obtained from this test are the expected quantities characterising an analysis sensitivity.

To extract the significance from data and Monte Carlo, it is possible to perform a series of toy experiments under a certain hypothesis, to obtain a sampling distribution. This can be computationally expensive, and an approximate method is typically used. This approximation is based on the Asimov dataset, which provides a full sampling distribution to extract the significance without the need of performing toy experiments.

The method used to establish the presence of a signal, or a limit on its production, is of frequentist origin in the case of ATLAS Higgs analyses. It relies on a likelihood ratio based test. This ratio is not only dependent on the parameter of interest, discriminating the background and signal hypotheses, but also on additional nuisance parameters. These are introduced to describe the uncertainties on the model (statistical and systematic), and are fitted from data. Often they are constrained in the likelihood by probability density functions (pdfs), derived from previous measurements. This procedure has a Bayesian interpretation, and this signal extraction method is often referred to as modified frequentist.

Details in the test statistic used, the Asimov dataset, the limit setting and the nuisance parameter treatment can be found in the following sections.

4.2. Hypothesis testing: the profile likelihood ratio

To understand the level of agreement between the measured data and the proposed model of the signal searched for, a hypothesis test is carried out. A physics analysis can be seen as a counting experiment, or a composition of several counting experiments. Therefore, the natural statistics to be used in such case is the Poisson statistics. The hypotheses to be tested are:

H_0 The null hypothesis. It corresponds to the known model, and, in the case of SM Higgs searches, to the SM without the presence of a Higgs boson. It is often referred to as the background-only (B) hypothesis.

H_1 The test hypothesis. It corresponds to the proposed model, that in the case of SM Higgs searches, is the SM Higgs boson. It is often referred to as the signal+background ($S + B$) hypothesis.

The difference between the null and the test hypothesis is defined by the parameter of interest (POI) μ, which varies between 0, corresponding to the null hypothesis, and 1, corresponding to the test hypothesis.

In a physics analysis, the data measurement of a specific variable, discriminating between H_0 and H_1, is tested against the two hypotheses, to reject or accept H_1. In the case of the $VH(b\bar{b})$ search described in this thesis, the discriminant variable taken into account is the reconstructed invariant mass of the b-jet pairs passing all the kinematic requirements ($m_{b\bar{b}}$), as shown in the example plot in fig. 4.1.

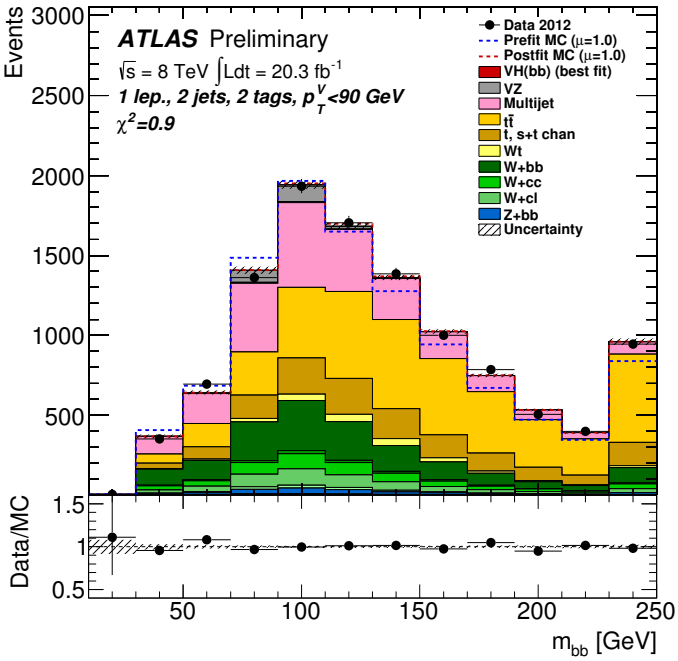

Figure 4.1.: The invariant mass of the b-jet pair after the kinematic selection for one of the categories of the $VH(b\bar{b})$ analysis presented in chapt. 6.

In this case, $m_{b\bar{b}}$ is the observable that is measured and used to build the histogram, which can be represented as: $\mathbf{n} = (n_1, n_N)$. The expectation value of each n_i can be written as:

$$E[n_i] = \mu s_i + b_i \ . \tag{4.1}$$

In equation 4.1, s_i is the number of signal events in the bin i, b_i the number of background events in the same bin, and the multiplicative factor μ is the previously described POI, also called signal strength. The number of signal and background events can be expressed as the probability for an event to be in the i-th bin:

$$s_i = s_{\text{tot}} \int_{\text{bin } i} f_s(x;\theta_s)dx \ , \tag{4.2}$$

$$b_i = b_{\text{tot}} \int_{\text{bin } i} f_b(x;\theta_b)dx \ . \tag{4.3}$$

The functions f_b and f_s are the probability density functions (pdfs) of the discriminant variable x in case of background and signal, while θ_b and θ_s are the parameters characterising their shapes. In the following definitions, the notation $\theta = (\theta_s, \theta_b, b_{\text{tot}})$ will be used, for simplicity. s_{tot} is fixed to the value indicated by the tested model.

A Poisson likelihood function for the whole distribution, represented by a set of bins, can be built, and has the following form:

$$L(\mu,\theta) = \prod_{i=1}^{N} \frac{(\mu s_i + b_i)^{n_i}}{n_i!} e^{-(\mu s_i + b_i)} \ . \tag{4.4}$$

The hypothesis testing is performed using a test statistic, for which it is necessary to define the profile likelihood ratio:

$$\lambda(\mu) = \frac{L(\mu, \hat{\hat{\theta}})}{L(\hat{\mu}, \hat{\theta})} \ . \tag{4.5}$$

In the numerator, $\hat{\hat{\theta}}$ is the conditional Maximum Likelihood (ML) estimator for a fixed value of μ. The denominator, instead, represents the unconditional likelihood, where both $\hat{\mu}$ and $\hat{\theta}$ are the ML estimators. It is to be noticed that $0 \leq \lambda \leq 1$, and that $\hat{\mu}$ can be negative, as long as $\mu s_i + b_i > 0$, allowing it to be Gaussian distributed.

The test statistics, t_μ, is defined as the negative logarithm of the profile likelihood ratio:

$$t_\mu = -2 \ln \lambda(\mu) \ . \tag{4.6}$$

The smaller the t_μ value, the higher the compatibility between the tested hypothesis and the data. The p-value quantifies the level of agreement between the data and the tested hypothesis:

$$p_\mu = \int_{t_{\mu,\text{obs}}}^{\infty} f(t_\mu|\mu)dt_\mu \ . \tag{4.7}$$

In equation 4.7, $t_{\mu,\text{obs}}$ is the observed value of the test statistics, and $f(t_\mu|\mu)$ is the pdf in case of a signal strength value of μ. The relation is illustrated in fig. 4.2, taken from [56].

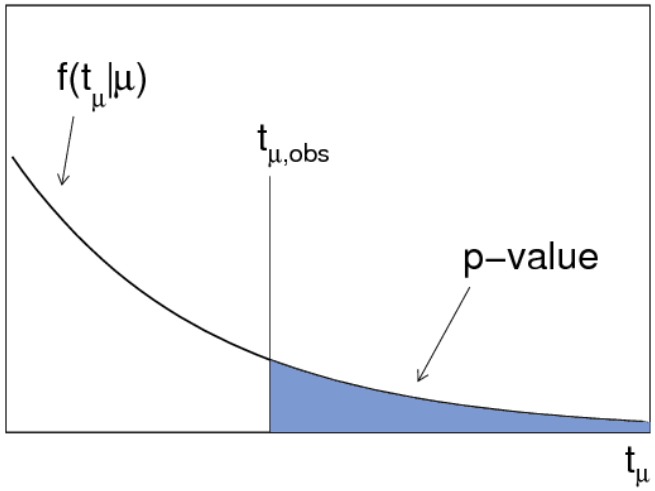

Figure 4.2.: The relation between the p-value for an observation of the test statistic, t_μ, and its distribution, as in [56].

4.3. Extracting the result: limits and observations

When looking at a signal, for example in a search for the Higgs boson, there are two possible outcomes: the exclusion and the observation. In case of no observed deviation of the data from the null hypothesis, an upper limit on the test hypothesis can be estimated considering the following test statistic based on the profile likelihood ratio defined in equation 4.5:

$$q_\mu = \begin{cases} -2\ln\lambda(\mu) & \hat{\mu} \leq \mu \\ 0 & \hat{\mu} > \mu \ . \end{cases} \tag{4.8}$$

q_μ in this case is set to zero for $\hat{\mu} > \mu$, because this condition does not imply a lower compatibility of the data with the hypothesised value of μ, therefore this is not used as a rejection region.

In the case of a discovery, corresponding to the evidence of a positive signal, a different definition of the test statistic is generally used:

$$q_0 = \begin{cases} -2 \ln \lambda(0) & \hat{\mu} \geq 0 \\ 0 & \hat{\mu} < 0 \ . \end{cases} \tag{4.9}$$

This is defined as the test of the $\mu = 0$ hypothesis, that, if rejected, corresponds to the observation of a new signal.

4.3.1. Approximate profile likelihood ratio and the Asimov dataset

To estimate the p-value of, or set an upper limit on, a tested hypothesis, the sampling distribution of the test statistic, $f(q_\mu|\mu)$, is needed. μ can be either 0, if H_0 is being tested, or it can refer to the value assumed for the data distribution. To estimate the expected significance of a hypothesis, or the expected limits on it, the distribution $f(q_\mu|\mu')$, where $\mu' = \mu$, is used to test the data distribution against a different parameter. When estimating the expected significance, assuming a precise signal model, the background only hypothesis has to be excluded, therefore the distribution $f(q_0|1)$ is generally used. When setting expected upper limits at 95% confidence level, the value of μ for which the expected p-value is 0.05 is found using the $f(q_\mu|0)$ distribution.

To obtain the distributions mentioned above, an approximate method, valid in the large sample limit, is used. When considering a test of the parameter μ, in the case of data distributed according to a strength parameter μ', the Wald approximation [57], valid in the case of having a single POI, can be used:

$$-2 \ln \lambda(\mu) = \frac{(\mu - \hat{\mu})^2}{\sigma^2} + \mathcal{O}(1/\sqrt{N}) \ . \tag{4.10}$$

In this case, $\hat{\mu}$ is distributed as a Gaussian with mean μ', and N is the size of the data sample. The Gaussian standard deviation, σ, can be obtained from the covariance matrix of the estimators of the nuisance parameters: $V_{ij} = \mathrm{cov}[\hat{\theta}_i, \hat{\theta}_j]$, where θ includes also the POI. Considering the large sample limit, where the ML estimator bias can be neglected, the covariance can be inverted, and expressed as the expected value of the Hessian matrix

of the $\ln L$.

$$V_{ij}^{-1} = -E\left[\frac{\partial^2 \ln L}{\partial\theta_i \partial\theta_j}\right] \ . \tag{4.11}$$

This holds with the assumption that the strength parameter is μ' and that the $\mathcal{O}(1/N)$ term can be neglected.

For a Gaussian distributed $\hat{\mu}$ and neglecting the $\mathcal{O}(1/N)$ term, the test statistic t_μ follows a non-central χ^2 distribution with one degree of freedom:

$$f(t_\mu;\Lambda) = \frac{1}{2\sqrt{t_\mu}}\frac{1}{\sqrt{2\pi}}\left[\exp\left(-\frac{1}{2}(\sqrt{t_\mu}+\sqrt{\Lambda})^2\right) + \exp\left(-\frac{1}{2}(\sqrt{t_\mu}-\sqrt{\Lambda})^2\right)\right] \ , \tag{4.12}$$

with a non-centrality parameter of:

$$\Lambda = \frac{(\mu-\mu')^2}{\sigma^2} \ . \tag{4.13}$$

To estimate the standard deviation σ, approximate methods based on an additional dataset, called Asimov dataset [56] can be used. The Asimov dataset is defined as the dataset that, when used to evaluate the estimators for all the parameters, gives as a result the true value of those parameters. It is named after the *Franchise* novel by I. Asimov, where one most representative voter was chosen to act as the whole electorate. Considering $\mu = \theta_0$ for simplicity of notation, it is possible to obtain the ML estimators of the parameters setting to zero the derivatives of the logarithm of the likelihood, presented in eq. 4.4. The $\ln L$ derivatives with respect to the θ_j parameters have the following form:

$$\frac{\partial \ln L}{\partial\theta_j} = \sum_{i=1}^{N}\left(\frac{n_i}{\mu' s_i + b_i} - 1\right)\frac{\partial(\mu' s_i + b_i)}{\partial\theta_j} \ . \tag{4.14}$$

Equation 4.14 is only valid if the Asimov data are equal to their expectation values: $n_{i,\mathrm{A}} = E[n_i] = \mu' s_i(\theta) + b_i(\theta)$. These values correspond to the limit of a very large Monte Carlo sample used to estimate them. Using the above result, the profile likelihood can be re-written as an Asimov likelihood:

$$\lambda_{\mathrm{A}}(\mu) = \frac{L_{\mathrm{A}}(\mu,\hat{\hat{\theta}})}{L_{\mathrm{A}}(\hat{\mu},\hat{\theta})} = \frac{L_{\mathrm{A}}(\mu,\hat{\hat{\theta}})}{L_{\mathrm{A}}(\mu',\theta)} \ . \tag{4.15}$$

This procedure can be used to estimate the standard deviation σ, using two different methods. The first, introduced previously, uses the Fisher information matrix. The explicit form of the second derivative is:

$$\begin{aligned}\frac{\partial^2 \ln L}{\partial\theta_j \partial\theta_k} = &\sum_{i=1}^{N} \left[\left(\frac{n_i}{\mu' s_i + b_i} - 1 \right) \frac{\partial^2(\mu' s_i + b_i)}{\partial\theta_j \partial\theta_k} + \right. \\ &\left. - \frac{\partial(\mu' s_i + b_i)}{\partial\theta_j} \frac{\partial(\mu' s_i + b_i)}{\partial\theta_k} \frac{n_i}{(\mu' s_i + b_i)^2} \right] .\end{aligned} \tag{4.16}$$

This expression is linear in n_i, and the expectation value can be found using the data information, equivalent to that of the Asimov dataset. Therefore, the expression for the inverse covariance is:

$$V_{jk}^{-1} = -E\left[\frac{\partial^2 \ln L}{\partial\theta_j \partial\theta_k}\right] = -\frac{\partial^2 \ln L_{\mathrm{A}}}{\partial\theta_j \partial\theta_k} = \sum_{i=1}^{N} \frac{\partial(\mu' s_i + b_i)}{\partial\theta_j} \frac{\partial(\mu' s_i + b_i)}{\partial\theta_k} \frac{1}{\mu' s_i + b_i} \ . \tag{4.17}$$

From it, the standard deviation σ can be extracted. It is dependent on the parameters chosen for the Asimov dataset.

The alternative method uses the information that $\hat{\mu} = \mu'$ for the Asimov dataset. Therefore:

$$-2 \ln \Lambda_{\mathrm{A}}(\mu) \approx \frac{(\mu - \mu')^2}{\sigma^2} = \Lambda \ . \tag{4.18}$$

This implies that the Asimov dataset provides an estimate of the non-centrality parameter characterising the pdf $f(q_\mu|\mu')$. Given that $q_{\mu,\mathrm{A}} = -2 \ln \Lambda_{\mathrm{A}}(\mu)$:

$$\sigma_{\mathrm{A}}^2 = \frac{(\mu - \mu')^2}{q_{\mu,\mathrm{A}}} \ . \tag{4.19}$$

The two methods are not completely equivalent, but give very similar results.

4.4. Limit setting and discovery of a new signal

In terms of the Asimov dataset, the test statistic for the discovery and limit setting can be re-evaluated as follows. In case of an upper limit, q_μ can be expressed as:

$$q_\mu = \begin{cases} \frac{(\mu-\hat{\mu})^2}{\sigma^2} & \hat{\mu} < \mu \\ 0 & \hat{\mu} > \mu \ , \end{cases} \tag{4.20}$$

with $\hat{\mu}$ following a Gaussian distribution with mean μ'.

For $\mu' = \mu$, the pdf of q_μ follows a half χ^2 distribution:

$$f(q_\mu|\mu) = \frac{1}{2}\delta(q_\mu) + \frac{1}{2}\frac{1}{\sqrt{2\pi}}\frac{1}{\sqrt{q_\mu}}e^{-\frac{q_\mu}{2}} \ , \tag{4.21}$$

from which the p-value can be extracted, according to eq. 4.7:

$$p_\mu = 1 - \Phi(q_\mu) \ . \tag{4.22}$$

Here, Φ is the cumulative distribution function of $\sqrt{q_\mu}$. The Gaussian significance, corresponding to the calculated p-value is defined as:

$$Z_\mu = \Phi^{-1}(1 - p_\mu) \ , \tag{4.23}$$

and therefore it is equal to q_μ in the described case.

The upper limit on μ is defined as the largest value of it for which its p-value equals a threshold α, at a confidence level (CL) of $1 - \alpha$. The correct value of μ is obtained setting $p_\mu = \alpha$ and solving for it:

$$\mu_{\text{up}} = \hat{\mu} + \sigma\Phi^{-1}(1 - \alpha) \ . \tag{4.24}$$

The threshold used to define an upper limit in the case of an Higgs analysis is the CL_S, defined as follows:

$$CL_S = \frac{p_{S+B}}{1 - p_B} \ . \tag{4.25}$$

In this expression, p_{S+B} is equivalent to the p-value in the case of the hypothesis H_1, where $\mu = 1$, and p_B is the p-value in the null hypothesis, as can be seen in fig. 4.3. The confidence level used in the Higgs analyses to set upper limits is 95%.

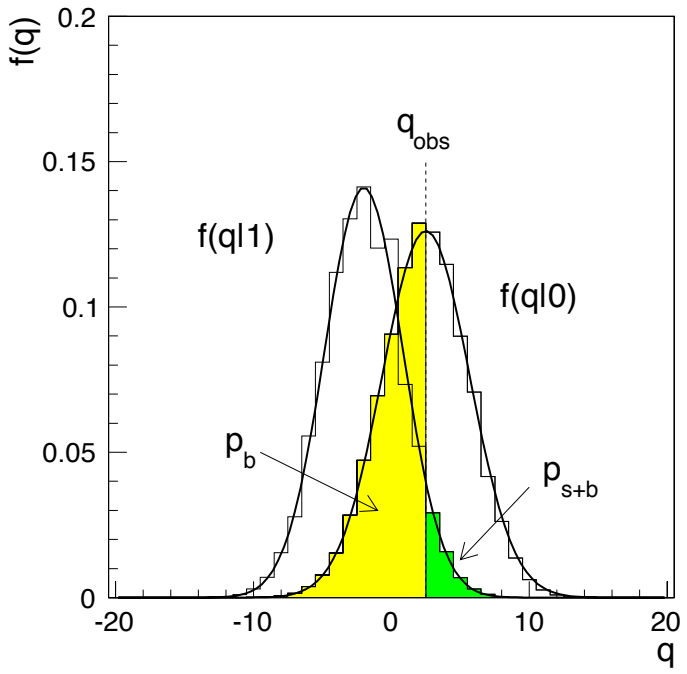

Figure 4.3.: Illustration of the distribution of the test statistics q under the assumption of $\mu = 1$ and $\mu = 0$, identifying p_{S+B} (in green) and p_B (in yellow), with respect to an observation q_{obs} [56].

In the case of a discovery, q_0 can be re-expressed as follows:

$$q_0 = \begin{cases} \hat{\mu}^2/\sigma^2 & \hat{\mu} \geq 0 \\ 0 & \hat{\mu} < 0 \ , \end{cases} \tag{4.26}$$

where $\hat{\mu}$ follows a Gaussian distribution with mean μ' and variance σ. In this case, for $\mu' = 0$ the p-value is:

$$p_0 = 1 - F(q_0|0) \ , \tag{4.27}$$

giving a significance of:

$$Z_0 = \Phi^{-1}(1 - p_0) = \sqrt{q_0} \ . \tag{4.28}$$

In general, a significance of 3 standard deviations (σ) is sufficient to state the evidence of a positive signal, but a significance higher than 5σ is required to claim an observation.

4.5. Nuisance parameter treatment

Another aspect of the statistical interpretation, not described previously, is the treatment of the systematic uncertainties on the measurement. They are introduced as nuisance parameters θ, of which the signal and background expectations are functions: $s(\theta)$ and $b(\theta)$ [58]. All the nuisance parameters are taken into account as uncorrelated, to have a factorised form in the likelihood. They are expressed by means of their pdfs $\rho(\theta|\tilde{\theta})$. The pdf is characterised by a parameter $\tilde{\theta}$ describing its best estimate and generally another parameter (σ) describing its width or shape. The use of the pdfs can be seen as common to the Bayesian and frequentist interpretations: they can be considered as posterior coming from the measurement of the $\tilde{\theta}$ parameter, following Bayes' theorem:

$$\rho(\theta|\tilde{\theta}) \sim p(\tilde{\theta}|\theta) \cdot \pi_\theta(\theta) \ . \tag{4.29}$$

The choice of a specific pdf is determined by the type of systematic that is considered, and the typical choices are easily interpreted in both frequentist and Gaussian contexts if considering a flat $\pi_\theta(\theta)$ prior. In the following text, the pdfBayesians generally used in a typical ATLAS Higgs analysis are described.

- A flat pdf is used when no prior constraint exists on a particular parameter, and it can be determined by the profile likelihood fit to the data. These are often referred to as freely floating parameters.
- A Γ distribution is used in the case of statistical uncertainties coming from the number of selected Monte Carlo events. The data event rate in the interesting region, n, is proportional to the number of Monte Carlo events N: $n = \alpha \cdot N$. The Γ distribution describes the uncertainty on the rate n associated with the observation of N events:

$$\rho(n) = \frac{1}{\alpha} \frac{(n/\alpha)^N}{N!} \exp\left(-\frac{n}{\alpha}\right) \ . \tag{4.30}$$

- The standard choice in case of shape systematics is a Gaussian pdf, as it suits well situations where a parameter can have both positive and negative values.

$$\rho(\theta) = \frac{1}{\sqrt{2\pi}\sigma} \exp\left(-\frac{(\theta - \tilde{\theta})^2}{2\sigma^2}\right) . \tag{4.31}$$

  This type of pdf does not suit the situation when a variable has to be always positive.

- To cover the cases of parameters bound to positive values, the choice is to use a log-normal distribution as pdf:

$$\rho(\theta) = \frac{1}{\sqrt{2\pi}\ln(\kappa)} \exp\left(-\frac{(\ln(\theta/\tilde{\theta}))^2}{2(\ln(\kappa))^2}\right) \frac{1}{\theta} . \tag{4.32}$$

  The parameter κ characterises the width of the log-normal distribution; a log-normal distribution with small values of κ is asymptotically a Gaussian, as can be seen in fig. 4.4. This type of pdf is the standard choice for the normalisation systematics.

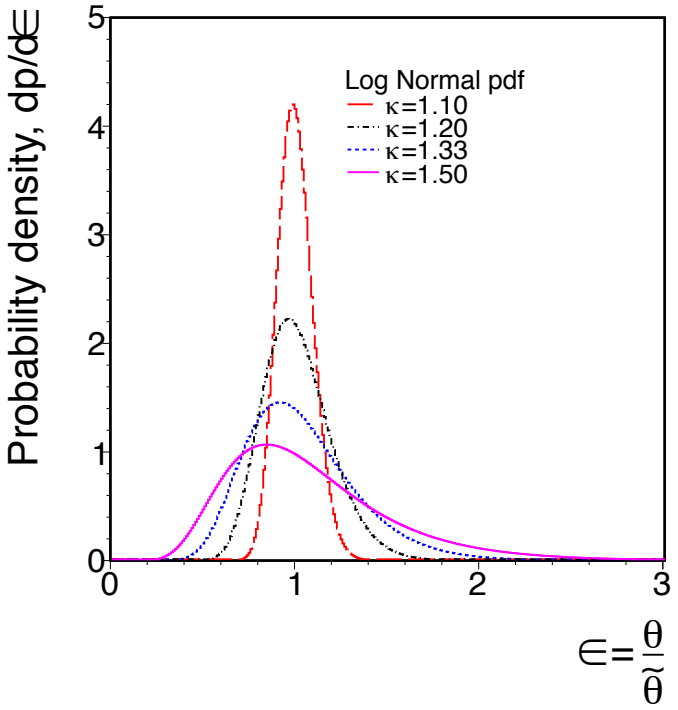

Figure 4.4.: Illustration of the log-normal distribution for different values of κ, taken from [58].

Chapter 5.

Monte Carlo samples and object definition

This chapter presents the initial requirements for the $VH \rightarrow \text{leptons} + b\bar{b}$ analysis, which will be described in more detail in the following chapters of this thesis, and will be indicated as $VH(b\bar{b})$. Firstly, the different Monte Carlo generators used to model the signal and background processes will be briefly described. Then, a description of the method used to identify the different physics objects forming the $VH(b\bar{b})$ final state will be provided, together with a list of the trigger used to select the most interesting events to analyse.

5.1. Monte Carlo generators used in the analysis

To obtain a reliable model of the $VH(b\bar{b})$ signal and its backgrounds, described in detail in sec. 2.5.1, different Monte Carlo (MC) generators are used. Each generator needs to include the various aspects of an event evolution, which can be summarised as follows:

1. Beam particles travel in opposite directions. They are generally characterised by parton distribution functions (PDFs), describing the energy and flavour composition of the beam. The partons in the beam can initiate branching processes, and start the initial state shower. This causes beam remnants carrying colour charge, with a relation with the final state particles. Only one parton per beam will initiate the hard process.

2. The hard process produces outcoming partons, determining the main characteristics of the process. Such outgoing partons can branch and create final state showers. Colour confinement guarantees that quarks and gluons produced in the interaction produce non-coloured hadron states. These hadrons could be unstable and decay further.

The hard process and the parton shower can be handled separately, by different generators. Once the events generated and showered, they are then passed to the simulation of the ATLAS detector, to take into account their interaction with the material. The ATLAS simulation is based on the GEANT4 program [59], and in some cases a parametric description of the material is used for the calorimeters. This alternative simulation is called ATLFAST-II [60], and reduces significantly the computational time.

The different generators used to model the $VH(b\bar{b})$ backgrounds can be subdivided into three main types: leading order (LO), resummed LO (or multi-leg) and next-to-leading order (NLO). A summary of the generators used for the various processes and their characteristics is given in the following paragraphs.

5.1.1. Pythia

The PYTHIA [61, 62] generator is designed for the description of tree level processes ($2 \to 2$). Events with higher multiplicities in the final state are obtained via the parton shower, treating the final state radiation. The final and initial state radiation are implemented via a parton shower structured in terms of branchings of the type $a \to bc$. These processes are: $e \to e\gamma$, $q \to qg$, $q \to q\gamma$, $g \to gg$ and $g \to q\bar{q}$. Each process is characterised by a splitting probability, function of the mother particle energy.

A virtuality scale Q^2 is associated to each parton and determines the time evolution of the branching cascade. Specifically, Q^2 increases in the initial state shower while approaching the hard scatter, and decreases in the final state shower. Generally the evolution stops at a cutoff value Q_0, and the maximum limit $Q_{\max}$ identifies the scale of the hard process.

The hadronisation process, that connects partons originated from the described branchings to form non coloured states (hadrons) is treated according to the string fragmentation model (known also as Lund model). Such model can be simplistically described as follows: in the case of a $q\bar{q}$ pair, the separation of the two causes a colour flux between them. Increasing the separation between the two, the potential energy of

this colour flux (which can be represented as a string) increases, until forming a new pair, $q'\bar{q}'$, between the original $q\bar{q}$ pair. This process happens iteratively, forming always new colour singlets (in the described case: $q\bar{q}'$ and $q'\bar{q}$).

In the $VH(b\bar{b})$ analysis, Pythia is used for modelling the signal, with the CTEQ6L1 PDFs [63] and the AUET2B tune [64] for the parton shower, hadronisation and multiple parton interactions. The total cross-sections and uncertainties on the signal process are taken from [41] with next-to-leading order (NLO) corrections as a function of p_{T}^{W} or p_{T}^{Z} applied [42, 65]. The decay branching ratios are calculated with Hdecay [66]. Eleven mass points are simulated for the Higgs signal, ranging from 110 to 150 GeV, in intervals of 5 GeV.

This generator is also used for modelling pileup events, as follows: minimum bias simulated events are produced, using MSTW 2008 LO PDFs [67] and the A2M tune [64, 68]. These minimum bias events are overlaid on the simulated signal and backgrounds according to the data luminosity profile. Both contributions from the same bunch crossing (in-time pile-up) and from the previous bunch crossing (out-of-time pile-up) are considered.

Pythia is also used as shower model interfaced with other generators, generally tuned to ATLAS data.

5.1.2. Herwig

Herwig [69] is a multipurpose generator, and similarly to Pythia, it is used to model leading order tree level processes and as parton shower interfaced with other generators.

The parton shower is treated using a coherent branching algorithm, assigning the energy fraction at each splitting, according to the DGLAP splitting functions. The available phase space is angularly-ordered, therefore, at each branching, the angular separation between the two partons decreases. The angular ordering is applied, although slightly differently, also to the initial state shower. In this case, it is considered with respect to the angle between the direction of the incoming hadron and that of the emitted parton.

This generator is used to model the diboson (WW, WZ and ZZ) backgrounds in the $VH(b\bar{b})$ analysis, as well as parton shower for some of the resummed or NLO generators. The CTEQ6L1 PDFs and the AUET2 tune are used for the diboson samples. The cross

sections at next-to-leading order are obtained from the MCFM generator [70], using the MSTW 2008 NLO PDFs [71].

5.1.3. Sherpa

SHERPA [72] is aimed at describing collision final states with multiplicities higher than two partons. It provides this prediction ($2 \to n$) at LO.

The technical implementation can be summarised as follows.

- The incoming beams are resolved with two steps. The first regards bremsstrahlung photon interactions, and the second is the PDF parameterisation to describe the parton content of the beam.
- The matrix element for arbitrarily large parton multiplicities in the final state at LO is calculated using the AMEGIC++ matrix element generator, and integrated to obtain the cross section of the process.
- The showering algorithm is based on DGLAP evolution equations, with a superimposed angular ordering.

Given the possibility of generation higher multiplicity final states using the matrix element, the possibility of double counting arises. In fact, the same event can be produced by the matrix element with higher multiplicity or by the $2 \to 2$ event with parton shower applied. Therefore a matching procedure, called CKKW [73], is applied to avoid the double counting possibility.

In the $VH(b\bar{b})$ analysis, SHERPA is used to model the V+jets backgrounds, where a good description of high multiplicity final states is crucial. In this case, it is interfaced with CT10 PDFs [74], simulating the processes at leading order (LO) in QCD, with massive b and c quarks. These backgrounds normalisation is extracted from the data, but in the kinematic requirement optimisation process, they are normalised to the next-to-next-to-leading order (NNLO) [75] cross sections.

5.1.4. PowHeg

POWHEG [76–78] provides NLO accuracy for the matrix element of different process. It is designed also to preserve the leading log accuracy in the parton shower, which is

generally obtained interfacing another generator with POWHEG. The events are handled generating first the hardest emission, guaranteeing the integrated quantities in the soft and collinear directions to have NLO precision.

In the $VH(b\bar{b})$ analysis, it is used to model the $t\bar{t}$ and single top (s-channel and Wt production) backgrounds, using CT10 PDFs. It is interfaced with PYTHIA6 [61] with CTEQ6L1 and the Perugia2011C tune [68] for the parton shower. The normalisation in the cut optimisation process is normalised to the next-to-next-to-leading order (NNLO) [79] cross sections. For the t-channel single top production, a different generator, ACERMC [80], interfaced with PYTHIA6 and the AUET2B tune, was used. The cross sections for single top production in the s-, t- and Wt channels are taken from theoretical calculations [81–83].

5.1.5. aMC@NLO

The aMC@NLO generator provides a fully automated calculation at NLO QCD of $Wb\bar{b} \to \ell\nu b\bar{b}$, analogous to the MCFM treatment [84]. In the calculation, the spin correlations of the final state leptons are fully taken into account. They are considered at the parton shower matching stage, together with the off-shell and interference effects. The matching to HERWIG++ is performed according to the MC@NLO formalism [45]. One-loop corrections are obtained with MADLOOP [85] using the Ossola-Papadopoulos-Pittau (OPP) reduction method [86] implemented in the CUTTOOLS program [87]. All the other contributions to the parton-level NLO cross section are dealt with by MADFKS [88], using the Frixione-Kunszt-Signer (FKS) formalism [89].

In the $VH(b\bar{b})$ analysis, this generator is used perform a truth level study aimed at understanding the modelling of the $Wb\bar{b}$ background. It is in fact difficult to isolate in the data a region with a high fraction of this process and low contamination of further backgrounds, such as $t\bar{t}$. Therefore a truth level study comparing the SHERPA description of the main kinematic variables used in the analysis to those of two NLO generators such as POWHEG and aMC@NLO, can help in understanding eventual modelling issues.

The aMC@NLO prediction for the $Wb\bar{b}$ process is generated using the electroweak parameters listed in table 5.1. The CT10 PDF set [74] is used for the computation, and defines the value of $\alpha_S(m_Z)$. The renormalisation and factorisation scales are evaluated based on the sum of the transverse masses of all final state particles and partons: H_{T}. The HERWIG++ parton shower uses CTEQ6L1 PDFs with the UE-EE-3 ATLAS tune [90].

Parameter and value	
m_W	80.419
G_F	1.166390×10^{-5}
m_t	173
$\alpha_S^{(NLO)}(m_Z)$	0.11798
Γ_W	2.0476
m_Z	91.118

Table 5.1.: List of electroweak physical parameters used in the generation of aMC@NLO $Wb\bar{b}$ events with the CT10 PDF set. Dimensional quantities are given in GeV.

The events are generated in the 4 flavour scheme that assumes massless final state b quarks. This is a good approximation, considering the minimum analysis requirement on the b-jet p_{T} at 20 GeV. The generation of the $Wb\bar{b}$ process at leading order is also performed with the same machinery, and a k-factor of 2.4, corresponding to the ratio of the NLO computed cross section to the LO one, is extracted.

5.2. Object definition and selection

The ATLAS $VH(b\bar{b})$ analysis is based on kinematic cuts, designed to reduce the main backgrounds described in sec. 2.5.1, and at the same time to identify the signal as efficiently as possible. The analysis is performed on three channels: $ZH \to \nu\bar{\nu}b\bar{b}$, $WH \to \ell\nu b\bar{b}$ and $ZH \to \ell^+\ell^- b\bar{b}$, each with different background contamination. Here only the basic requirements aimed at selecting the objects forming these channels final states will be described. A more detailed insight on the requirements specific to each channel will be given in the next chapter.

The basic requirement for an event to be selected is to have a primary vertex with at least 3 tracks with $p_{\mathrm{T}} > 0.4$ GeV. The primary vertex is identified as the vertex with the highest sum of the squares of the transverse momenta of the tracks associated to it.

5.2.1. Lepton identification

Leptons are classified using three different criteria, and are denoted, in terms of decreasing identification purity, as tight, medium and loose. Only some requirements are common to all the criteria for lepton identification. The pseudorapidity range is $|\eta| < 2.47$ for

electrons and $|\eta| < 2.5$ for muons with hits in the Inner Detector. In addition, muons are accepted in the $2.5 < |\eta| < 2.7$ interval, if they have a sufficient number of hits in the muon system, to increase the acceptance. All loose leptons are required to pass track isolation, to discriminate them from jets. The track isolation cut is implemented requiring that the sum of the p_{T} of the tracks within a cone of 0.2 radius around the identified lepton track has to be less than 10% of the lepton track p_{T}. The track isolation requirement is stricter in the tight lepton case, and the cut is tightened from 10% to 4%.

Quality cuts on the impact parameter variables are applied for electrons and muons identified in the inner detector: $d_0 < 0.1$ mm for both electrons and muons, and in addition $z_0 < 10$ mm for the muon case. The E_{T} threshold for loose leptons is 10 GeV, while for medium and tight leptons it is 25 GeV. In the tight lepton case, isolation in the calorimeter is also required: the sum of the calorimeter energy deposits in a 0.3 radius cone around the electron or muon must be smaller than 7% of the lepton energy.

The lepton requirements in the three channel analysis are:

- one medium and one loose lepton for the 2-lepton channel;
- only one tight lepton for the 1-lepton channel;
- no leptons of the loose type for the 0-lepton channel.

5.2.2. Jet identification, flavour tagging and missing transverse energy

Jets are reconstructed from 3D topological clusters in the calorimeter using the anti-k_{T} algorithm [91] with a radius parameter $R = 0.4$ and their energies are calibrated using p_{T} and η-dependent correction factors based on simulation and validated with data [92]. Jets are corrected for pile-up contributions using a technique based on jet areas [93]. Pile-up is further reduced applying a cut on the JVF variable, defined as:

$$\mathrm{JVF} = \frac{\sum p_{\mathrm{T}}(\text{tracks associated to jet matched to primary vertex})}{\sum p_{\mathrm{T}}(\text{all tracks associated to jet})} , \qquad (5.1)$$

with $p_{\mathrm{T}}^{\mathrm{track}} > 0.4$ GeV. For the $\sqrt{s} = 7$ TeV dataset the requirement is: JVF $> 75\%$. For the $\sqrt{s} = 8$ TeV dataset, instead, the requirement JVF $> 50\%$ is applied to jets with $p_{\mathrm{T}} < 50$ GeV and inside the tracker fiducial region.

Jets used to identify the Higgs signal are selected using different criteria from those used to veto events. The latter are required to have $p_{\mathrm{T}} > 20$ GeV in $|\eta| < 2.5$ and $p_{\mathrm{T}} > 30$ GeV in $2.5 < |\eta| < 4.5$. Signal jets, instead, are required to be within $|\eta| < 2.5$, the tracker fiducial volume, to allow b-tagging. The leading signal jet is required to have $p_{\mathrm{T}} > 45$ GeV, while the sub-leading jet is required to have $p_{\mathrm{T}} > 20$ GeV. These two jets are used to reconstruct the Higgs candidate.

The flavour of the reconstructed Monte Carlo jets is determined at hadron level: a jet is labelled as b-jet if there is a b hadron within a cone of 0.4 about the jet axis. The same definition applies to a c-jet, defined as a non-b-jet with a c hadron within a 0.4 cone. Non-heavy flavour jets are labelled as τ-jets if there is a τ within an 0.4 cone and all the other jets are labelled as light jets. Jets originating from b quarks are identified using algorithms exploiting the long lifetime of b hadrons. In this analysis, the MV1 [94–97] algorithm, briefly described in sec. 7.2, is used with a cut at the 70% efficiency working point for b-jets, with rejection factors of ~ 5 and ~ 150 for c and light jets respectively. The number of V+light-jet, V+c-jet and WW simulated events passing all the analysis cuts as well as the double b-tagging requirement on the signal jets is small. Therefore, to lower the statistical uncertainty on these backgrounds, a parametrisation of the number of c- and light-jets mis-tagged as b quarks is derived from data as a function of p_{T} and η. This is then applied as a re-weighting factor on the truth-labeled c and light jets for the mentioned backgrounds. The bias from this procedure is tested and found to be negligible. In the case of samples which contain real b-jets, instead, the direct tagging based on the MV1 algorithm is applied.

The missing transverse energy is measured from the negative vector sum of the transverse momenta of cluster energies in the calorimeter within $|\eta| < 4.9$ [98]. Further corrections are applied to cluster energies associated with a reconstructed object: jets, electrons, taus, photons and muons. A track-based missing transverse momentum ($p_{\mathrm{T}}^{\mathrm{miss}}$) is also calculated based on the vector sum of the transverse momenta of the tracks associated to the primary vertex.

5.3. Trigger selection

Here, details on the triggers used to select the most interesting events to this analysis are presented. In the 1- and 2-lepton channels, events are selected using the lowest

un-prescaled single lepton triggers. In the 0-lepton channel instead, the events are selected using triggers based on the missing transverse energy.

For the $\sqrt{s} = 7$ TeV dataset, the trigger applied is the lowest momentum single lepton trigger that does not have a prescale, with an 18 GeV threshold for muons and 20 or 22 GeV for electrons. The different electron trigger thresholds depend on the value of the instantaneous luminosity, which causes more pileup events if higher. This triggers are highly efficient, close to 100% in the electron case, and 90% for muons. The same triggers are used also in the 2-lepton case, supplemented by di-electron and di-muon triggers with 12 and 13 GeV thresholds respectively. $E_{\mathrm{T}}^{\mathrm{miss}}$ triggers with 70 GeV threshold are employed to select the 0-lepton events, and to supplement single lepton triggers in the 1-lepton channel. The choice of using $E_{\mathrm{T}}^{\mathrm{miss}}$ triggers to complement single lepton triggers in the 1-lepton channel is caused by the reduced muon chamber coverage in some regions. This recovers a 20% of the signal acceptance in this channel.

In the $\sqrt{s} = 8$ TeV case, the lowest un-prescaled single lepton triggers have thresholds of 24 GeV for both electrons and muons and include requirements on track isolation. This is aimed at discarding pile-up events, produced by the higher instantaneous luminosity. The inefficiencies due to the isolation cuts are partially compensated by supplementing these triggers with others with higher thresholds (60 GeV for electrons and 36 GeV for muons), without isolation requirements. In the 2-lepton analysis, events passing di-muon and di-electron triggers with the same thresholds as at $\sqrt{s} = 7$ TeV are selected. The 0-lepton channel events are required to satisfy the minimum $E_{\mathrm{T}}^{\mathrm{miss}}$ trigger threshold of 80 GeV, and the same trigger is used to supplement missing events in the 1-lepton channel.

Chapter 6.

VH $\rightarrow$ leptons+b$\bar{\text{b}}$ analysis strategy

This chapter describes the technique used to analyse $VH(b\bar{b})$ events. As mentioned in chapt. 5, the analysis is based on kinematic cuts, aimed at discriminating the signal from the large backgrounds in the three channels: $ZH \rightarrow \nu\bar{\nu}b\bar{b}$, $WH \rightarrow \ell\nu b\bar{b}$ and $ZH \rightarrow \ell^+\ell^- b\bar{b}$. The analysis cuts are optimised for each channel and subcategory as a function of $S/\sqrt{B}$. The subcategories are defined based on the transverse momentum of the vector boson, p_{T}^V, the number of jets in the final states, and the multiplicity of b-tagged jets.

The discriminant variable in the search is the invariant mass of the $b\bar{b}$ system. The shape of this distribution and its normalisation are affected by systematic uncertainties, coming from modelling and experimental sources. These systematics are taken into account in the statistical analysis, and cause a reduction of the sensitivity of the search.

The statistical analysis is performed using a profile likelihood fit, introduced in chapt. 4. It is aimed not only at testing the signal hypothesis, but also at evaluating from the data the normalisations of the largest backgrounds: $t\bar{t}$ and V+jets. Information on these backgrounds is extracted using specific regions included in the final fit. In some cases, only the information on the number of events in a region is used, in others the $m_{b\bar{b}}$ shape is also fitted.

6.1. Event selection and categorisation

The analysis uses 4.7 fb^{-1} of data collected at $\sqrt{s} = 7$ TeV and 20.3 fb^{-1} at $\sqrt{s} = 8$ TeV, corresponding to the full Run 1 dataset. The data used satisfy ATLAS data quality (DQ) requirements and good beam conditions. In the analysis of the $ZH \rightarrow \nu\bar{\nu}b\bar{b}$ channel, the

integrated luminosity of the $\sqrt{s} = 7$ TeV dataset is slightly reduced, 4.6 fb^{-1}, due to the different trigger used to collect these data.

Events are categorised according to different intervals of the recoiling vector boson transverse momentum, p_{T}^{V}, coherently across the three channels, and in the 0-lepton channel the transverse momentum of the vector boson corresponds to the $E_{\mathrm{T}}^{\mathrm{miss}}$:

- $p_{\mathrm{T}}^{V} \in [0 - 90]$ GeV for 1- and 2-lepton
- $p_{\mathrm{T}}^{V} \in [90 - 120]$ GeV for 1- and 2-lepton
- $p_{\mathrm{T}}^{V} \in [120 - 160]$ GeV for all three channels, because $E_{\mathrm{T}}^{\mathrm{miss}}$ triggers are 90% efficient at $E_{\mathrm{T}}^{\mathrm{miss}} = 120$ GeV
- $p_{\mathrm{T}}^{V} \in [160 - 200]$ GeV for all three channels
- $p_{\mathrm{T}}^{V} > 200$ GeV for all three channels.

The V+jet background composition in the Monte Carlo is classified as: Vbb, Vbc, Vbl, Vcc and Vcl, according to the following labelling which is based on the true flavour of the reconstructed jet:

- jets associated to a b quark are labelled as b-jets;
- jets not associated with a b quark, but matching a c quark, are labelled as c-jets;
- jets not associated with both b- and c quarks are labeled as light jets (l).

The analysis cuts are summarised in tables 6.1 and 6.2. The analysis categories take into account 2- and 3-jet final state regions with 2 b-tagged jets for all three channels. The cuts on $E_{\mathrm{T}}^{\mathrm{miss}}$ and m_{T}^{W} in the 1-lepton channel are aimed at selecting events consistent with a W boson and the $m_{\ell\ell}$ cut in the 2-lepton channel at selecting events consistent with a Z boson. Events are required to contain exactly two b-tagged jets, which are used to reconstruct the mass of the Higgs boson candidate. In the 3-jet regions, the two hardest jets are required to be b-tagged. In the 0-lepton channel, the azimuthal angle between the $E_{\mathrm{T}}^{\mathrm{miss}}$ direction and the $p_{\mathrm{T}}^{\mathrm{miss}}$ or the Higgs candidate direction, $E_{\mathrm{T}}^{\mathrm{miss}}$ and $p_{\mathrm{T}}^{\mathrm{miss}}$ cuts are effective in suppressing the QCD background. The $m_{\ell\ell}$ cut in the 2-lepton channel, together with the $E_{\mathrm{T}}^{\mathrm{miss}}$ cut reduces the $t\bar{t}$ background.

Further topological cuts, listed in table 6.2, are applied to enhance the signal over background ratio. These cuts are customised to each channel. In the 1-lepton analysis, an upper cut on m_{T}^{W} is applied to reduce the contamination from the top background.

Object	0-lepton	1-lepton	2-lepton
Leptons	0 loose leptons $p_{\mathrm{T}} > 10$ GeV	1 tight lepton, $p_{\mathrm{T}} > 25$ GeV +0 loose leptons, $p_{\mathrm{T}} > 10$ GeV	1 medium lepton $p_{\mathrm{T}} > 10$ GeV +1 loose lepton $p_{\mathrm{T}} > 10$ GeV
Jets	2 b-tags $p_{\mathrm{T}}^{\mathrm{jet}_1} > 45$ GeV $p_{\mathrm{T}}^{\mathrm{jet}_2} > 20$ GeV $+\leq 1$ extra jets		
Missing E_{T}	$E_{\mathrm{T}}^{\mathrm{miss}} > 120$ GeV $p_{\mathrm{T}}^{\mathrm{miss}} > 30$ GeV $\Delta\varphi(E_{\mathrm{T}}^{\mathrm{miss}}, p_{\mathrm{T}}^{\mathrm{miss}}) < \pi/2$ $\min[\Delta\varphi(E_{\mathrm{T}}^{\mathrm{miss}}, \mathrm{jet})] > 1.5$ $\Delta\varphi(E_{\mathrm{T}}^{\mathrm{miss}}, b\bar{b}) > 2.8$	$E_{\mathrm{T}}^{\mathrm{miss}} > 25$ GeV	$E_{\mathrm{T}}^{\mathrm{miss}} < 60$ GeV
Vector boson	-	$m_{\mathrm{T}}^{W} < 120$ GeV	$83 < m_{\ell\ell}/(\ \mathrm{GeV}) < 99$

Table 6.1.: Baseline event selection for the three lepton channels.

Cuts on the angular separation, $\Delta R_{b\bar{b}}$, between the two b-jets are tuned to different effects: the minimum cut reduces the V+jets background and the maximum is tightened at higher transverse momenta to profit from the increasing collimation between the jets.

	p_{T}^{V} (GeV)	0-90	90-120	120-160	160-200	> 200
All channels	$\Delta R_{b\bar{b}}$	0.7-3.4	0.7-3.0	0.7-2.3	0.7-1.8	< 1.4
1-lepton	$E_{\mathrm{T}}^{\mathrm{miss}}$ (GeV)	> 25				> 50
	m_{T}^{W} (GeV)	40-120			< 120	

Table 6.2.: Further topological cuts in the analysis. The 0-lepton analysis is only performed in the intervals with $p_{\mathrm{T}}^{V} > 120$ GeV.

The signal acceptance, together with the product of cross section and branching ratio is shown for the three channels in table 6.3. The acceptance is defined as the fraction of remaining events in the 2-tag signal region after performing the full event selection.

After the full selection is applied, the $m_{b\bar{b}}$ is recalculated in the signal regions using an improved jet calibration, including the energy of the muons lying within the jet and applying a p_{T}-dependent correction taking into account response biases caused by the resolution, as shown in fig. 6.1. This correction improves the mass resolution, leading to resolution values ranging between 12% and 10% for increasing p_{T}^{V} intervals. This is particularly useful to better discriminate between the signal and diboson events, as mentioned in sec. 2.5.1.

$m_H = 125$ GeV at $\sqrt{s} = 7$ TeV				
$(W/Z)(H \rightarrow b\bar{b})$	Cross section $\times$ BR (fb)	Acceptance [%]		
		0-lepton	1-lepton	2-lepton
$Z \rightarrow \ell^+\ell^-$	12.3	0.0	0.7	8.2
$W \rightarrow \ell\nu$	107.1	0.2	3.5	-
$Z \rightarrow \nu\nu$	36.4	2.2	-	-
$m_H = 125$ GeV at $\sqrt{s} = 8$ TeV				
$(W/Z)(H \rightarrow b\bar{b})$	Cross section $\times$ BR (fb)	Acceptance [%]		
		0-lepton	1-lepton	2-lepton
$Z \rightarrow \ell^+\ell^-$	15.3	0.0	0.9	8.4
$W \rightarrow \ell\nu$	130.2	0.2	3.3	-
$Z \rightarrow \nu\nu$	45.5	2.5	-	-

Table 6.3.: Signal cross section times Branching Ratio and acceptance for the three different channels.

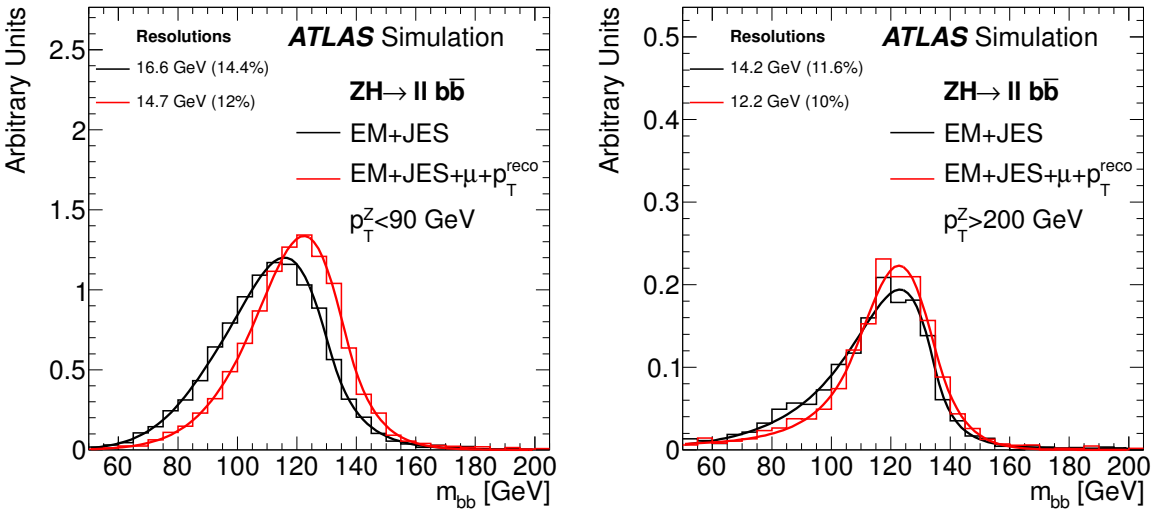

(a) $0 < p_{\mathrm{T}}^Z/(GeV) < 90$ **(b)** $p_{\mathrm{T}}^Z > 200$ GeV

Figure 6.1.: $m_{b\bar{b}}$ distribution in the lowest (6.1a) and the highest (6.1b) p_{T}^Z intervals for a Higgs boson with $m_H = 125$ GeV in the 2-lepton selection [99]. The distributions are shown using jets calibrated with the EM+JES calibration [92] (black line), and after adding muons coming from semileptonic b-decays within the jets, and correcting for resolution effects specific to the kinematics of the event (red line). The distributions are fit to a Bukin curve [100] and the parameter representing the width of its core is reported as the resolution.

6.2. Background modelling

As already mentioned in the previous section, the analysis presented is categorised in three lepton channels, with 2- and 3-jet final states, and p_{T}^{V} bins. Additional control regions are defined as follows:

- 0-tag control regions: contains all the events passing the full analysis cuts with two or three jets in the final state, if the jets fail the b-tagging requirement. It is used as a validation region for background modelling.
- 1-tag control regions: contains all the events passing the full analysis cuts with two or three jets in the final state, if only one jet is b-tagged. It is included in the final fit, described in sec. 9.1.
- 2-lepton $m_{\ell\ell}$ top control region: defined via the inversion of the $m_{\ell\ell}$ cut. It is used as a validation region for background modelling.
- 2-lepton top control region: defined using the same cuts as the 2-jet signal region, but requiring different flavour leptons in the final state. This region is included in the final fit.

The V+jet and $t\bar{t}$ normalisations are extracted in the final profile likelihood fit, using the information from the 1-tag and top control regions. The diboson and single top shape and normalisations are both taken from simulation, while the shape and normalisation are estimated from data for the multijet background.

The multijet background estimate in the 0-lepton channel is based on the ABCD method. Data events are classified into four exclusive regions, based on two variables, $\min[\Delta\varphi(E_{\mathrm{T}}^{\mathrm{miss}}, \mathrm{jets})]$ and $\Delta\varphi(E_{\mathrm{T}}^{\mathrm{miss}}, p_{\mathrm{T}}^{\mathrm{miss}})$, shown in fig. 6.2, and defined as:

- A: $\min[\Delta\varphi(E_{\mathrm{T}}^{\mathrm{miss}}, \mathrm{jets})] > 1.5$, $\Delta\varphi(E_{\mathrm{T}}^{\mathrm{miss}}, p_{\mathrm{T}}^{\mathrm{miss}}) < \pi/2$
- B: $\min[\Delta\varphi(E_{\mathrm{T}}^{\mathrm{miss}}, \mathrm{jets})] < 0.4$, $\Delta\varphi(E_{\mathrm{T}}^{\mathrm{miss}}, p_{\mathrm{T}}^{\mathrm{miss}}) < \pi/2$
- C: $\min[\Delta\varphi(E_{\mathrm{T}}^{\mathrm{miss}}, \mathrm{jets})] > 1.5$, $\Delta\varphi(E_{\mathrm{T}}^{\mathrm{miss}}, p_{\mathrm{T}}^{\mathrm{miss}}) > \pi/2$
- D: $\min[\Delta\varphi(E_{\mathrm{T}}^{\mathrm{miss}}, \mathrm{jets})] < 0.4$, $\Delta\varphi(E_{\mathrm{T}}^{\mathrm{miss}}, p_{\mathrm{T}}^{\mathrm{miss}}) > \pi/2$

Under the assumption that these two variables are almost uncorrelated in case of multijet background, the estimate of the normalisation of this background in the signal region

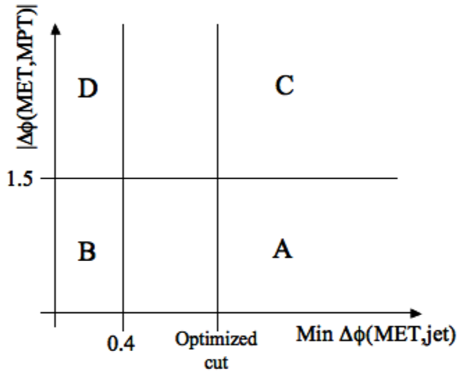

Figure 6.2.: The two-dimensional kinematic plane used for the signal region (A) multijet background estimate in the 0-lepton channel.

(A) is obtained as follows:

$$N_{\mathrm{QCD}}(A) = \frac{N(B)}{N(D)} \times N(C), \tag{6.1}$$

where $N(B)$, $N(C)$ and $N(D)$ represent the number of events in the regions B, C and D in the data, after applying all the event selection cuts except from these used to classify the regions. Contributions from other background sources are estimated from simulation and are removed before calculating the QCD contribution. The multijet background is found to be 1% of the total background.

For the 1-lepton channel multijet estimate, a template is extracted from a region obtained by reverting the lepton track isolation cut. The normalisation is estimated from a fit to the m_{T}^{W} distribution for electrons and the $E_{\mathrm{T}}^{\mathrm{miss}}$ for muons. The contribution of QCD to the total background in this region is found to range between 15% and 1%, decreasing as a function of p_{T}^{V}. In the 2-lepton channel, the multijet background is a small contribution, since it only comes from two misidentified leptons which have a combined invariant mass consistent with that of the Z boson. In case of two electrons, the multijet background is estimated from data by deriving a shape template from a multijet dominated sample and normalising it to the signal selection. The sample is obtained by reverting the track isolation requirement in a similar way to the 1-lepton case. To normalise the templates the di-electron invariant mass distribution is fitted after applying all the selection cuts, but without the b-tagging requirements. In the two muon case, an ABCD method-based estimate is performed on the sidebands of the di-muon invariant mass. The result is a $< 1\%$ contamination on the total background.

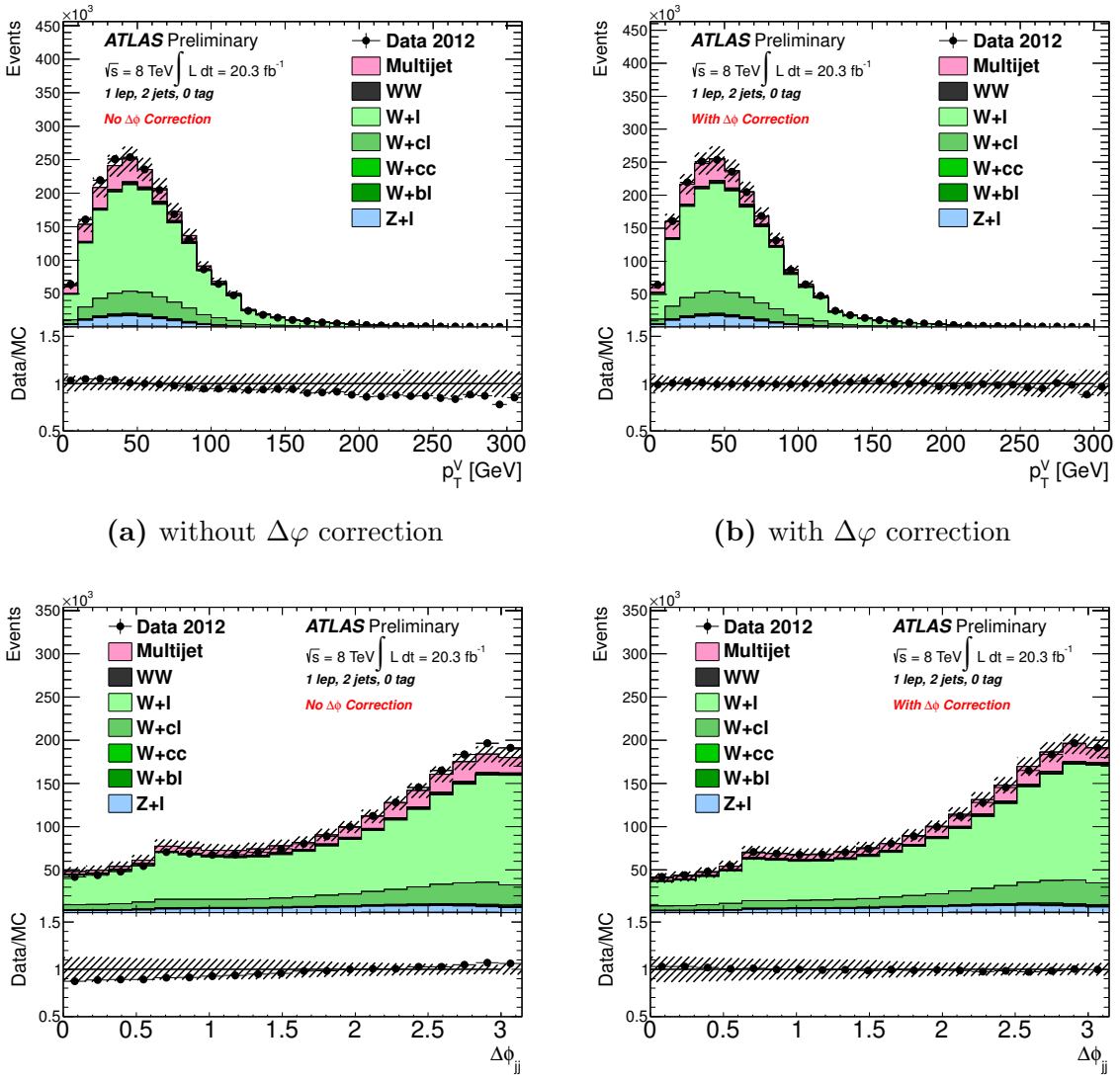

(a) without $\Delta\varphi$ correction

(b) with $\Delta\varphi$ correction

(c) without $\Delta\varphi$ correction

(d) with $\Delta\varphi$ correction

Figure 6.3.: The p_{T}^{W} (top) and $\Delta\varphi(j_1, j_2)$ (bottom) distributions before (left) and after (right) the linear reweighting in $\Delta\varphi(j_1, j_2)$ [99]. In the distributions 6.3b and 6.3d the improved agreement between data and Monte Carlo is visible.

Shapes for the $t\bar{t}$ and V+jets backgrounds are taken from simulation, and modelling corrections are applied to them, and are described here. A mis-modelling of the p_{T}^{V} variable is found in $t\bar{t}$-dominated regions, where it is caused by the excessive hardness of the top quark p_{T} spectrum predicted by PowHeg. Therefore a correction at generator level is applied to the $t\bar{t}$ samples for the the top and antitop quark p_{T} distributions. Studies performed in the 0-tag region show a mis-modelling of the p_{T}^{V} distribution in the Sherpa MC with respect to data, as can be seen in fig. 6.3a for W+jets. A precise modelling of this variable is very important, as the analysis relies on a p_{T}^{V} bin categorisation to

extract the result. Studies indicated that the azimuthal distance between the two leading jets, $\Delta\varphi(j_1, j_2)$, is the main source of this mis-modelling. This can be seen in fig. 6.3c for the W+jet case. The NLO generators give a better description of this variable than LO Sherpa, which is used as a baseline in the analysis [101]. Reweighting the $\Delta\varphi(j_1, j_2)$ with a linear function, corresponding to the mis-modelling slope, improves significantly the p_{T}^{V} agreement between data and Monte Carlo, as shown in fig. 6.3b. In addition, various other kinematic distributions, such as $m_{b\bar{b}}$, show improved agreement after the $\Delta\varphi$ reweighting. The reweighting is applied to both W and Z+jet backgrounds, and is derived independently in the two cases. It is also applied to all the flavour compositions of V+jets. The effectiveness of the correction was cross-checked in the 1-tag region, showing an analogous behaviour to the 0-tag. Further tests have been performed at generator level on $Wb\bar{b}$ events, and details can be found in sec. 6.4.

6.3. Systematic uncertainties

The systematic uncertainties affecting this analysis can be subdivided into three categories:

- the experimental uncertainties, affecting both the signal and the backgrounds;
- the theoretical uncertainties on the VH signal;
- the theoretical uncertainties on the background modelling.

The systematics can affect both the normalisation and the shape of the $m_{b\bar{b}}$ distribution, which is used as the discriminant variable in the final fit.

6.3.1. Experimental systematics

The experimental uncertainties taken into account affect: the trigger selection, the physics object reconstruction, identification, momentum and energy resolution and calibration. Many of these uncertainties have a very small impact on the $m_{b\bar{b}}$ distribution, i.e., at the sub-percent level. The largest systematics are those affecting the jet energy scale (referred to as JES) and the heavy flavour tagging.

The jet energy scale uncertainty [102] has different sources, which are independent. Therefore the uncertainty is split into 24 components, accounting for the different sources. The uncertainty on jets falling in the central pseudorapidity region ranges from 4% to 1%

in the p_{T} interval 20 GeV $-$ 1 TeV. The calibration of b-jets is affected by an additional uncertainty at the percent level. Uncertainties on the jet flavour determination are also included, and are typically large, as they account for the ability to distinguish between quark and gluon-originated jets. Smaller uncertainties connected to the $m_{b\bar{b}}$ resolution improvements are taken into account.

All the systematic errors on the jets are propagated to the $E_{\mathrm{T}}^{\mathrm{miss}}$ calculation. The uncertainties on the energy calibration and resolution of electrons and muons are very small, and they are also propagated to the $E_{\mathrm{T}}^{\mathrm{miss}}$ calculation. An additional uncertainty for the energy calibration of clusters in the calorimeter, which are not associated to any object, is taken into account for the missing transverse energy. An uncertainty on the $E_{\mathrm{T}}^{\mathrm{miss}}$ trigger is taken into account, and has a 5% effect in the $120 - 160$ GeV $E_{\mathrm{T}}^{\mathrm{miss}}$ interval and of $\approx 1\%$ in the $E_{\mathrm{T}}^{\mathrm{miss}} > 200$ GeV interval.

The uncertainty on flavour tagging from the b-, c- and light jet tagging efficiencies is measured in data. A calibration is applied to the jets in the Monte Carlo as Monte Carlo to data scale factors, based on the jet kinematic properties. These scale factors correspond to the ratios of the data values to the Monte Carlo ones, in specific kinematic ranges. They are derived using PowHeg+Pythia $t\bar{t}$ generated events. The b-tagging uncertainties are taken into account as ten independent systematic uncertainty components in the $\sqrt{s} = 7$ TeV dataset and seven components in the $\sqrt{s} = 8$ TeV case. The scale factors are generally close to 0.98, with typical uncertainties of $2\% - 3\%$, but increasing up to 5% for low p_{T} jets and up to 8% for jets with $p_{\mathrm{T}} > 200$ GeV. The analysis is less sensitive to the c and light components, therefore a smaller number of components is taken into account in this case. In the c-jet case, six components are taken into account, whilst for light-jets, only one component is considered. Small differences were observed in the b-tagging efficiencies between different generators. Therefore an additional uncertainty of 2% for b-jets, and 5% for c-jets, is applied to the V+jet sample, to account for the efficiency discrepancy between Sherpa and PowHeg.

The uncertainty on the integrated luminosity measurement is applied to both signal and background samples normalised from simulation. It is 2.8% for the $\sqrt{s} = 8$ TeV dataset and 1.8% for the $\sqrt{s} = 7$ TeV one. Finally, the multijet background normalisation uncertainty is estimated to be 100% for both 0- and 2-lepton channels. It is left free to float in the final profile likelihood fit for the 1-lepton channel, independently in the 1- and 2-tag region and in the 2- and 3-jet region. The uncertainty on the multijet template shapes is also considered, and it is obtained varying the isolation cuts used to define the multijet-enriched regions.

6.3.2. Theoretical systematics affecting the VH signal

The uncertainties on the signal, coming from theoretical predictions are described in this section. In the analysis, the WH and ZH signals are normalised to the inclusive cross sections from the Higgs boson cross section working group report [41, 42, 103]. For both WH and ZH signals the NNLO QCD and NLO EW parton-level computations are applied, and the relevant corrections are of the order of $5-7\%$. The relative uncertainty on the $H \rightarrow b\bar{b}$ branching ratio varies from 2.5% to 4.3% in the mass range $115-135$ GeV, and it is 3.3% at $m_H = 125$ GeV.

The uncertainties on the inclusive cross sections at $\sqrt{s} = 7$ and 8 TeV can be subdivided into PDF, renormalisation and factorisation scale uncertainties. In the final fit, the scale and PDF uncertainties are treated independently. PDF uncertainties, of the order of 3.5%, are correlated between WH and ZH production modes, where the initial state is dominated by $q\bar{q}$. Renormalisation and factorisation scale variations, ranging between 0.5 and 1.5%, are instead uncorrelated.

NLO QCD calculations obtained with the HAWK Monte Carlo are used to derive corrections in bins of p_{T}^V [104, 105]. These corrections are applied as a function of p_{T}^V to the LO WH and ZH signals generated with Pythia8, after rescaling to the inclusive NNLO QCD+EW cross sections. This results in an uncertainty of 2%, increasing to 2.6% in the highest p_{T}^V bin for the WH channel. Additional uncertainties on the signal acceptance are estimated comparing the results from three different generators: the baseline Pythia8, Herwig and Pythia6. The uncertainty in this case is estimated to be 10%.

6.3.3. Uncertainties on the background modelling

The most important background systematic uncertainties are those related to the discriminant quantities in the final fit. They affect the $m_{b\bar{b}}$ shape, the jet multiplicities, the flavour composition in the 2-tag regions and the p_{T}^V distribution.

The $t\bar{t}$ sample normalisation is left free to float in the fit, and can be extracted from the 2-lepton top control region, defined in sec. 6.2, and the 3-jet regions in the 1-lepton channel, where this background is dominant. The extrapolation of the result to the 2-jet signal region requires an uncertainty on the 3- to 2-jet ratio. This uncertainty is evaluated comparing the baseline Powheg+Pythia prediction with samples obtained

by varying the amount of initial and final state radiation (ISR and FSR), the parton shower and hadronisation, and the QCD matrix element ordering. The uncertainty on the ratio is found to be 5%. The flavour composition of the $t\bar{t}$ sample after the application of the double b-tagging requirement varies considerably in the different p_{T}^{V} bins, resulting in a high charm fraction in the highest p_{T}^{V} bins. As a consequence, the c-jet tagging efficiency and its uncertainty have a large impact on these bins. The $m_{b\bar{b}}$ shape systematic is evaluated using the same procedure as the 3- to 2-jet ratio, leading to a linear symmetric variation that increases (decreases) the distribution by 5% for an $m_{b\bar{b}}$ value of 50 GeV, and decreases (increases) it by 5% at $m_{b\bar{b}} = 200$ GeV. In addition, a systematic uncertainty of half the size of the correction on the top p_{T} described at the end of sec. 6.2 is applied.

The theoretical cross section uncertainties are taken into account for all three possible single top production channels: 4% on s-channel, 4% on the t-channel and 7% on Wt production [106]. Comparisons between generators and different hadronisation schemes are used to derive the uncertainties on $m_{b\bar{b}}$, p_{T}^{V} and the 3- to 2-jet ratio for single top. For the first, the variations are lower than 10% in the t-channel and up to 5% for the other two channels. In each p_{T}^{V} bin, a 5% uncertainty on the normalisation is assigned to each of the processes, and the 3- to 2-jet ratio is found to have uncertainties of 9% in the s-channel, 5% in the t-channel and 15% in the Wt channel.

The V+jet treatment is analogous in both the W and Z cases apart from the $m_{b\bar{b}}$ uncertainty estimate. Therefore only the W+jet treatment will be described here, apart from the $m_{b\bar{b}}$ case. The W+heavy flavour jet normalisation is floated freely in the final fit, and systematic uncertainties on the relative contributions of the $Wb\bar{b}$, Wbc and Wbl processes are taken into account, and calculated comparing NLO predictions to the Sherpa ones, as outlined in detail in sec. 6.4. The uncertainty assigned to the Wbl fraction is the largest and has a value of 30%. The Wcl background normalisation, largely contributing to the 1-tag region, is left free to float in the final fit, while the Wl component is fixed to its theoretical cross section with a 10% uncertainty. The uncertainty on the $\Delta\varphi(j_1, j_2)$ correction described in sec. 6.2, is considered as half of the correction. Additional uncertainties on the normalisation of the two highest p_{T}^{V} bins are 2 and 4% respectively, to account for the residual p_{T}^{W} mis-modelling after the application of the $\Delta\varphi(j_1, j_2)$ correction. The procedure used to derive the $m_{b\bar{b}}$ uncertainty for the W case is outlined in sec. 6.4. The resultant uncertainty is a slope increasing (decreasing) the distribution by 20% at $m_{b\bar{b}} = 50$ GeV and decreasing (increasing) it by 40% at

$m_{b\bar{b}} = 200$ GeV. In the Z case, it is estimated from a comparison to data, in the $m_{b\bar{b}}$ sidebands.

The last background to consider is the diboson production: WW, WZ and ZZ. The uncertainty on the cross section is estimated to be 5% for WW, 6% for ZZ and 7% for WZ, obtained varying the renormalisation and factorisation scales and using different PDF sets [42]. A correction to account for the minimum p_{T}^{V} cut of 10 GeV used at generator level in HERWIG is derived to be 8% using PYTHIA, and an uncertainty equivalent to half this correction is considered in the fit. The 3- to 2-jet ratio uncertainty is determined comparing the NLO predictions obtained with MCFM to the baseline HERWIG generator. A 25% uncertainty is assigned to this ratio after studying WZ and ZZ events. A comparison of the p_{T}^{V} distribution is performed for both the 2- and the 3-jet region between LO and NLO predictions, resulting in an uncertainty of $\sim$15% in the 2-jet case and much larger uncertainties ranging up to 25% in the ZZ case, 45% for WZ and 60% for WW in case of $p_{\mathrm{T}}^{V} > 120$ GeV.

6.3.4. Impact of systematic uncertainties

A summary of the impact of the systematic uncertainties on the signal and background yields is shown in tables 6.4 and 6.5. The percentage uncertainties on the total background are shown in table 6.4 before performing the profile likelihood fit (pre-fit). The dominant uncertainty for the 0-lepton channel is the 6.2% coming from the jet energy scale, jet energy resolution, missing energy and pile-up uncertainties. For the 1-lepton channel, the dominant pre-fit uncertainty comes again from the jet-related variables and is 6.0%. In the 2-lepton channel, the dominant uncertainty is the 9.8% error on the Z+jets modelling.

The percentage uncertainties on the signal before performing the final profile likelihood fit are shown in table 6.5. Apart from the 10% VH signal acceptance systematic, the dominant uncertainty for the 0-lepton channel is is related to the jets and $E_{\mathrm{T}}^{\mathrm{miss}}$, with an impact of 5.9%. For the 1-lepton channel, the dominant pre-fit uncertainty is the 6.1% uncertainty on the jets, and for 2-lepton the dominant uncertainty is b-tagging, with a 5.3% effect.

The two main experimental systematic uncertainties are the jet-related ones and the b-tagging efficiency. In the jet uncertainty case, the largest variations originate from the flavour composition uncertainty. In the b-tagging, the dominant uncertainties come from

Uncertainty [%]	0-lepton	1-lepton	2-lepton
b-tagging	4.23	3.77	4.50
c-tagging	3.64	4.37	2.28
light tagging	1.83	1.44	1.76
Jet/Pile-up/$E_{\mathrm{T}}^{\mathrm{miss}}$	6.24	6.03	3.55
Lepton	0.49	1.65	1.50
Top modelling	1.58	2.99	0.37
W modelling	1.49	1.88	0.00
Z modelling	4.51	0.08	9.77
Single-top modelling	0.29	0.65	0.04
Diboson	1.28	0.67	2.32
Multijet	0.47	0.81	0.00
Luminosity	2.77	2.68	2.80
Total	10.71	10.08	12.94

Table 6.4.: Summary of the sizes of the different systematic uncertainties on the total estimated background yield after full selection for the three channels at $\sqrt{s} = 8$ TeV before performing the final profile likelihood fit. The uncertainties are averaged over all p_{T}^{V} intervals in each category. The quoted total error is obtained by adding the individual components in quadrature in each p_{T}^{V} interval, and then averaging.

Uncertainty [%]	0-lepton	1-lepton	2-lepton
b-tagging	5.60	5.50	5.33
c-tagging	0.02	0.02	0.03
light tagging	0.03	0.06	0.04
Jet/Pile-up/$E_{\mathrm{T}}^{\mathrm{miss}}$	5.89	6.07	3.86
Lepton	0.00	1.72	1.30
VH $p_{\mathrm{T}}-$dependence	2.03	2.15	2.00
VH theory scale	1.35	0.04	1.60
VH theory PDF	3.01	3.42	3.50
VH acceptance	10.00	10.00	10.00
Luminosity	2.80	2.80	2.80
Total	14.00	14.15	13.18

Table 6.5.: Summary of the sizes of the different systematic uncertainties on the signal yield for $m_H = 125$ GeV after full selection for the three channels at $\sqrt{s} = 8$ TeV before performing the final profile likelihood fit. The uncertainties are averaged over all p_{T}^{V} intervals in each category. The quoted total error is obtained by adding the individual components in quadrature in each p_{T}^{V} interval, and then averaging.

the high-p_{T} region. The c-jet tagging efficiency also has a large contribution, particularly in the 1-lepton channel. These features are consistently observed in all three channels. The largest modelling uncertainties are the shape systematic variations on the $m_{b\bar{b}}$ and the p_{T} distributions of the vector boson in the $Wb\bar{b}$ and $t\bar{t}$ cases.

6.4. Wb$\bar{\text{b}}$ background studies

The $Wb\bar{b}$ process is one of the main backgrounds to the $WH \rightarrow \ell\nu b\bar{b}$ search. In the search strategy applied and described in this chapter, there is no specific control region where to compare directly the data to the Monte Carlo predictions for this process. Therefore, a generator level comparison has been performed to obtain an estimate of the main systematics on the modelling of this process. The baseline LO Sherpa prediction used in the analysis is compared to two different NLO calculations: aMC@NLO and PowHeg. The aMC@NLO v2.1 beta was used for the study, which is also a validation for this recently released generator version.

There are three main systematics to evaluate for the $VH(b\bar{b})$ analysis:

- **$\Delta\varphi_{b\bar{b}}$ systematic.** As described in sec. 6.2, data and Monte Carlo comparisons performed in the 0-tag control region showed the presence of a discrepancy between the data and the Sherpa predictions for W+jet events in the distribution of the azimuthal distance between the two leading jets. To understand the origin of this discrepancy, the variable has been investigated at generator level for $Wb\bar{b}$ events. Firstly, a comparison between Sherpa and the NLO Monte Carlos has been performed. Then, the aMC@NLO prediction has been compared using different PDFs for the matrix element calculation and varying the renormalisation and factorisation scales. These variations are aimed at giving an interpretation of the discrepancies between Sherpa and aMC@NLO.

- **$m_{b\bar{b}}$ systematic.** To estimate the di-b-jet invariant mass shape systematic for the $Wb\bar{b}$ background, the baseline Sherpa MC is compared to the aMC@NLO prediction, and the fit to their ratio is symmetrised and considered as a systematic distortion of the $m_{b\bar{b}}$ shape.

- **Flavour fraction in $Wb\bar{b}$ events.** In the final profile likelihood fit, described in sec. 9.1, the W+heavy flavour (hf) fraction is left free to float to allow it to adjust its normalisation to the data. It is considered as the sum of $Wb\bar{b}$, Wbc, $Wc\bar{c}$ and Wbl

events. A systematic error on this fraction of events is taken into account in the fit, and an estimate of its value is obtained from the generator level comparison. The number of events passing the selection cuts used for the Higgs analysis is calculated discriminating the cases where they are originating from $Wb\bar{b}$, Wbc or Wbl events, and the error on their ratio is estimated.

More details on the evaluation of these three uncertainties will be given in the following sections.

6.4.1. Methodology

A truth level analysis reproducing the one performed on the data is implemented as a Rivet [107] routine. This selection is applied to the three generated sets of events: $Wb\bar{b}$ with aMC@NLO and PowHeg and $W+ \geq 1b$ with Sherpa. This procedure allows to compare the three generators, using a similar selection to the one employed to extract the WH signal process. The selection cuts applied for this truth-level analysis are:

- lepton minimum transverse momentum: $p_{\mathrm{T}}^{\mathrm{lep}} > 20$ GeV
- lepton maximum pseudorapidity: $|\eta^{\mathrm{lep}}| < 2.5$
- minimum missing transverse energy: $E_{\mathrm{T}}^{\nu} > 25$ GeV
- minimum transverse W-boson mass: $m_{\mathrm{T}}^{W} > 40$ GeV
- minimum transverse jet momentum: $p_{\mathrm{T}}^{\mathrm{lead}} > 45\,\mathrm{GeV}$, $p_{\mathrm{T}}^{\mathrm{sublead}} > 20$ GeV
- maximum jet pseudorapidity: $|\eta^{j}| < 2.5$ for signal jets, $|\eta^{j}| < 4.5$ for veto jets
- exactly two signal jets originating from b-hadrons.

The distributions of the main kinematic variables, comparing Sherpa to aMC@NLO and PowHeg, are shown in fig. 6.4 and 6.5, and the invariant mass distribution before and after identifying the two leading jets as originating from b quarks is shown in fig. 6.6.

6.4.2. Systematic extraction

In the following paragraphs, the methods used to extract the three uncertainties previously introduced are described, and the corresponding results are given.

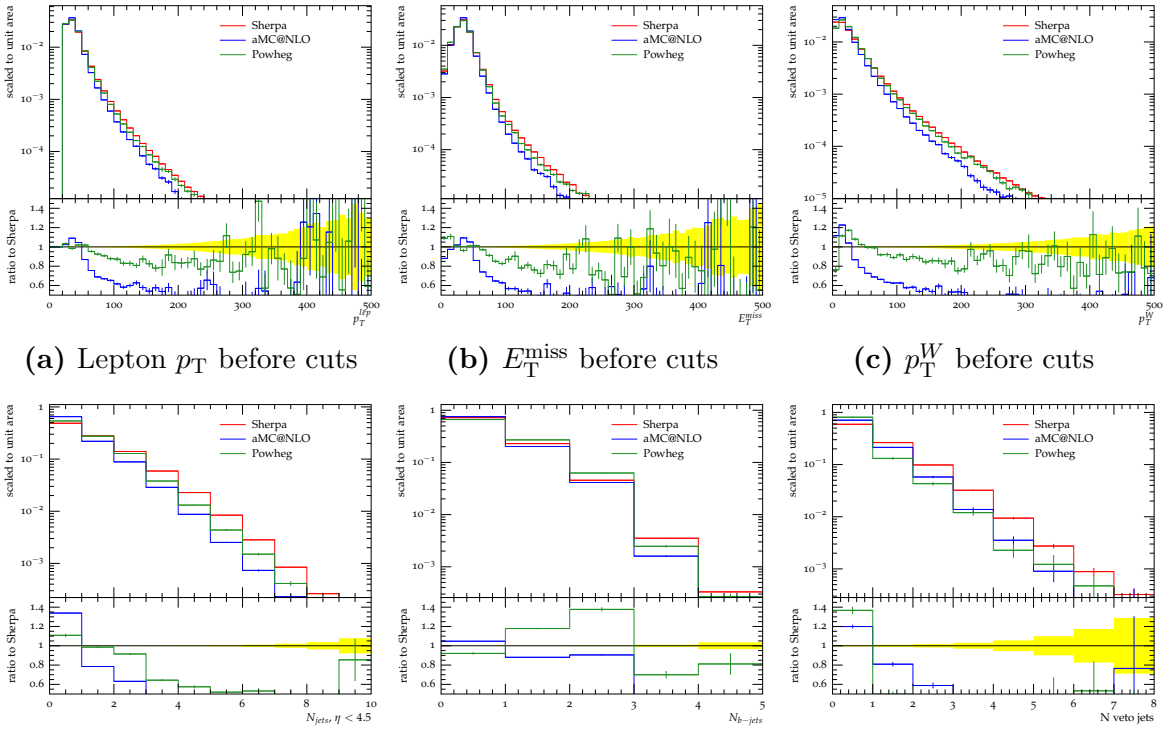

(a) Lepton p_{T} before cuts **(b)** $E_{\mathrm{T}}^{\mathrm{miss}}$ before cuts **(c)** p_{T}^{W} before cuts

(d) Number of jets in $|\eta| < 4.5$ **(e)** Number of b-jets **(f)** Number of veto jets

Figure 6.4.: The main kinematic distributions for $Wb\bar{b}$ events generated with SHERPA (red), aMC@NLO (blue) and POWHEG (green). The ratio to SHERPA is shown, and the yellow band represents the statistical uncertainty on it.

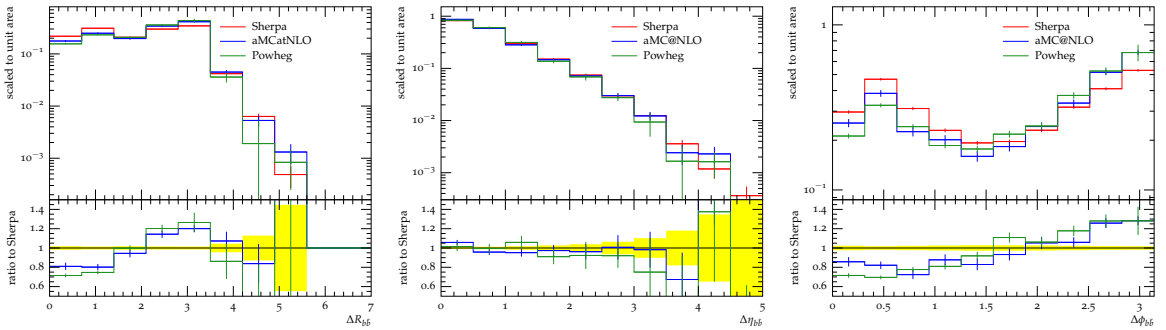

(a) $\Delta R_{b\bar{b}}$ **(b)** $\Delta\eta_{b\bar{b}}$ **(c)** $\Delta\varphi_{b\bar{b}}$

Figure 6.5.: Angular variable distributions for $Wb\bar{b}$ events generated with SHERPA (red), aMC@NLO (blue) and POWHEG (green). The ratio to SHERPA is shown, and the yellow band represents the statistical uncertainty on it.

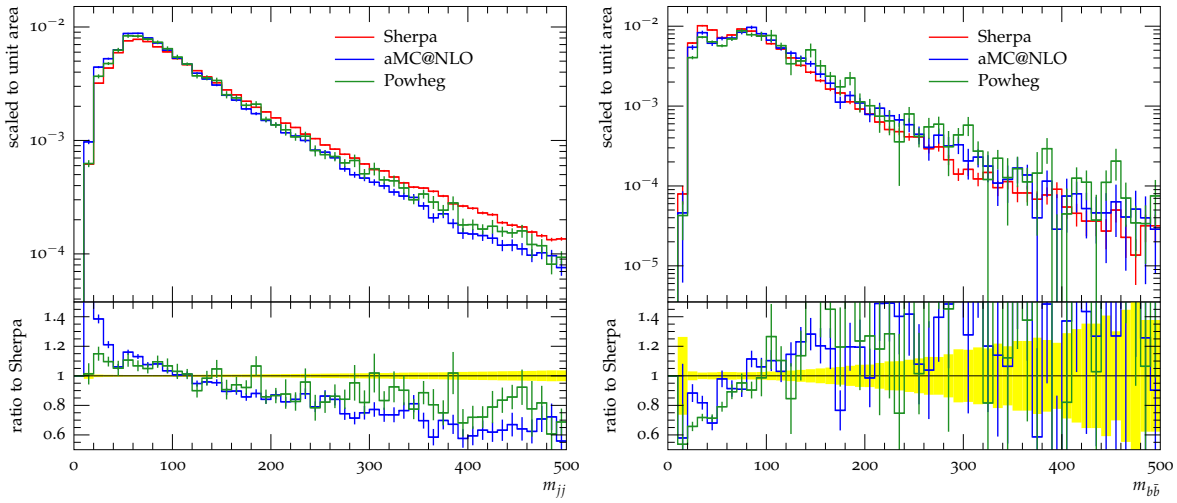

(a) Before truth-association to b quarks **(b)** After truth-association to b quarks

Figure 6.6.: The invariant mass distribution of the two leading jets for $Wb\bar{b}$ events generated with SHERPA (red), aMC@NLO (blue) and POWHEG (green). The ratio to SHERPA is shown, and the yellow band represents its statistical uncertainty.

$\Delta\varphi_{b\bar{b}}$ systematic studies

As described in sec. 6.2, studies performed on W+light jet events showed a discrepancy in the Monte Carlo description of the $\Delta\varphi(j_1, j_2)$ variable when compared to the data. This data to Monte Carlo comparison cannot be performed in the case of $Wb\bar{b}$ events, for which a dedicated control region does not exist. Therefore the generator level study performed here is aimed at understanding the $\Delta\varphi_{b\bar{b}}$ modelling. The $\Delta\varphi_{b\bar{b}}$ distribution, displayed in fig. 6.5c, shows a clear discrepancy between the two NLO predictions and SHERPA. The slope, with a maximal discrepancy of $\sim 20\%$ in the ratio between SHERPA and the NLO Monte Carlos, shows an effect consistent with the discrepancy seen between the data and SHERPA in the 0-tag region, described in sec. 6.2.

This is in agreement with a generator level study performed by the SHERPA collaboration on W+jets events comparing LO and NLO predictions to unfolded ATLAS data [101]. This study demonstrates the agreement in $\Delta\varphi$ between the NLO SHERPA prediction and the ATLAS data, as can be seen in fig. 6.7.

The effect of the application of the reweighting in $\Delta\varphi(j_1, j_2)$ derived from data and applied in the analysis described in sec. 6.8 to the truth level $\Delta\varphi_{b\bar{b}}$ distribution is shown in fig. 6.8 on the main kinematic variables.

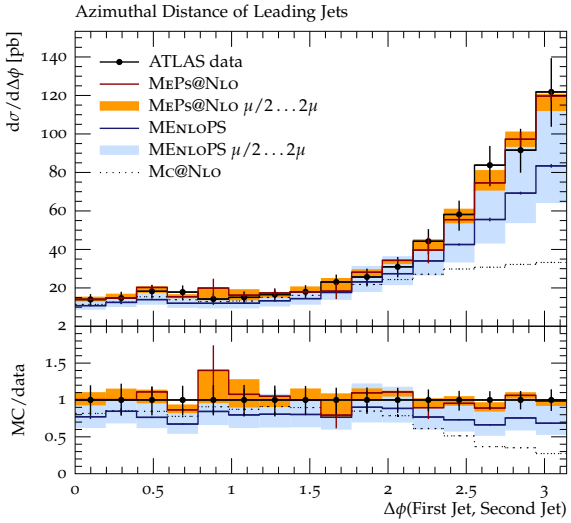

Figure 6.7.: The distribution of the azimuthal distance between the leading and sub-leading jet for W+jet events in SHERPA, compared to unfolded ATLAS data, as in [101].

To understand the source of the discrepancy between the SHERPA and aMC@NLO predictions in the $\Delta\varphi_{b\bar{b}}$ variable, studies comparing different PDFs and varying the factorisation and renormalisation scales on aMC@NLO have been performed. The aim of these studies is to understand if the difference between the two generators can be covered by any of these effects. Three different PDF sets were used: CT10, MSTW 2008 and NNPDF23 [108]. Only the central values were taken into account for this study, without calculating the full set of PDF variations. The relative $\Delta\varphi_{b\bar{b}}$ plots can be seen in fig. 6.9, alongside the factorisation and renormalisation scale variations up and down of a factor of two.

From the plots in fig. 6.9, no deviation consistent with SHERPA is visible. All deviations from the nominal are within 5%, apart from the bin corresponding to the jet edge, where out-of cone radiation is expected to have different behaviour when varying the PDFs or scales. It can thus be concluded that the discrepancy between SHERPA and the data seen in $\Delta\varphi(j_1, j_2)$ seems to originate from a non-accurate description of the variable by the LO MC. This discrepancy can be recovered using an NLO prediction of W+jet production.

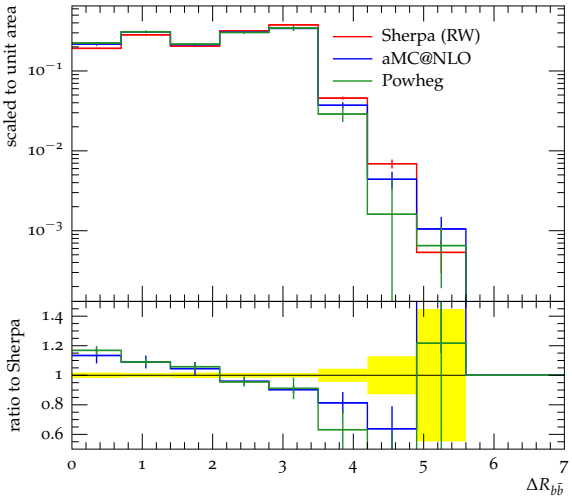

(a) $\Delta R_{b\bar{b}}$

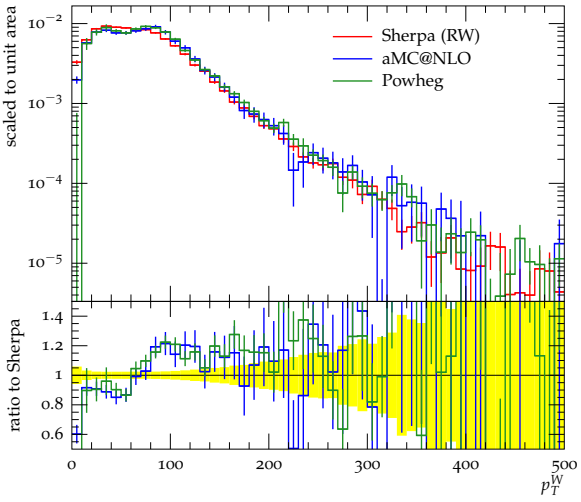

(b) p_{T}^{W} distribution after cuts

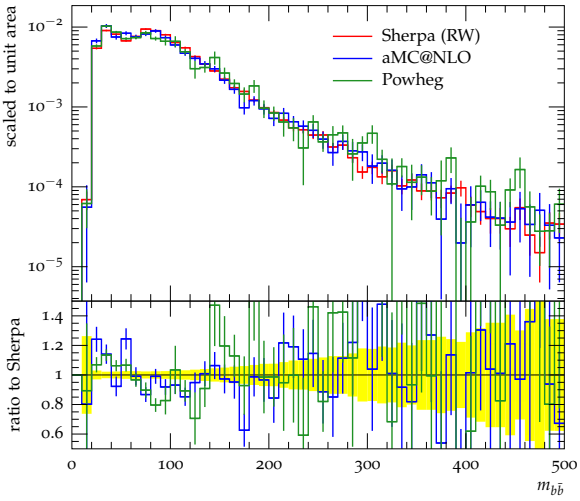

(c) $m_{b\bar{b}}$

Figure 6.8.: The main kinematic distributions for $Wb\bar{b}$ events generated with SHERPA (red), aMC@NLO (blue) and POWHEG (green) after reweighting SHERPA to the data. The ratio to SHERPA is shown, and the yellow band represents its statistical uncertainty.

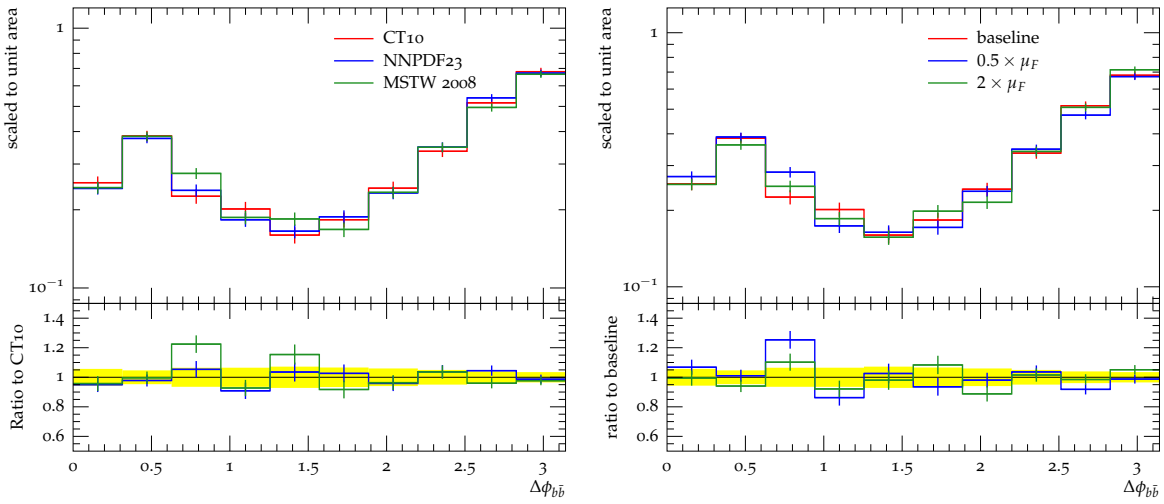

(a) PDF variations **(b)** μ_F variations

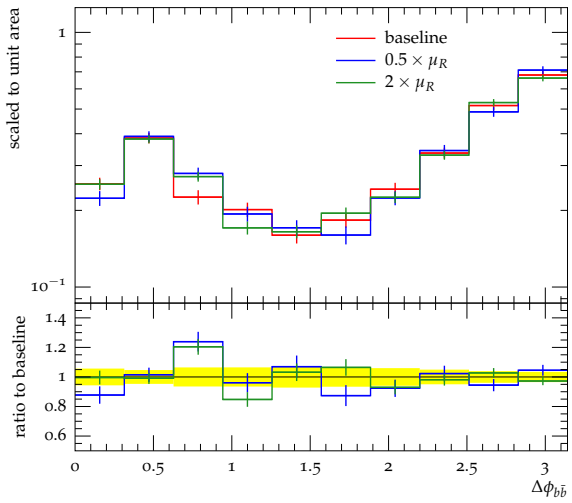

(c) μ_R variations

Figure 6.9.: The $\Delta\varphi_{b\bar{b}}$ distributions for $Wb\bar{b}$ events generated with aMC@NLO varying the PDF sets in the matrix element calculation (6.9a) and the factorisation (6.9b) and renormalisation (6.9c) scales. The ratio to the baseline aMC@NLO configuration is shown, and the yellow band represents the statistical uncertainty on it.

$m_{b\bar{b}}$ systematic studies

To estimate the $m_{b\bar{b}}$ shape systematic on the $Wb\bar{b}$ process, the same $\Delta\varphi(j_1, j_2)$ reweighting used in the analysis is applied to the $\Delta\varphi_{b\bar{b}}$ distribution generated with SHERPA. Thus the distribution in fig. 6.8c is used to estimate the shape uncertainty coming from the NLO prediction on the $Wb\bar{b}$ background. The ratio between aMC@NLO and SHERPA is fitted, and the resulting slope, shown in fig. 6.10, is symmetrised and used as shape distortion for $m_{b\bar{b}}$ in the statistical analysis for the $Wb\bar{b}$ background.

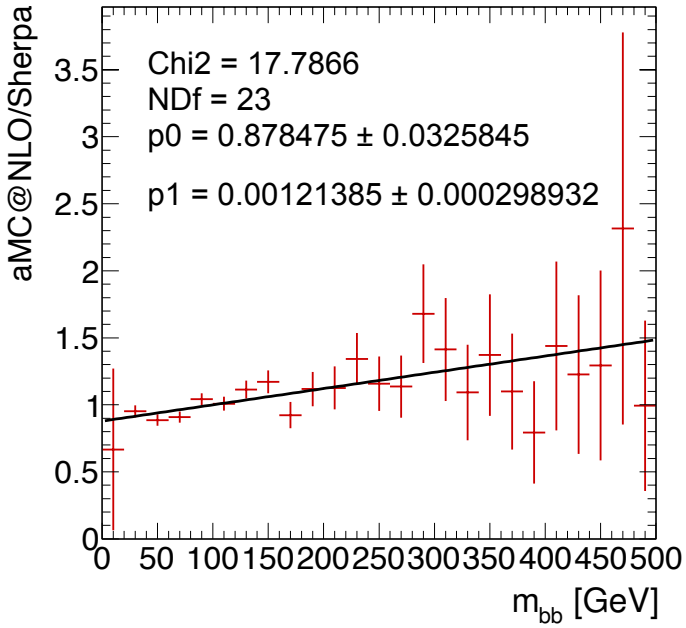

Figure 6.10.: Linear fit to the ratio of aMC@NLO to SHERPA, the slope is used as shape systematic on the $Wb\bar{b}$ background. The parameters p_0 and p_1 refer to the y axis shift and the slope of the line respectively.

Flavor fraction evaluation

In a final state with a leptonically decaying W and two central jets with $p_T > 20$ GeV, where at least one of them is matched to a b-hadron (or its decays products), the fraction of events where the second jet is matched to a b, a c or a light hadron is also studied with the three generators. The relative contribution of $bb + bc$ and bl final states is compared between the generators, to estimate the uncertainty on the ratio bb/bl (considering

$bb = bb + bc$). Figure 6.11 shows the calculated fractions, from which an uncertainty of 30% on the bb/bl ratio is extracted.

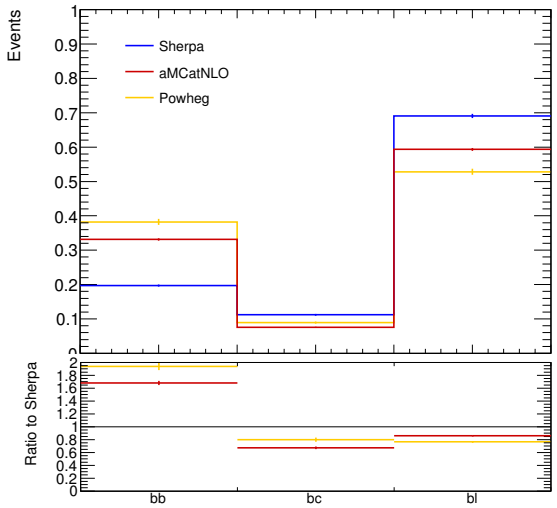

Figure 6.11.: Relative fractions of bb, bc and bl events, selected as described in the text. The ratios shown are calculated with respect to SHERPA.

Chapter 7.

$WH \to \ell\nu b\bar{b}$ feasibility study using jet substructure

This chapter describes preliminary results of a feasibility study using jet substructure techniques to reduce the $VH(b\bar{b})$ channel backgrounds. The study is performed only on the WH channel, using the $\sqrt{s} = 7$ TeV dataset.

7.1. Jet substructure techniques for $VH(b\bar{b})$ searches

As presented in sec. 2.5.1, even in the simplified regime of vector boson associated production, the backgrounds from $W+$jet, $Z+$jet and $t\bar{t}$ production dominate the signal production, with typical $VH(b\bar{b})$ signal to background ratios of the order of 5% [109]. However, it is possible to extract a cleaner signal sample by looking only at events where the Higgs and the weak boson both have high-p_{T} ($\gtrsim 200$ GeV), paying the cost of reducing the signal cross section to approximately 5% of the inclusive one.

Focussing only on high-p_{T} candidates is well justified, as most of the background cross sections decrease more rapidly than the signal with p_{T} of the recoiling vector boson system. In addition, a higher fraction of the $b\bar{b}$ pairs falls within the acceptance of the ATLAS b-tagging, partially mitigating the loss in signal cross-section. As a result of the large Lorentz boost of the Higgs boson, the $b\bar{b}$ pair tends to be close together in the detector. In this case, jet substructure techniques studies performed on 14 TeV simulated events demonstrated improved signal to background discrimination [110, 111]. The technique used involves finding large Cambridge/Aachen jets [112, 113] and then

looking backwards in the clustering history for hard splittings which indicate the decay of a heavy particle [114]. This will be described in detail in the following paragraphs.

As already mentioned, the idea lying behind the method is that a fast-moving Higgs produces two high momentum b-jets almost collinear in the laboratory frame. Thus, they can be identified as a single wide jet, for which the substructure is studied afterwards. The developed method has to take into account the dependence of the separation between the two jets from the transverse momentum of the Higgs, which can be approximated as follows (assuming $p_{\mathrm{T}}^{H} \gg m_H$):

$$R_{b\bar{b}} \simeq \frac{1}{\sqrt{z(1-z)}} \frac{m_H}{p_{\mathrm{T}}^{H}} \ , \tag{7.1}$$

where z and $1-z$ are the momentum fractions of the two quarks. Moreover, the study of the substructure of the boosted wide jet has to include any gluons emitted by the b-jets and to exclude any contribution coming from the underlying event, to obtain the best mass resolution.

The jet algorithm which best fits the scope of the analysis is the Cambridge/Aachen (C/A) algorithm. It provides a hierarchical clustering structure based on the angle between the different components of the jet. The algorithm calculates the angular distance $\left(\Delta R = \sqrt{(\Delta\eta)_{ij}^2 + (\Delta\varphi)_{ij}^2}\right)$ between two objects i and j, which are candidates to be assigned to the final jet, and always recombines the closest ones, until all the separations between the objects exceed an initially set value. The main difference between this algorithm and the anti-k_{T} algorithm [91], which is standard in most ATLAS analyses, is the angular ordering, replacing the inverse momentum ordering. The un-clustering process applied on an angularly ordered jet can easily reveal hard structures present in it, as partons coming from the decay of a heavy resonance tend to be more separated than gluons from radiation and their mother particles.

The substructure study for a high-p_{T} jet, j, relies on two dimensionless parameters, μ and y_{cut}. The algorithm is implemented as follows:

1. the last step of the clustering is undone, resulting into two jets: j_1, j_2, chosen to have: $m_{j_1} > m_{j_2}$;

2. the mass drop and the asymmetry of the splitting are checked. The mass drop condition is expressed as $m_{j_1} < \mu m_j$, where μ quantifies the drop. A splitting is

considered symmetric if the following relation holds:

$$y = \frac{\min(p^2_{T,j_1}, p^2_{T,j_2})}{m^2_j} \Delta R^2_{j_1,j_2} > y_{\text{cut}} \ . \tag{7.2}$$

If both the conditions are satisfied, then j is a possible Higgs candidate and the algorithm terminates.

3. If the conditions at step 2 are not satisfied, j_1 is labeled as j and the algorithm starts again from step 1.

To consider j as the Higgs candidate, both j_1 and j_2 have to pass b-tagging requirements. The identified jet j will then contain the two b quarks together with emitted gluon radiation. The value of μ is chosen considering that the condition $\mu = 1/\sqrt{3}$ corresponds to a Mercedes-like configuration, where the two b quarks and a gluon are produced at equal angular distance. If the two b quarks and a gluon are produced at equal angular distance (Mercedes-like configuration), μ has a value of $1/\sqrt{3}$. Studies performed in [114] showed $\mu = 0.67$ is optimal for a Higgs boson of 120 GeV mass and $p_{\text{T}} > 200$ GeV at $\sqrt{s} = 14$ TeV. Similarly, the optimised value for y_{cut} was found to be 0.09, taking into account the composition of the backgrounds, including both b and light quark jets. The variable y, presented in eq. 7.2, can also be redefined as $\min(z_{j_1}, z_{j_2})/\max(z_{j_1}, z_{j_2})$ and its main role is to remove the asymmetric configurations, mainly coming from soft gluon divergences in light quark and single b-jet cases.

A further step is necessary to improve the mass resolution: the filtering of the Higgs neighbourhood, as sketched in fig. 7.1. This procedure consists in resolving the jet substructure components as other jets with a finer angular scale: $R_{\text{filt}} < R_{b\bar{b}}$. The three hardest jets are taken as the Higgs decay products, and the two highest momentum ones are both required to be tagged as b-jets. The third jet should therefore contain the hard radiation $\left(\mathcal{O}(\alpha_S)\right)$, providing an efficient reconstruction of the decay products, improving the mass resolution. The choice in this case is $R_{\text{filt}} = \min(0.3, R_{b\bar{b}}/2)$.

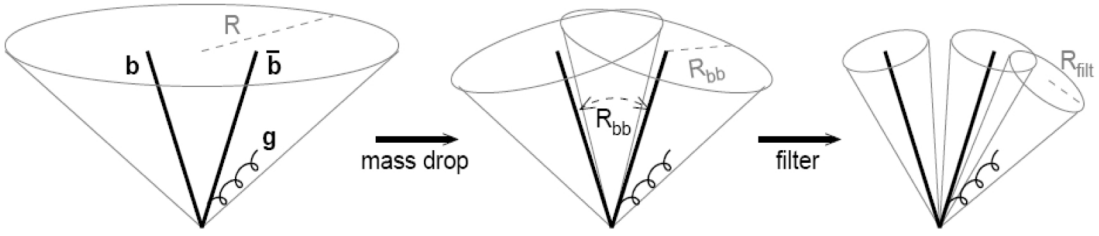

Figure 7.1.: Scheme of the split-filtering procedure applied for jet substructure studies.

7.2. Analysis strategy

The main aim of this study of jet substructure algorithms for the $VH(b\bar{b})$ search is to obtain a comparison of the performance of a high-p_{T} jet substructure based analysis versus a standard cut-based analysis [109], similar to that presented in chapt. 6, in the same region of the phase space. For this study the focus will be on the WH channel, which is the most sensitive one, and for which the comparison between the two methods has been performed.

The data analysed are taken from the good run list, according to the ATLAS data quality (DQ) criteria, coming from stable beams and collected at $\sqrt{s} = 7$ TeV. The total integrated luminosity is 4.7 fb^{-1}. Different generators from those listed in sec. 5.1 are used to model the various backgrounds. The $WH \to \ell\nu b\bar{b}$ signal is generated using Herwig++ [115] interfaced with PowHeg [116] to include the next-to-leading order (NLO) processes contributing to the process. The $Wb\bar{b}$ background is modelled using Sherpa [72] generated only for high-p_{T}^{W}, with a generator level cut at $p_{\mathrm{T}}^{W} > 100$ GeV. Alpgen [117] interfaced with Herwig [69] is used to simulate $W+ \geq 1$ c-jet and $W+ \geq 1$ light-jet. Single top and $t\bar{t}$ productions are modelled by the MC@NLO [118] generator interfaced with Herwig. Diboson events (ZZ, WZ, WW) are simulated using Herwig.

The cuts aim first of all at selecting events coming from true interaction vertices, with a requirement of at least three tracks originating from the primary vertex. The trigger applied is the same described in sec. 5.3.

The identification of the W boson is performed first, requiring a lepton, e or μ, with $p_{\mathrm{T}} > 20$ GeV to pass tight selection criteria, and to satisfy track and calorimeter isolation cuts to suppress the QCD background. The lepton in the event has to be unique, thus additional leptons are vetoed to reduce the Z channel background. Overlap removal between electrons, muons and jets in the event is performed, as the same calorimeter deposit or track can be identified as a different object. This is exploited using a ΔR cut, vetoing muons within $\Delta R > 0.2$ from electrons, and jets at $\Delta R > 0.4$ from leptons. The events are required to have a significant missing transverse energy: $E_{\mathrm{T}}^{\mathrm{miss}} > 25$ GeV. This is used, together with the lepton information, to calculate the transverse mass of the W candidate, defined as:

$$m_{\mathrm{T}}^{W} = \sqrt{2p_{\mathrm{T}}^{\ell}E_{\mathrm{T}}^{\mathrm{miss}}(1 - \cos\Delta\varphi_{\ell\nu})} \; . \tag{7.3}$$

Only events with $m_{\mathrm{T}}^{W} > 40$ GeV are retained. After the W has been identified in the event, a cut on $p_{\mathrm{T}}^{W} > 200$ GeV is applied to restrict the phase space to the boosted region, and the following selection is performed to find the Higgs candidate.

In the cut-based analysis, only events with two jets having $p_{\mathrm{T}} > 25\,\mathrm{GeV}$ in the central region ($|\eta| < 2.5$) in the final state are taken into account. Events with additional jets with p_{T} greater than 20 GeV are vetoed within $|\eta| < 4.5$. The invariant mass of the H candidate is reconstructed using only events where both jets are b-tagged usingthe MV1 [95] algorithm at the 70% efficiency working point.

In the substructure analysis case, after the W selection, a C/A jet with $R = 1.2$ passing the splitting-filtering algorithm and calibrated in mass, energy and pseudorapidity according to the ATLAS standard calibration for large radius jets [119], is retained only if it falls into the central pseudorapidity region and has a p_{T} higher than 180 GeV. The jet is not considered if within $\Delta R < 1.2$ from an electron. In this analysis, a jet veto is crucial to reduce the $t\bar{t}$ background. Therefore, events which have at least one anti-k_{T} 0.4 jet at $\Delta R > 1.2$ from the C/A 1.2 jet are removed, for consistency with the standard analysis [109].

The Higgs candidate mass in the substructure-based analysis is identified as the calibrated mass of the C/A 1.2 jet passing all the requirements, if the two highest p_{T} sub-jets are both b-tagged. To do this, the MV1 tagging algorithm at the 70% efficiency working point is applied to the sub-jets. Fig. 7.2a shows the invariant mass of the C/A 1.2 jets passing all the selection cuts, before b-tagging the sub-jets. The background shapes and normalisations in these plots are taken from the Monte Carlo predictions. No QCD contribution is taken into account, because of the high-p_{T} phase space considered, and the double b-tag requirement. The data and Monte Carlo agreement at low mass values is poor, and this can be explained by the absence of a QCD background estimate. The b-tagging cut, though, suppresses this contribution, and in the Higgs candidate mass distribution in fig. 7.2b, the data and Monte Carlo agreement is good.

A preliminary evaluation of the significance using the integral in the $110 - 130$ GeV mass region, gives $S/\sqrt{B} = 0.34$. This represents a small gain with respect to the same region in the cut-based analysis, where $S/\sqrt{B} \sim 0.25$.

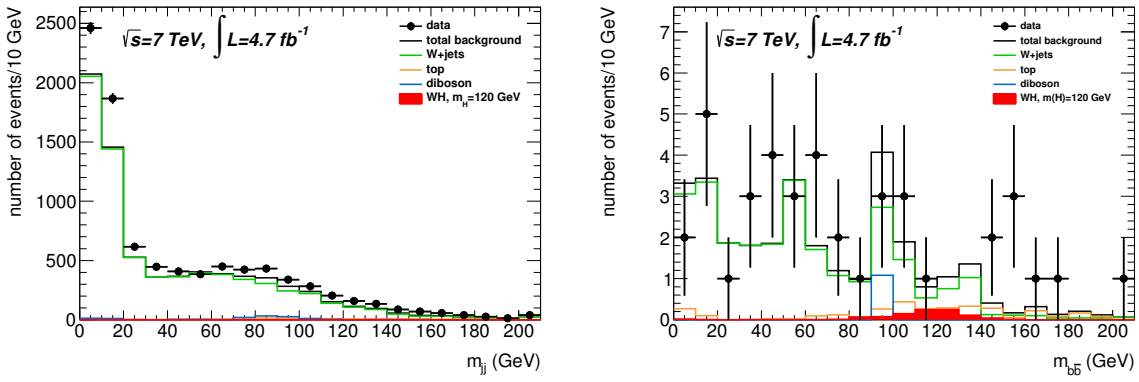

(a) **(b)**

Figure 7.2.: Higgs candidate invariant mass before applying b-tagging (7.2a) and with two b-tagged sub-jets (7.2b).

7.3. Results

Limits are set on $\sigma/\sigma_{\mathrm{SM}}$ for the $WH \to \ell\nu b\bar{b}$ process, when $p_{\mathrm{T}}^{W} > 200$ GeV, for both the jet substructure-based and the standard cut-based analysis. The signal hypothesis has been tested for five different mass points, ranging from 115 to 135 GeV. A profile likelihood fit to the invariant mass distribution of the reconstructed Higgs candidate, $m_{b\bar{b}}$, is used to perform the test. Only the two main backgrounds to the process, $t\bar{t}$ and $Wb\bar{b}$ are taken into account for this result. A 10% normalisation systematic uncertainty is applied on both backgrounds.

The limits on $\sigma/\sigma_{\mathrm{SM}}$ are derived using the CL_S method computed via a profile likelihood ratio on the binned $m_{b\bar{b}}$ distributions, following the formalism described in chapt. 4. The normalisation systematics are considered as nuisance parameters and constrained within their expected uncertainty by a log-normal distribution. As can be seen in fig. 7.3, there is no substantial difference in the predicted exclusion limits between the two methods: in both cases the 95% C.L. limit is $\sim 8\times$ SM for a Higgs boson of 125 GeV mass. This test is performed without taking into account the main experimental and theoretical systematic uncertainties in both the standard and substructure-based analysis. It does not show any significant gain from the application of the jet substructure method on the $\sqrt{s} = 7$ TeV dataset.

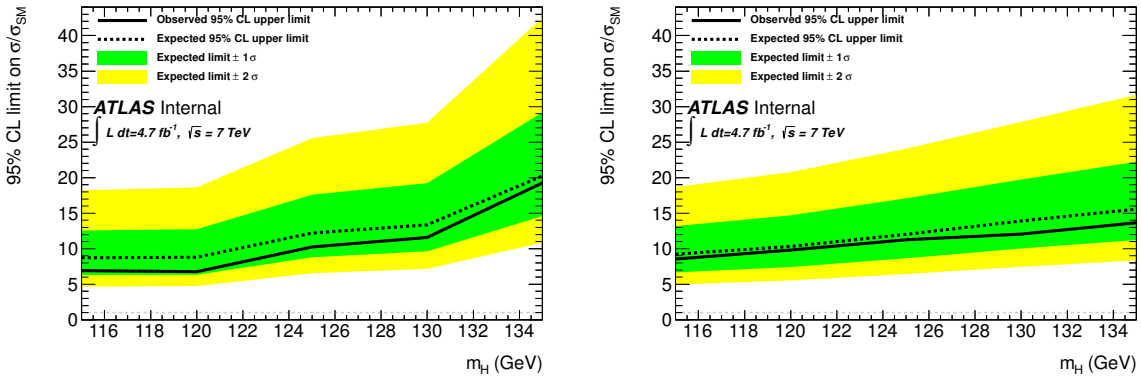

(a) jet substructure **(b)** standard analysis

Figure 7.3.: 95% C.L. limits on $\sigma/\sigma_{\mathrm{SM}}$ in case of the jet substructure analysis (7.3a) and the standard analysis restricted to the high-p_{T} signal region (7.3b). In both cases only a 10% normalisation uncertainty is taken into account on the backgrounds.

7.4. Conclusions

A preliminary test on the effectiveness of using jet substructure techniques in the search for $WH \to \ell\nu b\bar{b}$ has been described. The study, performed at $\sqrt{s} = 7$ TeV, shows similar performance when applying jet substructure-based techniques and a standard cut-based analysis [109], considering the same phase space, and without taking into account systematic uncertainties.

The introduction of systematic uncertainties, which are larger in the case of jet substructure, would affect the presented result, worsening the performance of jet substructure-based analysis with respect to the standard one. The small statistics in the high vector boson transverse momentum region also introduces difficulties in constraining the main backgrounds because of the large uncertainties associated to them.

Therefore, a jet substructure-based analysis of the $VH(b\bar{b})$ channel at $\sqrt{s} = 7$ TeV does not improve the standard result. The significantly higher centre of mass energy foreseen for the LHC Run 2 will lead to a larger number of high-p_{T} VH events. The new data taking period will thus allow for further studies of the $VH(b\bar{b})$ process using jet substructure-based techniques.

Chapter 8.

Preliminary VH($b\bar{b}$) results using $4.7 + 13.0$ fb^{-1} luminosity

The results [99] presented in this chapter are obtained using 13 fb^{-1} of integrated luminosity at $\sqrt{s} = 8$ TeV and 4.7 fb^{-1} at $\sqrt{s} = 7$ TeV delivered by the LHC and collected by ATLAS respectively in 2012 and 2011. The analysis strategy described in chapt. 6 is relative to the full Run 1 dataset analysis, and is an improvement of the one presented in this chapter. For this reason, only the differences present in this analysis will be outlined in this chapter, together with the results.

This analysis was presented at the HCP 2012 conference [120], a few months after the observation of a boson with mass $\sim$125 GeV by both the ATLAS and CMS collaborations [29], [30], and it includes the first observation of the $VZ(Z \to b\bar{b})$ process at ATLAS.

8.1. Differences in the analysis strategy

As the analysis outlined in chapt. 6 is an improvement with respect to the one presented here, a list of the main differences between the two is provided in the following:

- the Monte Carlo statistics is a factor of 5 lower, affecting the statistical uncertainty and the modelling of the main backgrounds;
- the choice of generators is less coherent across channels and processes, particularly in the V+jet case;

- the event selection is specific to each channel, and less categories are used in the final fit;
- the lepton isolation cuts, used in the 1-lepton channel selection, are looser, causing a higher multi-jet background contamination;
- the forward jets with $p_{\mathrm{T}} > 20$ GeV are used to veto events;
- the missing transverse energy triggers are not employed to select events in the 1-lepton channel;
- the fit uses different signal regions, and a different p_{T}^{V} bin categorisation;
- the top control regions, used in the final fit, are defined as the 3-jet region with two final state b-tags in the 1-lepton channel, and the $m_{\ell\ell}$ sideband in the 2-lepton channel.

The background processes are modelled using different event generators, most of which are in common with the ones described in sec. 5.1. Only the differences will be listed here. For $t\bar{t}$ production, MC@NLO [118] with CT10 NLO PDFs [74], using Herwig [69] with the AUET2B tune is used. The PowHeg [76–78] generator with MSTW 2008 NLO PDFs [71] for $\sqrt{s} = 7$ TeV data and with CT10 NLO PDFs for $\sqrt{s} = 8$ TeV, interfaced with the Pythia6 program, is used to simulate $W+ \geq 1$ b jet events. $W+\geq 1$ c and $W+\geq 1$ light-jet productions are generated via Alpgen [117] interfaced with Herwig. Different generators are used for the $\sqrt{s} = 7$ TeV and $\sqrt{s} = 8$ TeV datasets for Z+light and heavy flavour jets. For $\sqrt{s} = 8$ TeV all are produced with the Sherpa generator [72] with CTEQ6L1 PDFs, while for the $\sqrt{s} = 7$ TeV case heavy flavours are produced with Sherpa, with the same $\sqrt{s} = 8$ TeV settings, and light flavours with Alpgen, analogously to W+jets.

In the case of W+jets, the overlap between the PowHeg and Alpgen samples is expected to be large: events with real b-jets are therefore removed from the Alpgen $W+\geq 1$ c and $W+\geq 1$ jet samples and are considered only if coming from the PowHeg $W+ \geq 1b$ sample. Furthermore events with no b-jets are removed from the PowHeg sample. In the case of Z+jets, the overlap between the $Z+\geq 1$ b, $Z+\geq 1$ c and the $Z+\geq 1$ light samples is expected to be significantly smaller. For $\sqrt{s} = 7$ TeV data all the Sherpa samples are combined, and their overlap is handled internally by the CKKW [73] matching procedure, while for the $\sqrt{s} = 8$ TeV case, events with at least one b- or c-jet are taken from the Sherpa Z+heavy flavour sample ($Z+\geq 1$ b and $Z+\geq 1$ c), and the rest is taken from the Alpgen Z+light-jet sample.

8.1.1. Object and event selection

The selection cuts described in this section were determined and optimised without looking at the data in the signal region. The analysis is subdivided in 16 signal region categories depending on the number of leptons, the transverse momentum of the vector boson candidate and the number of jets. A scheme of these categories is shown in table 8.1, and the selection applied is described in the following.

Number of leptons	Number of jets	p_{T} range (GeV)				
0	2 3	-	-	$120 < E_{\mathrm{T}}^{\mathrm{miss}} < 160$	$160 < E_{\mathrm{T}}^{\mathrm{miss}} < 200$	$E_{\mathrm{T}}^{\mathrm{miss}} > 200$
1	2	$p_{\mathrm{T}}^{W} > 50$	$50 < p_{\mathrm{T}}^{W} < 100$	$100 < p_{\mathrm{T}}^{W} < 150$	$150 < p_{\mathrm{T}}^{W} < 200$	$p_{\mathrm{T}}^{W} > 200$
2	2	$p_{\mathrm{T}}^{Z} > 50$	$50 < p_{\mathrm{T}}^{Z} < 100$	$100 < p_{\mathrm{T}}^{Z} < 150$	$150 < p_{\mathrm{T}}^{Z} < 200$	$p_{\mathrm{T}}^{Z} > 200$

Table 8.1.: Signal region categories used in the analysis, based on the number of leptons and jets in the final state and the vector boson p_{T} interval.

Most of the object selection is analogous to what described in sec. 5.2, therefore, only the differences will be pointed out in the following.

In the 1- and 2-lepton channels, events are selected using the lowest un-prescaled single lepton triggers. In the 0-lepton channel instead, the events are selected using triggers based on the missing transverse energy. The method used is the same described in sec. 5.3, but missing transverse energy triggers are not employed in the 1-lepton channel.

All leptons classified as loose are required to pass track isolation: the sum of the p_{T} of the tracks within a cone of 0.2 radius of the identified lepton track has to be less than 10% of the lepton track p_{T}. A lepton is considered as isolated in the calorimeter if the sum of the energy deposits in a 0.3 cone around it is smaller then 14% of the lepton transverse momentum, and calorimeter isolation is only requested in case of tight leptons.

The event selection is summarised in tables 8.2 and 8.3. The cuts are similar to those listed in sec. 6.1, with some differences in the topological selection.

Object	0-lepton	1-lepton	2-lepton
Leptons	0 loose leptons	1 tight lepton + 0 loose leptons	1 medium lepton + 1 loose lepton
Jets	2 b-jets, $p_T^1 > 45$ GeV, $p_T^2 > 20$ GeV, $+ \leq 1$ loose jets	$+ \leq 0$ loose jets	-
MET	$E_T^{miss} > 120$ GeV, $p_T^{miss} > 30$ GeV, $\Delta\varphi(E_T^{miss}, p_T^{miss}) < \pi/2$, $\min[\Delta\varphi(E_T^{miss}, \text{jet})] > 1.5$, $\Delta\varphi(E_T^{miss}, b\bar{b}) > 2.8$	-	$E_T^{miss} < 60$ GeV
Vector Boson Mass	-	$m_T^W < 120$ GeV	$83 < m_Z < 99$ GeV

Table 8.2.: Basic event selection for the three lepton categories.

0-lepton channel					
E_T^{miss} GeV	120-160		160-200		>200
$\Delta R(b,\bar{b})$	$0.7 < \Delta R < 2$		$0.7 < \Delta R < 1.7$		$\Delta R < 1.5$
1-lepton channel					
p_T^W GeV	0-50	50-100	100-150	150-200	>200
$\Delta R(b,\bar{b})$	$0.7 < \Delta R$			$0.7 < \Delta R < 1.6$	$\Delta R < 1.4$
MET	$E_T^{miss} > 25$ GeV				$E_T^{miss} > 50$ GeV
m_T^W	$m_T^W > 40$ GeV			-	-
2-lepton channel					
p_T^Z GeV	0-50	50-100	100-150	150-200	>200
$\Delta R(b,\bar{b})$	$0.7 < \Delta R$			$0.7 < \Delta R < 1.8$	$\Delta R < 1.6$

Table 8.3.: Further topological cuts for the three lepton channels in separate p_T^W or p_T^Z intervals.

8.1.2. Background treatment

The backgrounds are estimated using a combination of data-driven and MC-based techniques. The three channels are mainly affected by different backgrounds:

- 0-lepton: W/Z+jets and top
- 1-lepton: W+jets and top
- 2-leptons: Z+jets.

Most background shapes are taken from simulation and their normalisation is estimated using control regions in the data. The only two exceptions are the multijet background, for which a template shape is estimated from data and is normalised by fitting it in the signal region, and the diboson background, for which both normalisation and shape are taken from simulation. To obtain the background normalisations from data different control regions are used. They are defined by altering or inverting some event selection cut. They are chosen carefully to have similar properties to the signal region and a high level of purity in the considered background.

The multijet background estimate is analogous to what described in sec. 6.2. Another important estimate obtained from data is the flavour fraction in V+jets production (where $V = W, Z$). Scale factors have thus been derived to normalise the $Z + c$-jet, $Z+$ light-jet, $W + c$-jet, $W+$ light-jet backgrounds, while the $Z + b$-jet and $W + b$-jet background normalisations are derived directly in the final fit. These scale factors are obtained from a simultaneous extended maximum likelihood fit to data in the 2-, 1- and 0-b-tag regions of the 1- and 2-lepton analyses. Also the top control regions are fitted for the 1- and 2-lepton channels. In addition, in the 2-b-tag region, the invariant mass distribution of the two candidate b-jets is fitted.

The free parameters in the fit are the $Z + b$-jet, $Z + c$-jet, $Z+$ light-jet, $W + b$-jet, $W + c$-jet, $W+$ light-jet and top scale factors, and the background composition of the pre tag and 1-tag control regions can be seen in fig. 8.1, and the signal and top control regions for 1- and 2-lepton channels can be seen in fig. 8.2c, 8.2d, 8.3a and 8.3b. The fit results are shown in Table 8.4 for both $\sqrt{s} = 7$ TeV and $\sqrt{s} = 8$ TeV datasets, as scale factors for the cross sections of the various backgrounds. The results are consistent between the datasets, with the exception of the $Z + c$-jet production. Two different Monte Carlos were used to simulate the process: the $\sqrt{s} = 7$ TeV and $\sqrt{s} = 8$ TeV events are produced respectively with ALPGEN and SHERPA. In ALPGEN, the component of $Z + c$ coming from charm production in Z+light sample is suppressed, due to the low statistic of the sample.

The error on the scale factors, $\sigma(\texttt{SF})$, quoted in table 8.4, is estimated considering the statistical uncertainty ($\sigma_{\text{stat}}(\texttt{SF})$) and all the systematic uncertainties ($\sigma_{\text{sys}}(\texttt{SF})$) taken into account for the nominal analysis, described in sec. 8.1.3. It is calculated using the

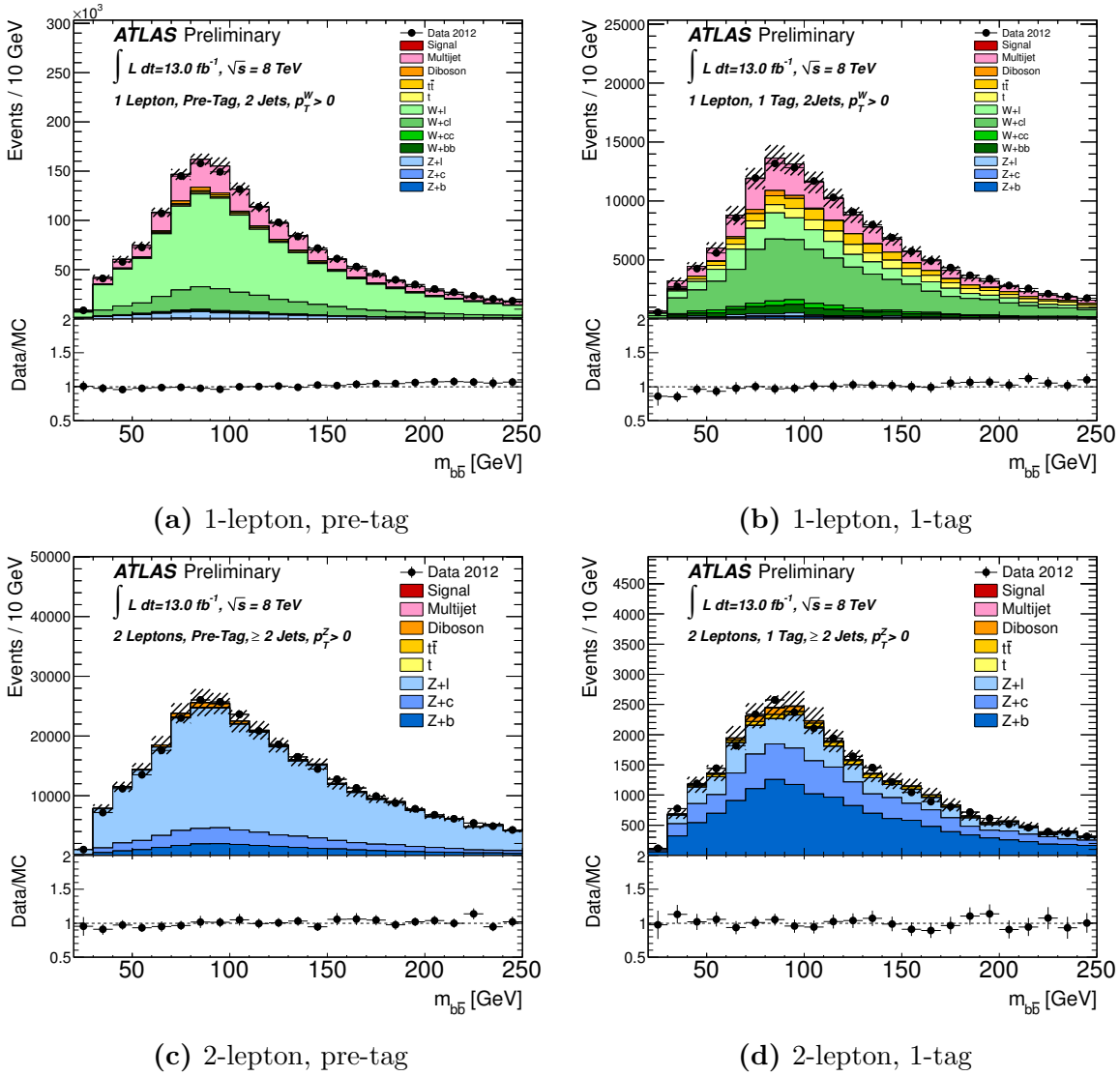

(a) 1-lepton, pre-tag

(b) 1-lepton, 1-tag

(c) 2-lepton, pre-tag

(d) 2-lepton, 1-tag

Figure 8.1.: The m_{jj} distributions for 1- and 2-lepton channel in the pre- and 1-tag regions [99]. Their normalisation is input to the flavour fit.

	$\sqrt{s}$ = 7 TeV	$\sqrt{s}$ = 8 TeV
$Z + c$-jets	1.99 ± 0.51	0.71 ± 0.23
$Z+$ light-jets	0.91 ± 0.12	0.98 ± 0.11
$W + c$-jets	1.04 ± 0.23	1.04 ± 0.24
$W+$ light-jets	1.03 ± 0.08	1.01 ± 0.14

Table 8.4.: Estimated scale factors for V+jet flavour component and top. The quoted error includes both statistical and systematic uncertainties.

following formula:

$$\sigma\left(\mathtt{SF}\right) = \sqrt{\sigma^2_{\text{stat}}\left(\mathtt{SF}\right) + \sum_{i=0}^{N_{\text{syst}}} \left(\mathtt{SF}_{\text{syst}_i} - \mathtt{SF}_{\text{nom}}\right)^2}\,. \tag{8.1}$$

Since the method is based on the ratio of expected 0-, 1- and 2-b-tag events, it relies on the calibrated b-tagging efficiency for light-, c- and b-jets as obtained from data measurements which corresponds to the dominant part of the systematic uncertainty. A 30% uncertainty on the $V + c$-jet backgrounds is taken into account as a systematic uncertainty in the final fit.

Some control regions are used to study the level of agreement between data and simulation. The pre-tag region is one of these. It has high statistics and is dominated by the V+light jet backgrounds. In this region a discrepancy between data and Monte Carlo in the modelling of the p_{T}^V distribution is observed. The p_{T}^V distribution in data falls more rapidly than what is predicted by the simulation. This behaviour, a deviation of the data/MC ratio at high-p_{T}^V, is observed in the pre-tag region for both W and Z events at $\sqrt{s} = 7$ TeV. The slope is consistent between the two processes, and the discrepancy is seen in the Alpgen modelling. A similar dependence, with larger uncertainties, is also observed after a applying a single b-tag, in the region dominated by vector boson and charm production. A correction, softening the simulated p_{T}^V distribution in the highest bins, reducing it by $5 - 10\%$, is applied to the Alpgen generated samples. This correction is applied as a systematic uncertainty, to account for further mis-modelings from different sources. This systematic is a preliminary version of the $\Delta\varphi_{jj}$ one, described in detail in sec. 6.2, which is not applied in this version of the analysis.

Top quark control regions are obtained selecting events with 1-lepton and 3 jets or 2-leptons, $60 < m_{\ell\ell} < 76$ GeV or $106 < m_{\ell\ell} < 150$ GeV and $E_{\text{T}}^{\text{miss}} > 60$ GeV. The 1-lepton sample purity reaches 90%. In the 1-lepton channel, the 4 jet 2 tag sample provides a region which is over 90% pure in $t\bar{t}$. A relatively large mis-modeling is observed for $t\bar{t}$ as a function of p_{T}^W, similar to what found for V+jets. An analogous behaviour is also observed in the 3-jet sample. This behaviour is considered as mis-modeling of p_{T}^W distribution caused by the $t\bar{t}$ generator (MC@NLO). Thus a correction factor up to $\sim 15\%$ is derived from the 4-jet sample in each p_{T}^W bin and is applied to the 2-jet sample. A systematic uncertainty is assigned to the correction, and is obtained as the residual mis-modelling in the 3-jet region, after applying the correction. The top p_{T} reweighting described in sec. 6.2, is not applied in this case.

The $m_{b\bar{b}}$ distributions after the full selection and the background corrections are shown in fig. 8.3 for the $\sqrt{s} = 8$ TeV dataset for all three lepton channels, inclusively in p_{T}^{V}.

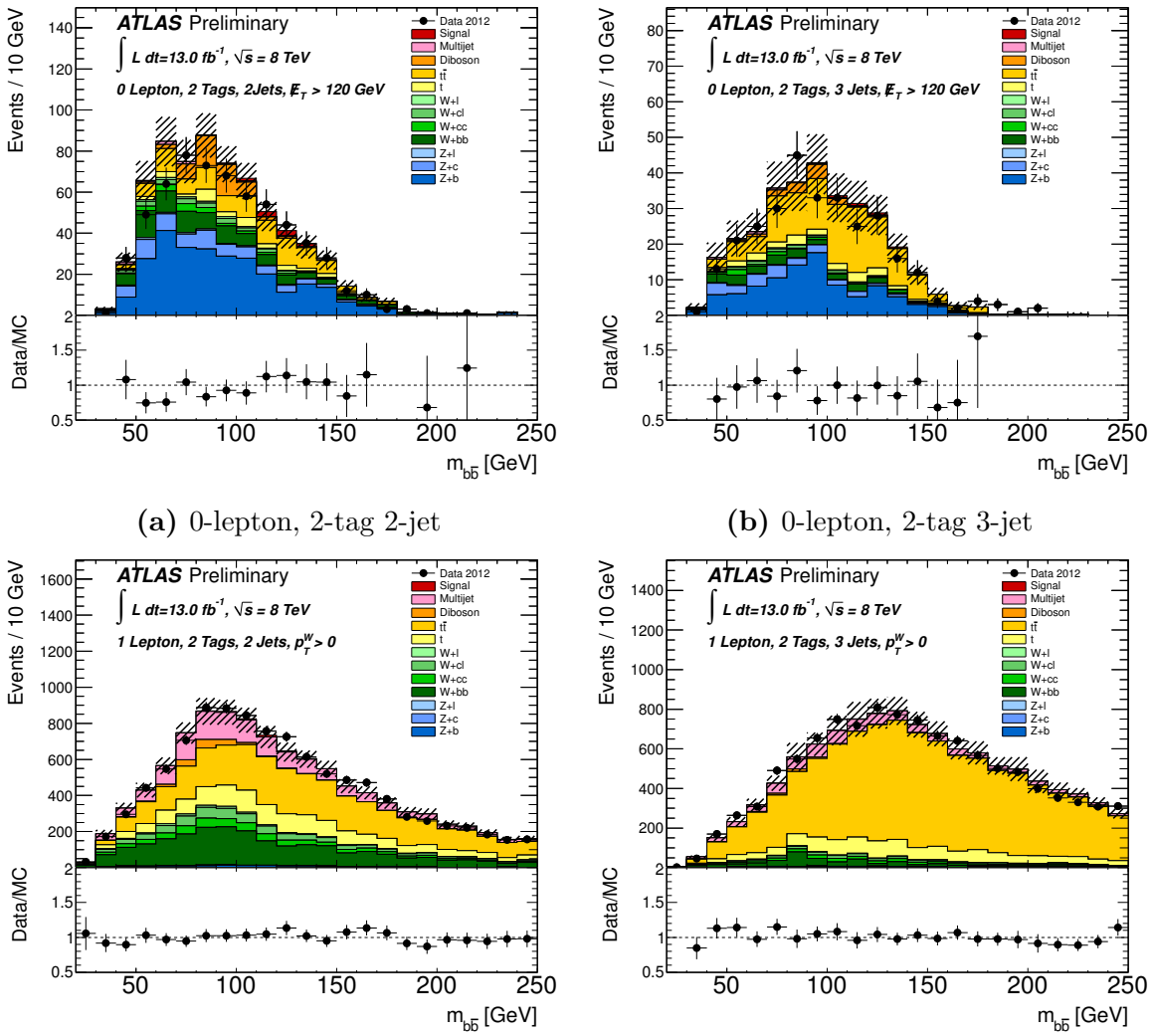

(a) 0-lepton, 2-tag 2-jet

(b) 0-lepton, 2-tag 3-jet

(c) 1-lepton, 2-tag 2-jet

(d) 1-lepton, 2-tag 3-jet

Figure 8.2.: $m_{b\bar{b}}$ distributions used as inputs for the final profile likelihood fit, for the 0- and 1-lepton categories [99].

8.1.3. Systematic uncertainties

The systematic uncertainties considered in this analysis are similar to those described in sec. 6.3, with some slight difference, reported here. The experimental systematic uncertainties with the highest impact in all channels are those relative to the flavour

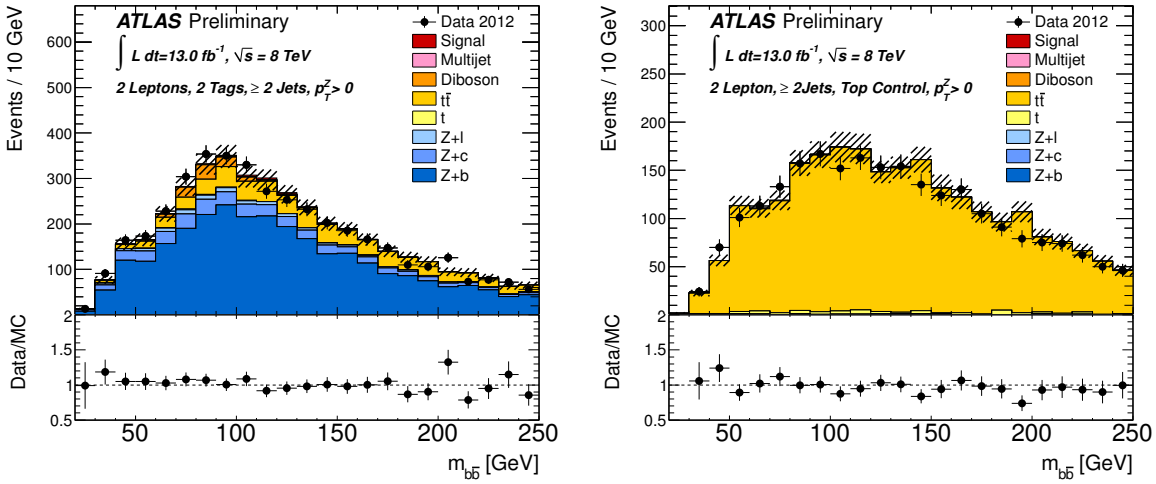

(a) 2-lepton, signal region **(b)** 2-lepton, top control region

Figure 8.3.: $m_{b\bar{b}}$ distributions used as inputs for the final profile likelihood fit for the 2-lepton category [99].

tagging efficiency and the jet energy scale. The tagging efficiencies are calibrated on data separately for true b, c and light jets. These calibrations are applied as Monte Carlo to data scale factors, dependent on the p_{T} of the tagged jet. The uncertainties on the scale factors are considered as the statistical and systematic uncertainties of the calibrations. Six systematic variations are considered for b-jets, and together with one for light- and one for c-jets are taken into account in the final fit.

Seven components are used instead to model the jet energy scale. They correspond to in-situ estimates, a flavour uncertainty on the quark-gluon sample composition, one on the b-jet energy scale, and in- and out-of-time pile up-related systematics. In the final fit it is assumed that the different components of the jet energy scale are uncorrelated. An uncertainty on the jet resolution is also taken into account, as well as a systematic taking into account the uncertainty on the p_{T}-dependent correction applied to improve the $m_{b\bar{b}}$ resolution.

The following background uncertainties are taken into account: 15% on the ratio of $t\bar{t}$ to single top production, 30% on the ratio of $W + c$ to W+jets and 30% on the ratio of $Z + c$ to Z+jets. An 11% uncertainty on the diboson cross-section is included as well.

Given the difficulties in modelling the large V+jet background, dedicated studies on its uncertainties have been performed. In the 2-lepton case, it is possible to isolate regions with high purity in $Z + b$ events, thus the uncertainty on the modelling can be obtained from the direct comparison of data and simulation in the $m_{b\bar{b}}$ sidebands. In the

$W + b$ case, it is not possible to obtain a pure control region in the data. Therefore, the uncertainty is derived from the comparison of different Monte Carlo generator predictions. The systematics on these background have two sources: the $m_{b\bar{b}}$ distribution shape, taken from Monte Carlo, and the p_{T}^{V} shape, strongly related to the normalisation, derived from data. The sidebands of the $m_{b\bar{b}}$ distribution in the signal region of the 2-lepton category are pure in $Z + b$ and are used to estimate these uncertainties. The uncertainty on the $W + b$ background is estimated comparing the predictions of different generators (Sherpa and PowHeg) after applying the full event selection of the 1-lepton analysis. The uncertainty on the $m_{b\bar{b}}$ shape is parametrised as a linear distortion. For the p_{T}^{W} uncertainty, an envelope of $\pm 5\%$ in the first two p_{T}^{W} bins and of $\pm 10\%$ in the others, based on the observed deviations, described in sec. 8.1.2, is taken into account.

The uncertainties applied on the signal are the same as the ones described in sec. 6.3, apart from the 10% acceptance uncertainty, which is not included in this version of the analysis.

A summary of the impact of the systematic uncertainties on the total background for each channel and the signal is shown in tables 8.5 and 8.6 for the $\sqrt{s} = 8$ TeV dataset. The uncertainties are presented in percent and grouped into categories obtained averaging over p_{T}^{V} bins. The total error is obtained adding in quadrature the various components per p_{T}^{V} bins and averaging afterwards. The most significant uncertainties are:

- MC statistics (8.3%) on the backgrounds of the 0-lepton channel;
- jet-related systematics (7.0%) on the backgrounds of the 1-lepton channel;
- b-tagging (6.9%) on the 2-lepton backgrounds;
- jets and $E_{\mathrm{T}}^{\mathrm{miss}}$ (19%, 25%) on the 0-lepton signal;
- b-tagging (8.8%, 8.6%) on the 1- and 2-lepton signals.

Uncertainty (%)	0-lepton	1-lepton	2-leptons
b-tagging	6.5	6.0	6.9
c-tagging	7.3	6.4	3.6
light tagging	2.1	2.2	2.8
Jets/pile-up/$E_{\mathrm{T}}^{\mathrm{miss}}$	20	7.0	5.4
Leptons	0.0	2.1	1.8
Top modelling	2.7	4.1	0.5
W+jets modelling	1.8	5.4	0.0
Z+jets modelling	2.8	0.1	4.7
Diboson	0.8	0.3	0.5
Multijet	0.6	2.6	0.0
Luminosity	3.6	3.6	3.6
Statistical	8.3	3.6	6.6
Total	25	15	14

Table 8.5.: Summary of the size of the systematic uncertainties on the total background for all three lepton channels for the $\sqrt{s} = 8$ TeV dataset.

Uncertainty (%)	0-lepton		1-lepton	2-leptons
	ZH	WH	WH	ZH
b-tagging	8.9	9.0	8.8	8.6
Jets/pile-up/$E_{\mathrm{T}}^{\mathrm{miss}}$	19	25	6.7	4.2
Leptons	0.0	0.0	2.1	1.8
$H \to b\bar{b}$ BR	3.3	3.3	3.3	3.3
VH p_{T}-dependence	5.3	8.1	7.6	5.0
VH theory PDF	3.5	3.5	3.5	3.5
VH theory scale	1.6	0.4	0.4	1.6
Statistical	4.9	18	4.1	2.6
Luminosity	3.6	3.6	3.6	3.6
Total	3.6	3.6	3.6	3.6

Table 8.6.: Summary of the size of the systematic uncertainties on the signal for all three lepton channels for the $\sqrt{s} = 8$ TeV dataset [99].

8.2. VZ($b\bar{b}$) cross check

To gauge the correctness of the background estimate, a cross check on a known signal is performed. Thus, the diboson production in the channels $WZ \to \ell\nu b\bar{b}$, $ZZ \to \ell^+\ell^- b\bar{b}$ and $ZZ \to \nu\bar{\nu} b\bar{b}$ is studied. Given the aim of demonstrating the reliability of the described Higgs analysis, the event selection is kept the same as what described in section 8.1.1.

A feasibility study using a counting experiment is presented in the following. The sensitivity to the $VZ(Z \to b\bar{b})$ signal is estimated for each channel, optimising the diboson signal mass interval. Three different ranges are taken into account, symmetric around 90 GeV: [60-120] GeV, [70-110] GeV and [80-100] GeV. The ratio $S/\sqrt{B}$ is evaluated for each range, and the interval maximising its value is found to be the intermediate one. The results are summarised in tables 8.7 and 8.8. The significance in the diboson case does not increase with p_{T}^{V}, as opposed to the Higgs case.

A fit to the $m_{b\bar{b}}$ peak is performed after the selection cuts on the VZ signal MC, giving a resolution value of ≈ 12 GeV. An example plot can be found in fig. 8.4, for the 0-lepton channel and the $\sqrt{s} = 8$ TeV dataset.

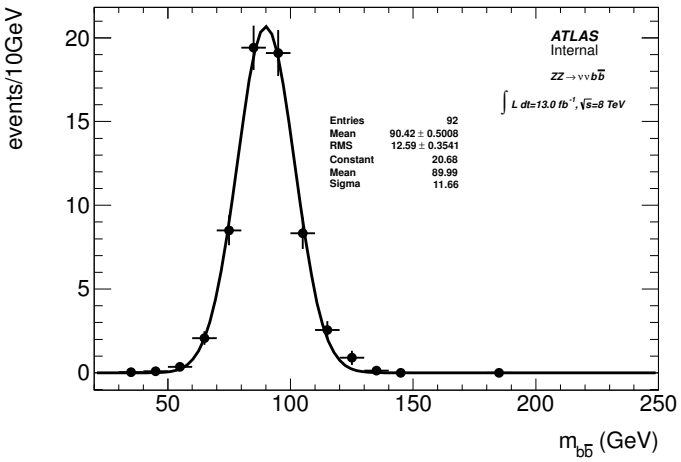

Figure 8.4.: The invariant dijet mass distribution in the three lepton channels for the diboson signal MC in the 0-lepton channel at $\sqrt{s} = 8$ TeV, fitted with a Gaussian to obtain the resolution of $m_{b\bar{b}}$.

Channel	0-lepton, 2-jet		
	$m_{b\bar{b}}$/GeV$\in [60,120]$	$m_{b\bar{b}}$/GeV$\in [70,110]$	$m_{b\bar{b}}$/GeV$\in [80,100]$
$E_{\mathrm{T}}^{\mathrm{miss}}$/GeV$\in [120,160]$	0.72	0.75	0.73
$E_{\mathrm{T}}^{\mathrm{miss}}$/GeV$\in [160,200]$	0.92	1.04	1.12
$E_{\mathrm{T}}^{\mathrm{miss}}$/GeV$> 200$	0.95	1.20	1.33
Inclusive	1.43	1.62	1.71
$\sum_{p_t^V\ bins}(S/\sqrt{B})^2$		1.86	
Channel	1-lepton		
	$m_{b\bar{b}}$/GeV$\in [60,120]$	$m_{b\bar{b}}$/GeV$\in [70,110]$	$m_{b\bar{b}}$/GeV$\in [80,100]$
p_t^W/GeV$\in [0,50]$	0.37	0.39	0.31
p_t^W/GeV$\in [50,100]$	0.32	0.34	0.27
p_t^W/GeV$\in [100,150]$	0.20	0.22	0.15
p_t^W/GeV$\in [150,200]$	0.17	0.19	0.15
p_t^W/GeV> 200	0.12	0.13	0.14
Inclusive	0.56	0.60	0.47
$\sum_{p_t^V\ bins}(S/\sqrt{B})^2$		0.61	
Channel	2-lepton		
	$m_{b\bar{b}}$/GeV$\in [60,120]$	$m_{b\bar{b}}$/GeV$\in [70,110]$	$m_{b\bar{b}}$/GeV$\in [80,100]$
p_t^Z/GeV$\in [0,50]$	0.78	0.80	0.70
p_t^Z/GeV$\in [50,100]$	0.76	0.81	0.68
p_t^Z/GeV$\in [100,150]$	0.54	0.57	0.56
p_t^Z/GeV$\in [150,200]$	0.44	0.47	0.37
p_t^Z/GeV> 200	0.35	0.43	0.43
Inclusive	1.30	1.37	1.20
$\sum_{p_t^V\ bins}(S/\sqrt{B})^2$		1.42	

Table 8.7.: $S/\sqrt{B}$ for each channel and each p_t^V bin and inclusive, estimated using distribution integrals at $\sqrt{s} = 7$ TeV.

Channel	0-lepton, 2-jet		
	$m_{b\bar{b}}$/GeV$\in [60,120]$	$m_{b\bar{b}}$/GeV$\in [70,110]$	$m_{b\bar{b}}$/GeV$\in [80,100]$
$E_{\mathrm{T}}^{\mathrm{miss}}$/GeV$\in [120,160]$	1.49	1.66	1.66
$E_{\mathrm{T}}^{\mathrm{miss}}$/GeV$\in [160,200]$	1.23	1.42	1.33
$E_{\mathrm{T}}^{\mathrm{miss}}$/GeV$> 200$	1.36	1.59	1.52
Inclusive	2.47	2.79	2.72
$\sum_{p_t^V\ bins}(S/\sqrt{B})^2$		2.94	
Channel	1-lepton		
	$m_{b\bar{b}}$/GeV$\in [60,120]$	$m_{b\bar{b}}$/GeV$\in [70,110]$	$m_{b\bar{b}}$/GeV$\in [80,100]$
p_t^W/GeV$\in [0,50]$	1.16	1.20	1.01
p_t^W/GeV$\in [50,100]$	1.13	1.18	0.96
p_t^W/GeV$\in [100,150]$	0.69	0.71	0.62
p_t^W/GeV$\in [150,200]$	0.85	0.96	0.95
p_t^W/GeV> 200	0.72	0.78	0.88
Inclusive	1.97	2.07	1.78
$\sum_{p_t^V\ bins}(S/\sqrt{B})^2$		2.21	
Channel	2-lepton		
	$m_{b\bar{b}}$/GeV$\in [60,120]$	$m_{b\bar{b}}$/GeV$\in [70,110]$	$m_{b\bar{b}}$/GeV$\in [80,100]$
p_t^Z/GeV$\in [0,50]$	1.36	1.46	1.30
p_t^Z/GeV$\in [50,100]$	1.28	1.40	1.19
p_t^Z/GeV$\in [100,150]$	0.84	0.90	0.69
p_t^Z/GeV$\in [150,200]$	0.79	0.86	0.69
p_t^Z/GeV> 200	0.65	0.77	0.77
Inclusive	2.23	2.41	2.08
$\sum_{p_t^V\ bins}(S/\sqrt{B})^2$		2.49	

Table 8.8.: $S/\sqrt{B}$ for each channel and each p_t^V bin and inclusive, estimated using distribution integrals for $\sqrt{s} = 8$ TeV.

8.3. Fit strategy

The distribution of the di-jet invariant mass is used as a discriminant to detect the possible presence of a signal, which, in the presented analysis, is either the diboson production with a Z boson decaying to a pair of b-quarks or the Higgs boson signal. A likelihood function is used to describe the binned $m_{b\bar{b}}$ distribution expected for the signal and the main backgrounds. The likelihood function is separated into different categories based on the three channels, 0-, 1- and 2-leptons, and divided into several p_{T}^{V} bins per channel: 5 bins for the 1- and 2-lepton channels, and 3 bins for the 0-lepton channel, as described in sec. 8.1. Additional top control regions in the 1- and 2-lepton channels, described in 8.1.2, are taken into account and fitted simultaneously. When the VZ signal is fitted, instead, no separation is made in p_{T}^{V} categories, as no significant enhancement in the signal-over-background ratio is expected from the high p_{T}^{V} region, as shown in tables 8.7 and 8.8. The likelihood function includes a Poisson term for each bin, as described in chapt. 4.

Systematic uncertainties are handled as nuisance parameters, with shape and normalisation components, constrained with a Gaussian or log-normal distribution, respectively, within their expected uncertainties. In addition, statistical uncertainties on the Monte Carlo expectations are considered bin-by-bin, on the sum of the expected background yield in each of the bins. Given the high number of systematic uncertainties, often with small or no effect on some backgrounds, the number of considered parameters is reduced, in order to avoid instabilities in the fit and additional computational complexity. Therefore, only systematic deviations larger than 0.05% from the nominal are considered in the fit. A further precaution taken to avoid the introduction of noise from unstable nuisance parameters in the fit is an ad hoc smoothing, based on re-binning the systematic variation curves applying a 5% statistical uncertainty threshold on each bin.

The fit is performed using the profile likelihood method, discussed in sec. 4.2. The overall top, $W + b$ and $Z + b$ background normalisations are left free to vary in the fit, without any constraint. The remaining background normalisations are fixed within their uncertainties. The V+light jets and $V + c$ jet samples are normalised using the scale factors obtained from the flavour fit presented in sec. 8.1.2, independently in $\sqrt{s} = 7$ TeV and $\sqrt{s} = 8$ TeV data.

The exclusion limits on $\sigma/\sigma_{\mathrm{SM}}$ are derived using the CL_S [121] method. In the VZ case, the p_0 value, the probability for background events to mimic the interesting signal,

is calculated as well, together with the signal strength $\hat{\mu}$ and its uncertainty at the maximum of the likelihood.

8.4. VZ($b\bar{b}$) observation

The observation of the diboson $VZ(Z \to b\bar{b})$ peak is crucial to demonstrate the feasibility of observing the Higgs boson decaying to a pair of b-quarks, validating the statistical procedure adopted to extract the Higgs signal as well as the background estimate. The statistical analysis is performed in six categories fitted simultaneously as reported in sec. 8.3. These are defined as follows:

- 0-, 1-lepton: 2- and 3-jet regions
- 2-lepton: signal and top control region.

The other difference with respect to the Higgs analysis is that the WH and ZH processes are considered as backgrounds, with their normalisation fixed to the Standard Model prediction, as well as the WW process, on which a 11% cross-section normalisation uncertainty is applied. An excess in the data compared to the background is observed at the expected value of the Z mass. In fig. 8.5 the background-subtracted data distributions are compared to the VZ signal hypotheses, shown in red.

The combined measurement of the three channels and the $\sqrt{s} = 7$ TeV and $\sqrt{s} = 8$ TeV datasets gives a best fit value for the diboson of $\mu_D = 1.1^{+0.18}_{-0.19}(\text{sys}) \pm 0.24(\text{stat})$, with a Gaussian significance of 4σ and a local p_0 of 3.7×10^{-5}. The values for $\sqrt{s} = 7$ TeV and $\sqrt{s} = 8$ TeV separately are summarised in table 8.9. This result is in good agreement with Standard Model expectation, and represents the first observation of this process performed by the ATLAS collaboration. From the fit to the separate channels on the 8 TeV dataset, the following values are obtained for the observed (expected) significance: 0.8 (1.0) in the 1-lepton channel, 2.8 (1.6) in the 2-lepton channel and 2.3 (2.1) in the 0-lepton channel. These numbers show that the excess in the observed significance is driven with respect to the expected one by the 2-lepton channel.

After the presentation of this result at the HCP 2012 conference [120], a study on the $VZ(Z \to b\bar{b})$ result using a p_{T}^{V} binned fit was performed. The study shows consistency between the expected significance obtained, but a difference in the observed value with respect to the inclusive p_{T}^{V} bin fit. The study has been performed only on the $\sqrt{s} = 8$ TeV

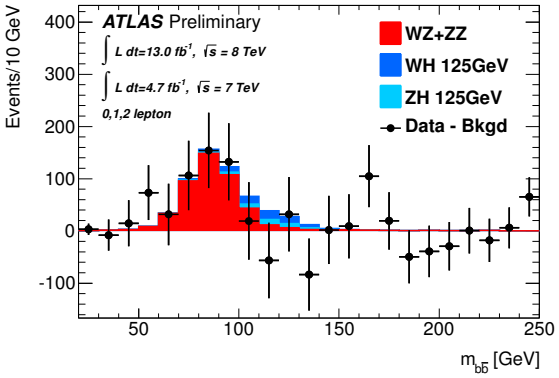

(a) full dataset

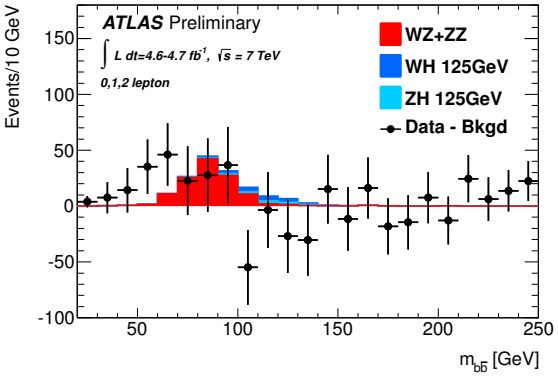

(b) $\sqrt{s} = 7$ TeV

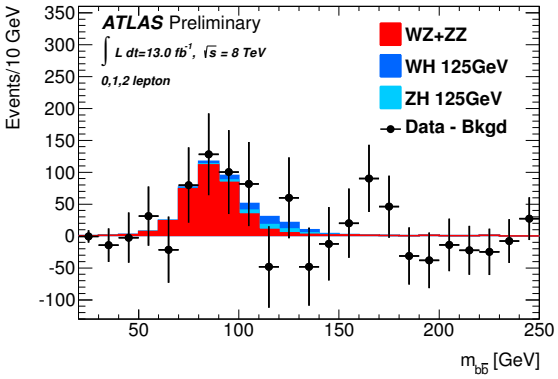

(c) $\sqrt{s} = 8$ TeV

Figure 8.5.: The invariant mass distribution after the profile likelihood fit of the background-subtracted data compared to the signal hypothesis of $VZ(Z \to b\bar{b})$. Fig. 8.5a shows the combination of the three channels and the two datasets, while fig. 8.5b and 8.5c show the combination of the three channels for the $\sqrt{s} = 7$ TeV and $\sqrt{s} = 8$ TeV datasets respectively.

Dataset	$\hat{\mu}$	Significance		p_0	
		observed	expected	observed	expected
$\sqrt{s} = 7$ TeV	$0.87^{+0.18}_{-0.12}(\text{sys.})^{+0.40}_{-0.39}(\text{stat.})$	2σ	2.4σ	0.02	8.9×10^{-3}
$\sqrt{s} = 8$ TeV	$1.2^{+0.19}_{-0.18}(\text{sys.})^{+0.30}_{-0.29}(\text{stat.})$	3.4σ	2.9σ	0.4×10^{-3}	2.2×10^{-3}

Table 8.9.: Best fit value, Gaussian significance and p_0 for the combination of the three channels in the two datasets.

dataset, and the results per channel are shown in table 8.10, compared with the ones from the inclusive p_{T}^V fit. The difference between expected and observed corresponds to a $\sim 15\%$ more in the observed for the p_{T}^V inclusive fit and a $\sim 20\%$ less in the observed in the binned fit. The two expected significances, instead, coincide as expected.

Fit	$\hat{\mu}$	Significance	
		observed	expected
with p_{T}^V bins	0.77 ± 0.4	2.2σ	2.9σ
without p_{T}^V bins	1.2 ± 0.38	3.4σ	2.9σ

Table 8.10.: Best fit value and Gaussian significance for the combination of the three channels in case of a fit performed with categories binned in p_{T}^V or not.

Further tests to investigate the source of this discrepancy have been performed. At first the channels have been fitted in couples, considering both the case of p_{T}^V bins or inclusive p_{T}^V, to identify the source of the deficit. The excess in the fit without p_{T}^V bins is driven by the 2-lepton channel, as already discussed. The results, shown in table 8.11, show that the deficit is not driven by a specific channel, and just confirm the 2-lepton excess.

Significance for	0- + 2-lepton		1- + 2-lepton		0- + 1-lepton	
	obs.	exp.	obs.	exp.	obs.	exp.
with p_{T}^V bins	1.9σ	2.5σ	1.8σ	2.2σ	1.9σ	2.4σ
without p_{T}^V bins	3.3σ	2.5σ	2.7σ	2.1σ	2.1σ	2.3σ

Table 8.11.: Gaussian significance combining two channels at a time in case of a fit performed with categories binned in p_{T}^V or not.

Another test has been performed, allowing for the isolation of the deficit. The fit has been performed only for the low p_{T}^V range, removing the bins with $p_T^{W/Z} > 150$ GeV and $E_{\mathrm{T}}^{\mathrm{miss}} > 160$ GeV. In this case the observed significance, combining the three channels is 2.6σ and the expected is 2.4σ. This is a confirmation of the poor modelling of the diboson in the high-p_{T}^V region, caused by a less boosted spectrum with respect to the Higgs, and low Monte Carlo statistics in the diboson samples.

8.5. Higgs results

The fit for the VH signal is performed as described in sec. 8.3. The background normalisations are allowed to vary within their errors or to vary freely for $W + b$, top and $Z + b$ backgrounds. The final scale factor results are given for the $\sqrt{s} = 7$ TeV and $\sqrt{s} = 8$ TeV datasets in table 8.12.

	$\sqrt{s} = 7$ TeV	$\sqrt{s} = 8$ TeV
Top	1.10 ± 0.14	1.29 ± 0.16
$Z + b$	1.22 ± 0.20	1.11 ± 0.15
$W + b$	1.19 ± 0.23	0.79 ± 0.20

Table 8.12.: Scale factors obtained from the profile likelihood fit to the data for $V + b$ and top backgrounds [99]. The quoted errors include both statistical and systematic uncertainties.

	0-lepton, 2-jet			0-lepton, 3-jet		
Bin	$E_{\mathrm{T}}^{\mathrm{miss}}$ (GeV)					
	120-160	160-200	> 200	120-160	160-200	> 200
ZH	2.9	2.1	2.6	0.8	0.8	1.1
WH	0.8	0.4	0.4	0.2	0.2	0.2
Top	89	25	8	92	25	10
$W + c$, light	30	10	5	9	3	2
$W + b$	35	13	13	8	3	2
$Z + c$, light	35	14	14	8	5	8
$Z + b$	144	51	43	41	22	16
Diboson	23	11	10	4	4	3
Multijet	3	1	1	1	1	0
Total bkg	361	127	98	164	63	42
	± 29	± 11	± 12	± 13	± 8	± 5
Data	342	131	90	175	65	32

Table 8.13.: Expected number of signal and background events and observed data for the 0-lepton channel in the $\sqrt{s} = 8$ TeV dataset after the profile likelihood fit. The expected signal events are shown for $m_H = 125$ GeV. The error quoted on the total background represents one standard deviation of the profiled nuisance parameters including both statistical and systematic errors.

The expected number of events in the simulation after fit, including full systematic uncertainties and compared to data are shown in tables 8.13-8.15.

	1-lepton				
Bin	p_{T}^{W} (GeV)				
	0-50	50-100	100-150	150-200	> 200
ZH	0.3	0.4	0.1	0.0	0.0
WH	10.6	12.9	7.5	3.6	3.6
Top	1440	2276	1120	147	43
$W + c$, light	580	585	209	36	17
$W + b$	770	778	288	77	64
$Z + c$, light	17	17	4	1	0
$Z + b$	50	63	13	5	1
Diboson	53	59	23	13	7
Multijet	890	522	68	14	3
Total bkg	3810	4310	1730	297	138
	± 150	± 86	± 90	± 27	± 14
Data	3821	4301	1697	297	132

Table 8.14.: Expected number of signal and background events and observed data for the 1-lepton in the $\sqrt{s} = 8$ TeV dataset after the profile likelihood fit. The expected signal events are shown for $m_H = 125$ GeV. The error quoted on the total background represents one standard deviation of the profiled nuisance parameters including both statistical and systematic errors.

	2-lepton				
Bin	p_{T}^{Z} (GeV)				
	0-50	50-100	100-150	150-200	> 200
ZH	4.7	6.8	4.0	1.5	1.4
WH	0.0	0.0	0.0	0.0	0.0
Top	230	310	84	3	0
$W + c$, light	0	0	0	0	0
$W + b$	0	0	0	0	0
$Z + c$, light	201	230	91	12	15
$Z + b$	1010	1180	469	75	51
Diboson	37	39	16	6	4
Multijet	12	3	0	0	0
Total bkg	1500	1770	665	97	72
	± 90	± 110	± 47	± 12	± 12
Data	1485	1773	657	100	69

Table 8.15.: Expected number of signal and background events and observed data for the 2-lepton channel in the $\sqrt{s} = 8$ TeV dataset after the profile likelihood fit. The expected signal events are shown for $m_H = 125$ GeV. The error quoted on the total background represents one standard deviation of the profiled nuisance parameters including both statistical and systematic errors.

The $m_{b\bar{b}}$ distribution plots of the highest p_{T}^{V} bin for each signal region after performing the profile likelihood fit are shown in fig. 8.6.

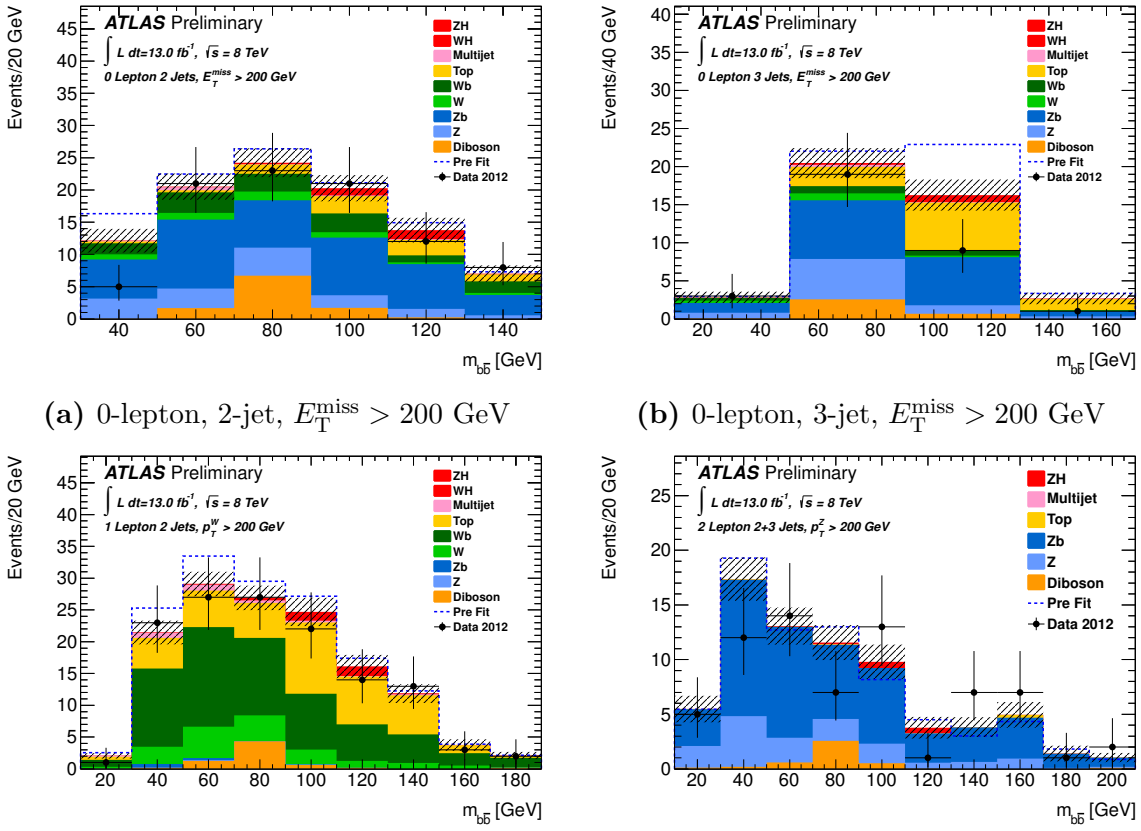

(a) 0-lepton, 2-jet, $E_{\mathrm{T}}^{\mathrm{miss}} > 200$ GeV

(b) 0-lepton, 3-jet, $E_{\mathrm{T}}^{\mathrm{miss}} > 200$ GeV

(c) 1-lepton, $p_{\mathrm{T}}^{W} > 200$ GeV

(d) 2-lepton, $p_{\mathrm{T}}^{Z} > 200$ GeV

Figure 8.6.: The $m_{b\bar{b}}$ distribution for the highest p_{T}^{V} bin in each signal region category of the fit [99]. The background expectation is shown both after the profile likelihood fit (solid) and before (dashed). The hashed band indicates the size of the statistical and systematic uncertainty after the fit.

For each Higgs boson mass hypothesis, a one-sided upper limit is placed on the ratio of the Higgs boson production cross section to its SM value, $\mu = \sigma/\sigma_{\mathrm{SM}}$, at the 95% confidence level (CL), following the technique described in chapt. 4. The observed (expected) limit for a 125 GeV Higgs mass is 1.8 (1.9) times the Standard Model prediction, and a Higgs boson of 110 GeV mass is excluded, as can be seen in fig. 8.7a.

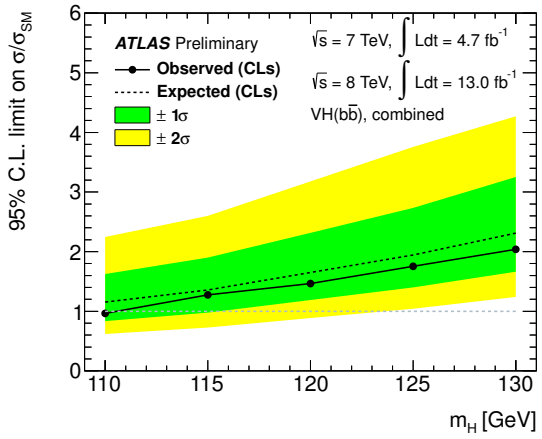

(a) full dataset

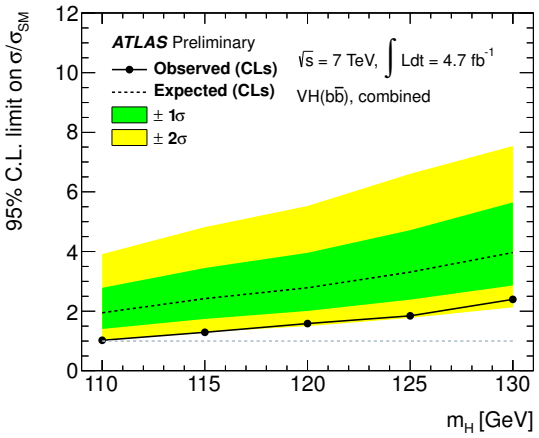

(b) $\sqrt{s} = 7$ TeV

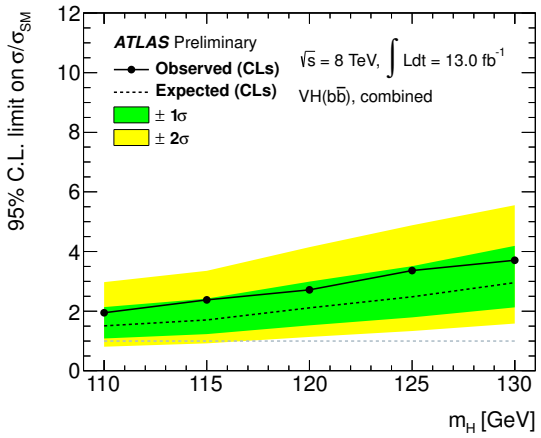

(c) $\sqrt{s} = 8$ TeV

Figure 8.7.: 95% Confidence Level limit on $\sigma/\sigma_{\mathrm{SM}}$ calculated using the CL_S method for the $\sqrt{s} = 7$ TeV and $\sqrt{s} = 8$ TeV datasets separately (8.7b, 8.7c) and their combination (8.7a) [99].

The expected and observed p_0 and Gaussian significance have been calculated for the 110-130 GeV Higgs mass range, and are shown in fig. 8.8.

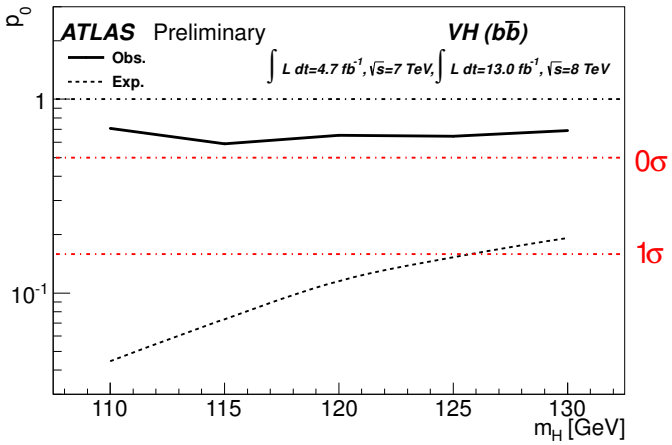

Figure 8.8.: p_0 and Gaussian significance.

8.6. Conclusions

The results shown in this chapter were presented preliminarily in November 2012 by the ATLAS collaboration, and are based on the full 7 TeV dataset and a part of the data collected at $\sqrt{s} = 8$ TeV. The first observation of the $VZ(Z \to b\bar{b})$ signal has been shown, observed with a 4σ significance. The Higgs boson limits on $\sigma/\sigma_{\mathrm{SM}}$ for $m_H = 125$ GeV are 1.8 (1.9) observed (expected). The deficit seen, leading to a negative $\hat{\mu}$ value, is driven by the $\sqrt{s} = 7$ TeV dataset analysis, where the data undershoot significantly the MC prediction. Further studies have been performed, including the full Run 1 dataset, and the results are presented in the next chapter.

Chapter 9.

VH $\rightarrow$ leptons + b$\bar{\text{b}}$ Run 1 analysis results

This chapter describes the statistical analysis for the search of $VH(b\bar{b})$ in the full Run 1 dataset. The events are selected according to the cuts described in sec. 6.1. A profile likelihood fit is performed, using the di-b-jet invariant mass ($m_{b\bar{b}}$) as discriminant variable. The systematic uncertainties presented in sec. 6.3 are taken into account as nuisance parameters of the likelihood, and treated according to the procedure described in sec. 4.5. In the following sections, the fit model adopted will be outlined and the results of the $VH \rightarrow$ leptons + $b\bar{b}$ search will be presented.

9.1. Fit model

The statistical analysis of the data employs a binned likelihood function, $\mathcal{L}(\mu, \theta)$, constructed as the product of Poisson probability terms. The signal strength parameter, μ, multiplies the expected Standard Model Higgs boson production cross section in each bin. The dependence of the signal and background predictions on the systematic uncertainties is described by nuisance parameters, θ, constrained by different probability density functions (pdfs). The expected number of signal and background events in each bin is a function of θ. A test statistic t_μ is then constructed according to the profile likelihood ratio: $t_\mu = -2\ln(\mathcal{L}(\mu, \hat{\hat{\theta}}_\mu)/\mathcal{L}(\hat{\mu}, \hat{\theta}))$, where $\hat{\mu}$ and $\hat{\theta}$ are the parameters that maximise the likelihood (with the constraint $0 \leq \hat{\mu} \leq \mu$), and $\hat{\hat{\theta}}_\mu$ are the nuisance parameter values that maximise the likelihood for a given μ. This test statistic is used to measure the compatibility of the background only model with the observed data and for exclusion

intervals derived with the CL_S method. More details on the procedure can be found in chapt. 4.

The fit is performed using different regions, containing information on the signal and the main backgrounds. The high statistics in some of the regions included in the fit helps to constrain the experimental uncertainties, such as the jet energy scale. A validation of the analysis procedure is provided by the extraction of the diboson signal, VZ with $Z \rightarrow b\bar{b}$. The discriminant variable employed in the fit is the invariant mass of the two selected b-jets, $m_{b\bar{b}}$.

9.1.1. Processes and categorisation

The nominal shapes and normalisations for most backgrounds are estimated from Monte Carlo simulations, and the corrections described in sec. 6.2 are applied to them. The nominal distributions are typically normalised to NNLO or NLO cross-sections, as described in sec. 5.1. The signal and backgrounds can be classified in the following groups:

- signal VH (2 sub-processes): WH and ZH;
- W+jets (5 sub-processes): Wl, Wcl, $Wc\bar{c}$, Wbl and $Wb\bar{b}$;
- Z+jets (5 sub-processes): Zl, Zcl, $Zc\bar{c}$, Zbl and $Zb\bar{b}$;
- $t\bar{t}$;
- diboson (3 sub-processes): WW, WZ and ZZ;
- single top (3 sub-processes): s-channel, t-channel and Wt productions;
- QCD multijet.

In total, there are six background groups (18 sub-groups) and one signal group (2 sub-groups).

The fit is performed simultaneously on 57 regions, which can be summarised, in order of complexity, as follows:

- **channels**: the analysis consists of 3 channels, selected according to the charged lepton multiplicities in the final state (0-, 1- and 2-lepton);

- **jet multiplicities**: exclusive regions with either 2 or 3 jets in the final state are treated separately in the profile likelihood fit;
- ***b*-tagging multiplicities**: there is a further subdivision based on the number of b-tagged jets in the final state (1- and 2-tag);
- $\boldsymbol{p_{\mathrm{T}}^{V}}$ **bins**: each of these regions is further split into p_{T}^{V} intervals, defined in chapt. **??**, to exploit the higher sensitivity of the high-boost region;
- **top control region**: referred to as top $e\mu$ control region, is presented in sec. 6.2;

The $m_{b\bar{b}}$ shape information, together with its normalisation, is extracted from the 2-tag signal regions. No shape information is used in the fit in any of the 1-tag and top control regions, where only the yields are fitted. A summary of the treatment of each category in the fit is shown in table 9.1.

Channel	1-tag, 2-jet	1-tag, 3-jet	2-tag, 2-jet	2-tag, 3-jet	top $e\mu$
0-lepton	3 × N	3 × N	3 × S	3 × S	-
1-lepton	5 × N	5 × N	7 × S	5 × S	-
2-lepton	5 × N	5 × N	5 × S	5 × S	5 × N

Table 9.1.: The regions entering the profile likelihood fit. N labels the regions in which only the total yield in the $m_{b\bar{b}}$ distribution is fitted, while S labels the regions in which both the $m_{b\bar{b}}$ shape and normalisation are fitted in each p_{T}^{V} bin.

9.1.2. Systematic variation interpretation

Many nuisance parameters are used to describe the uncertainties in the profile likelihood fit. They can be subdivided into different categories: those of experimental nature, and those coming from modelling uncertainties. The experimental systematic uncertainties are related to the physics objects used in the analysis: jets, b-jets, leptons and missing transverse energy and are discussed in detail in sec. 6.3, together with the modelling-related.

The result of the fit to the data is carefully scrutinised, addressing some specific points, listed here. The nuisance parameters, after performing the fit, can get values different from the nominal input. This can be detected checking the pulls of each parameter, corresponding to the difference in terms of standard deviations of the parameter value after and before the fit. If the pulls are large, it can be a symptom of a mis-modelling

of the examined parameter. The error, given by the $\pm 1\sigma$ deviation from the nominal value, on each nuisance parameter can be modified by the profiling procedure. This can indicate either an initial overestimate of the systematic error or the degeneracy of the examined parameter with another one. Eventual constraints on the post-fit errors can be studied using the Asimov dataset, defined in sec. 4.3.1, to check whether the constraint power on the pre-fit uncertainty comes from a physics source. The nuisance parameters input in the fit are in principle all un-correlated but, given the complexity of the model, eventual degeneracies can be spotted by checking the correlation matrix of all the nuisance parameters and the $\hat{\mu}$ parameter. More details on these studies can be found in the following sections.

These checks using pulls and correlations have been performed several times. At first a blinding procedure has been applied, allowing to test different nuisance parameter configurations, using the correlations and pulls to spot eventual errors in the model, and to choose the final one. The blinding procedure was applied as follows:

- the cuts listed in sec. 6.1 were optimised excluding the $m_{b\bar{b}}$ region $100 - 150$ GeV;
- the fit model was chosen without performing a fit to the data, but fitting only the Asimov dataset.

9.1.3. Free parameters in the fit

The normalisations of the main backgrounds are floated in the profile likelihood fit: Wcl, W+heavy flavour jets (hf), Zcl, Z+hf, $t\bar{t}$ and multijet for the 1-lepton channel only. This allows their determination directly from data. The term hf embeds three components: bl, cc and bb. An additional nuisance parameter constrained by a log-normal distribution for each component is introduced to correctly model the relative ratios among the flavour components. Additional normalisation parameters for each flavour component are introduced for the 3-jet region as well.

The normalisation of the multijet background is floated independently in each b-tag and jet multiplicity region. In the 2-tag 3-jet region, the multijet normalisation is fixed to its nominal value with a 50% log-normal constraint, because it represents only the 2% of the total background composition. The same happens for the 1-tag 3-jet region only in the $\sqrt{s} = 7$ TeV dataset, because there is not enough power to constrain this background, which is just 8% of the total 1-lepton background yield in this region.

9.1.4. Nuisance parameter treatment

Limited statistics in the MC nominal distributions can produce systematic templates with large fluctuations, introducing instabilities in the fit. Therefore, the uncertainties are treated according to the following procedure:

- reduce statistical fluctuations by rebinning. Bins in the $m_{b\bar{b}}$ distribution are merged until the nominal distribution of the systematic variation has less than 5% statistical uncertainty;
- separate normalisation changes from shape variations. In the fit model shape variations do not cause any change to the yield in each p_{T}^{V} bin;
- neglect the uncertainty on the normalisation or shape if the variation is smaller than 0.5%;
- neglect the normalisation uncertainty if both up and down variations cause a shift of the distribution in the same direction.

For the remaining nuisance parameters after applying this procedure, the normalisation uncertainties are taken into account as constrained by a log-normal distribution and the shape uncertainties by a Gaussian function.

9.1.5. Nuisance parameter correlations

All the systematics discussed in sec. 6.3 are included in the fit, if satisfying the criteria listed in sec. 9.1.4. Some parameters are further split in the fit model to take into account the correlations across processes and regions. The treatment is described in the following.

The jet flavour composition and response parameters are correlated only across similar processes. These systematics represent the uncertainties on the identification of the quark- or gluon-originated jets, therefore the assumption of a different composition between the various processes is made. There are four flavour composition nuisance parameters, and four for the flavour response in the fit, relative to the four main groups of processes:

1. W+jets (light and heavy flavour),
2. Z+jets (light and heavy flavour),
3. top (single top and $t\bar{t}$),

4. signal-like (diboson and VH signal).

The top p_{T} systematic is considered in the fit as three different parameters:

- one for the 2-lepton channel alone,
- one for the 2-jet region of the 1- and 0-lepton channels,
- one for the 3-jet region of the 0- and 1-lepton channels.

The $\Delta\varphi$ systematics, for both W and Z+jets, are considered as independent across the 2- and 3-jet regions and the flavour compositions (V+hf, Vcl, V+light), for a total of twelve nuisance parameters. The $t\bar{t}$ $m_{b\bar{b}}$ systematic is included in the fit as five nuisance parameters:

- one for the 2-lepton channel,
- one for the $p_{\mathrm{T}}^{V} < 120$ GeV interval in the 2-jet region in the 1-lepton channel,
- one for the $p_{\mathrm{T}}^{V} < 120$ GeV interval in the 3-jet region in the 1-lepton channel,
- one for the $p_{\mathrm{T}}^{V} > 120$ GeV interval in the 2-jet region correlating the 0- and 1-lepton channels,
- one for the $p_{\mathrm{T}}^{V} > 120$ GeV interval in the 3-jet region correlating the 0- and 1-lepton channels.

The reason for splitting the top $m_{b\bar{b}}$ systematic is mainly kinematic: in the 1-lepton channel case, in the high p_{T}^{V} region, partially because of the ΔR cut, the two jets selected as b quarks are generally bc, one of which is from the W decay, as explained in sec. 2.5.1. This is consistent with what is observed in the 0-lepton channel, for which only the three highest p_{T}^{V} bins are employed. In the low p_{T}^{V} region, instead, the two jets used to calculate $m_{b\bar{b}}$ are generally two real b quarks. In the 2-lepton case, instead, the $t\bar{t}$ contribution mostly comes from the fully leptonic channel, where both W bosons decay to $\ell\nu$, therefore the two final state jets are originating from b quarks.

The multijet shape nuisance parameters ($m_{b\bar{b}}$ and p_{T}^{V}) are only present for the 1-lepton channel and un-correlated across b-tag and jet multiplicities.

The diboson systematics are all un-correlated across production modes (WW, WZ, ZZ), apart from the 25% 3-jet region normalisation uncertainty, which is correlated across the three processes. All the other systematics are correlated across processes, channels, p_{T}^{V} bins, jet and b-tag multiplicities.

9.1.6. Systematic treatment when combining the 7 and 8 TeV datasets

When combining the data collected at two different centre of mass energies, it is important, where appropriate, to properly take into account the correlations among the systematics. The nuisance parameters can only be used as input to the profile likelihood fit as fully correlated or un-correlated. The full correlation is exploited by using the same parameter in different regions, while a parameter is un-correlated if treated as a set of independent parameters in different regions. In general, the systematic uncertainties evaluated with different methods or using different MC models for the two datasets are treated as un-correlated, while they are considered as a single parameter if they are extracted coherently in the two datasets.

All the b, c and light efficiencies are un-correlated between 7 and 8 TeV, as they are extracted independently in the 7 and 8 TeV datasets. For the same reason, the uncertainty on the pileup interaction modelling and the $E_{\mathrm{T}}^{\mathrm{miss}}$ systematics are treated as independent parameters in the two datasets. All the modelling parameters, including top p_{T} and $\Delta\varphi$ are instead correlated between the two datasets, as are the experimental lepton systematics, as their evaluation method is the same. The treatment of the jet energy scale (JES) nuisance parameters is dependent on the method used to estimate them. Therefore, only fourteen parameters out of twenty four are treated as independent in each dataset.

9.2. Results

In this section, the outcome of the fit presented in sec. 9.1 is shown, in the hypothesis of a Higgs boson with $m_H = 125$ GeV. Table 9.2 shows the fitted yields in the 2-tag regions for all the three lepton channels.

2-jet, 2-tag sample													
	0-lepton			1-lepton					2-lepton				
Process	$E_{\mathrm{T}}^{\mathrm{miss}}$ [GeV]			p_{T}^{W} [GeV]					p_{T}^{Z} [GeV]				
	120-160	160-200	>200	0-90	90-120	120-160	160-200	> 200	0-90	90-120	120-160	160-200	>200
$ZH \to \nu\bar{\nu}b\bar{b}$	1.7	1.0	1.0	0.0	0.0	0.0	0.0	0.0	0.0	0.0	0.0	0.0	0.0
$ZH \to \ell^+\ell^-b\bar{b}$	0.0	0.0	0.0	0.2	0.0	0.0	0.0	0.0	2.2	0.6	0.4	0.2	0.2
$WH \to \ell\nu b\bar{b}$	0.5	0.2	0.0	8.2	1.9	0.0	1.1	1.2	0.0	0.0	0.0	0.0	0.0
VH total	2.2	1.1	1.2	8.4	1.9	1.3	1.1	1.2	2.2	0.6	0.4	0.2	0.2
Top	310.9	50.1	12.7	6723.8	1788.5	714.7	177.2	65.3	438.8	75.6	16.4	1.2	0.0
W+c, light	53.8	11.9	9.0	1272.1	185.4	68.2	28.3	26.5	0.0	0.0	0.0	0.0	0.0
W+b	91.1	24.4	20.0	1960.8	333.2	140.2	59.8	53.7	0.0	0.0	0.0	0.0	0.0
Z+c, light	60.8	17.2	17.4	46.5	5.1	1.1	0.7	0.2	192.8	35.1	14.1	3.7	3.7
Z+b	532.4	142.7	96.3	206.1	30.7	8.0	3.7	1.5	1867.6	384.3	144.5	30.8	21.1
WW	1.4	0.3	0.5	21.3	3.1	1.9	0.8	0.9	0.0	0.0	0.0	0.0	0.0
VZ	50.9	21.6	19.2	252.0	40.1	25.6	15.3	13.3	98.3	17.4	9.7	4.3	4.2
Multijet	10.8	2.4	1.6	2623.0	118.2	21.6	10.5	2.1	0.0	0.0	0.0	0.0	0.0
Total Bkg.	1111 ± 22	270 ± 5	177 ± 5	13097 ± 117	2502 ± 34	980 ± 18	295 ± 7	162 ± 7	2595 ± 43	512 ± 10	184 ± 4	40 ± 1	29 ± 1
Data	1142	286	175	13107	2498	992	290	181	2567	517	167	50	24

3-jet, 2-tag sample													
	0-lepton			1-lepton					2-lepton				
Process	$E_{\mathrm{T}}^{\mathrm{miss}}$ [GeV]			p_{T}^{W} [GeV]					p_{T}^{Z} [GeV]				
	120-160	160-200	>200	0-90	90-120	120-160	160-200	> 200	0-90	90-120	120-160	160-200	>200
$ZH \to \nu\bar{\nu}b\bar{b}$	0.5	0.3	0.4	0.0	0.0	0.0	0.0	0.0	0.0	0.0	0.0	0.0	0.0
$ZH \to \ell^+\ell^-b\bar{b}$	0.0	0.0	0.0	0.1	0.0	0.0	0.0	0.0	1.0	0.3	0.2	0.1	0.1
$WH \to \ell\nu b\bar{b}$	0.1	0.1	0.0	2.4	0.7	0.0	0.5	0.7	0.0	0.0	0.0	0.0	0.0
VH total	0.6	0.3	0.4	2.5	0.7	0.6	0.6	0.7	1.0	0.3	0.2	0.1	0.1
Top	308.0	63.2	19.1	13149.7	2935.0	1103.6	345.7	177.4	297.3	54.3	13.7	0.9	0.4
W+c, light	17.2	4.6	3.8	428.1	66.7	29.2	14.5	15.7	0.0	0.0	0.0	0.0	0.0
W+b	35.2	10.5	8.3	706.2	121.1	59.7	31.0	33.8	0.0	0.0	0.0	0.0	0.0
Z+c, light	16.2	6.2	7.5	19.6	2.6	0.9	0.5	0.2	124.2	26.1	12.4	4.0	5.1
Z+b	134.6	51.3	40.5	133.8	18.2	5.3	3.0	1.6	1134.7	238.1	112.5	31.2	27.0
WW	0.6	0.2	0.1	8.2	1.5	0.8	0.3	0.4	0.0	0.0	0.0	0.0	0.0
VZ	9.3	4.0	4.5	52.5	10.0	7.3	5.0	6.0	34.8	6.7	4.1	1.8	2.3
Multijet	7.1	1.3	0.8	878.5	45.0	11.7	5.0	1.5	0.0	0.0	0.0	0.0	0.0
Total Bkg.	528 ± 13	141 ± 3	85 ± 3	15374 ± 122	3199 ± 35	1218 ± 19	405 ± 10	236 ± 8	1590 ± 32	325 ± 7	143 ± 4	38 ± 2	35 ± 2
Data	570	131	88	15380	3217	1185	387	238	1599	308	157	35	33

Table 9.2.: The fitted numbers of signal and background events in the MC and the observed yields for the data. The table shows the yields for each lepton channel in p_{T}^{V} intervals for $0 < m_{b\bar{b}} < 500$ GeV. The numbers are quoted for the combined 7 and 8 TeV datasets. The fitted numbers of signal events are shown for the WH and ZH production separately for $m_H = 125$ GeV. The errors on the total background correspond to $\pm 1\sigma$ error on the fitted nuisance parameters, taking into account both the systematic and statistical uncertainties.

The most important systematic uncertainties, and their impact on the total background and signal yields, after performing the profile likelihood fit, are shown in tables 9.3 and 9.4. These can be compared to the pre-fit tables, 6.4 and 6.5, in sec. 6.3.4. The effect of the profiling procedure can be seen on the reduction of the errors.

In the background case, shown in table 9.3, the jet-related systematic uncertainty is reduced from 6.2% to 2.4% in the 0-lepton channel, and from 6% to 2.3% in the 1-lepton channel. The most important systematics in these channels after the fit are b-tagging, 2.9% in the 0-lepton case, and the top modelling-related uncertainties, 3.1% in the 1-lepton case. In the 2-lepton channel, the Z+jet modelling is still the most important uncertainty, but it is reduced from 9.8% to 4.5%.

Uncertainty [%]	0-lepton	1-lepton	2-lepton
b-tagging	2.88	2.54	3.12
c-tagging	2.10	2.66	1.29
light tagging	1.19	1.00	1.10
Jet/Pile-up/$E_{\mathrm{T}}^{\mathrm{miss}}$	2.37	2.26	1.38
Lepton	0.47	1.24	1.23
Top modelling	1.50	3.08	0.48
W modelling	1.35	2.33	0.00
Z modelling	2.48	0.06	4.53
Single-top modelling	0.27	0.61	0.03
Diboson	0.93	0.57	1.54
Multijet	0.52	0.66	0.00
Luminosity	2.31	2.23	2.33
Total	2.62	2.63	3.20

Table 9.3.: A summary of the sizes of the components of the systematic uncertainties on the total estimated background yield, after performing the profile likelihood fit for the three channels at $\sqrt{s} = 8$ TeV. The uncertainties are shown as a percentage and grouped into categories. They are averaged over all p_{T}^{V} intervals in each category. The quoted total error is obtained by adding the individual components in quadrature in each p_{T}^{V} interval, and then averaging.

For the signal, shown in table 9.4, the jet-related systematics for the 0- and 1-lepton channels are also strongly reduced, respectively from 5.9% to 3.2%, and from 6.1% to 3%. The b-tagging systematic is still dominant in the 2-lepton channel, but is reduced from 5.3% to 3.6%. It is also the systematic with higher post-fit impact in the 0- and 1-lepton channels, with an effect of 3.7% for both.

Uncertainty [%]	0-lepton	1-lepton	2-leptons
b-tagging	3.73	3.69	3.59
c-tagging	0.01	0.02	0.02
light tagging	0.02	0.05	0.03
Jet/Pile-up/$E_{\mathrm{T}}^{\mathrm{miss}}$	3.17	2.96	1.87
Lepton	0.00	1.30	1.06
VH $p_{\mathrm{T}}-$dependence	2.03	2.15	2.00
VH theory scale	1.34	0.04	1.60
VH theory PDF	2.98	3.42	3.50
VH acceptance	10.00	10.00	10.00
Luminosity	2.33	2.33	2.33
Total	12.06	12.17	11.93

Table 9.4.: A summary of the sizes of the components of the systematic uncertainties on the signal yield for $m_H = 125$ GeV, after performing the profile likelihood fit for the three channels at $\sqrt{s} = 8$ TeV. The uncertainties are shown as a percentage and grouped into categories. They are averaged over all p_{T}^V intervals in each category. The quoted total error is obtained by adding the individual components in quadrature in each p_{T}^V interval, and then averaging.

Therefore, after profiling, the b-tagging and jet-related systematics still have the highest impact, but their effect is reduced of a factor of two at least. In the signal case, the largest modelling uncertainty contribution comes from the p_{T} dependence and the PDF uncertainty. In the background case, instead, the most significant systematics are those related to the modelling of the largest backgrounds: V+jets and $t\bar{t}$.

Further studies on the impact of the systematic uncertainties on the parameter μ show that jet-related systematics do not significantly affect the extraction of the signal, despite their large values. The other significant systematics, b-tagging, top and V+jet modelling, instead, do affect the signal evaluation significantly. In particular there is a high correlation between the signal strength evaluation and the top modelling systematics. Fig. 9.1 represents the impact of the nuisance parameters on the extracted Higgs signal strength. This indicates the systematics mostly affecting the signal evaluation, that could be therefore studied more in detailed and improved for a future result. Fig. 9.2, instead, shows all nuisance parameters which have a correlation above 25% with at least one other nuisance parameter in the final fit.

The scale factors of the freely floating backgrounds extracted from the fit are listed in table 9.5. These numbers correspond to the multiplicative factors between the nominal

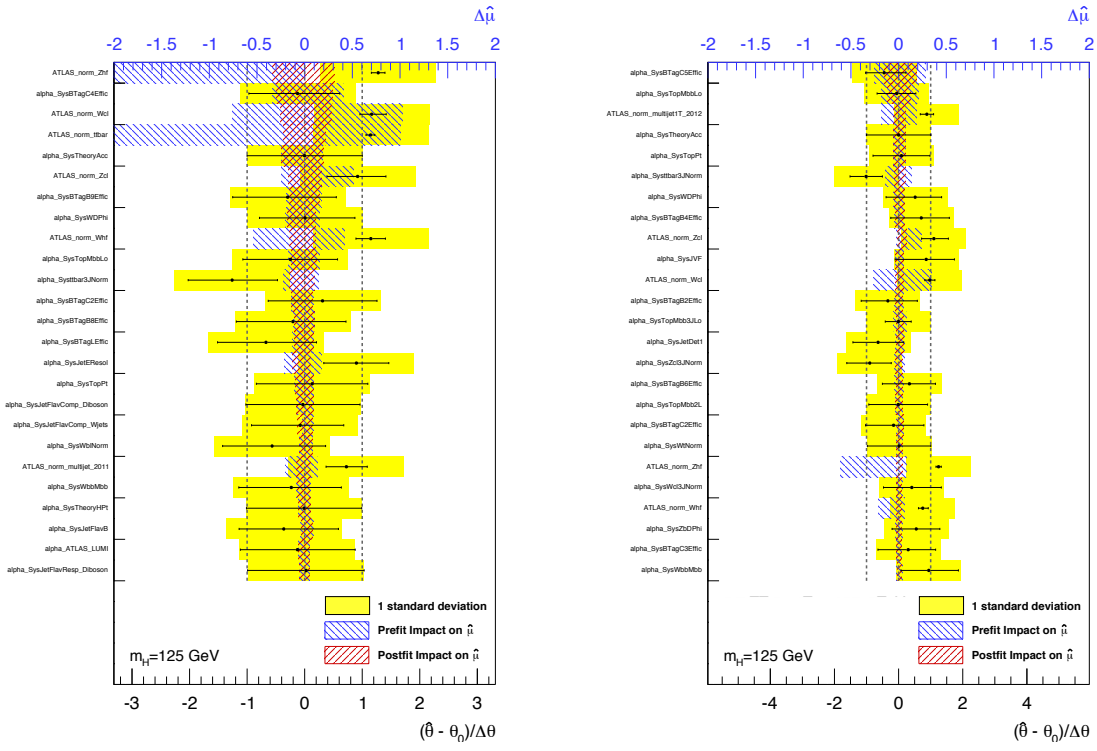

(a) $\sqrt{s} = 7$ TeV **(b)** $\sqrt{s} = 8$ TeV

Figure 9.1.: Impact of the nuisance parameters on $\hat{\mu}$, in decreasing order of post-fit effect for 7 (9.1a) and 8 TeV (9.1b). Only the most significant nuisance parameters in terms of impact on $\hat{\mu}$ are shown in the plot. The x axis at the bottom shows the number of standard deviations from the nominal input value of each nuisance parameter. The dashed vertical lines indicate the $\pm 1\sigma$ band. The x axis at the top in blue represents the fractional variation on $\hat{\mu}$ caused by each of the nuisance parameters on the y axis. Around each pull point both post (in black) and pre-fit (in solid yellow) one sigma errors are shown, highlighting the eventual constraints. The blue hatched areas, centred in 0, represent the symmetrised fractional variation on $\hat{\mu}$ caused by the pre-fit value of the nuisance parameters on the y axis. The red hatched areas, instead show the post-fit effect.

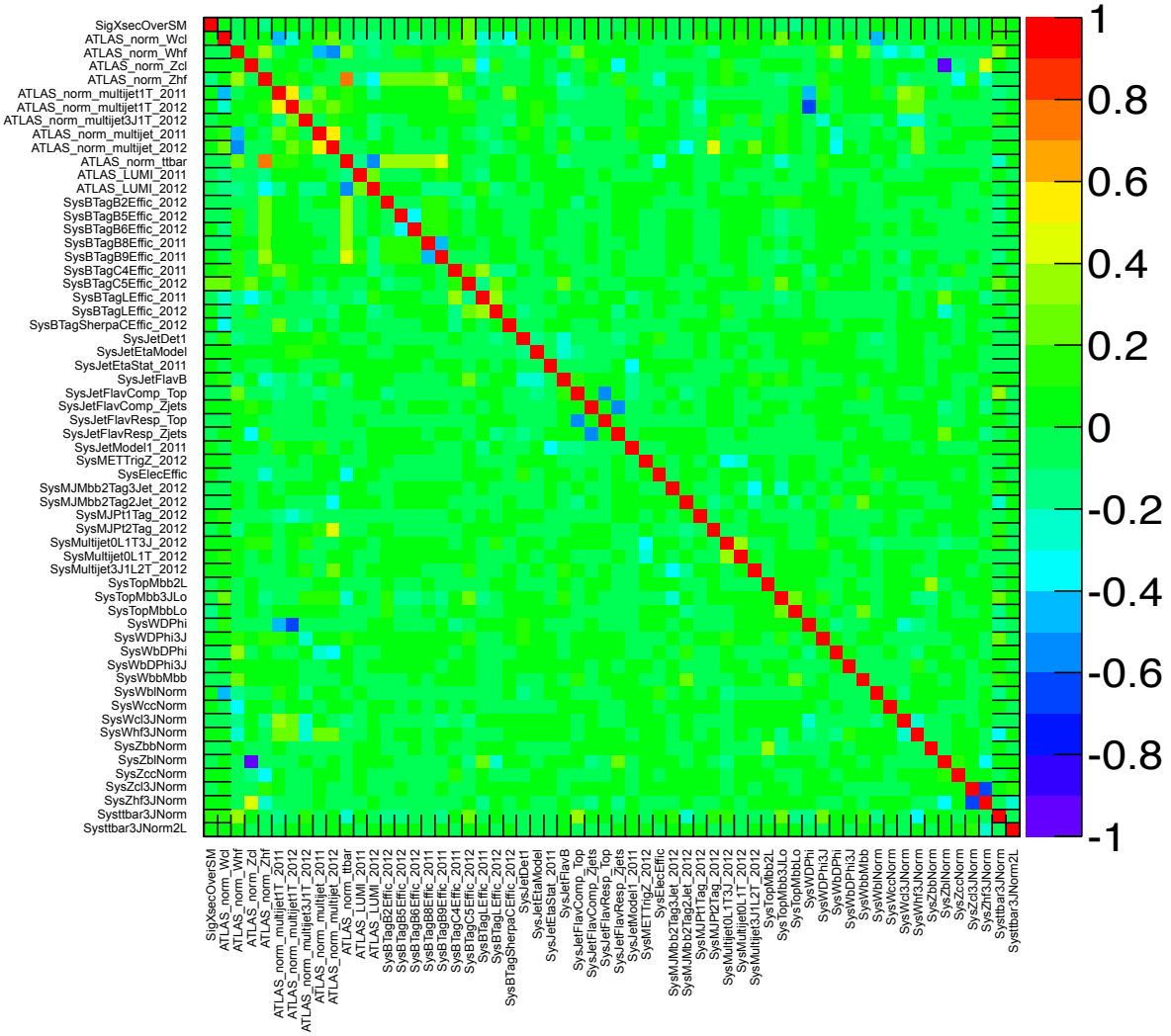

Figure 9.2.: The correlation between the nuisance parameters for the combined $\sqrt{s} = 7$ TeV and $\sqrt{s} = 8$ TeV datasets. Only the parameters with at least one high correlation are shown, selected with a 25% threshold.

cross sections obtained from the MC simulation and the cross sections estimated using the profile likelihood fit: $\sigma_{\text{fit}} = \text{SF} \times \sigma_{\text{nom}}$.

Parameter	$\sqrt{s} = 7$ TeV	$\sqrt{s} = 8$ TeV	combined dataset
Wcl	$1.18^{+0.22}_{-0.22}$	$0.97^{+0.16}_{-0.16}$	$1.05^{+0.14}_{-0.14}$
W+hf	$1.13^{+0.26}_{-0.26}$	$0.76^{+0.15}_{-0.15}$	$0.89^{+0.15}_{-0.15}$
Zcl	$0.92^{+0.53}_{-0.53}$	$1.14^{+0.38}_{-0.38}$	$0.89^{+0.48}_{-0.48}$
Z+hf	$1.27^{+0.12}_{-0.12}$	$1.25^{+0.08}_{-0.08}$	$1.30^{+0.07}_{-0.07}$
$t\bar{t}$	$1.14^{+0.08}_{-0.08}$	$1.11^{+0.06}_{-0.06}$	$1.13^{+0.05}_{-0.05}$
multijet 1-tag 2-jet, $\sqrt{s} = 7$ TeV	$0.20^{+0.44}_{-0.44}$	–	$0.59^{+0.40}_{-0.40}$
multijet 2-tag 2-jet, $\sqrt{s} = 7$ TeV	$0.74^{+0.35}_{-0.35}$	–	$0.95^{+0.24}_{-0.24}$
multijet 1-tag 2-jet, $\sqrt{s} = 8$ TeV	–	$0.89^{+0.21}_{-0.21}$	$0.94^{+0.17}_{-0.17}$
multijet 1-tag 3-jet, $\sqrt{s} = 8$ TeV	–	$1.16^{+0.26}_{-0.26}$	$1.28^{+0.19}_{-0.19}$
multijet 2-tag 2-jet, $\sqrt{s} = 8$ TeV	–	$0.98^{+0.13}_{-0.13}$	$0.97^{+0.13}_{-0.13}$

Table 9.5.: Scale factors obtained from the final profile likelihood fit for the backgrounds left free to float without priors. The results of the fit combining the $\sqrt{s} = 7$ TeV and $\sqrt{s} = 8$ TeV datasets are shown, as well as those from separate fits performed on the two datasets.

Study of problematic nuisance parameters in the fit

Some of the checks performed to better understand the behaviour of the fit and spot eventual problems in the statistical model used to extract the signal are listed in the following. The summary plot of the pulls of the nuisance parameters to be scrutinised is presented in fig. 9.3. The pull is defined as the difference from the nuisance parameter value after and before the fit, $(\theta_{\text{fit}} - \theta_{\text{prefit}})$, in units of standard deviations. The error on the pull is the 1σ arrow obtained after performing the fit, to be compared to the pre-fit error, shown as the green band centred around zero.

In the following paragraphs, some nuisance parameters presenting large pulls or constraints after performing the profile likelihood fit will be analysed in detail. This study helps in identifying the sources of the discrepancies seen. These nuisance parameters shown in the plot are isolated from the others requiring them to have either a constraint

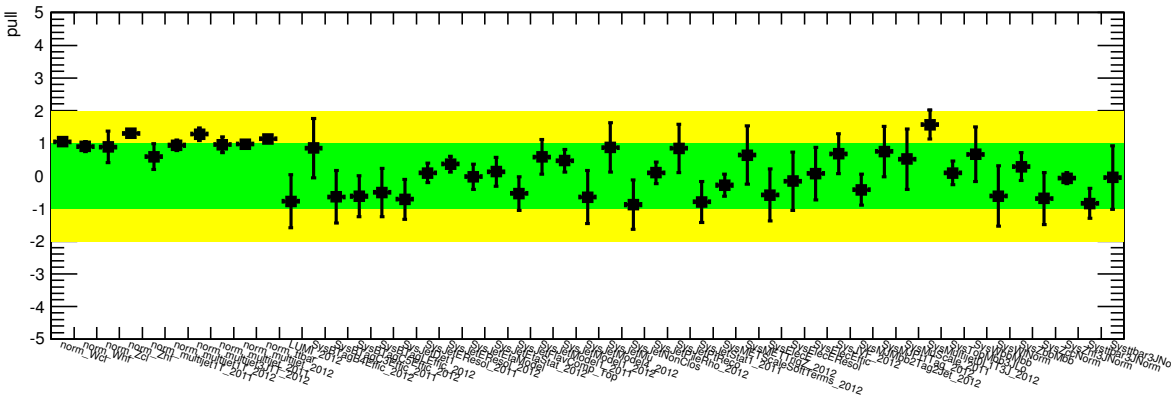

Figure 9.3.: Pulls of the combined fit for a Higgs boson signal with $m_H = 125$ GeV nuisance parameters in case of constraints larger than 50% or pulls larger than 0.5σ. The full dataset has been used in the fit. The first 10 points on the left are not actual pulls, but represent the scale factors of the freely floating backgrounds after performing the fit.

larger than 50% on the postfit error or a pull larger than 0.5σ from the nominal value. In the following, some of the parameters shown in the plot will be discussed in detail.

In general, when a pull or a constraint is observed, the model is broken down into components, and the various categories are fitted separately. This helps in understanding which specific region is the source of the pulled or constrained parameter. Constraints can also be verified with fits to the Asimov dataset, introduced in sec. 4.3.1. If a constraint is present in such fit, this means that the analysis has enough statistical power and the constraint is real. Otherwise, the effect can be an artefact of the fit and can indicate a degeneracy of the parameter considered with others. This can be cross-checked looking at the correlations between the parameters, shown in fig. 9.2.

Several jet energy scale related systematics are either pulled or constrained. The presence of the 1-tag high statistics regions in the fit can explain the power to constrain some of these parameters, but a detailed scrutiny on them is performed.

The jet energy resolution is strongly constrained in the global fit. $\sqrt{s} = 7$ TeV and $\sqrt{s} = 8$ TeV separate fits have been checked as well as the separate channels fits. In all these cases the jet energy resolution is constrained. Tests have been performed also by fitting the Asimov dataset, and the jet energy resolution parameter is constrained in this case as well. Part of the constraint has been verified to appear already when performing a fit just to the yields in all the regions. The constraint increases once the $m_{b\bar{b}}$ shape is added in the fit for the 2-tag region. Furthermore, the jet energy resolution is pulled

away from zero in the 7 TeV fit. The pulls and the constraints come primarily from the 2-lepton fit.

The jet systematic accounting for the η modelling is a rather large variation, of the order of 5% on $t\bar{t}$ events in the 1-lepton channel. Detailed studies on this parameter have been performed. The constraint on it is introduced by adding the $m_{b\bar{b}}$ shape in the 2-tag 3-jet region in the 1-lepton channel. In fact, when fitting this region alone, the error on the pull changes from 0.56 to 0.85σ when the $m_{b\bar{b}}$ shape is added or only the yields are fitted. The constraint is confirmed by a fit to the Asimov dataset.

One of the jet modelling systematics in the 8 TeV dataset (in fig. 9.3 indicated as SysJetModel4_2012) is pulled to -0.65σ in the fit. Further investigations performed fitting the 8 TeV dataset alone show no strong pull: 0.14σ when fitting only the yields, and 0.28σ in the fit with $m_{b\bar{b}}$ shape. The pull in the global fit is a fine tuning effect. It is useful to remind that this parameter has a pre-fit overall effect of $\sim 1\%$, so this does not significantly affect the final result.

All the other jet energy scale systematic variations shown in fig 9.3 are very small with respect to the nominal ($\leq 2\%$), therefore pulls or constraints on them do not significantly affect the final result. Likewise, the pulled electron energy systematic has a very small pre-fit effect, of $\sim 2\%$.

The nuisance parameter relative to the modelling of the top $m_{b\bar{b}}$ shape in the low p_{T}^{V} bins of the 3-jet region in the 1-lepton channel is constrained, mainly because of the high statistical power of the regions it affects. After applying the top p_{T} reweighting, the $t\bar{t}$ $m_{b\bar{b}}$ is checked in the 2- and 3-jet region separately, showing a different behaviour in the ratios between PowHeg showered with Pythia using the Perugia tune, which is the baseline in the analysis, and PowHeg showered with Jimmy.

The $Zb\bar{b}$ $m_{b\bar{b}}$ shape modelling nuisance parameter is significantly constrained in the global fit. It shows a large correlation with the top $m_{b\bar{b}}$ shape parameter relative to the 2-lepton channel. A detailed study has been performed on the $Zb\bar{b}$ $m_{b\bar{b}}$ parameter by breaking down the 0- and 2-lepton effects. The parameter has a strong pull when fitting the 0-lepton channel alone at 8 TeV and a strong constraint in the 2-lepton case. Both effects have been looked at and the pull in the 0-lepton fit is found to be strongly driven by the 2-tag 2-jet region, where it has a value of 1.1σ. Looking at the likelihood slice relative to this parameter, shown in fig. 9.4, it is clear that the pull is coherent in the three p_{T}^{V} bins and the main effect comes from the $120 < p_{\mathrm{T}}^{V}(\mathrm{GeV}) < 160$ region. In the 2-lepton fit of the 8 TeV dataset, after identifying the region with the largest constraint

to be the 2-tag 2-jet, with an error on the pull of 0.66σ, a fit to the Asimov dataset has been performed. This confirms the constraint, with an error of 0.61σ in this region. The 2-lepton channel has a large contribution of Z+jets, both from light and heavy flavour, and does have enough statistics to constrain the Z+hf component, and its shape.

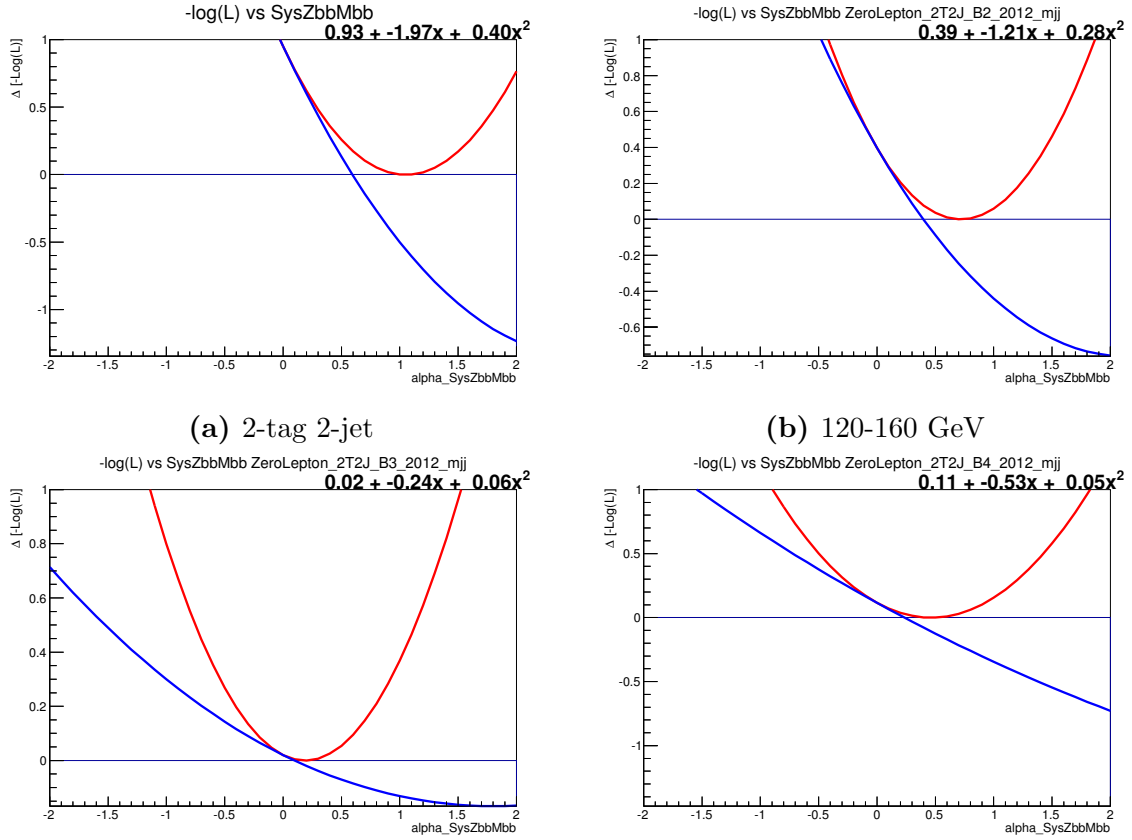

(a) 2-tag 2-jet **(b)** 120-160 GeV

(c) 160-200 GeV **(d)** $>$ 200 GeV

Figure 9.4.: Likelihood slices relative to the $m_{b\bar{b}}$ nuisance parameter of the $Zb\bar{b}$ background in the $\sqrt{s} = 8$ TeV 0-lepton fit performed only in the 2-tag 2-jet region. The red curve represents the likelihood, in the hypothesis of no correlations with the other nuisance parameters of the fit, taking into account the prior on the parameter. The blue curve is instead the likelihood slice if no prior is present.

The Z+hf normalisation parameter specific to the 3-jet region is constrained, because of the large statistical power in the 2-lepton channel. It has significant correlations with the Zcl floating normalisation and anti-correlations with the Z+hf floating normalisation, the $Zb\bar{b}$ $m_{b\bar{b}}$ shape parameter and the Zcl 3-jet region normalisation. The error on the pull in the combined fit is 0.22σ, mainly coming from the 2-lepton channel, where it has an error of 0.24σ if fitting the 8 TeV dataset alone. There is also a slight constraint on this parameter in the 0-lepton channel in the 8 TeV dataset, where the error on the pull is 0.62σ in the 2-tag region. The constraint in the 2-lepton case originates equally from 1-

and 2-tag regions and is partially an effect of the inclusion of the $m_{b\bar{b}}$ shape in the latter. The fit to the Asimov dataset performed on the 1-tag region confirms the constraint, and the relative likelihood slice can be seen in fig. 9.5. This parameter presents some redundancies with the others, as demonstrated by its correlations, and is constrained because of the high Z+hf statistics in the 2-lepton sample.

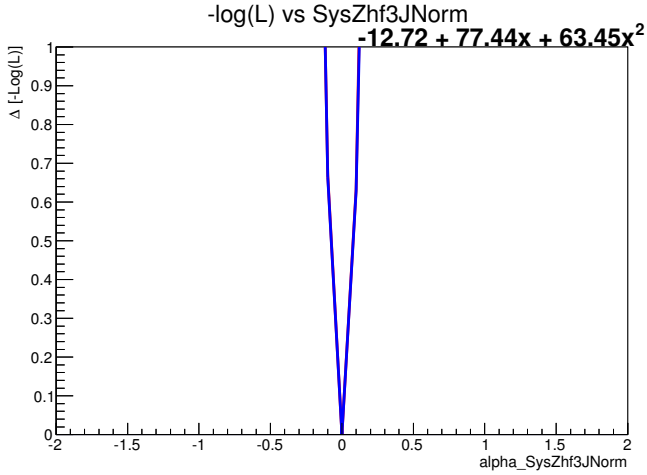

Figure 9.5.: Likelihood slice relative to the Z+hf 3-jet normalisation nuisance parameter in the 8 TeV 2-lepton fit in the 1-tag region. The red curve represents the likelihood, in the hypothesis of no correlations with the other nuisance parameters of the fit, taking into account the prior on the parameter. The blue curve is instead the likelihood slice if no prior is present. Here the two curves coincide, showing clearly the constraint on this parameter.

The $t\bar{t}$ 3-jet relative normalisation is pulled negatively and constrained. The 3-jet region in the 1-lepton channel has high statistics and is almost pure in top events, allowing for constraints on the normalisation. Moreover, this parameter is correlated with the W+hf floating normalisation and the flavour composition parameter for top. It is also anti-correlated with the $t\bar{t}$ floating normalisation and the W+hf 3-jet normalisation, confirming the strict interplay of the W+hf and $t\bar{t}$ sample normalisations and the difficulties to disentangle the first from the latter, because of the lack of a pure control region for W+hf.

The $m_{b\bar{b}}$ nuisance parameter for $Wb\bar{b}$ is pulled to $\sim 0.5\sigma$. A dedicated study showed that this is mostly coming from the bin $90 < p_{\mathrm{T}}^{V} < 120$ GeV, where the input model of $m_{b\bar{b}}$ shows some discrepancies with the data. The pull of $\sim 1\sigma$ on the 8 TeV luminosity in the combined fit is driven by the 2-lepton channel. This effect is not present when fitting the other two channels separately.

The isolation of these effects is crucial to optimise the fit model and the systematic evaluation in the subsequent iterations of the analysis. A deep understanding of the effect of the systematics on the final result in a complex fit as the one used in this analysis is an index of reliability of the result.

9.2.1. Extraction of the signal

The distributions of the di-b-jet invariant mass of the two signal jets are used in the final step of the analysis to test the possible presence of a Higgs boson signal. The normalisations of the top, Wb, Wcl, Zb, and Zcl backgrounds are allowed to float freely in the fit. The normalisations of the other backgrounds are constrained within their uncertainties according to the treatment described previously.

The $m_{b\bar{b}}$ distributions from the 8 TeV dataset obtained from the fit are shown in fig. 9.6 to 9.9 for the 2-tag region with two jets in the final state, and in fig. 9.10 to 9.13 for the case of three jets in the final state. As the systematic profiling can modify both the shape and normalisation of the background, the total background expectation, as input of the fit, is indicated with a dashed blue line. The profile likelihood fit shrinks the systematic uncertainties, and the resultant uncertainty after the fit is indicated with the dashed band. The Higgs signal, shown in red, is normalised to the result of the fit. Generally, good agreement between data and MC is observed within the quoted systematic uncertainties.

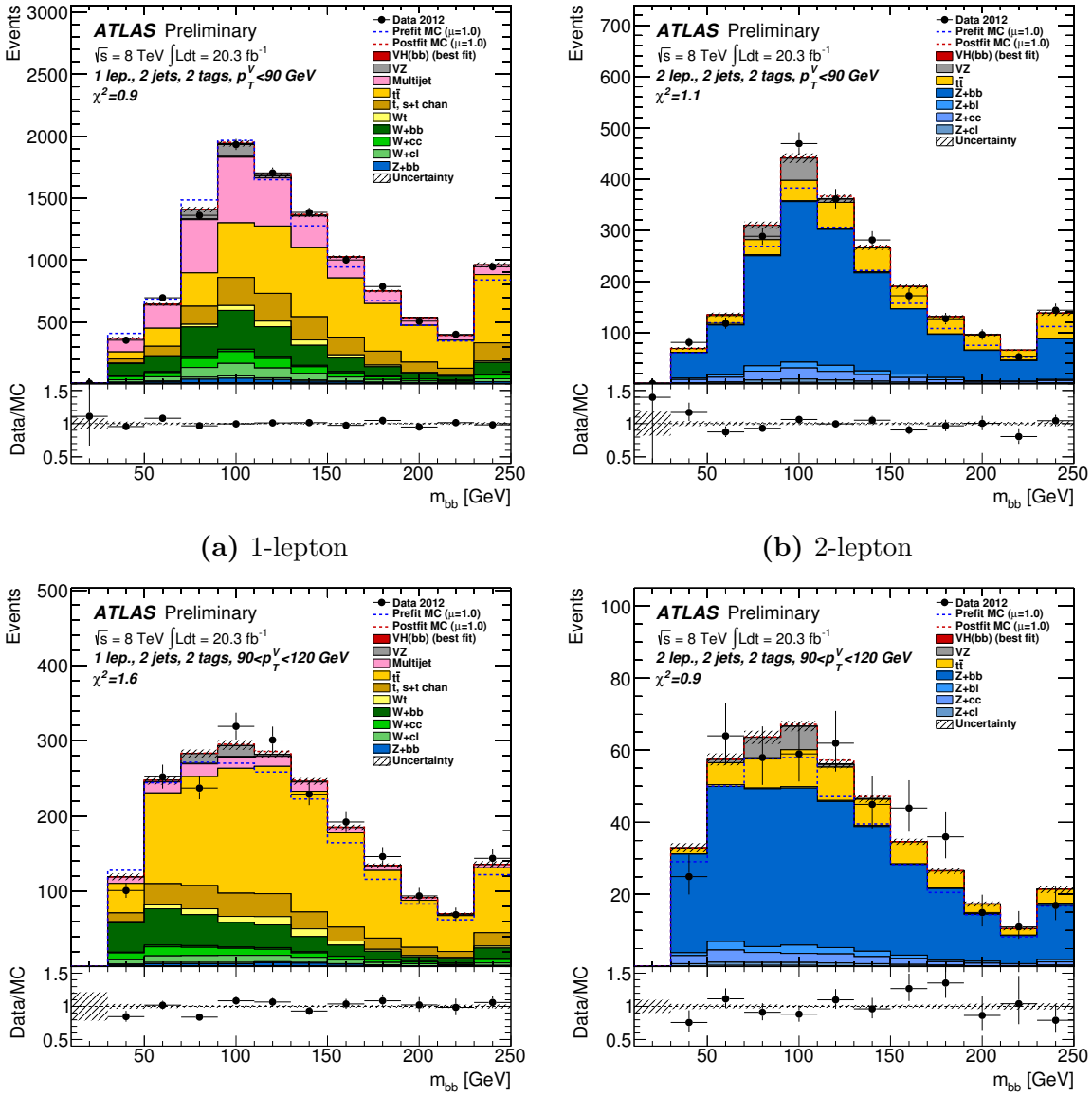

(a) 1-lepton **(b)** 2-lepton

(c) 1-lepton **(d)** 2-lepton

Figure 9.6.: Post-fit invariant mass distributions in the $p_{\mathrm{T}}^{V} < 90$ GeV (top) and $90 < p_{\mathrm{T}}^{V}/(\mathrm{GeV}) < 120$ (bottom) bins for the 2-tag 2-jet region at $\sqrt{s} = 8$ TeV for data and Monte Carlo expectation. The last bin contains the distribution overflow. The hatched black area represents the total error after the profile likelihood fit, the dashed blue line represents the total background distribution input in the fit. The dashed red area represents the total background distribution in the hypothesis of a SM Higgs signal of mass 125 GeV ($\mu = 1$), while the signal is renormalised to its best fit value after the fit. The solid area shows the various background components, with their post-fit normalisation values.

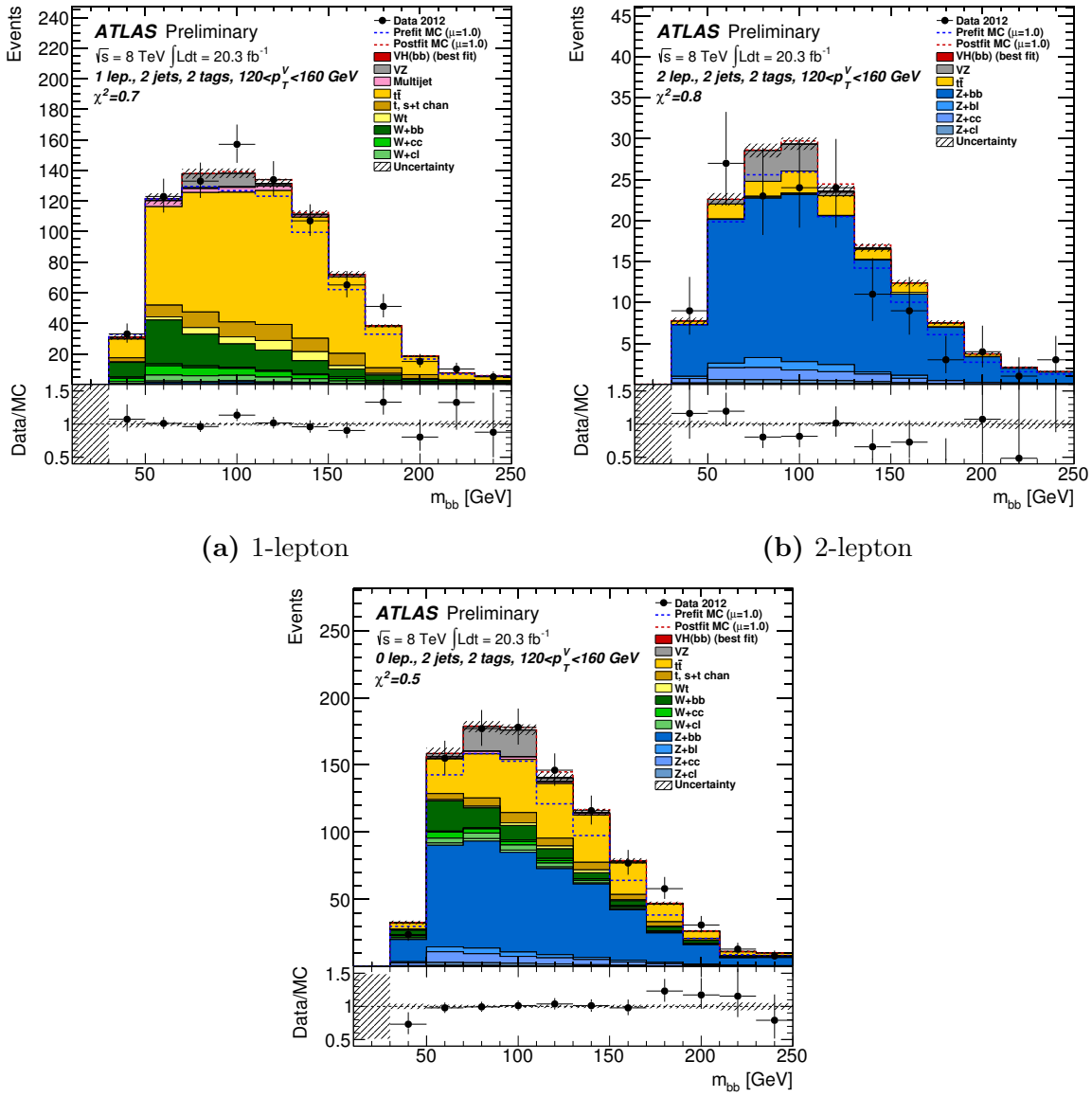

(a) 1-lepton **(b)** 2-lepton

(c) 0-lepton

Figure 9.7.: Post-fit invariant mass distributions in the $120 < p_{\mathrm{T}}^{V}/(\mathrm{GeV}) < 160$ bin for the 2-tag 2-jet region at $\sqrt{s} = 8$ TeV for data and Monte Carlo expectation. The last bin contains the distribution overflow. The hatched black area represents the total error after the profile likelihood fit, the dashed blue line represents the total background distribution input in the fit. The dashed red area represents the total background distribution in the hypothesis of a SM Higgs signal of mass 125 GeV ($\mu = 1$), while the signal is renormalised to its best fit value after the fit. The solid area shows the various background components, with their post-fit normalisation values.

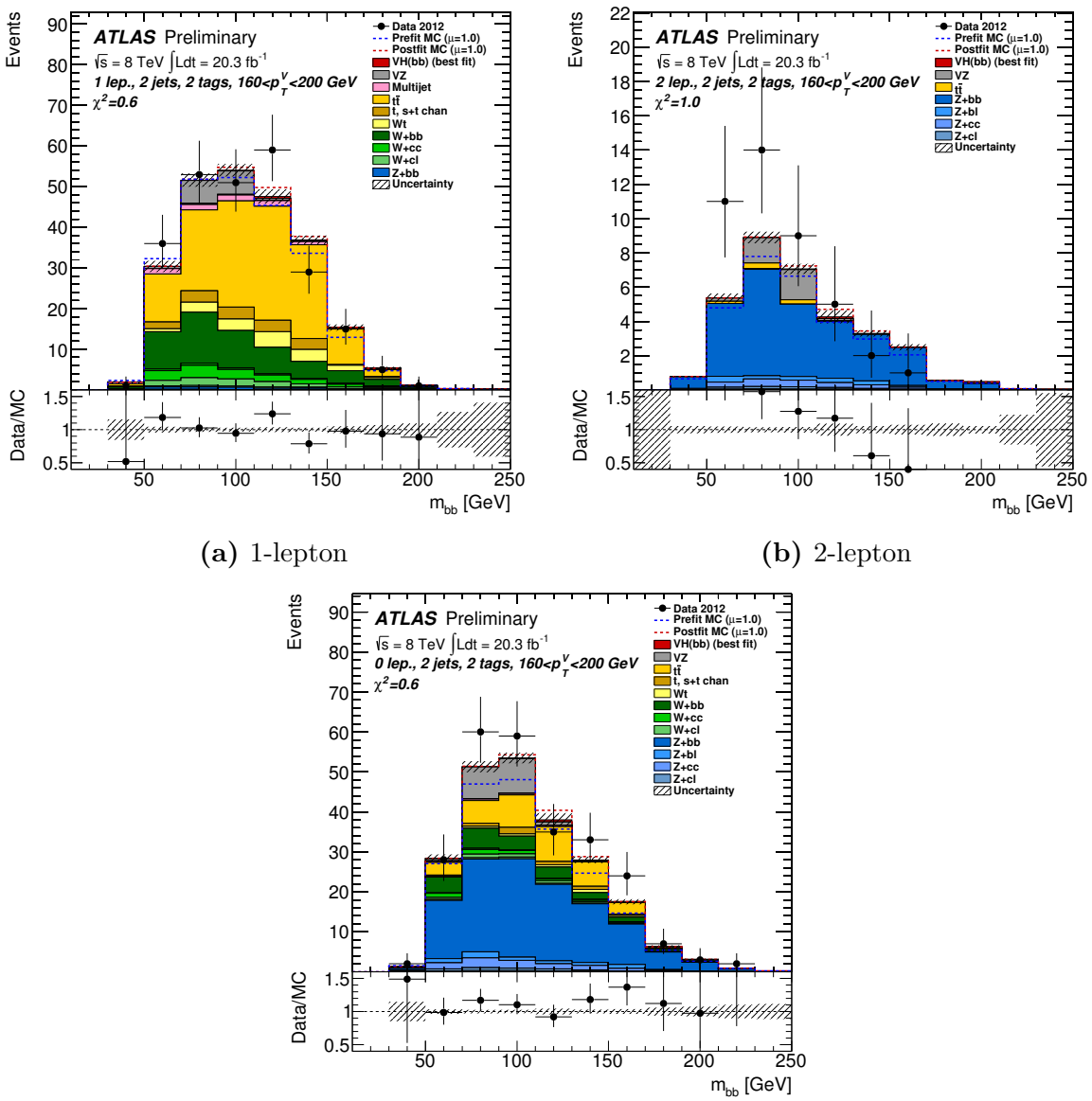

(a) 1-lepton **(b)** 2-lepton

(c) 0-lepton

Figure 9.8.: Post-fit invariant mass distributions in the $160 < p_{\mathrm{T}}^{V}/(\mathrm{GeV}) < 200$ bin for the 2-tag 2-jet region at $\sqrt{s} = 8$ TeV for data and Monte Carlo expectation. The last bin contains the distribution overflow. The hatched black area represents the total error after the profile likelihood fit, the dashed blue line represents the total background distribution input in the fit. The dashed red area represents the total background distribution in the hypothesis of a SM Higgs signal of mass 125 GeV ($\mu = 1$), while the signal is renormalised to its best fit value after the fit. The solid area shows the various background components, with their post-fit normalisation values.

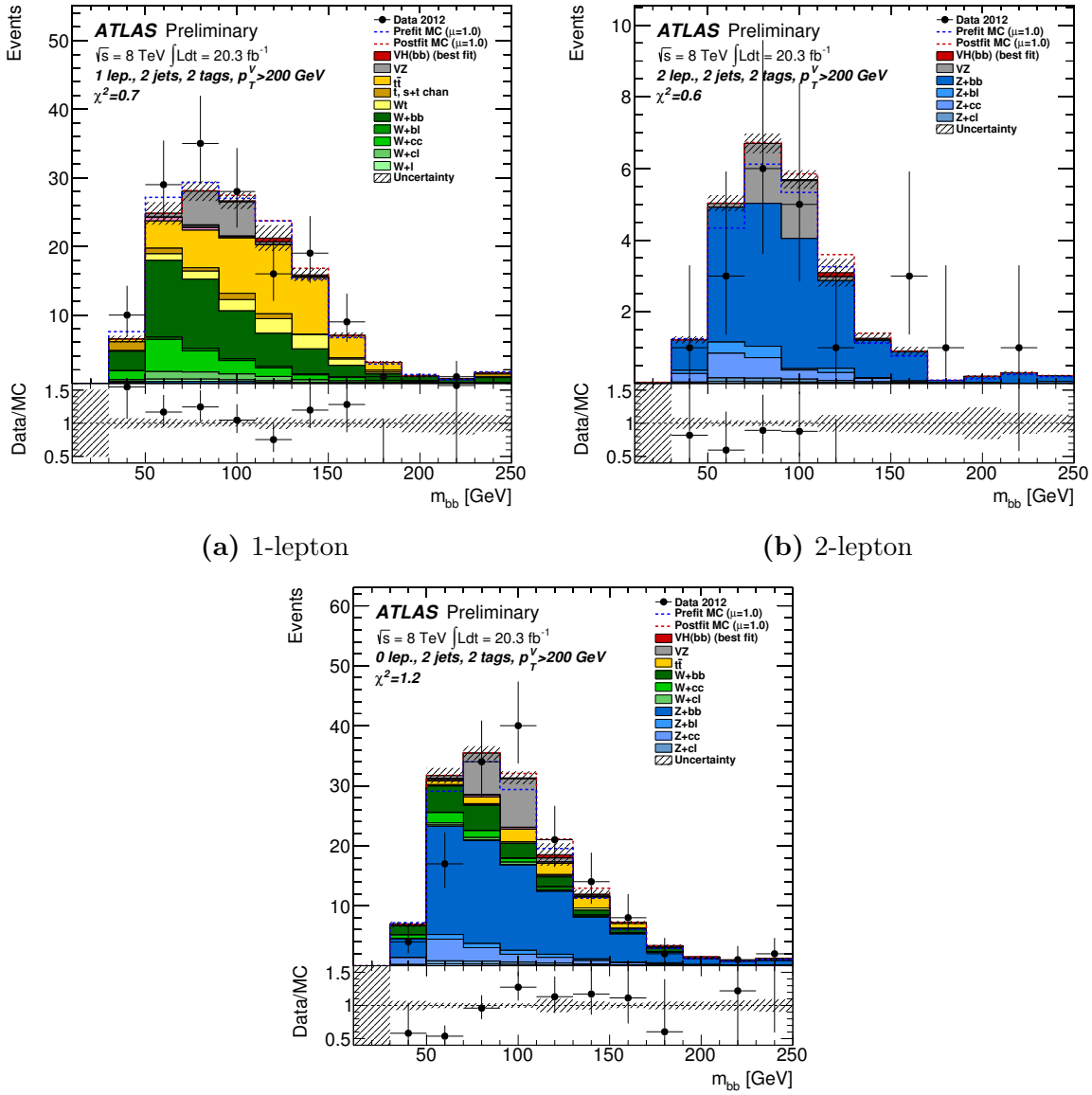

(a) 1-lepton **(b)** 2-lepton

(c) 0-lepton

Figure 9.9.: Post-fit invariant mass distributions in the $p_{\mathrm{T}}^{V} > 200$ GeV bin for the 2-tag 2-jet region at $\sqrt{s} = 8$ TeV for data and Monte Carlo expectation. The last bin contains the distribution overflow. The hatched black area represents the total error after the profile likelihood fit, the dashed blue line represents the total background distribution input in the fit. The dashed red area represents the total background distribution in the hypothesis of a SM Higgs signal of mass 125 GeV ($\mu = 1$), while the signal is renormalised to its best fit value after the fit. The solid area shows the various background components, with their post-fit normalisation values.

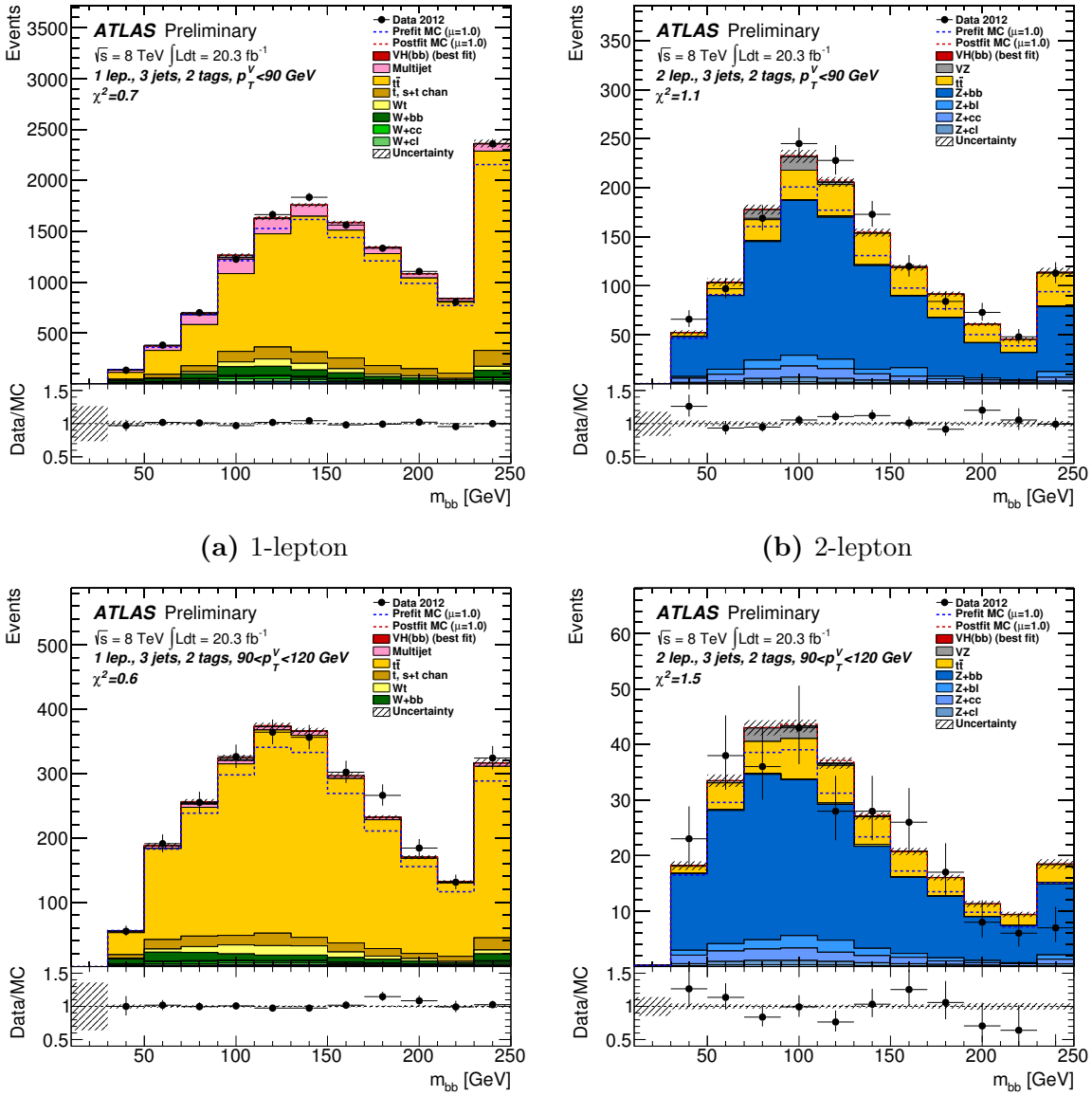

(a) 1-lepton **(b)** 2-lepton

(c) 1-lepton **(d)** 2-lepton

Figure 9.10.: Post-fit invariant mass distributions in the $p_{\mathrm{T}}^{V} < 90$ GeV (top) and $90 < p_{\mathrm{T}}^{V}/(\mathrm{GeV}) < 120$ (bottom) bins for the 2-tag 3-jet region at $\sqrt{s} = 8$ TeV for data and Monte Carlo expectation. The last bin contains the distribution overflow. The hatched black area represents the total error after the profile likelihood fit, the dashed blue line represents the total background distribution input in the fit. The dashed red area represents the total background distribution in the hypothesis of a SM Higgs signal of mass 125 GeV ($\mu = 1$), while the signal is renormalised to its best fit value after the fit. The solid area shows the various background components, with their post-fit normalisation values.

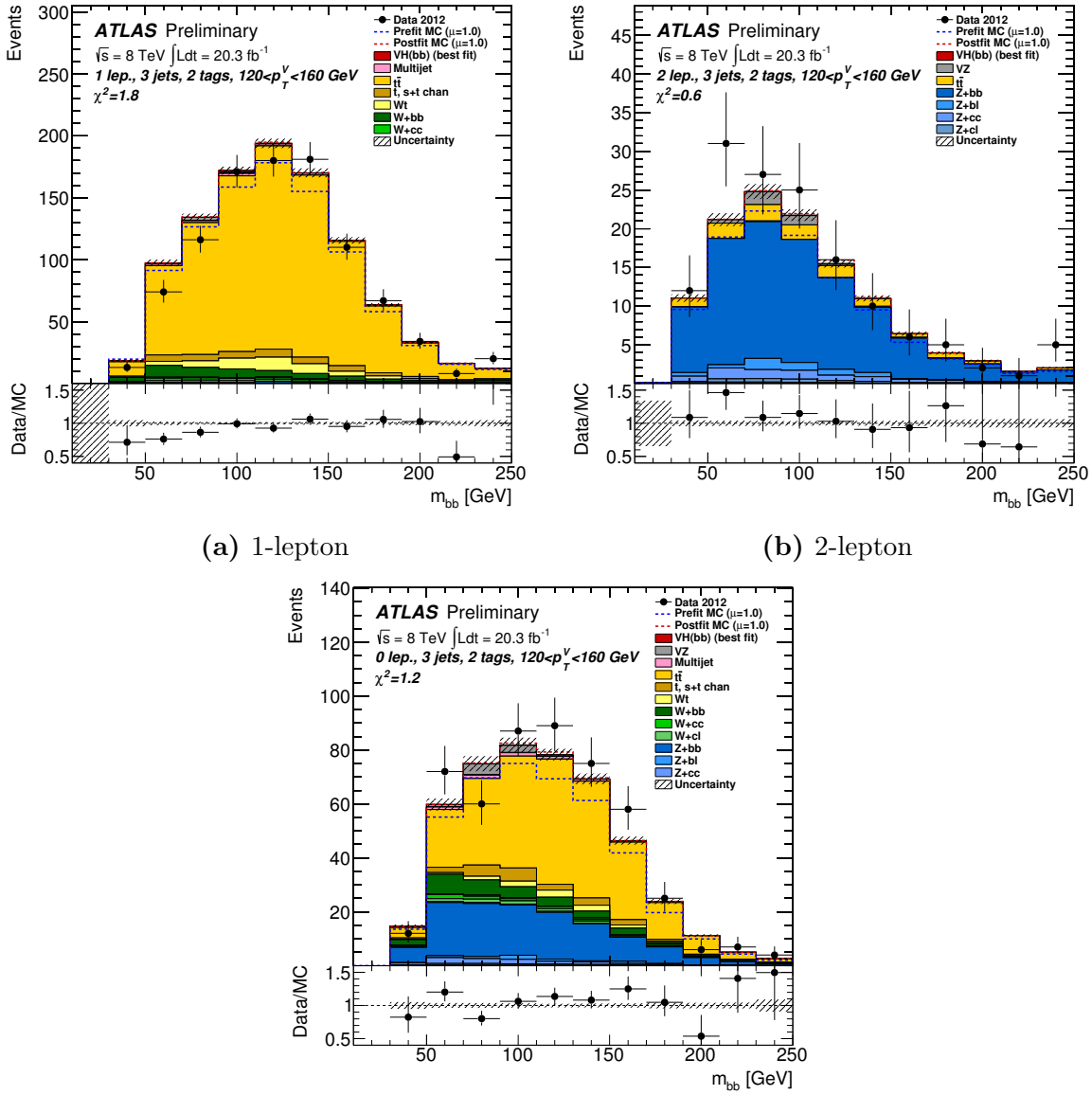

(a) 1-lepton

(b) 2-lepton

(c) 0-lepton

Figure 9.11.: Post-fit invariant mass distributions in the $120 < p_{\mathrm{T}}^{V}/(\mathrm{GeV}) < 160$ bin for the 2-tag 3-jet region at $\sqrt{s} = 8$ TeV for data and Monte Carlo expectation. The last bin contains the distribution overflow. The hatched black area represents the total error after the profile likelihood fit, the dashed blue line represents the total background distribution input in the fit. The dashed red area represents the total background distribution in the hypothesis of a SM Higgs signal of mass 125 GeV ($\mu = 1$), while the signal is renormalised to its best fit value after the fit. The solid area shows the various background components, with their post-fit normalisation values.

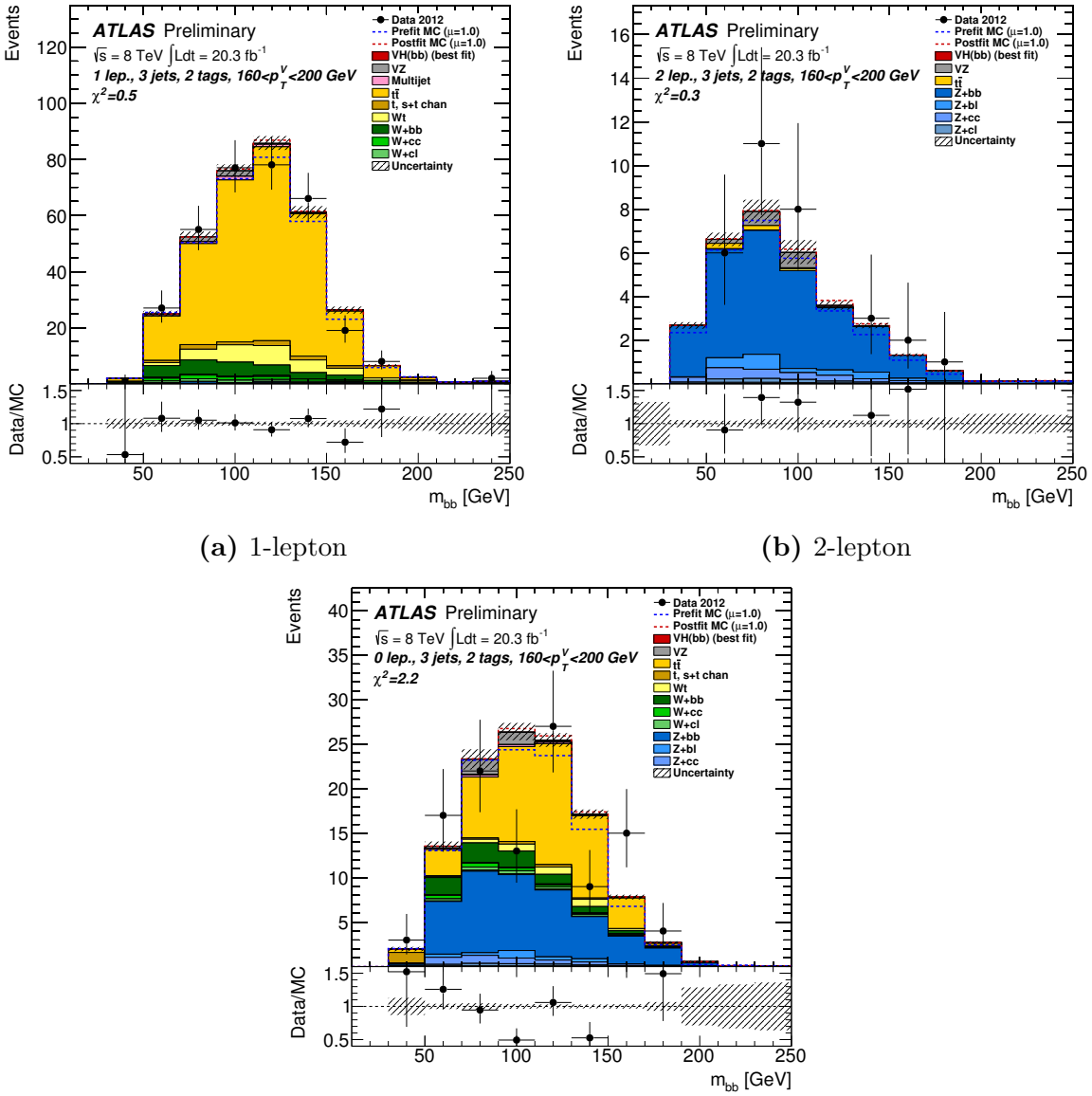

(a) 1-lepton **(b)** 2-lepton

(c) 0-lepton

Figure 9.12.: Post-fit invariant mass distributions in the $160 < p_{\mathrm{T}}^{V}/(\mathrm{GeV}) < 200$ bin for the 2-tag 3-jet region at $\sqrt{s} = 8$ TeV for data and Monte Carlo expectation. The last bin contains the distribution overflow. The hatched black area represents the total error after the profile likelihood fit, the dashed blue line represents the total background distribution input in the fit. The dashed red area represents the total background distribution in the hypothesis of a SM Higgs signal of mass 125 GeV ($\mu = 1$), while the signal is renormalised to its best fit value after the fit. The solid area shows the various background components, with their post-fit normalisation values.

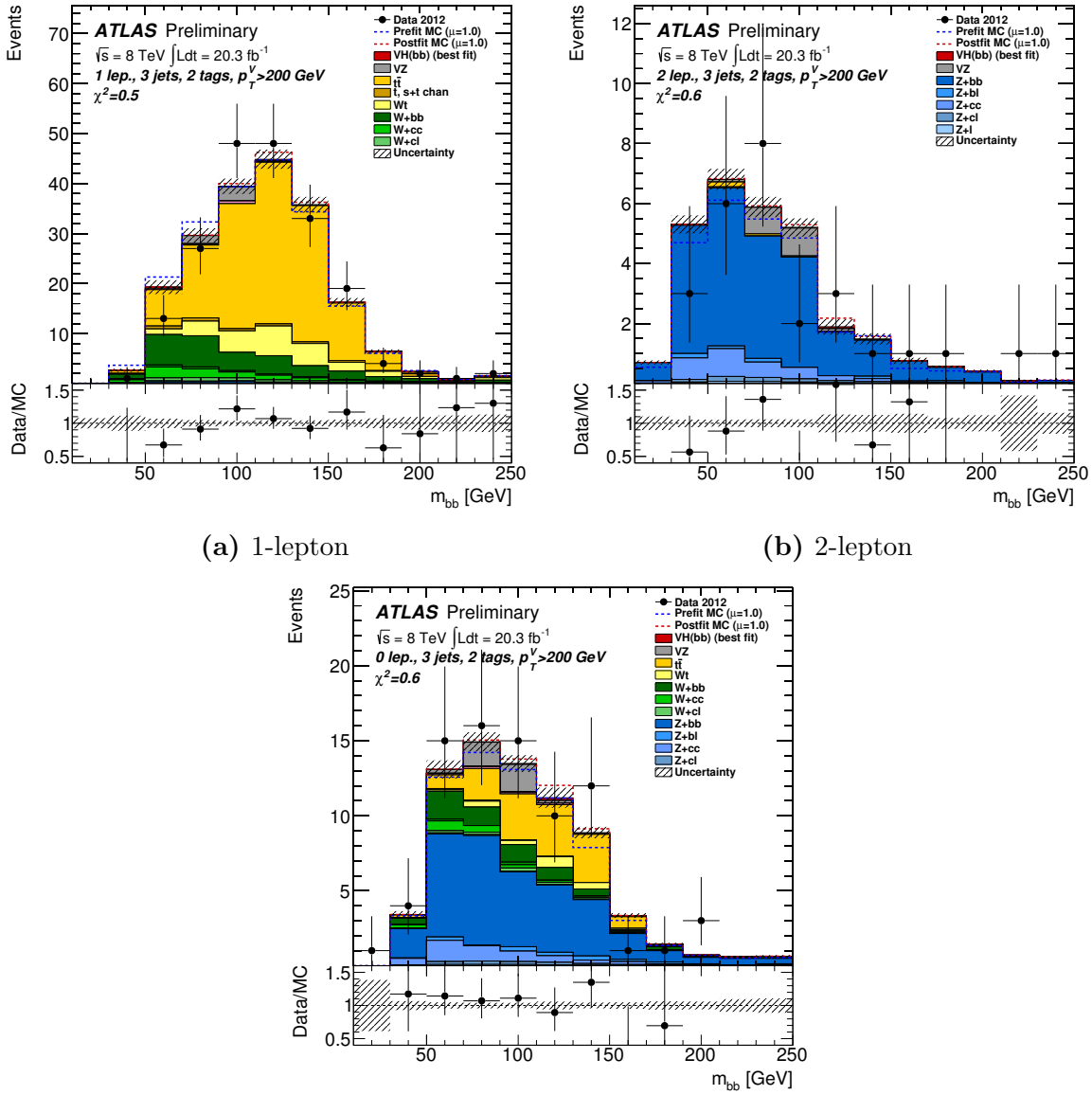

(a) 1-lepton **(b)** 2-lepton

(c) 0-lepton

Figure 9.13.: Post-fit invariant mass distributions in the $p_{\mathrm{T}}^{V} > 200$ GeV bin for the 2-tag 3-jet region at $\sqrt{s} = 8$ TeV for data and Monte Carlo expectation. The last bin contains the distribution overflow. The hatched black area represents the total error after the profile likelihood fit, the dashed blue line represents the total background distribution input in the fit. The dashed red area represents the total background distribution in the hypothesis of a SM Higgs signal of mass 125 GeV ($\mu = 1$), while the signal is renormalised to its best fit value after the fit. The solid area shows the various background components, with their post-fit normalisation values.

9.2.2. Diboson observation

To gauge the correctness of the background estimate and the fit configuration, a cross check using the $VZ(Z \rightarrow b\bar{b})$ signal is performed, as already done in the previous version of the analysis, described in chapt. 8. Given the aim of demonstrating the reliability of the described Higgs analysis, the event selection is kept the same as that described in sec. 6.1, optimised for the VH search, and not for VZ. The WH and ZH processes are considered as backgrounds in the fit, with their normalisation fixed to the Standard Model prediction for $m_H = 125$ GeV. Also the WW process is considered as a background.

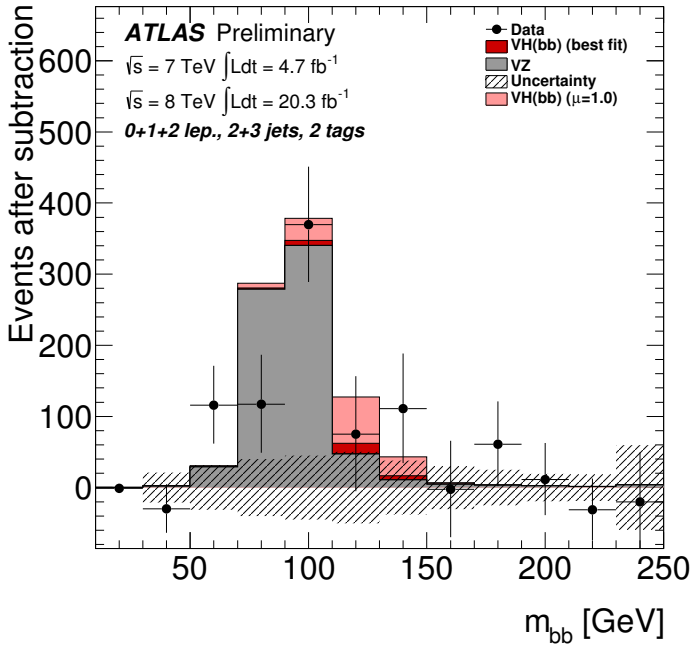

Figure 9.14.: The $m_{b\bar{b}}$ distribution in data after subtraction of all backgrounds except diboson processes, and including the SM Higgs boson production from WH and ZH channels. The Monte Carlo backgrounds are normalised according to the results of the profile likelihood fit in both datasets.

Fig. 9.14 shows the $m_{b\bar{b}}$ distribution in the data, after subtracting all the background events except the $VZ(Z \rightarrow b\bar{b})$ contributions and the SM Higgs boson production from WH and ZH channels. The backgrounds are normalised according to the result of the profile likelihood fit. An excess in the data is observed, located at the expected mass for the vector boson signal, with an observed (expected) significance of 4.8σ (5.1σ).

Fig. 9.15 compares the signal strength obtained in the three channels separately at 7 and 8 TeV and for the combination of the two datasets. For each centre of mass

energy and sub channel, a separate profile likelihood fit was performed, therefore the nuisance parameters are not necessarily identical in each case. This causes, for example, the combined 7 TeV result to have a μ-value higher than the three channel individual results. This effect is more significant for the 0-lepton channel because there are no strong constraints on the main backgrounds when fitting this channel alone, given the absence of control regions.

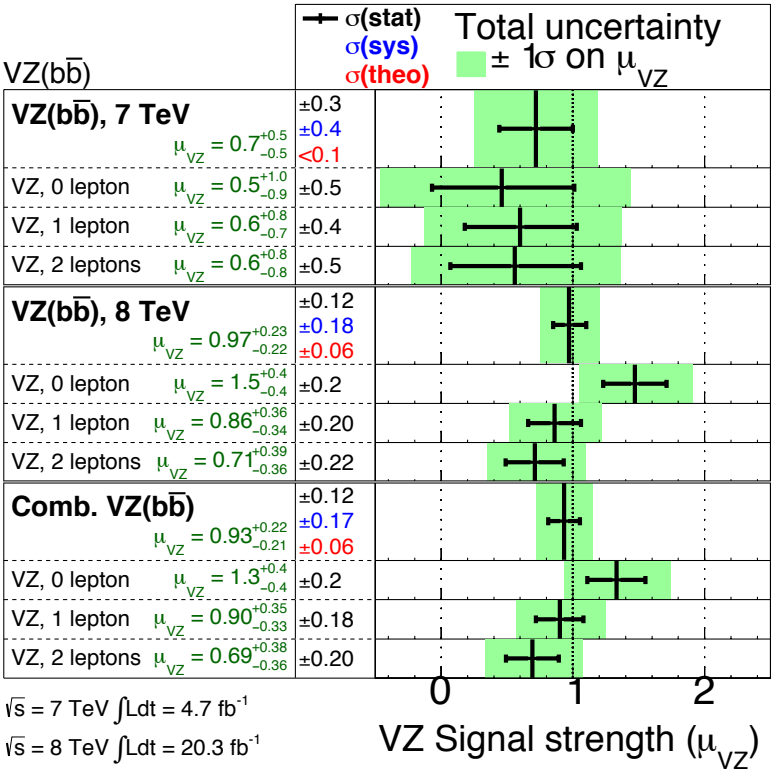

Figure 9.15.: The fitted μ_{VZ} values for the 7 and 8 TeV datasets and their combination. The table includes the results from independent fits to the separate 7 and 8 TeV datasets, and to each channel.

All the channels result in μ values consistent with the SM expectation. After combining the three channels and including all systematic uncertainties a value of $\mu_{VZ} = 0.93^{+0.22}_{-0.21}$ is found, in agreement with the Standard Model expectation of $\mu_{VZ} = 1$.

9.2.3. Higgs results

The profile likelihood fit with the Higgs boson signal strength, $\hat{\mu}$, floating is performed with the diboson contribution constrained to its SM value within its uncertainty, described in sec. 6.3.3.

For the Higgs boson mass hypothesis of 125 GeV, a one-sided upper limit is placed on the ratio of the Higgs boson production cross section to the Standard Model background only hypothesis at 95% confidence level (CL). The results are obtained combining the 0-, 1- and 2-lepton channels, and using the full Run 1 dataset.

The probability p_0 of obtaining a result at least as signal-like as the observed one from the background-only hypothesis is calculated using $q_0 = -2\ln(\mathcal{L}(0, \hat{\hat{\theta}}_\mu)/\mathcal{L}(\hat{\mu}, \hat{\theta}))$ as test statistic. For $m_H = 125$ GeV, the p_0 value is 0.36 in the absence of signal, corresponding to a significance of 0.36 standard deviations (σ). This result has to be compared to an expected p_0 of 0.05, corresponding to a 1.64σ significance in the presence of a SM Higgs boson with 125 GeV mass, combining $\sqrt{s} = 7$ TeV and $\sqrt{s} = 8$ TeV datasets. Fig. 9.16 shows the p_0 value as function of m_H.

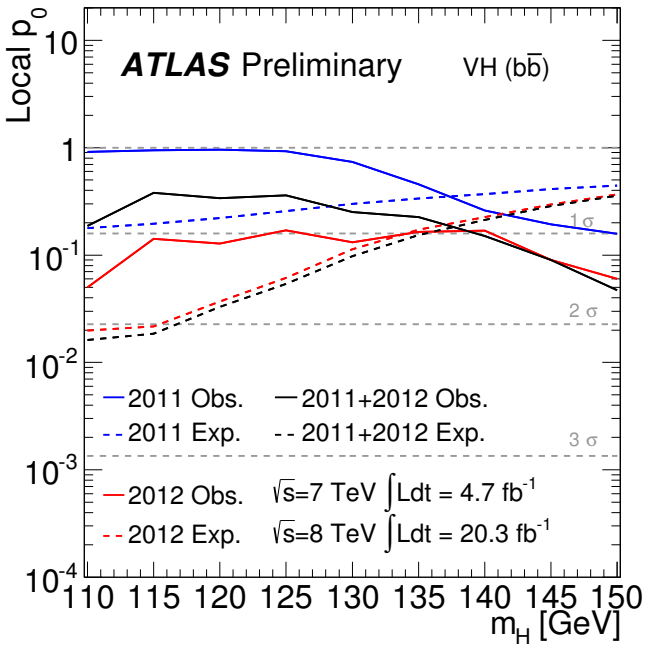

Figure 9.16.: The observed local p_0 as a function of the Higgs boson mass. The dashed curves shows the expected local p_0 under the hypothesis of a SM Higgs boson signal at the mass indicated on the x axis. The results are shown separately for the 7 TeV dataset, in blue, the 8 TeV one, in red, and their combination, in black.

Fig. 9.17 shows the results for the 95% CL exclusion limits on $\sigma/\sigma_{\mathrm{SM}}$ in the mass range 100−150 GeV. The observed (expected) CL_S limit on the $\sigma/\sigma_{\mathrm{SM}}$ is 2.0 (3.3), 1.9 (1.3) and 1.4 (1.2) times the SM expectation at $m_H = 125$ GeV for the $\sqrt{s} = 7$ TeV, $\sqrt{s} = 8$ TeV datasets and their combination respectively.

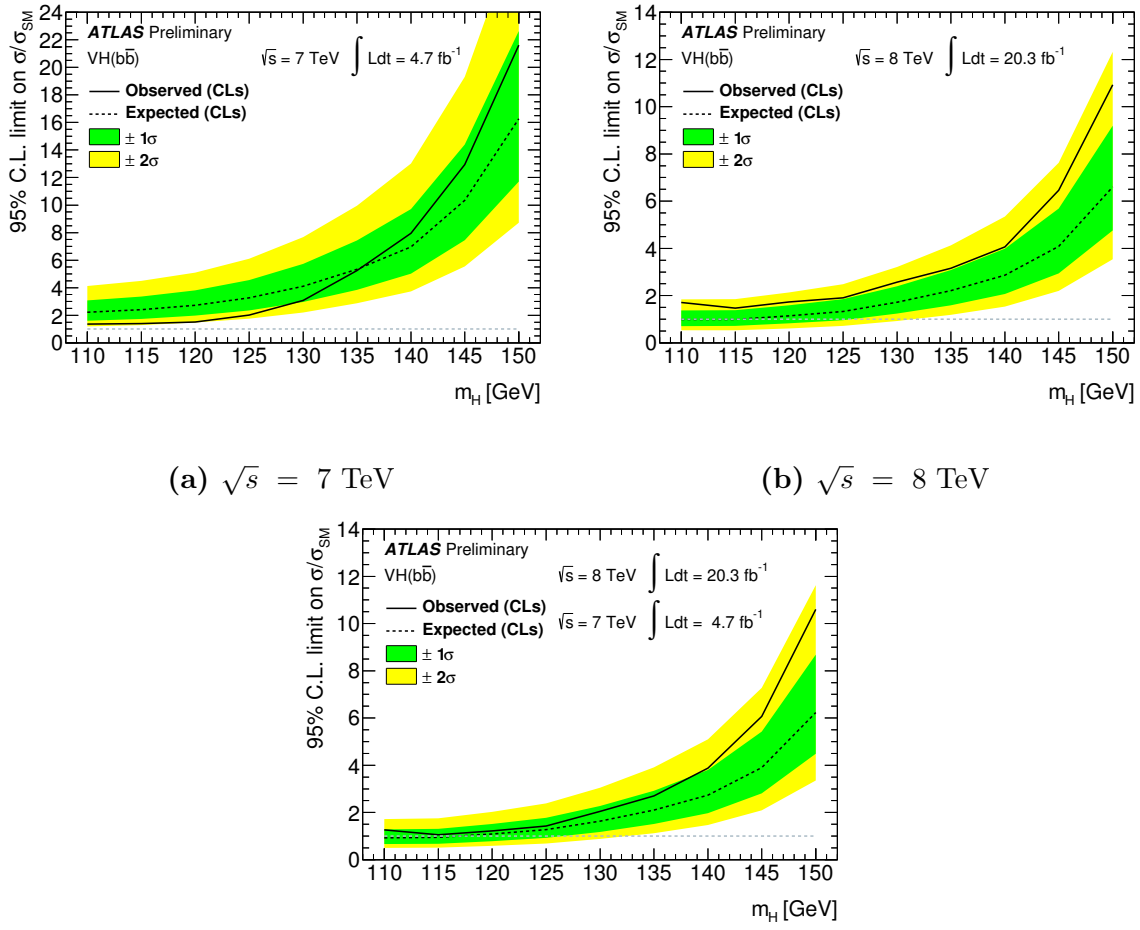

(a) $\sqrt{s} = 7$ TeV **(b)** $\sqrt{s} = 8$ TeV

(c) combination

Figure 9.17.: Expected (dashed) and observed (solid) 95% C.L. upper limits on the normalised signal strength as a function of m_H for all channels and data taking periods combined for the 7 TeV and 8 TeV and the combination.

There is little sensitivity to a possible excess in the 7 TeV dataset, where the data are undershooting the Monte Carlo prediction. This yields to a negative $\hat{\mu}$ value, consistent with the background only expectation within 2σ, compatibly with what already observed in the previous version of the analysis, discussed in chapt. 8. In the 8 TeV dataset, a slight excess is observed, consistent with both background and signal hypotheses.

The combined fitted signal strength parameter value is $\hat{\mu} = 0.2^{+0.7}_{-0.6}$ for $m_H = 125$ GeV. The fitted $\hat{\mu}$ values are shown in fig. 9.18 for the 7 and 8 TeV datasets separately, and for their combination, as well as for the three channels separately and combined. These results come from different fits, performed as follows:

- considering six parameters of interest, one for each channel and dataset,
- considering three parameters of interest, one for each channel, for the two datasets combined,
- considering two parameter of interest, one per dataset, combining the channels,
- considering a single parameter of interest, for the combination of channels and datasets.

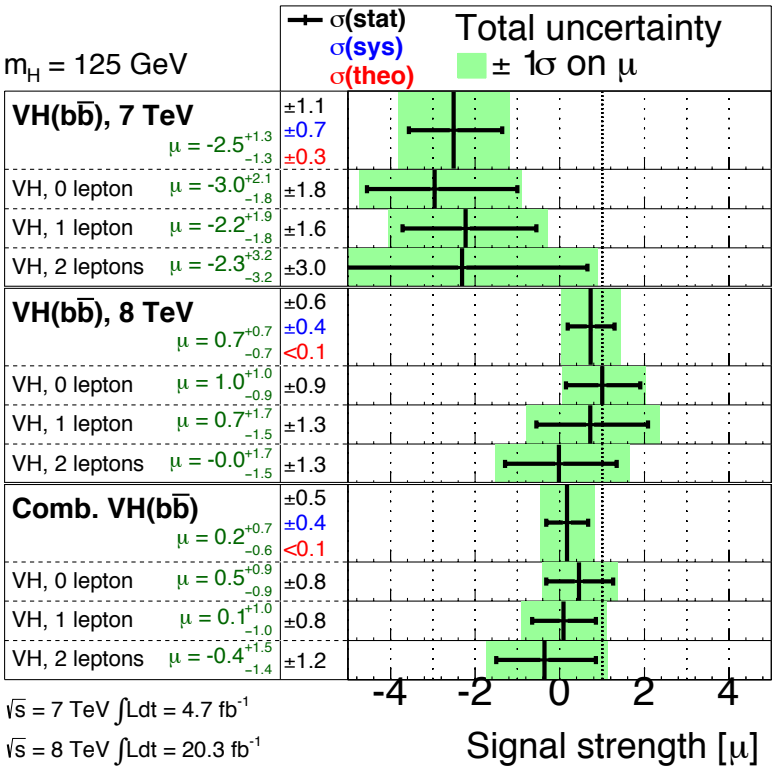

Figure 9.18.: The fitted $\hat{\mu}$ values for the hypothesis of a Standard Model Higgs boson with 125 GeV mass, for the 7 and 8 TeV datasets and their combination. The result of a fit to the full dataset is shown, performed with six parameters of interest, one for each channel in the two separate 7 and 8 TeV datasets. The result of the fit to the combined dataset using two parameters of interest, one per centre of mass energy is also shown. Lastly, the result of the fit to the combined dataset using three parameters of interest, one per lepton channel is quoted.

To visualise the statistical significance of a possible excess, fig. 9.19 shows the $m_{b\bar{b}}$ distribution of the VZ and VH signals from all channels and categories combined, with each individual contribution weighted by the expected significance of each category. The plot shows only the two signals, after subtracting the contributions from the backgrounds, normalised according to the result of the profile likelihood fit. The post-fit uncertainty coming from both statistics and systematics is also shown in the plot.

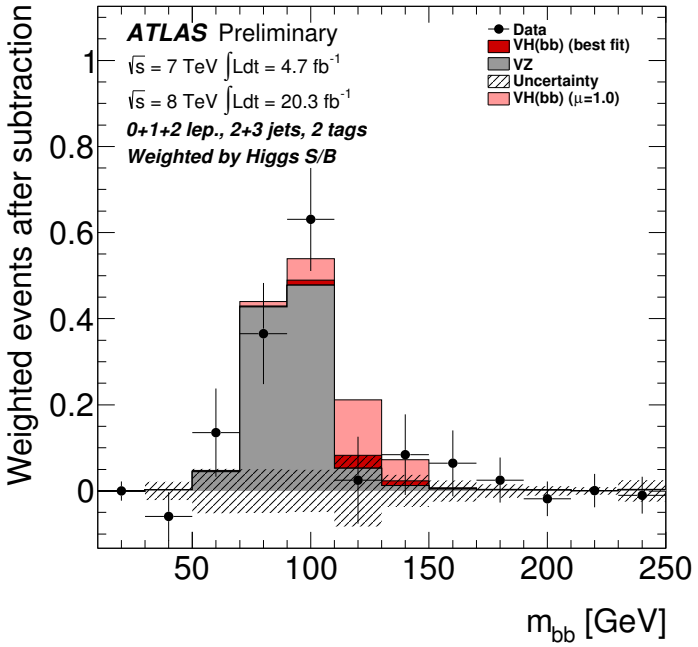

Figure 9.19.: The $m_{b\bar{b}}$ distribution in data after the subtraction of all backgrounds except for the diboson processes and the associated WH and ZH productions of a SM Higgs boson with $m_H = 125$ GeV. In the distribution, the contributions from all channels and centre of mass energies are summed, weighted by their respective values of signal-over-background ratio. The backgrounds are normalised according to the results of the profile likelihood fit. The Higgs boson signal contribution is shown both with its fitted signal strength (in red) and its expected one in the hypothesis of a SM Higgs boson with $m_H = 125$ GeV (in pink). The size of the combined statistical and the post fit systematic uncertainty is indicated by the hatched band.

Chapter 10.

Discussion of the results

The ATLAS experiment has performed searches in most of the channels mentioned in sec. 2.4 [122–137]. In July 2012, the combination of the results from various channels, mainly driven by $H \to Z^{(*)}Z \to 4\ell$, $H \to \gamma\gamma$ and $H \to WW^{(*)} \to \ell\nu\ell\nu$, led to the observation of a new particle of $\sim$125 GeV mass [29]. The observation was confirmed at the same time by the CMS collaboration [30], and is probably the most important result of the last decade of physics studies at colliders. This is an encouraging result, though not final yet, and many questions on the nature of this observed particle are still to be answered, starting from its coupling to fermions.

With the dataset recorded during the LHC Run 1, detailed in sec. 3.1, studies aimed at characterising the newly discovered particle in terms of mass, spin and couplings, have been performed by both collaborations. In the following, the ATLAS results [3, 4] on the characterisation of the observed particle will be presented and the $H \to b\bar{b}$ searches performed by ATLAS, the TeVatron experiments and CMS will be discussed, to shed light on the nature of the observed particle.

10.1. ATLAS results on the search for a SM Higgs boson

Firstly, an overview of the ATLAS results in the characterisation of the observed resonance will be given.

10.1.1. Mass and coupling characterisation

The nature of the observed particle has been investigated in terms of mass, production strengths and couplings, using the bosonic decay modes: $H \to \gamma\gamma$, $H \to Z^{(*)}Z \to 4\ell$ and $H \to WW^{(*)} \to \ell\nu\ell\nu$. The results are obtained with the full Run 1 dataset, consisting of $\sim$4.7 fb^{-1} collected at $\sqrt{s}$ = 7 TeV and $\sim$20.7 fb^{-1} at $\sqrt{s}$ = 8 TeV.

The mass measurement is performed only in the $H \to \gamma\gamma$ and $H \to Z^{(*)}Z \to 4\ell$ channels, being the ones with the best mass resolution. The analysis uses as inputs the results from the two separate analyses [122, 126] and combines them via a profile likelihood ratio defined as a function of the mass m_H. More details on the statistical procedure used can be found in chapt. 4. The signal strengths $\mu_{4\ell}$ and $\mu_{\gamma\gamma}$ are left free to float in the fit as independent parameters, to account for possible different deviations from the SM of the two decay modes. The measured mass of the observed resonance is $m_H = 125.5 \pm 0.2(\text{stat})^{+0.5}_{-0.6}(\text{sys})$ GeV. The overall signal strength of the excess is evaluated for the measured value of m_H=125.5 GeV, and is obtained from all the three channels. Its value is $\mu = 1.33 \pm 0.14(\text{stat}) \pm 0.15(\text{sys})$. The separate signal strengths for each channel and their categories are summarised in fig. 10.1. The CMS collaboration reports a mass measurement for the new particle of $125.7 \pm 0.3(\text{stat}) \pm 0.3(\text{sys})$ GeV [138]. For this measured mass value, the corresponding best fit value quoted by CMS is $\hat{\mu} = 0.80 \pm 0.14$.

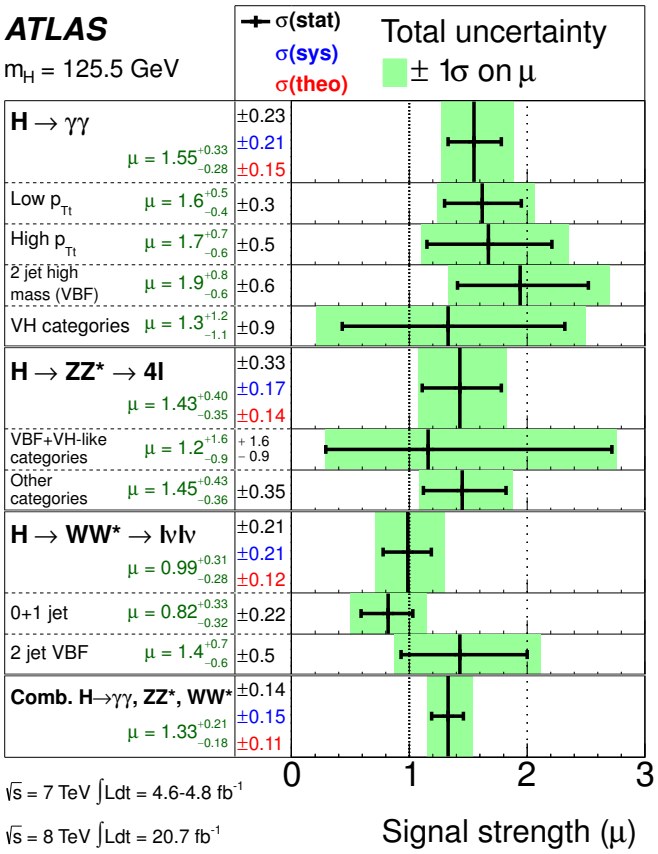

Figure 10.1.: Measured production strengths for a Higgs boson of mass $m_H = 125.5$ GeV, normalised to the SM expectations, for diboson final states and their combination [4]. The results are also given for the main categories of each analysis. The best-fit values are shown by the solid vertical lines, with the total $\pm 1\sigma$ uncertainty indicated by the shaded band, and the statistical uncertainty by the superimposed horizontal error bars. The numbers in the second column specify the contributions of the symmetrised statistical uncertainty (first), the total experimental and theoretical systematic uncertainty (second), and the theory uncertainty (third) on the signal cross section separated from the other uncertainties. For the individual categories only the statistical uncertainty is reported.

The categorisation of the different analyses is aimed at discriminating among the various production modes. This allows to evaluate the overall ratio between fermionic-type and bosonic-type productions:

$$\frac{\mu_{\mathrm{VBF}+VH}}{\mu_{gg\mathrm{F}+t\bar{t}H}} = 1.4^{+0.4}_{-0.3}(\mathrm{stat})^{+0.6}_{-0.4}(\mathrm{sys}) \ . \tag{10.1}$$

This result corresponds to a 3.3σ evidence of the VBF and VH production modes, and is illustrated, compared to the expected SM result, in fig. 10.2.

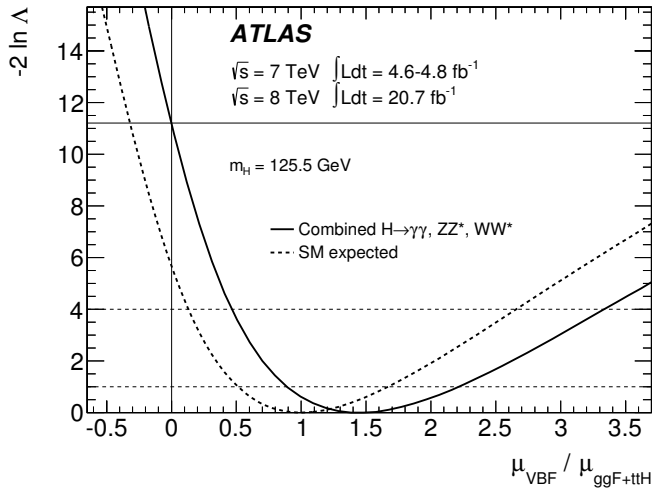

Figure 10.2.: Likelihood curve for the ratio $\mu_{\mathrm{VBF}+VH}/\mu_{gg\mathrm{F}+t\bar{t}H}$ for the combination of the $H \to \gamma\gamma$, $H \to Z^{(*)}Z \to 4\ell$ and $H \to WW^{(*)} \to \ell\nu\ell\nu$ channels and a Higgs boson mass $m_H = 125.5$ GeV [4]. The dashed curve shows the SM expectation, and the horizontal dashed lines indicate the 68% and 95% confidence level (CL).

To determine the couplings, the following assumptions have been taken into account:

- the observed signal comes from a single resonance;
- the following approximation is valid:

$$\sigma \cdot BR(i \to H \to f) = \frac{\sigma_i \cdot \Gamma_f}{\Gamma_H} \ , \tag{10.2}$$

  where σ_i is the production cross section for the mode i, Γ_f the partial decay width in the state f, and Γ_H the total Higgs decay width;
- the observed particle is a scalar boson with even parity.

The coupling scale factor κ_j is then defined such that the following relation holds:

$$\frac{\sigma \cdot BR(i \to H \to f)}{\sigma_{\mathrm{SM}}(i \to H) \cdot BR_{\mathrm{SM}}(H \to f)} = \frac{\kappa_i^2 \kappa_f^2}{\kappa_H^2} \ . \tag{10.3}$$

A profile likelihood fit is performed with different parameters of interest (POIs). The POI can be either κ_f or κ_V, or their ratio λ_{fV}. The ratio between the coupling to the W and Z bosons, λ_{WZ}, is also studied. This results in a 5σ observation of the coupling to fermions, driven by the top loop in the ggF production mode. It also sets a constraint at the 10% level on the coupling to vector bosons, and a value of λ_{WZ} consistent with the SM expectations. Furthermore, no anomalous coupling in the $H \to \gamma\gamma$ and $gg \to H$ modes is found.

10.1.2. Spin and parity determination of the newly discovered particle

A combination of the spin analyses with the individual bosonic channels is performed [123, 126, 131]. The aim is to confirm the hypothesis of spin-parity 0^+ while testing against the alternatives 0^-, $1^\pm$ and 2^+, using the angular variables of the decay products. The $J^P = 2^+$ hypothesis is tested for different fractions of the possible ggF and $q\bar{q}$ annihilation production modes, using the hypothesis of a graviton-like particle.

Not all the channels are used to test the various hypotheses, and a summary of the employed ones for the tested spin and parity values can be found in table 10.1. Each decay mode is analysed only taking into account events produced via gluon fusion, and the full Run 1 dat set is used to extract the result.

The results are evaluated using the likelihood:

$$q = \ln \frac{\mathcal{L}_0(\hat{\hat{\theta}}_0)}{\mathcal{L}_2(\hat{\hat{\theta}}_2)} \ , \tag{10.4}$$

and the CL_S confidence interval defined as:

$$1 - CL_S(2^+) = 1 - \frac{p(2^+)}{1 - p(0^+)} \ . \tag{10.5}$$

Exclusion limits at 95% confidence level (CL) are set on the alternative hypotheses. The results are summarised in table 10.1. This analysis demonstrates that the preferred spin

value for the observed particle is 0, with even parity, consistent with the SM Higgs boson hypothesis.

Alternative hypothesis	Channels analysed	CL of exclusion
0^-	$H \to Z^{(*)}Z \to 4\ell$	97.8%
1^+	$H \to Z^{(*)}Z \to 4\ell$, $H \to WW^{(*)} \to \ell\nu\ell\nu$	99.97%
1^-	$H \to Z^{(*)}Z \to 4\ell$, $H \to WW^{(*)} \to \ell\nu\ell\nu$	99.7%
2^+	$H \to Z^{(*)}Z \to 4\ell$, $H \to WW^{(*)} \to \ell\nu\ell\nu$, $H \to \gamma\gamma$	$> 99.9\%$

Table 10.1.: Exclusion limits at 95% CL for the four J^P hypotheses tested against the SM Higgs boson 0^+ spin-parity.

10.1.3. H $\to \tau^+\tau^-$ evidence

The search for $H \to \tau^+\tau^-$ is of great importance, because it demonstrates the coupling of the Higgs boson to fermions. The ATLAS analysis [6] performed on 20.3 fb^{-1} at $\sqrt{s} = 8$ TeV provides a result based on all the possible final states, with both hadronic and leptonic τ decays. Three separate channels are therefore considered: $\tau_{\text{lep}}\tau_{\text{lep}}$, $\tau_{\text{lep}}\tau_{\text{had}}$ and $\tau_{\text{had}}\tau_{\text{had}}$, with different background compositions. This analysis is further subdivided into two categories, aimed at discriminating VBF-produced events from ggF and VH-produced ones. The VH events are analysed only in the case of hadronically decaying vector bosons. The large backgrounds to this channel, often of strong nature, require the use of a boosted decision tree (BDT) to better discriminate the signal.

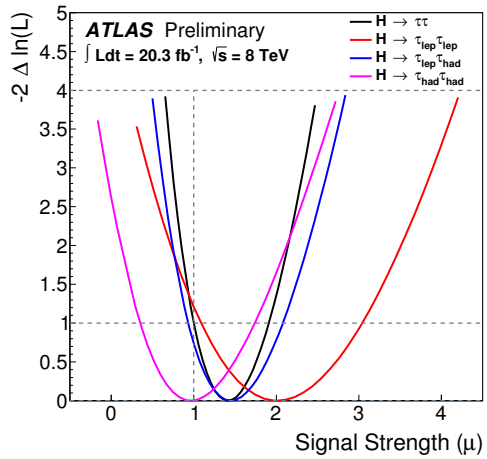

Figure 10.3.: The likelihood dependence on μ is reported, with the deviation from the maximum likelihood, $-2\Delta\ln(\mathcal{L})$ on the y axis [6].

A BDT is defined and trained for each channel and category, and is generally based on kinematic variables and event shapes. The final BDT score is then used as discriminant variable for the statistical analysis. Given the large backgrounds, several control regions are defined to compare data and simulation of a particular process, far from the range where the signal is expected. An excess of events with high BDT score is found and the observed (expected) significance of this excess is 4.1σ (3.2σ), corresponding to a Higgs boson mass of 125 GeV. The signal strength associated to such mass value is $1.4^{+0.5}_{-0.4}$, and is detailed in fig. 10.3 and 10.4. This result is the first observation of the coupling of the Higgs-like particles to fermions, in particular to the third generation leptons.

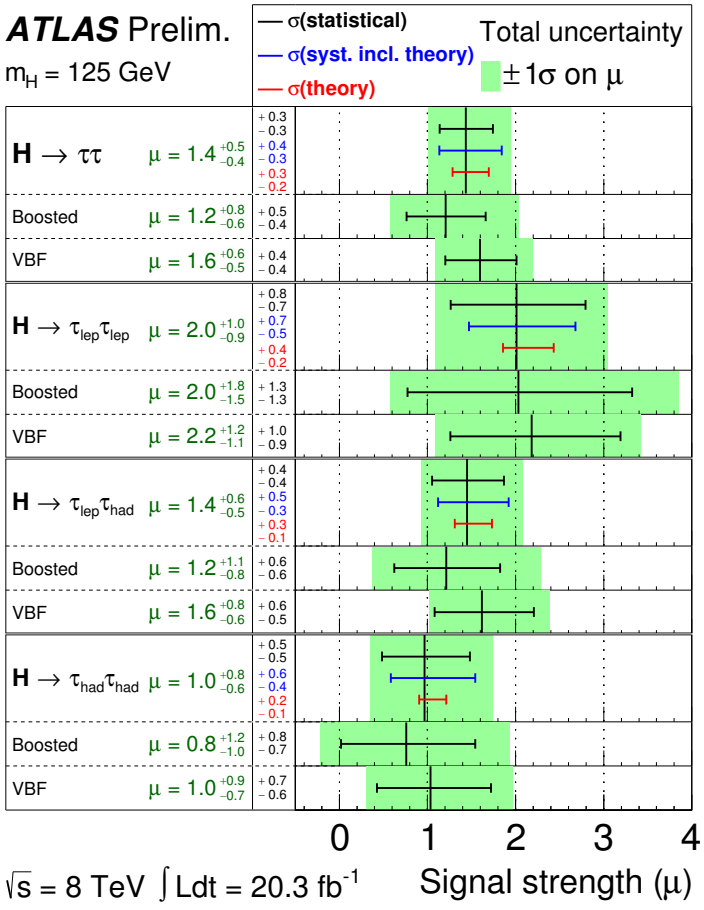

Figure 10.4.: The best-fit value for the signal strength μ in the individual $H \to \tau^+\tau^-$ channels and the combination [6]. The green band indicates the total 1σ uncertainty on the measurement.

10.2. $H \to b\bar{b}$ search status

In the following paragraphs, the $t\bar{t}H(H \to b\bar{b})$ searches carried out by ATLAS will be described, followed by $H \to b\bar{b}$ search results from the TeVatron experiment result combination, and the CMS results.

10.2.1. Search for $t\bar{t}H(H \to b\bar{b})$ with the ATLAS experiment

The results of the search for $t\bar{t}H(H \to b\bar{b})$ by ATLAS [137] are obtained analysing data for an integrated luminosity of 4.7 fb^{-1} collected at a centre of mass energy of 7 TeV. A mass range of 110 GeV $< m_H <$ 140 GeV has been analysed, looking for deviations from the Standard Model background predictions.

The $t\bar{t}H(H \to b\bar{b})$ process can occur with three different topologies:

- fully leptonic, where both the W bosons from the top quark decay to $\ell\nu$;
- semi-leptonic, where only one W boson decays to leptons, and the other to a quark pair;
- fully hadronic, where both W bosons decay to quarks.

In this analysis, only the semi-leptonic mode has been taken into account, providing a clean enough signature for triggering, and a reasonably large branching ratio.

Typical events present a large jet multiplicity in the final state, namely six or more jets, of which four are originating from b quarks. There is typically an isolated high-p_{T} lepton (either electron or muon) and large missing transverse energy. The largest background is $t\bar{t}$+jets production, with $t\bar{t}b\bar{b}$ being an irreducible component of it. To enhance the sensitivity and the signal to background ratio, the analysis has been split into categories, based on the jet and b-jet multiplicities in the events. A kinematic fit is used to discriminate the $t\bar{t}H(H \to b\bar{b})$ process from the $t\bar{t}b\bar{b}$ background, and correctly assign $b\bar{b}$ pairs to the parent particle. It obtains a better resolution of the invariant mass of the pair of b-jets, identified as coming from the Higgs decay ($m_{b\bar{b}}$). The $m_{b\bar{b}}$ variable is used as a discriminant in the signal regions, together with the $H_{\mathrm{T}}^{\mathrm{had}}$ variable, used in the regions with lower jet and b-jet multiplicities. The $H_{\mathrm{T}}^{\mathrm{had}}$ variable is defined as the scalar sum of the transverse momenta of all the jets identified in the event.

A profile likelihood fit is used to determine the final sensitivity of the search. Limits are set on $\sigma/\sigma_{\mathrm{SM}}$ and the cross section times branching ratio of the $t\bar{t}H(H \to b\bar{b})$ production: $\sigma_{t\bar{t}H} \times BR(H \to b\bar{b})$, and are shown in fig. 10.5. For a Higgs boson of 125 GeV mass, the observed (expected) 95% CL limit on $\sigma/\sigma_{\mathrm{SM}}$ is 13.1 (10.5) times the SM.

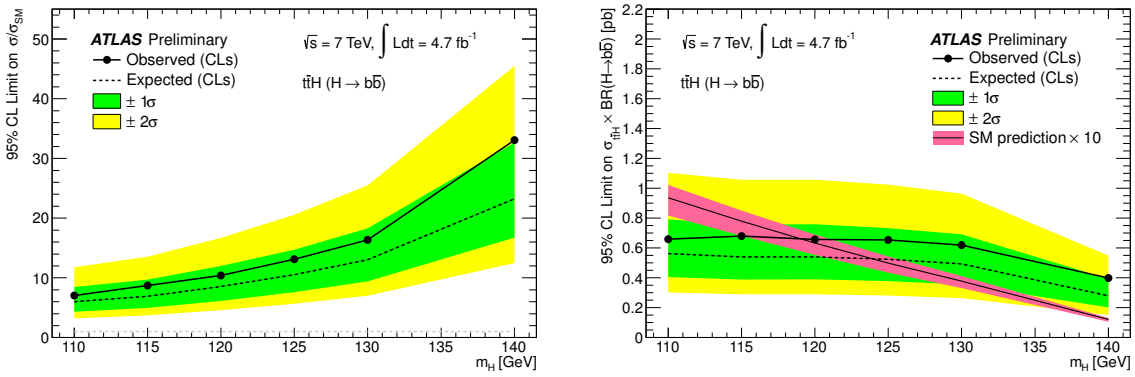

(a) **(b)**

Figure 10.5.: Observed and expected 95% CL upper limits on $\sigma/\sigma_{\mathrm{SM}}$ (10.5a) and $\sigma_{t\bar{t}H} \times BR(H \to b\bar{b})$ (10.5b) [137]. For the latter, the SM prediction as a function of m_H is also shown, scaled up by a factor of 10 for better readability.

10.2.2. H → bb̄ searches at the TeVatron

The TeVatron experiments, CDF and DØ, collected up to 9.7 fb^{-1} of data at a centre of mass energy of 1.96 TeV. These data were analysed looking for a SM Higgs boson, and the driving channel of the search was $VH(b\bar{b})$. At the TeVatron, vector boson associated production was favoured over gluon fusion, as the collisions took place between proton and antiproton beams.

The combination of CDF and DØ results is performed in the mass range $100 - 150$ GeV, for the three leptonic decay modes of the vector boson: $ZH \to \ell^+\ell^- b\bar{b}$, $WH \to \ell\nu b\bar{b}$ and $ZH \to \nu\bar{\nu}b\bar{b}$ [5]. The analysis is performed using multivariate techniques (MVA). They are optimised for each sub-channel and each Higgs mass point investigated. It is important to stress the performance of the two separate experiment b-tagging algorithms employed, with a 80% efficiency and 10% mis-identification rate in the case of DØ, and a 70% efficiency and 5% mis-identification rate for the case of CDF.

The background estimates and the effectiveness of the analysis are validated with the extraction of the diboson $VZ(Z \to b\bar{b})$ signal, observed in agreement with the SM

predictions, and shown in fig. 10.6. The MVA discriminant is trained for the diboson signal instead of the Higgs in such case. The statistical analysis is performed using two alternative methods, to cross check the results:

- the Bayesian method, generally used by the CDF experiment;
- the modified frequentist method, employed by DØ and described in chapt. 4.

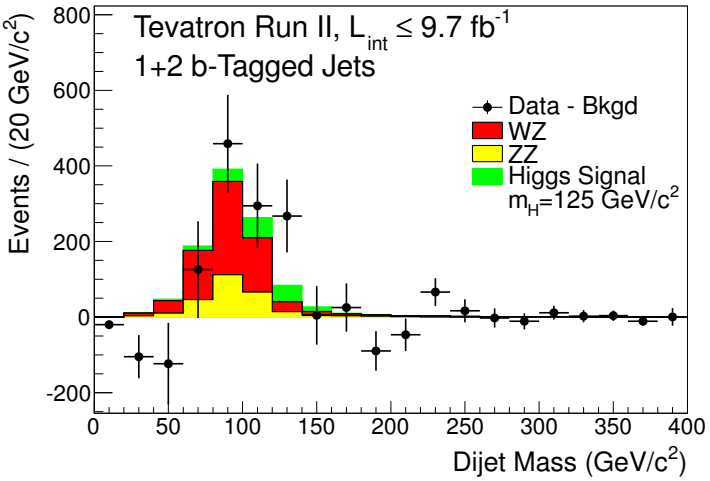

Figure 10.6.: Background-subtracted distribution of the reconstructed dijet mass, summed over all the channels [5]. The VZ signal and the background contributions are fit to the data, and the fitted background is subtracted. The expected SM Higgs, with a 125 GeV mass is also shown in green.

Upper limits are set on $\sigma/\sigma_{\mathrm{SM}}$, as well as on the product of cross section and branching ratio, $(\sigma_{WH} + \sigma_{ZH}) \times BR(H \to b\bar{b})$, and the results are shown in fig. 10.7. These plots are obtained using the Bayesian method, but a cross check with a modified frequentist method gives analogous results. The combination of CDF and DØ measurements provides an exclusion at 95% CL of the mass range 100 GeV $< m_H <$ 106 GeV. This limit is slightly lower than what the previous exclusion up to $m_H = 114.4$ GeV, obtained in the LEP2 searches for $ZH(b\bar{b})$ [139]. The best fit value of $(\sigma_{WH} + \sigma_{ZH}) \times BR(H \to b\bar{b})$ is $0.23^{+0.09}_{-0.08}$.

An excess is observed through the whole range, with a global significance in the interval 115 GeV $< m_H <$ 150 GeV of 3.1σ, and a local significance for $m_H = 125$ GeV of 2.8σ. This number is obtained considering the look elsewhere effect, taking into account the possibility of a background fluctuation in the whole scanned mass range influencing the p_0 value. Fig. 10.8 shows the values of the local p_0 and significance as a function of the predicted Higgs mass.

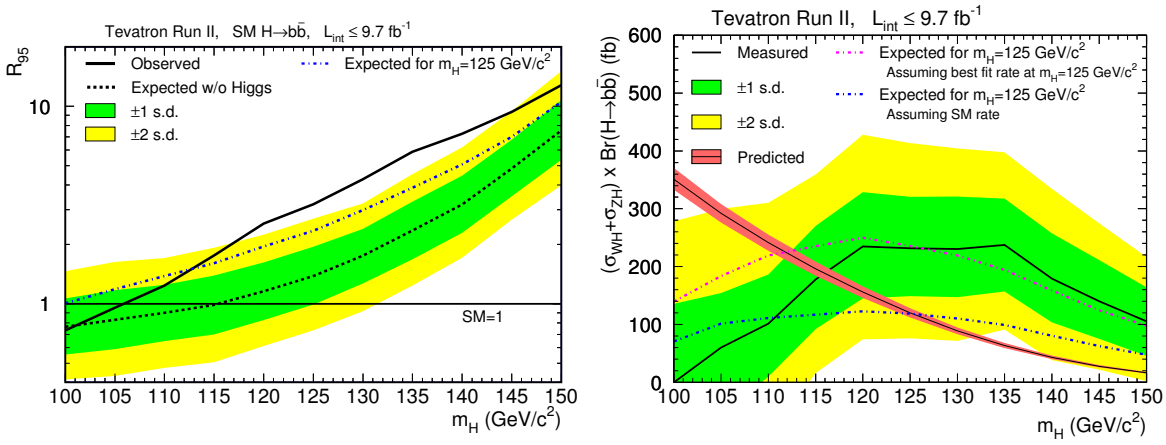

(a) **(b)**

Figure 10.7.: In fig. 10.7a: observed (solid) and expected (dashed) 95% Bayesian credibility level upper limits on $\sigma/\sigma_{\rm SM}$ (denoted as R_{95}) as a function of the Higgs boson mass [5]. The blue dot-dashed line shows the median expected limit of the hypothesis of a SM Higgs boson of $m_H = 125$ GeV. Fig. 10.7b shows the best fit value of $(\sigma_{WH} + \sigma_{ZH}) \times BR(H \to b\bar{b})$ as a function of m_H. The SM prediction is shown as a smooth, falling curve with a narrow band indicating the theoretical uncertainty. The expected cross section fit values, assuming a SM Higgs boson with $m_H = 125$ GeV, are shown with dot-dashed lines for the cases of the expected SM rate (blue) and the best fitted rate from data (magenta).

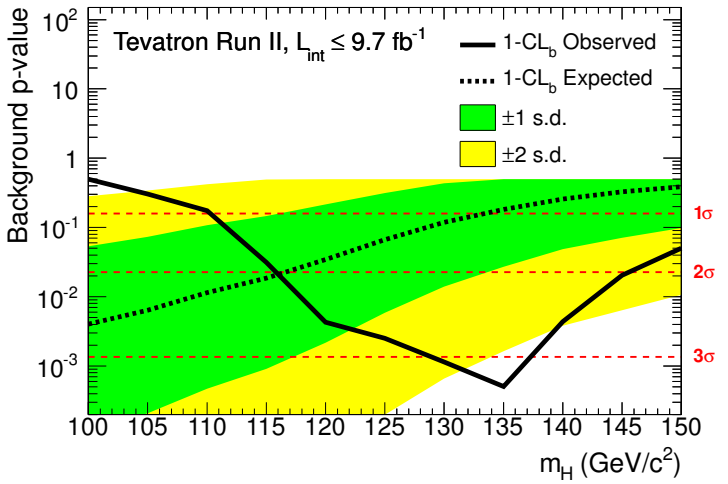

Figure 10.8.: The p-value as a function of m_H for the background-only hypothesis [5]. The expected values assuming for the presence of a SM signal are also shown.

10.2.3. CMS searches for H → bb̄

The CMS experiment has performed searches in three possible production modes of the Higgs boson, with $b\bar{b}$ final states. The results from the analyses with the $t\bar{t}H(H \to b\bar{b})$, $VH(b\bar{b})$ and VBF $H \to b\bar{b}$ channels are presented in the following paragraphs.

tt̄H analysis with bb̄ and $\tau^+\tau^-$ final states

A search for $t\bar{t}H$ produced events in three decay modes has been performed by the CMS experiment [140] on the 19.5 fb^{-1} dataset collected at $\sqrt{s} = 8$ TeV. The investigated channels are:

- lepton+jet, considering semileptonic $t\bar{t}$ decays and $H \to b\bar{b}$ final states;
- di-lepton, considering di-leptonic $t\bar{t}$ decays and $H \to b\bar{b}$ final states;
- tau, considering semileptonic $t\bar{t}$ decays and $\tau^+\tau^-$ final states.

The main background to this search arises from $t\bar{t}$+jet events. A boosted decision tree (BDT) based analysis is performed to better discriminate between signal and background, and the BDT score is used as input to the statistical analysis. This search is combined with a previous CMS result on $t\bar{t}H(H \to b\bar{b})$ events performed on the $\sqrt{s} = 7$ TeV dataset.

The b-tagging algorithm employed, CVS [141], guarantees a 70% efficiency on b identification, 20% on c, and 2% mistag rate on light-initiated jets. The analysis is subdivided in categories, based on the number of jets and b-tagged-jets in the final state, to enhance the sensitivity. The BDT training is performed category-by-category. In the case of final states with more that five jets and at least four b-tagged ones, a χ^2 test is used to identify the correct pair of b-jets as the Higgs decay products, using the information on the invariant mass.

Given the low sensitivity of the channel, and the absence of a clear excess over the background, 95% CL upper limits on $\sigma/\sigma_{\rm SM}$ are set, using the modified frequentist approach described in chapt. 4. The result for a Higgs boson of 125 GeV mass is an observed (expected) limit of 5.2 (4.1) times the SM background-only hypothesis. The limit results are shown in fig. 10.9 for the full mass range of the combined analysis, and for the significant $m_H = 125$ GeV value for each separate channel. The best fit value for

a Higgs mass of 125 GeV is also estimated, resulting in $\hat{\mu} = 0.85^{+2.47}_{-2.41}$ for the combination of all channels. The value is shown for each separate channel in fig. 10.10.

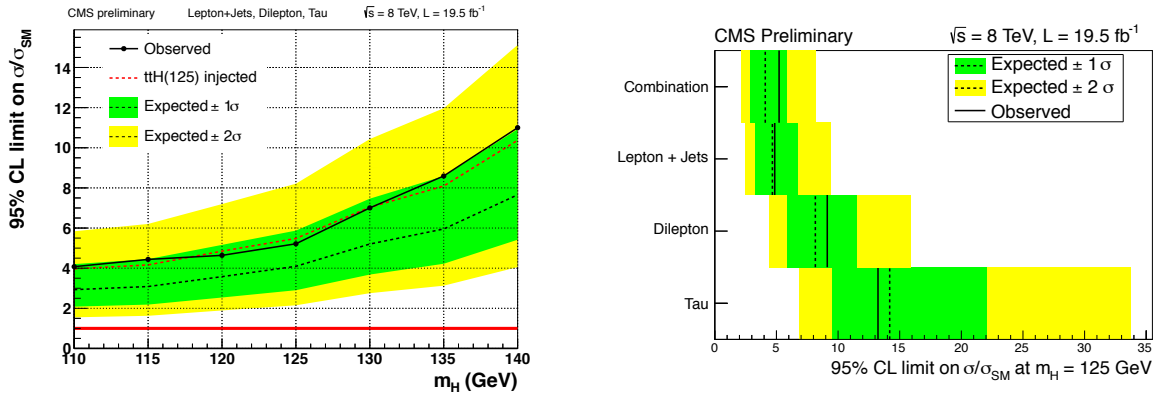

(a) (b)

Figure 10.9.: In fig. 10.9a, the observed and expected 95% CL upper limits on the signal strength parameter are shown for the combined channels, as a function of m_H [140]. In fig. 10.9b, the limits are shown only for the hypothesised Higgs mass of 125 GeV, and separately for each channel contributing to the $t\bar{t}H$ analysis.

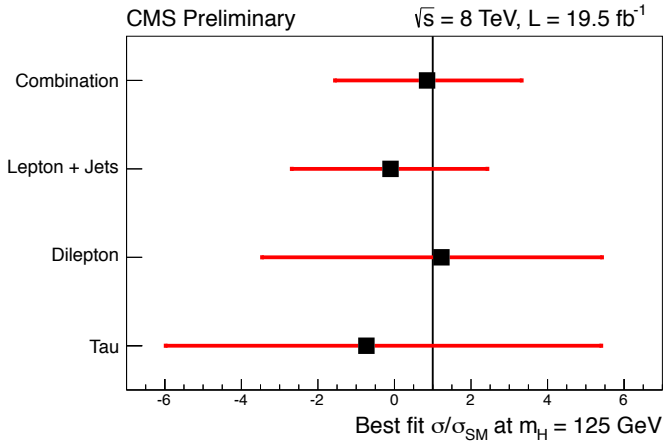

Figure 10.10.: The best-fit value for the signal strength, $\hat{\mu}$, for the separate channels of the $t\bar{t}H$ analysis, and their combination, in the hypothesis of a SM Higgs with a mass of 125 GeV [140].

VH($b\bar{b}$) searches

The CMS $VH(b\bar{b})$ search [142] is performed on four sub-channels: $W \to \ell\nu$, $Z \to \ell^+\ell^-$, $Z \to \nu\bar{\nu}$ and $W \to \tau\nu$, where ℓ is intended as e or μ. Only $W \to \tau\nu$ events with the τ

lepton decaying hadronically in the one-prong mode are analysed. The search is performed on the dataset collected at $\sqrt{s} = 7$ TeV and $\sqrt{s} = 8$ TeV, corresponding respectively to integrated luminosities of 5.1 and 18.9 fb^{-1}, on the mass range 110 GeV $< m_H <$ 135 GeV.

The analysis uses a BDT discriminant to obtain the maximum possible signal sensitivity. It is categorised in regions of boost of the VH system, selected based on the transverse momentum of the vector boson, p_{T}^{V}. Only events with $p_{\mathrm{T}}^{V} > 100$ GeV are taken into account in the search. The mass resolution, originally of 10%, is reduced by an additional $15 - 25\%$, depending on the category and channel, thanks to multivariate regression techniques, and a BDT-based recalculation of the true b energy.

The BDT employed for the analysis is trained against the different backgrounds separately for each category, and the procedure is validated looking for the diboson $VZ(Z \to b\bar{b})$ signal. Fourteen BDT distributions are the input to the final profile likelihood fit, to extract either the diboson or the Higgs signal. A 7σ excess is observed in the analysis for the $VZ(Z \to b\bar{b})$ signal, consistent with the SM rate, with a best-fit value for the signal strength $\hat{\mu}_{VZ}$ of $1.19^{+0.28}_{-0.23}$. The invariant mass distribution of the di-b-jet pair is presented in fig. 10.11, showing the clear excess due to $VZ(Z \to b\bar{b})$.

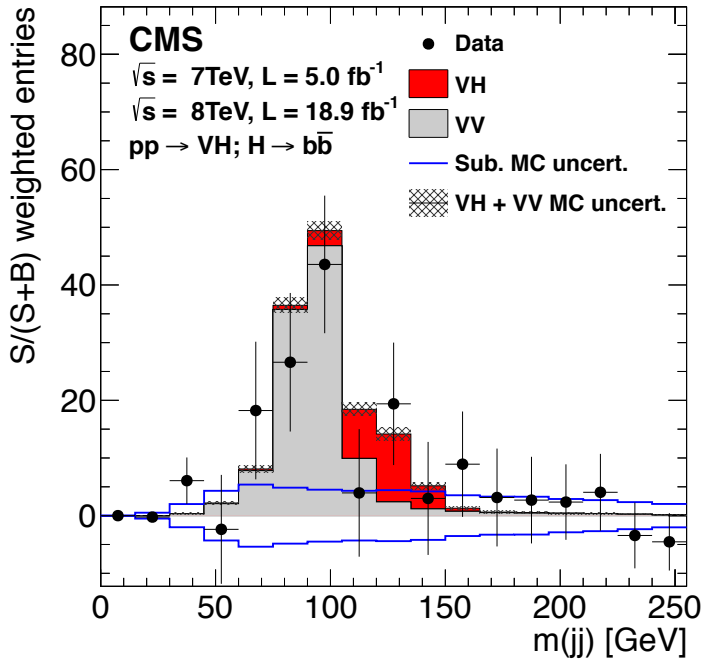

Figure 10.11.: Di-jet invariant mass distribution, showing the data after subtracting all the backgrounds, except the diboson [142]. The entries are weighted according to the $S/(S+B)$ ratio.

95% CL upper limits on $\sigma/\sigma_{\mathrm{SM}}$ are shown in fig. 10.12a, and the observed (expected) value for a 125 GeV SM Higgs boson is 1.89 (0.95). The p_0 value as a function of the Higgs mass is also shown in fig. 10.12b, and the local significance of the excess for $m_H = 125$ GeV is found to be 2.1σ. The observed excess is consistent with the hypothesis of a SM Higgs boson of 125 GeV mass decaying to a b quark pair, with a fitted signal strength of 1.0 ± 0.05.

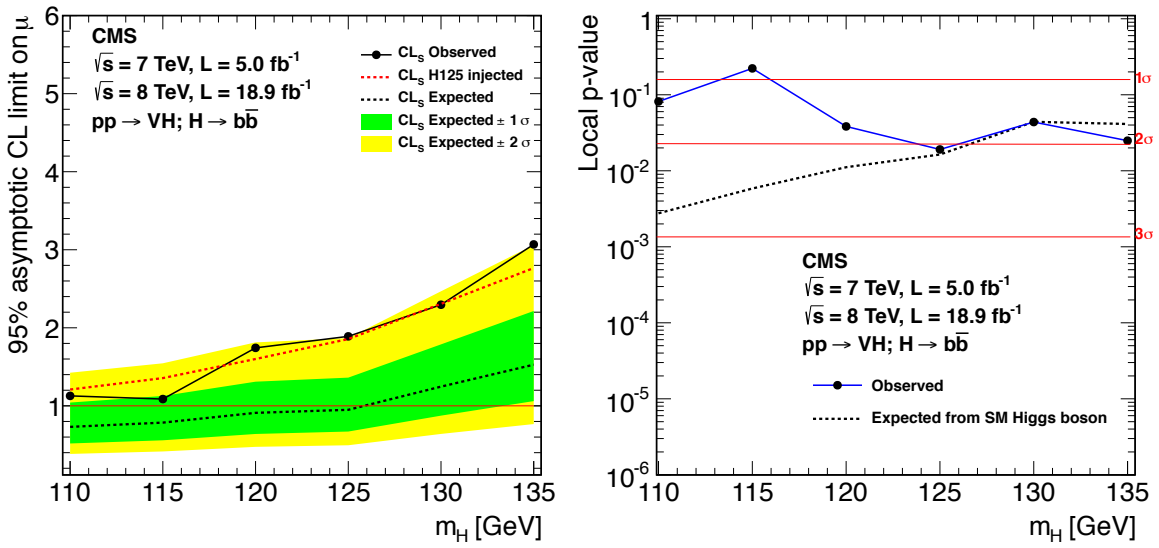

(a) **(b)**

Figure 10.12.: The expected and observed 95% CL upper limits (10.12a) on $\sigma/\sigma_{\mathrm{SM}}$ [142]. The red dashed line represents the expected limit obtained from the sum of expected backgrounds and the SM Higgs boson signal with a mass of 125 GeV. The local p-value and corresponding Gaussian significance for the background-only hypothesis (10.12b), to account for the observed excess of events in the data.

VBF H → bb̄ search

The CMS experiment performed a search for $H \to b\bar{b}$ produced via vector boson fusion [143] on 19 fb^{-1} collected at $\sqrt{s} = 8$ TeV. This search scans the mass range 115 GeV $< m_H <$ 135 GeV, setting 95% CL limits on the $\sigma/\sigma_{\mathrm{SM}}$. The topology of such events present two high-momentum forward jets, well separated in pseudorapidity, from the initial state quarks radiating the vector bosons, and two central b-jets, coming from the Higgs decay. The main backgrounds to the search are: multi-jet production, V+jets, where the vector boson decays hadronically, $t\bar{t}$ events with semileptonic or hadronic decays, and single top production with hadronically decaying W bosons.

To better discriminate between signal and background, a multivariate technique, based on an artificial neural network (ANN) is used. The output is then fitted using the profile likelihood method, and upper limits are set on the process. As a cross check on the background estimate, the VBF production of a Z boson decaying to a $b\bar{b}$ pair is studied, and an excess with a 2.5σ significance is found, consistent with the SM prediction. The 95% CL limit on $\sigma/\sigma_{\mathrm{SM}}$ is shown in fig. 10.13, and its observed (expected) value for $m_H = 125$ GeV is 3.6 (3.0) times the SM background. The limit is strongly affected by the statistical uncertainty on the background, given by the small number of events passing the selection. The best fit value for the signal strength $\hat{\mu}$ is calculated to be 0.7 ± 1.4.

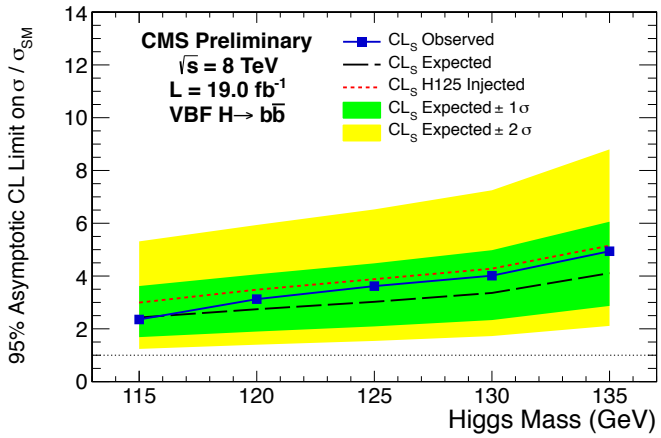

Figure 10.13.: Expected (dashed) and observed (solid blue) 95% confidence level limits on the signal cross section in units of the SM expected cross section, as a function of the Higgs mass [143]. The red curve represents the expected limits with the injection of a SM Higgs boson with mass 125 GeV.

10.3. Discussion of the results

As presented in sec. 10.1, a new particle of ≈ 125 GeV mass has been observed when performing searches for a SM Higgs boson by the ATLAS and CMS collaborations. The evidence for this particle comes from the combination of different production and decay modes, and is detected by the ATLAS experiment in both the $H \to Z^{(*)}Z \to 4\ell$ and $H \to \gamma\gamma$ channels individually. A consistent excess is also observed in the $H \to WW^{(*)} \to \ell\nu\ell\nu$ and, more recently, $H \to \tau^+\tau^-$ decay modes. The 4σ excess in the $H \to \tau^+\tau^-$ mode is a rather crucial result, as it represents the first direct proof that the observed Higgs-like boson does decay to fermions.

Studies performed on the bosonic decay channels indicate the scalar nature of the particle [4]. Using these channels, the ATLAS collaboration extracts a mass value of $125.5 \pm 0.2(\text{stat})^{+0.5}_{-0.6}(\text{sys})$ GeV, and a best fit signal strength value of $1.33 \pm 0.14(\text{stat}) \pm 0.15(\text{sys})$ [3]. The analysis leads also to a 5σ indirect evidence of the coupling of the new particle to fermions, coming from the top loop dominating the gluon fusion mediation. This is only valid, though, under the assumption of a SM Higgs boson, with the couplings described in chapt. 2.

The $H \to b\bar{b}$ channel is crucial for the final determination of the nature of the newly observed particle. In fact, an observation in this channel would directly confirm the coupling to quarks of the third generation. As discussed in sec. 9.2.3 and 10.2.1, none of the $H \to b\bar{b}$ searches have so far reported a 3σ observation of the process consistent with the mass value of 125.5 GeV. The $VH(b\bar{b})$ results from CMS and the TeVatron experiments, quoting an excess of 2.1σ and 2.8σ respectively at the preferred mass value, are pointing towards this evidence, but they do not provide a final answer.

The ATLAS $VH(b\bar{b})$ result shows a very small excess, when analysing the full LHC Run 1 dataset. This is strongly driven by a downward fluctuation in the $\sqrt{s} = 7$ TeV dataset, and the interesting invariant mass distributions where this effect is visible can be found in app. A. This feature has been investigated, and several improvements and optimisations were introduced. These reduced slightly the deficit with respect to the previous version of the analysis [99], but without significant changes to the $\sqrt{s} = 7$ TeV result. The 20.3 fb^{-1} $\sqrt{s} = 8$ TeV dataset, instead, presented an excess in the full mass interval analysed, with a local significance of $\sim 1\sigma$ at 125 GeV. This is more consistent with the CMS and TeVatron combination results, although the excess is smaller.

The main difference between the ATLAS analysis and the other experiment results on the $VH(b\bar{b})$ analysis is the employment of multivariate techniques. The ATLAS collaboration, in fact, has performed an analysis based on kinematic cuts, optimised as a function of $S/\sqrt{B}$, while all the other results rely on the higher discriminant power of BDT or MVA. Another crucial difference with respect to the CMS analysis is in the general approach. The CMS analysis only concentrates on a high-p_{T}^{V} region, where the $S/\sqrt{B}$ has larger values. ATLAS, on the other hand, uses the low-p_{T}^{V} region to extract the normalisations of the main backgrounds, and constrain the main systematics in the profile likelihood fit, taking advantage of the high statistical power of this region. This approach allows to extract the maximal information from data on the main backgrounds, some of which have not been measured yet on the full Run 2 dataset. It is also very effective in controlling the larger systematics, and their effect on the result. The two

different approaches lead to discrepant results. ATLAS is currently investigating the potential of an MVA-based analysis, as well as alternative optimisations.

The other channels, $t\bar{t}H(H \to b\bar{b})$ and VBF $H \to b\bar{b}$, do not reach the required sensitivity, given the large backgrounds in both cases and the low production rate in the $t\bar{t}H(H \to b\bar{b})$ case.

The data from the LHC Run 2 will shed light on the $H \to b\bar{b}$ search and will give an answer on the decay of the new observed particle to fermions. Alternative techniques, such as those investigating the substructure of jets, introduced in sec. 7.1, could be exploited, particularly given the higher centre of mass energy (13 TeV) foreseen for the collisions. Benefitting from the high boost of the Higgs decay products, such techniques, already successfully applied by both ATLAS and CMS on top and heavy resonance searches, will be particularly effective in the high-p_{T}^{V} region, where the $S/\sqrt{B}$ is higher, and the b-jets from the Higgs decay are more collimated.

New techniques will be needed for tagging b-jets in higher luminosity environments during Run 2, where more tracks will be present in the detector. To help in this goal, an additional pixel layer will be installed into the ATLAS detector. It is called insertable B-layer (IBL), and it will be closer to the interaction point It will complement the existing pixel layers, adding an additional tracking point. This will aid to achieve higher impact parameter resolution.

With new technologies and techniques, the ATLAS and CMS experiments will be able to provide an answer on the coupling of the Higgs boson with b-jets during LHC Run 2.

Chapter 11.

Conclusions

This thesis has presented the latest results obtained by the ATLAS experiment in the search for a standard model (SM) Higgs boson in the $VH \to \text{leptons} + b\bar{b}$ channel. The experimental apparatus was introduced and described in detail, as well as the theoretical formulation of a typical statistical analysis applied to Higgs searches in ATLAS.

After describing the theoretical framework, details on the backgrounds to the $VH \to \text{leptons} + b\bar{b}$ process have been given, demonstrating how they can affect the signal, and what strategies can be employed to reduce them.

The main Mote Carlo generators used to model the signal and the various backgrounds have been introduced, together with the definition of the objects forming the interesting event final states. The analysis cuts aimed at optimising $S/\sqrt{B}$, have been presented, followed by a discussion on the background modelling and the relative systematic uncertainties. The experimental uncertainties affecting the analysis were also described, and in particular, the method used to evaluate the modelling systematic uncertainties on the irreducible $Wb\bar{b}$ background was presented in detail.

A feasibility study, performed on the 4.7 fb^{-1} dataset collected at $\sqrt{s} = 7$ TeV, testing the effectiveness of a jet substructure-based analysis on the $WH \to \ell\nu b\bar{b}$ search, has been presented. This technique was found not to improve the results obtained with a standard kinematic cut-based analysis. Jet substructure techniques could be employed after raising the collision centre of mass energy and collecting a larger amount of data, during the LHC Run 2 data taking period.

Then the preliminary results of the $VH(b\bar{b})$ analysis, using up to 13 fb^{-1} of $\sqrt{s} = 8$ TeV data were presented, with a particular stress on the first observation at ATLAS of the $VZ(Z \to b\bar{b})$ production, used a cross check of the reliability of the $VH(b\bar{b})$ fit. The

description of these results is followed by an overview of the most recent results, using the full Run 1 dataset. The model used to fit the data, i.e., to extract the signal strength and the normalisations of the main backgrounds, has been described. The treatment of the systematic uncertainties as nuisance parameters of the fit and their correlations has also been discussed. The fit was tested on the $VZ \to \text{leptons} + b\bar{b}$ signal, showing an excess consistent with the Z boson mass of 4.8σ (5.1σ) observed (expected) significance, at a rate consistent with the SM prediction.

For a SM Higgs boson with a mass of 125 GeV the observed (expected) limit on $\sigma/\sigma_{\text{SM}}$is 1.4 (1.3), and no significant excess is found for a Higgs mass value of 125 GeV. The measured signal strength at $m_H = 125$ GeV is $0.2 \pm 0.5(\text{stat}) \pm 0.4(\text{sys})$. This result has been compared to other $H \to b\bar{b}$ searches performed by CMS and the TeVatron experiments, also taking into account the most up-to-date results from ATLAS on the Higgs search in other channels, showing the evidence for a scalar particle with 125 GeV mass, consistent with the SM Higgs boson. The prospects for future analyses of the process during Run 2 of the LHC have been discussed.

No clear evidence of $H \to b\bar{b}$ has been found yet, therefore this represents one of the key searches at the LHC experiments to be completed in the near future by Run 2.

Appendix A.

VH →leptons+$b\bar{b}$ Run 1 analysis additional mass and p_T^V plots

The $m_{b\bar{b}}$ distributions from the fit to the 7 TeV dataset are shown in fig. A.1-A.9.

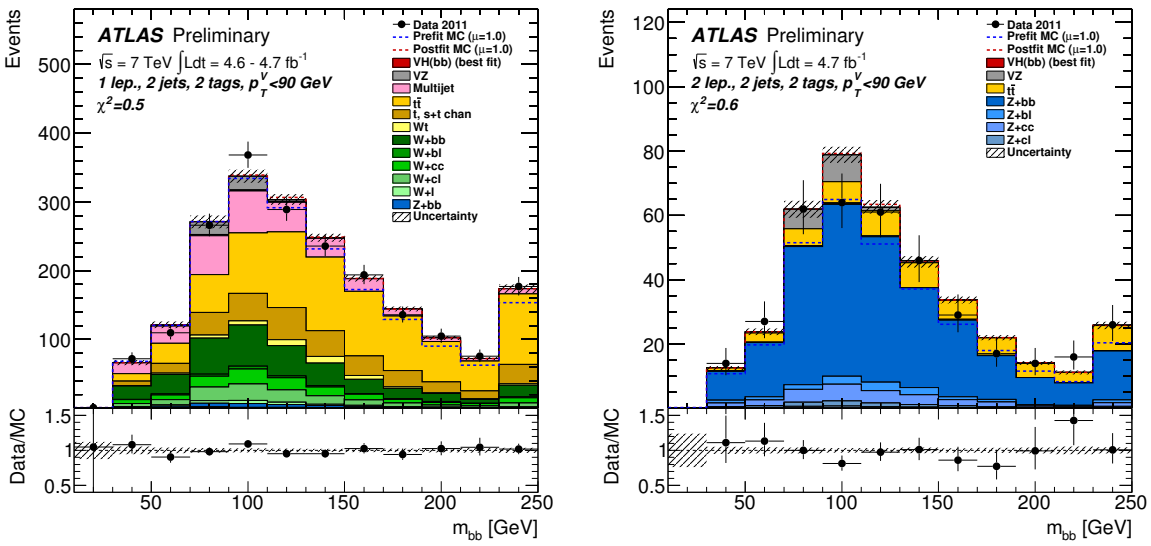

(a) 1-lepton **(b)** 2-lepton

Figure A.1.: Post-fit invariant mass distributions in the $p_{\mathrm{T}}^{V} < 90$ GeV bin of the 2-tag 2-jet region at $\sqrt{s} = 7$ TeV for data and Monte Carlo expectation. The last bin contains the distribution overflow. The hatched black area represents the total error after the profile likelihood fit, the dashed blue line represents the total background distribution input in the fit. The dashed red area represents the total background distribution in the hypothesis of a SM Higgs signal of mass 125 GeV ($\mu = 1$), while the signal is renormalised to its best fit value after the fit. The solid area shows the various background components, with their post-fit normalisation values.

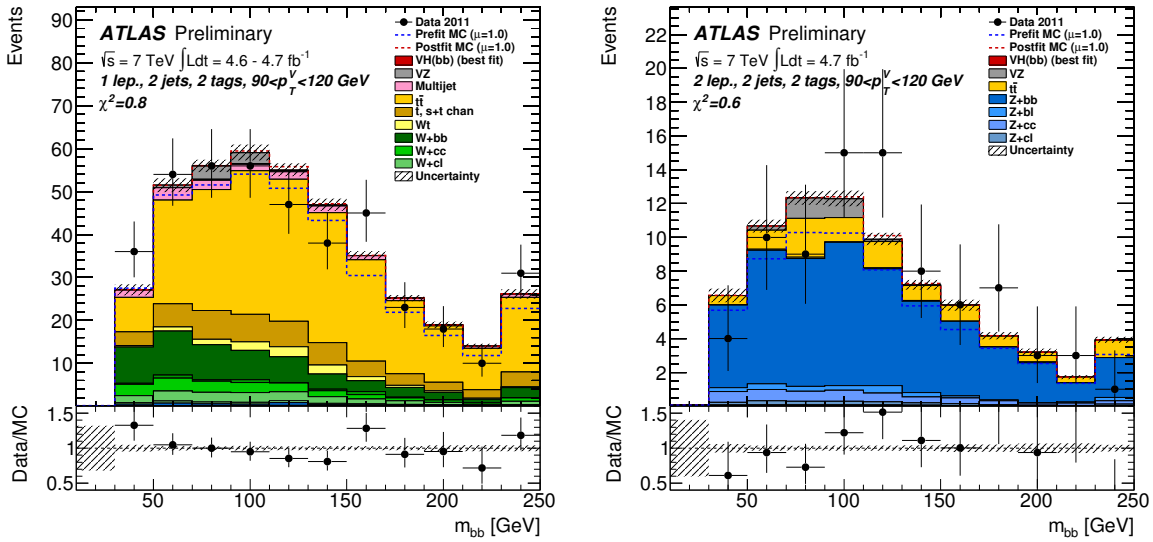

(a) 1-lepton **(b)** 2-lepton

Figure A.2.: Post-fit invariant mass distributions in the $90 < p_{\mathrm{T}}^V/(GeV) < 120$ bin of the 2-tag 2-jet region at $\sqrt{s} = 7$ TeV for data and Monte Carlo expectation. The last bin contains the distribution overflow. The hatched black area represents the total error after the profile likelihood fit, the dashed blue line represents the total background distribution input in the fit. The dashed red area represents the total background distribution in the hypothesis of a SM Higgs signal of mass 125 GeV ($\mu = 1$), while the signal is renormalised to its best fit value after the fit. The solid area shows the various background components, with their post-fit normalisation values.

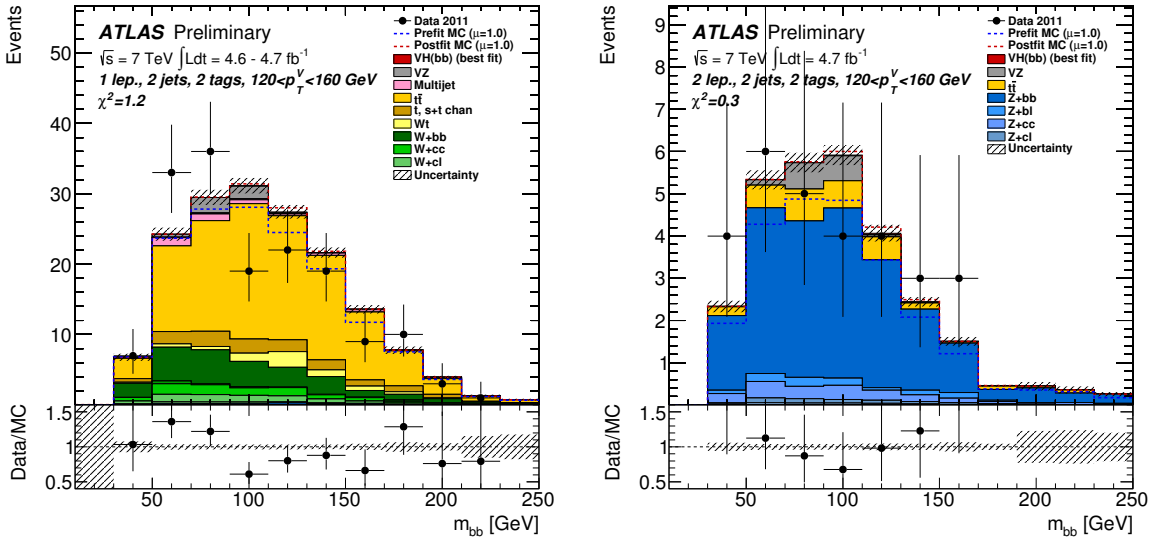

(a) 1-lepton **(b)** 2-lepton

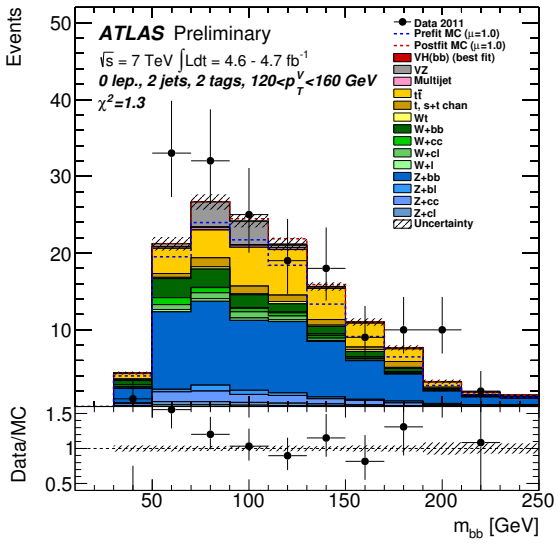

(c) 0-lepton

Figure A.3.: Post-fit invariant mass distributions in the $120 < p_{\mathrm{T}}^{V}/(GeV) < 160$ bin of the 2-tag 2-jet region at $\sqrt{s} = 7$ TeV for data and Monte Carlo expectation. The last bin contains the distribution overflow. The hatched black area represents the total error after the profile likelihood fit, the dashed blue line represents the total background distribution input in the fit. The dashed red area represents the total background distribution in the hypothesis of a SM Higgs signal of mass 125 GeV ($\mu = 1$), while the signal is renormalised to its best fit value after the fit. The solid area shows the various background components, with their post-fit normalisation values.

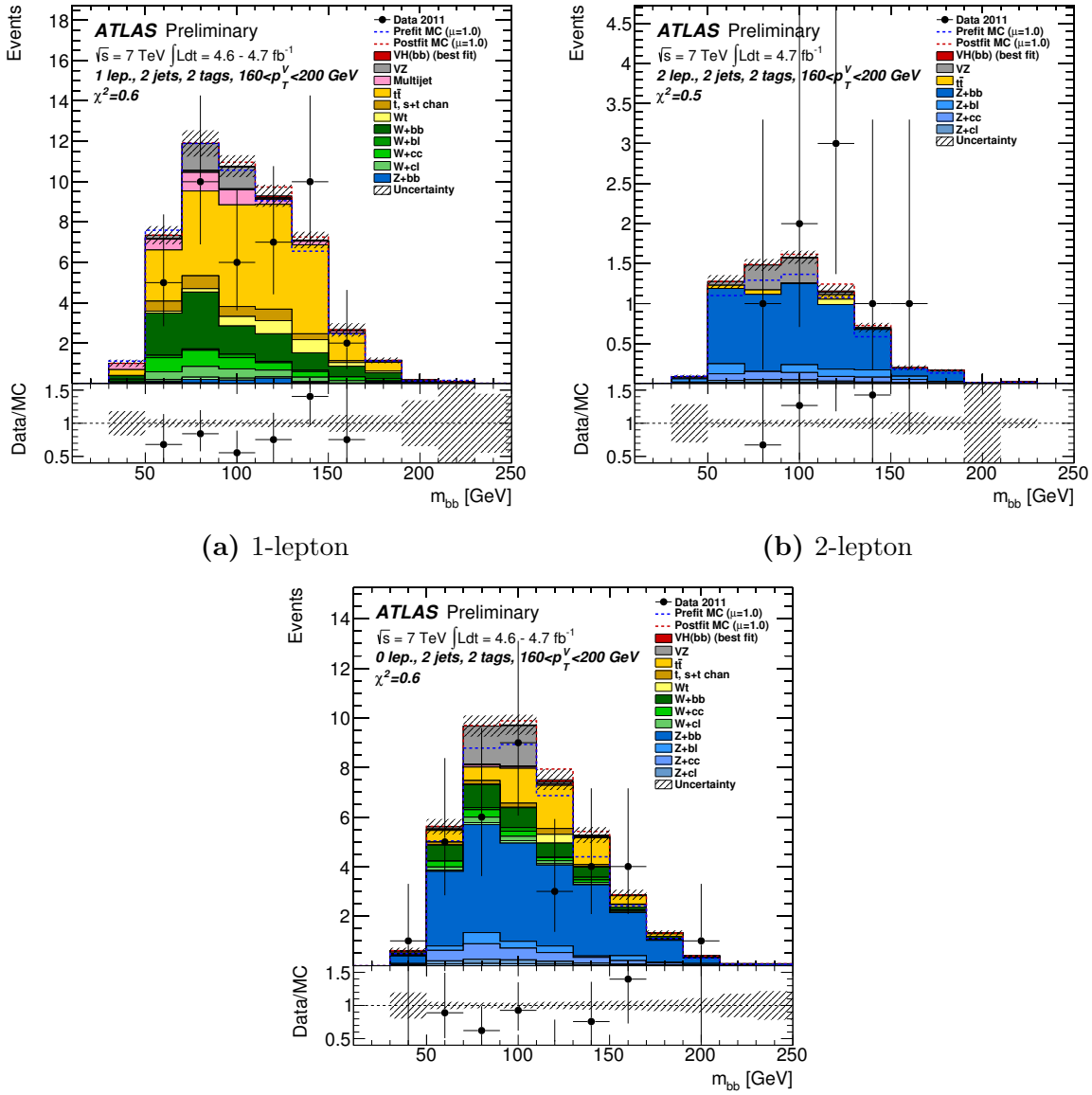

(a) 1-lepton

(b) 2-lepton

(c) 0-lepton

Figure A.4.: Post-fit invariant mass distributions in the $160 < p_{\mathrm{T}}^V/(GeV) < 200$ bin of the 2-tag 2-jet region at $\sqrt{s} = 7$ TeV for data and Monte Carlo expectation. The last bin contains the distribution overflow. The hatched black area represents the total error after the profile likelihood fit, the dashed blue line represents the total background distribution input in the fit. The dashed red area represents the total background distribution in the hypothesis of a SM Higgs signal of mass 125 GeV ($\mu = 1$), while the signal is renormalised to its best fit value after the fit. The solid area shows the various background components, with their post-fit normalisation values.

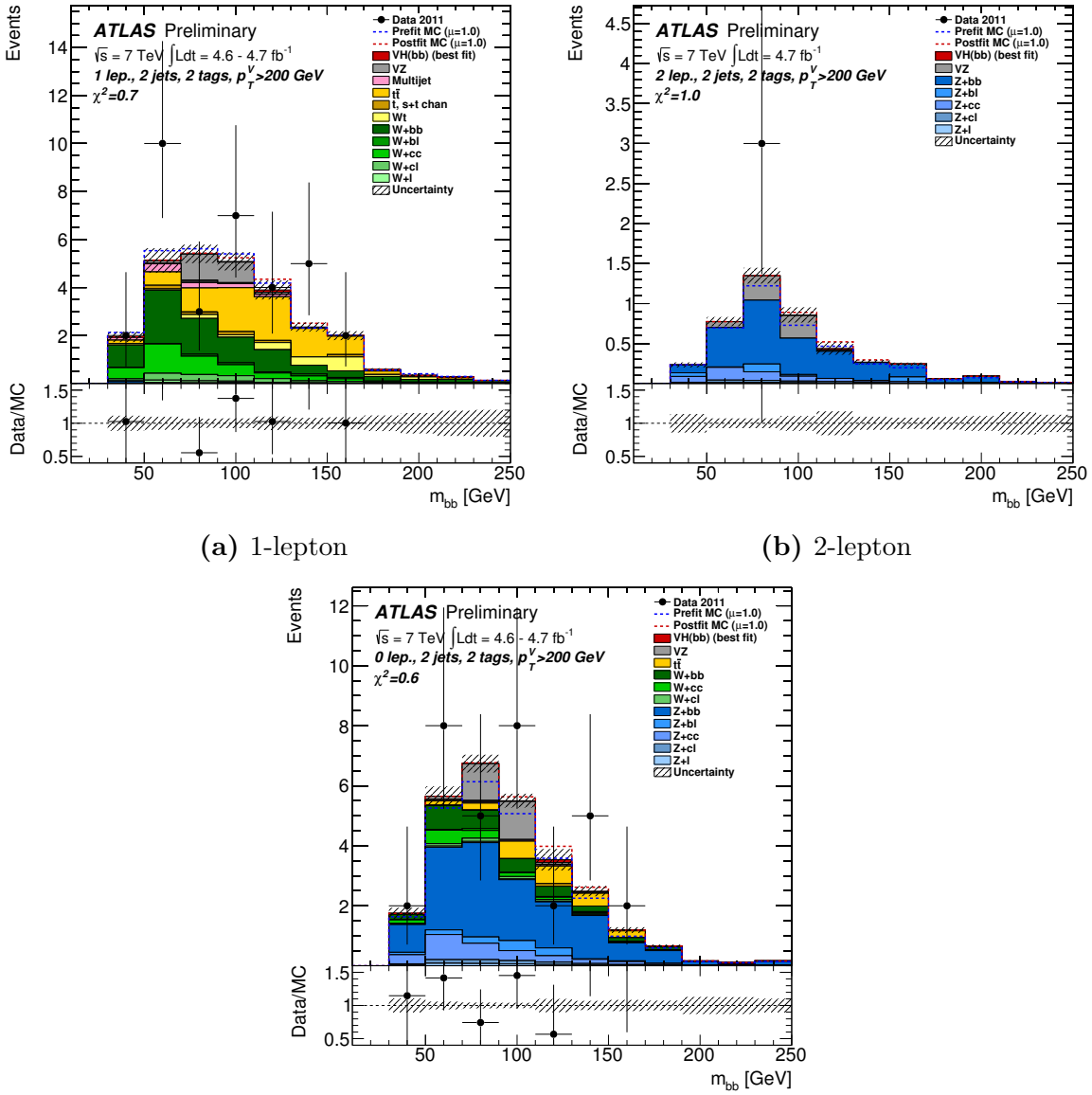

(a) 1-lepton **(b)** 2-lepton

(c) 0-lepton

Figure A.5.: Post-fit invariant mass distributions in the $p_{\mathrm{T}}^{V} > 200$ GeV bin of the 2-tag 2-jet region at $\sqrt{s} = 7$ TeV for data and Monte Carlo expectation. The last bin contains the distribution overflow. The hatched black area represents the total error after the profile likelihood fit, the dashed blue line represents the total background distribution input in the fit. The dashed red area represents the total background distribution in the hypothesis of a SM Higgs signal of mass 125 GeV ($\mu = 1$), while the signal is renormalised to its best fit value after the fit. The solid area shows the various background components, with their post-fit normalisation values.

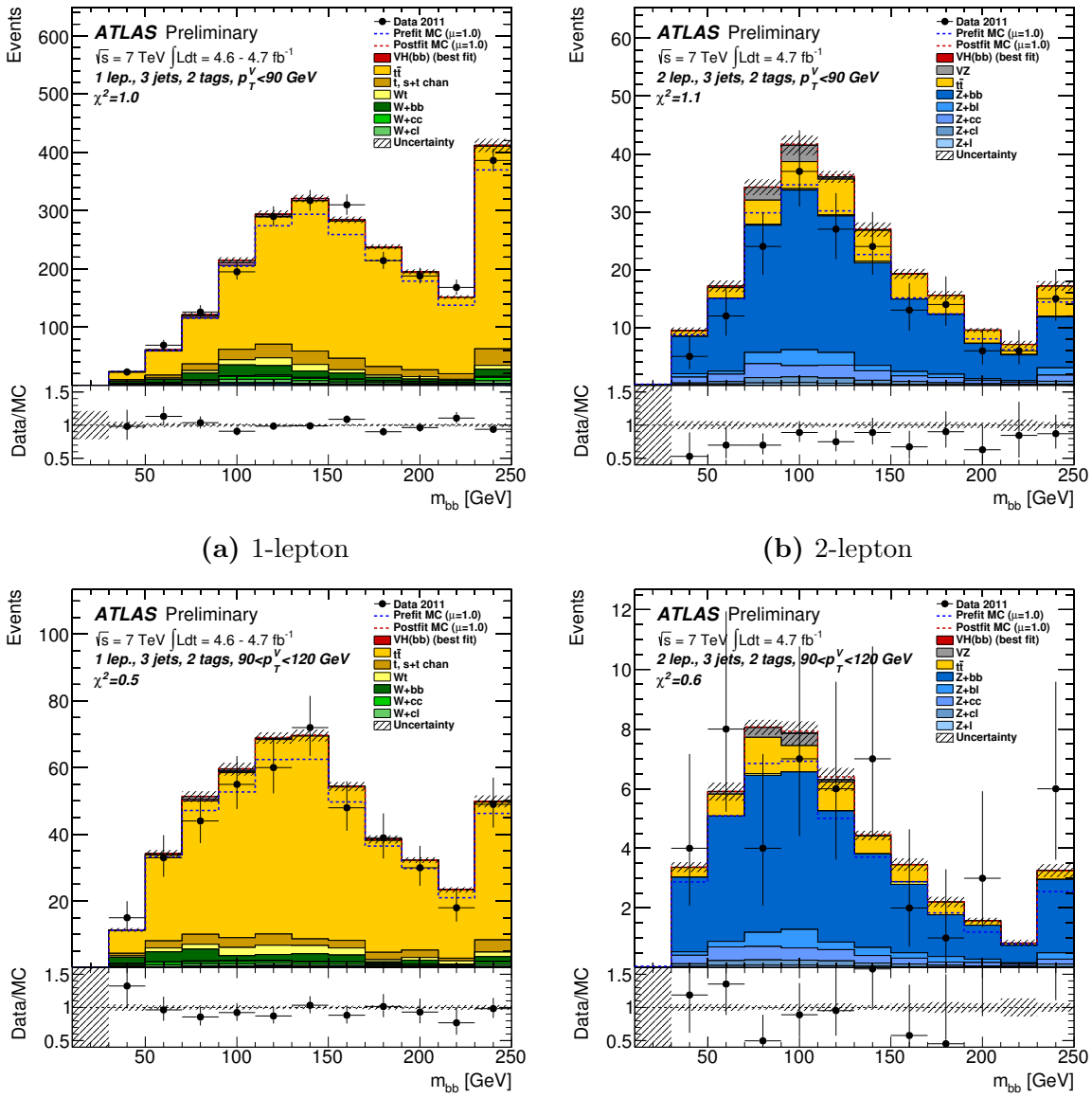

(a) 1-lepton **(b)** 2-lepton

(c) 1-lepton **(d)** 2-lepton

Figure A.6.: Post-fit invariant mass distributions in the $p_{\mathrm{T}}^V < 90$ GeV bin (A.6a, A.6b) and in the $90 < p_{\mathrm{T}}^V/(GeV) < 120$ bin (A.6c, A.6d) of the 2-tag 3-jet region at $\sqrt{s} = 7$ TeV for data and Monte Carlo expectation. The last bin contains the distribution overflow. The hatched black area represents the total error after the profile likelihood fit, the dashed blue line represents the total background distribution input in the fit. The dashed red area represents the total background distribution in the hypothesis of a SM Higgs signal of mass 125 GeV ($\mu = 1$), while the signal is renormalised to its best fit value after the fit. The solid area shows the various background components, with their post-fit normalisation values.

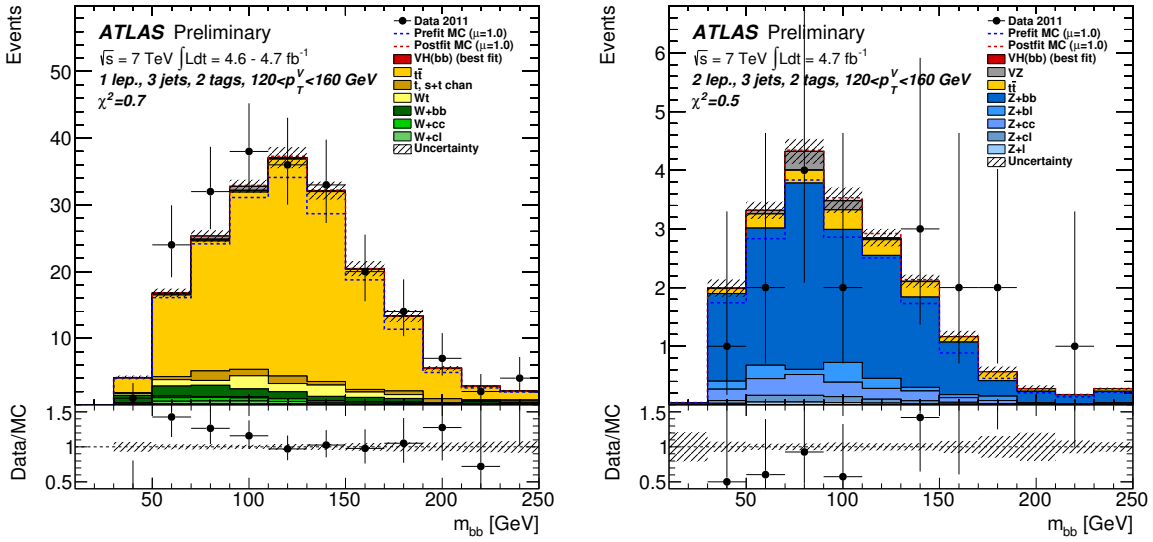

(a) 1-lepton **(b)** 2-lepton

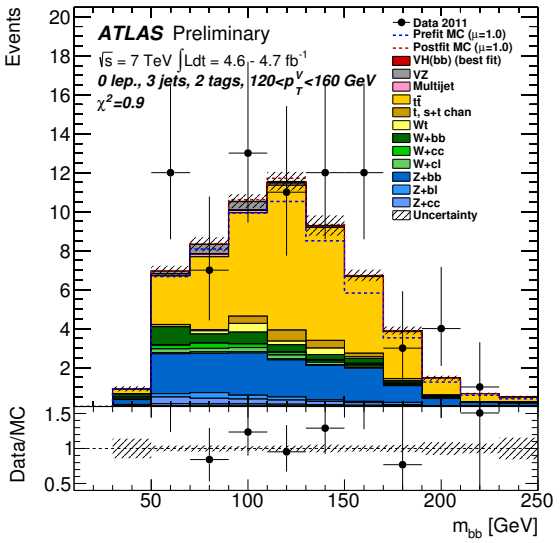

(c) 0-lepton

Figure A.7.: Post-fit invariant mass distributions in the $120 < p_{\mathrm{T}}^{V}/(GeV) < 160$ bin of the 2-tag 3-jet region at $\sqrt{s} = 7$ TeV for data and Monte Carlo expectation. The last bin contains the distribution overflow. The hatched black area represents the total error after the profile likelihood fit, the dashed blue line represents the total background distribution input in the fit. The dashed red area represents the total background distribution in the hypothesis of a SM Higgs signal of mass 125 GeV ($\mu = 1$), while the signal is renormalised to its best fit value after the fit. The solid area shows the various background components, with their post-fit normalisation values.

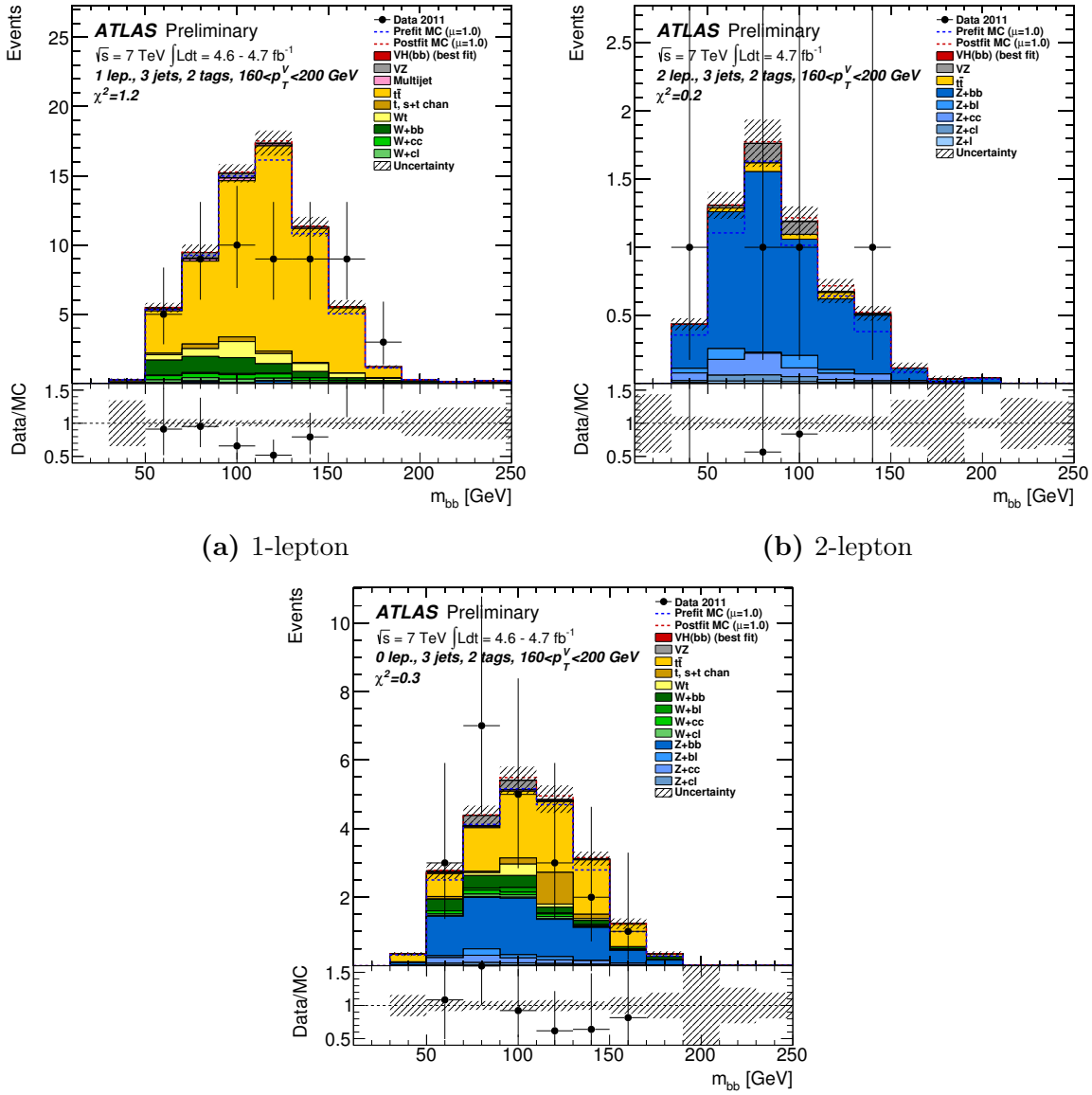

(a) 1-lepton **(b)** 2-lepton

(c) 0-lepton

Figure A.8.: Post-fit invariant mass distributions in the $160 < p_{\mathrm{T}}^V/(GeV) < 200$ bin of the 2-tag 3-jet region at $\sqrt{s} = 7$ TeV for data and Monte Carlo expectation. The last bin contains the distribution overflow. The hatched black area represents the total error after the profile likelihood fit, the dashed blue line represents the total background distribution input in the fit. The dashed red area represents the total background distribution in the hypothesis of a SM Higgs signal of mass 125 GeV ($\mu = 1$), while the signal is renormalised to its best fit value after the fit. The solid area shows the various background components, with their post-fit normalisation values.

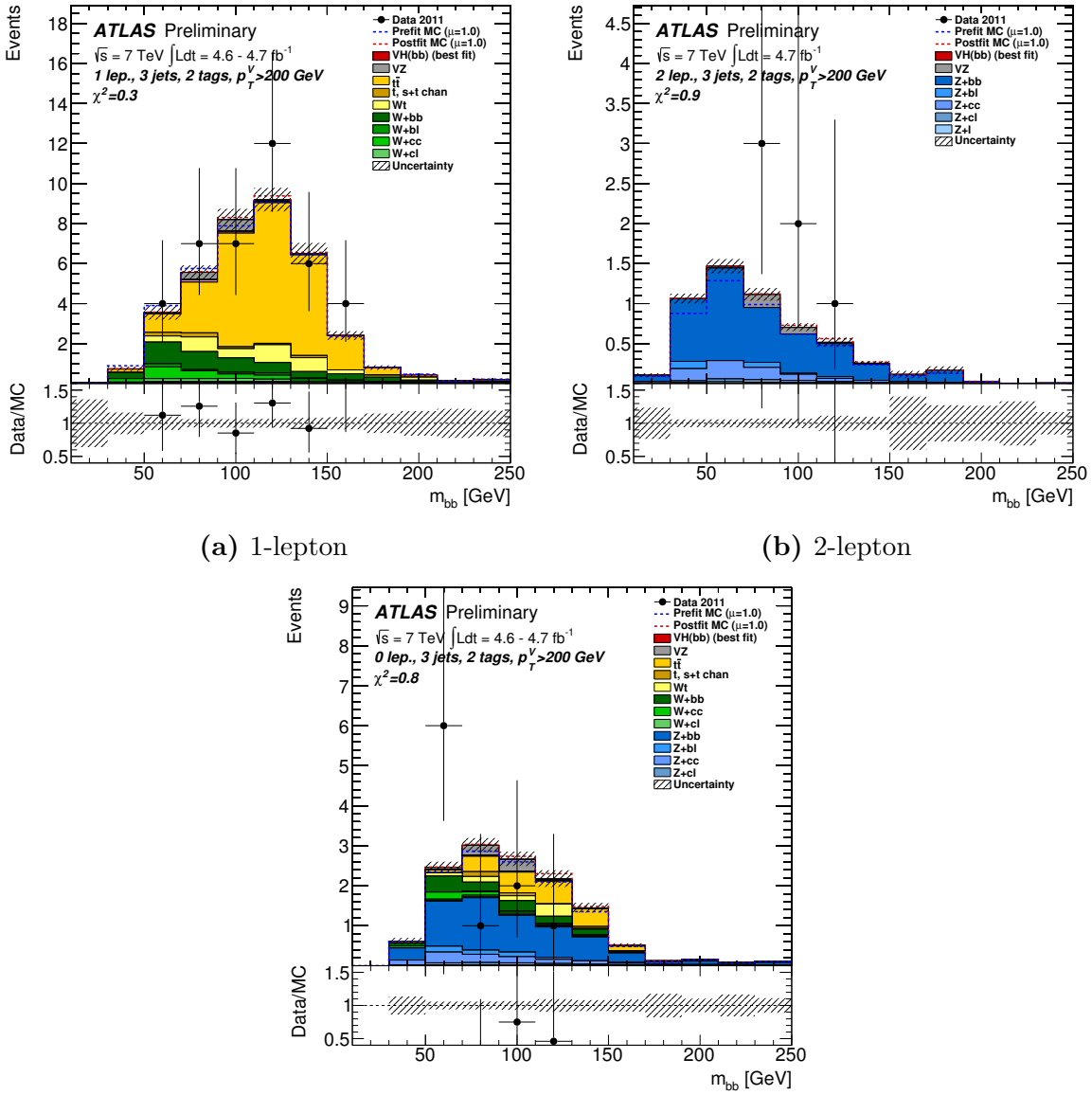

(a) 1-lepton **(b)** 2-lepton

(c) 0-lepton

Figure A.9.: Post-fit invariant mass distributions in the $p_{\mathrm{T}}^V > 200$ GeV bin of the 2-tag 3-jet region at $\sqrt{s} = 7$ TeV for data and Monte Carlo expectation. The last bin contains the distribution overflow. The hatched black area represents the total error after the profile likelihood fit, the dashed blue line represents the total background distribution input in the fit. The dashed red area represents the total background distribution in the hypothesis of a SM Higgs signal of mass 125 GeV ($\mu = 1$), while the signal is renormalised to its best fit value after the fit. The solid area shows the various background components, with their post-fit normalisation values.

The p_{T}^V distributions obtained after performing the profile likelihood fit for the combined datasets are shown from fig. A.10 to fig. A.13.

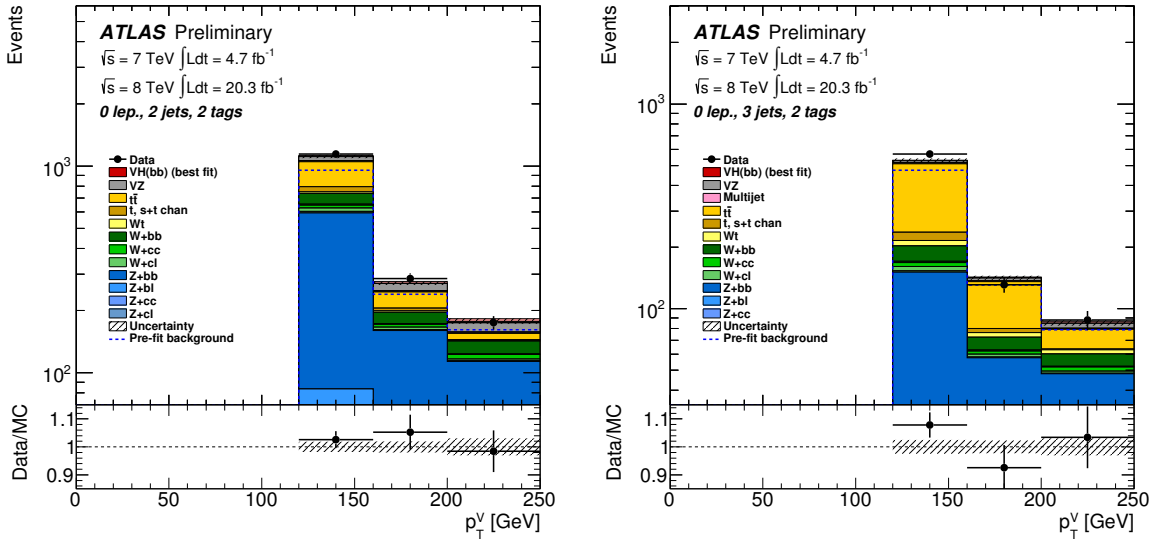

(a) 2-jet region

(b) 3-jet region

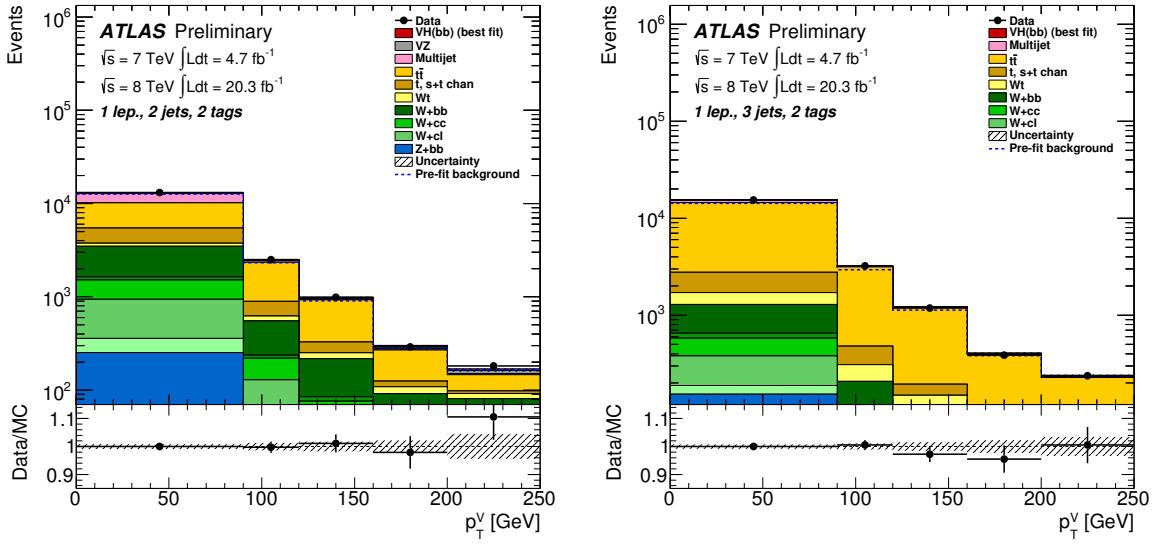

(c) 2-jet region

(d) 3-jet region

Figure A.10.: The p_{T}^V distribution in the data compared to the simulation for the 2-jet and 3-jet 2-tag regions of the 0-lepton (top) and 1-lepton (bottom) channels. The Higgs boson signal ($m_H = 125$ GeV) and background contributions after the global fit are shown as filled histograms. The size of the combined statistical and systematic uncertainty on the fitted signal and background is indicated by the hashed band. The dashed blue histogram shows the total background as expected from the Monte Carlo simulation before the fit. The entries in overflow are included in the last bin.

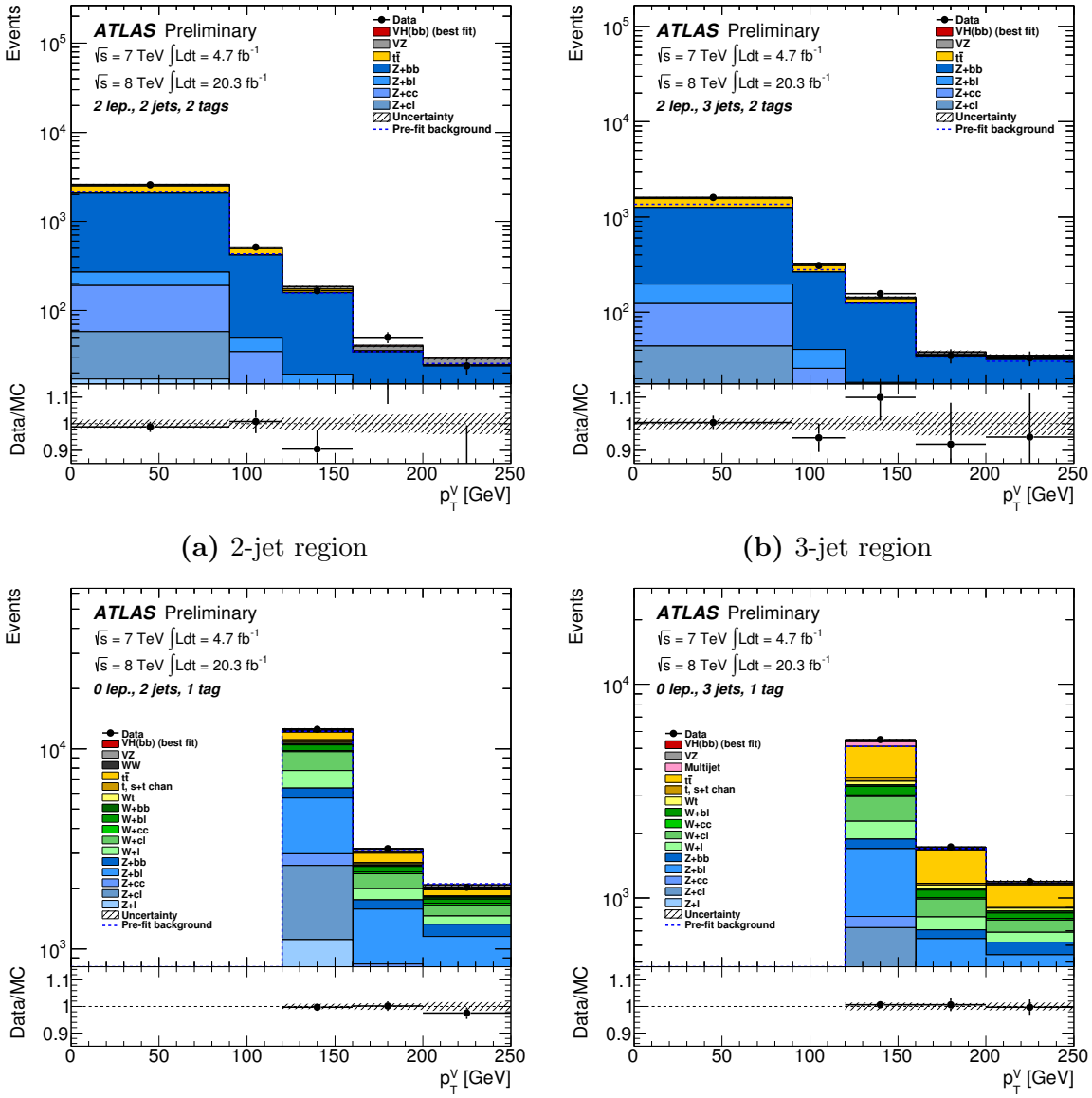

(a) 2-jet region

(b) 3-jet region

(c) 2-jet region

(d) 3-jet region

Figure A.11.: The p_{T}^V distribution in the data compared to the simulation for the 2-jet and 3-jet 2-tag regions of the 2-lepton channel (top) and for the 2-jet and 3-jet 1-tag regions of the 0-lepton channel (bottom). The Higgs boson signal ($m_H = 125$ GeV) and background contributions after the global fit are shown as filled histograms. The size of the combined statistical and systematic uncertainty on the fitted signal and background is indicated by the hashed band. The dashed blue histogram shows the total background as expected from the Monte Carlo simulation before the fit. The entries in overflow are included in the last bin.

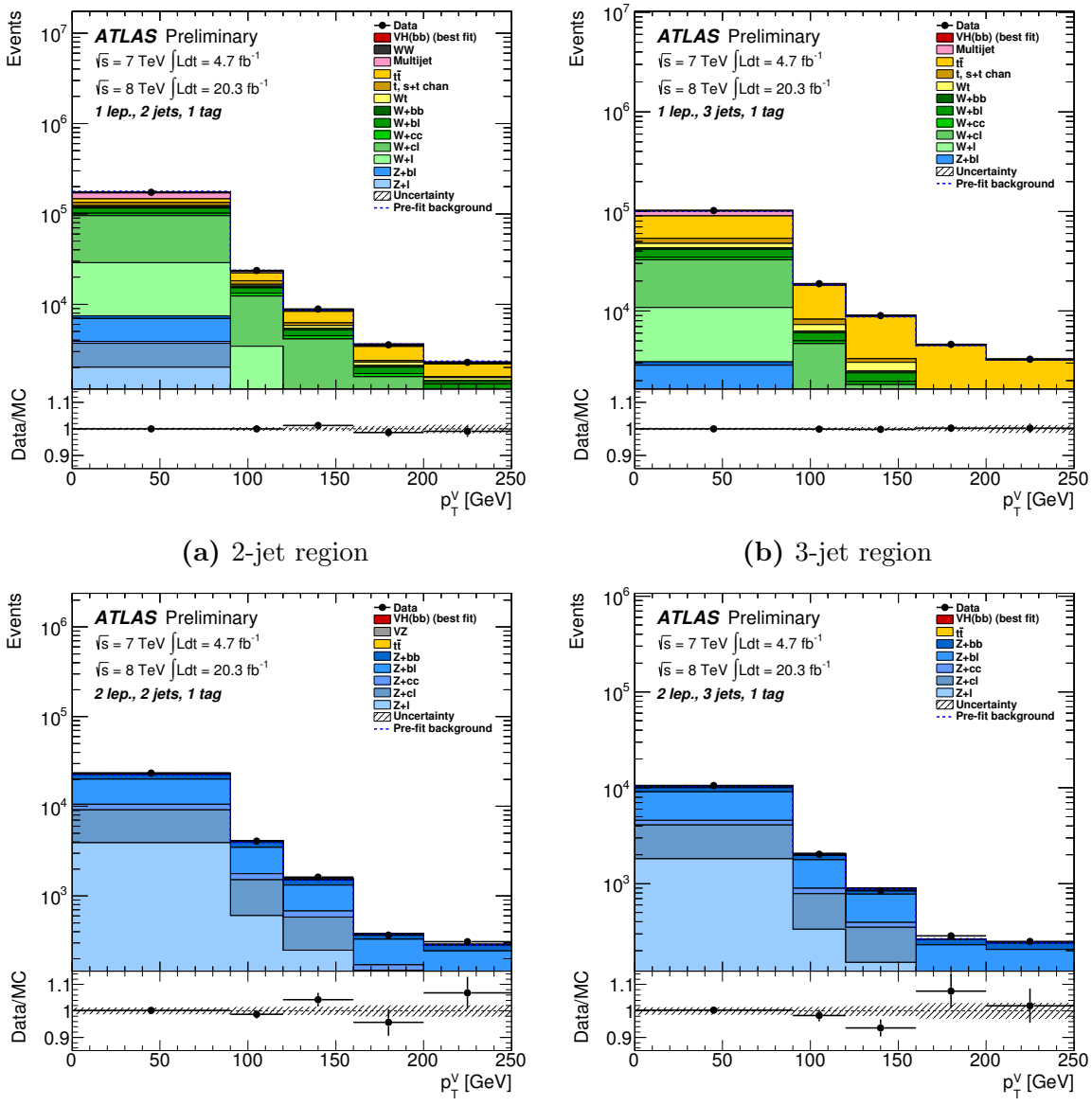

(a) 2-jet region

(b) 3-jet region

(c) 2-jet region

(d) 3-jet region

Figure A.12.: The p_{T}^{V} distribution in the data compared to the simulation for the 2-jet and 3-jet 1-tag regions of the 1-lepton channel (top) and of the 2-lepton channel (bottom). The Higgs boson signal ($m_H = 125$ GeV) and background contributions after the global fit are shown as filled histograms. The size of the combined statistical and systematic uncertainty on the fitted signal and background is indicated by the hashed band. The dashed blue histogram shows the total background as expected from the Monte Carlo simulation before the fit. The entries in overflow are included in the last bin.

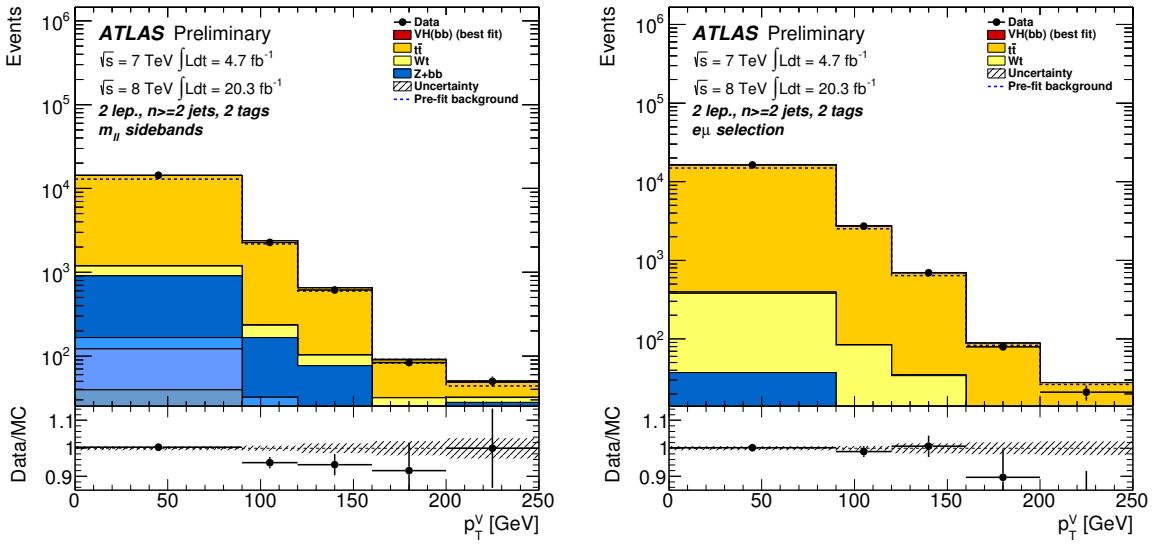

(a) $m_{\ell\ell}$ sidebands **(b)** different flavour leptons

Figure A.13.: The p_{T}^V distribution in the data compared to the simulation for the $m_{\ell\ell}$ sidebands (A.13a) and different flavour lepton (A.13b) top control regions of the 2-lepton channel. The Higgs boson signal ($m_H = 125$ GeV) and background contributions after the global fit are shown as filled histograms. The size of the combined statistical and systematic uncertainty on the fitted signal and background is indicated by the hashed band. The dashed blue histogram shows the total background as expected from the Monte Carlo simulation before the fit. The entries in overflow are included in the last bin.

References

[1] ATLAS Collaboration, G. Aad et al., *The ATLAS Experiment at the CERN Large Hadron Collider*, JINST **3** (2008) S08003.

[2] CMS Collaboration, S. Chatrchyan et al., *The CMS experiment at the CERN LHC*, JINST **3** (2008) S08004.

[3] ATLAS Collaboration, G. Aad et al., *Evidence for the spin-0 nature of the Higgs boson using ATLAS data*, Phys.Lett. **B726** (2013) 120–144, arXiv:1307.1432 [hep-ex].

[4] ATLAS Collaboration, G. Aad et al., *Measurements of Higgs boson production and couplings in diboson final states with the ATLAS detector at the LHC*, Phys.Lett. **B726** (2013) 88–119, arXiv:1307.1427 [hep-ex].

[5] CDF Collaboration, D0 Collaboration, T. Aaltonen et al., *Evidence for a particle produced in association with weak bosons and decaying to a bottom-antibottom quark pair in Higgs boson searches at the Tevatron*, Phys.Rev.Lett. **109** (2012) 071804, arXiv:1207.6436 [hep-ex].

[6] ATLAS Collaboration, *Evidence for Higgs Boson Decays to the $\tau^+\tau^-$ Final State with the ATLAS Detector*, Tech. Rep. ATLAS-CONF-2013-108, CERN, Geneva, Nov, 2013.

[7] TeVI Group Collaboration, *Design Report Tevatron 1 project*, Tech. Rep. FERMILAB-DESIGN-1984-01, 1984.

[8] CDF Collaboration, P. T. Lukens, *The CDF IIb detector Technical design report*, Tech. Rep. FERMILAB-TM-2198, CDF-DOC-CDF-PUBLIC-6261, FERMILAB-PROPOSAL-0924, FERMILAB-DESIGN-2003-01, 2003.

[9] D0 Collaboration, V. Abazov et al., *D0 Run IIB upgrade technical design report*, Tech. Rep. FERMILAB-PUB-02-327-E, FERMILAB-DESIGN-2002-01, 2002.

[10] G. 't Hooft, *The birth of asymptotic freedom*, Nuclear Physics B **254** (1985) no. 0, 11 – 18. http://www.sciencedirect.com/science/article/pii/0550321385902068.

[11] M. Böhm et al., *Gauge Theories of the Strong and Electroweak Interaction*. Vieweg+Teubner Verlag, 2001. http://books.google.co.uk/books?id=8wkt7zAFTjsC.

[12] I. Aitchison and A. Hey, *Gauge Theories in Particle Physics: A Practical Introduction*. IoP Publishing, 1989.

[13] M. Y. Han and Y. Nambu, *Three-Triplet Model with Double SU(3) Symmetry*, Phys. Rev. **139** (1965) B1006–B1010. http://link.aps.org/doi/10.1103/PhysRev.139.B1006.

[14] M. Gell-Mann, *Quarks*, Acta Phys.Austriaca Suppl. **9** (1972) 733–761.

[15] H. Fritzsch et al., *Advantages of the Color Octet Gluon Picture*, Phys.Lett. **B47** (1973) 365–368.

[16] S. Weinberg, *A Model of Leptons*, Phys. Rev. Lett. **19** (1967) 1264–1266. http://link.aps.org/doi/10.1103/PhysRevLett.19.1264.

[17] A. Salam, *Weak and Electromagnetic Interactions*, in *Elementary particle theory*, pp. 367–377. Almquist & Wiksell.

[18] S. L. Glashow, *Partial-symmetries of weak interactions*, Nuclear Physics **22** (1961) no. 4, 579 – 588. http://www.sciencedirect.com/science/article/pii/0029558261904692.

[19] S. L. Glashow et al., *Weak Interactions with Lepton-Hadron Symmetry*, Phys. Rev. D **2** (1970) 1285–1292. http://link.aps.org/doi/10.1103/PhysRevD.2.1285.

[20] E. Paschos, *Electroweak Theory*. Cambridge University Press, 2007. http://books.google.co.uk/books?id=TZTNU-zsoCkC.

[21] E. Fermi, *Tentativo di una Teoria Dei Raggi β*, Il Nuovo Cimento **11** (1934) no. 1, 1–19. http://dx.doi.org/10.1007/BF02959820.

[22] P. Higgs, *Broken symmetries, massless particles and gauge fields*, Physics Letters **12** (1964) no. 2, 132 – 133. http://www.sciencedirect.com/science/article/pii/0031916364911369.

[23] P. W. Higgs, *Broken Symmetries and the Masses of Gauge Bosons*, Phys. Rev. Lett. **13** (1964) 508–509. http://link.aps.org/doi/10.1103/PhysRevLett.13.508.

[24] P. W. Higgs, *Spontaneous Symmetry Breakdown without Massless Bosons*, Phys.Rev. **145** (1966) 1156–1163.

[25] F. Englert and R. Brout, *Broken Symmetry and the Mass of Gauge Vector Mesons*, Phys. Rev. Lett. **13** (1964) 321–323. http://link.aps.org/doi/10.1103/PhysRevLett.13.321.

[26] G. S. Guralnik et al., *Global Conservation Laws and Massless Particles*, Phys. Rev. Lett. **13** (1964) 585–587. http://link.aps.org/doi/10.1103/PhysRevLett.13.585.

[27] T. Kibble, *Symmetry breaking in nonAbelian gauge theories*, Phys.Rev. **155** (1967) 1554–1561.

[28] R. Tenchini and C. Verzegnassi, *The Physics of the Z and W Bosons*. World Scientific, 2008.

[29] ATLAS Collaboration, G. Aad et al., *Observation of a new particle in the search for the Standard Model Higgs boson with the ATLAS detector at the LHC*, Phys.Lett. **B716** (2012) 1–29, arXiv:1207.7214 [hep-ex].

[30] CMS Collaboration, S. Chatrchyan et al., *Observation of a new boson at a mass of 125 GeV with the CMS experiment at the LHC*, Phys.Lett. **B716** (2012) 30–61, arXiv:1207.7235 [hep-ex].

[31] J. F. Gunion et al., *The Higgs Hunter's Guide*, Front.Phys. **80** (2000) 1–448.

[32] M. B. Einhorn, *The Standard Model Higgs boson*. North-Holland, Amsterdam, Netherlands, 1991.

[33] M. Sher, *Electroweak Higgs potential and vacuum stability*, Physics Reports **179** (1989) no. 5–6, 273 – 418. http://www.sciencedirect.com/science/article/pii/0370157389900616.

[34] A. D. Linde, *Dynamical Symmetry Restoration and Constraints on Masses and Coupling Constants in Gauge Theories*, JETP Lett. **23** (1976) 64–67.

[35] S. Weinberg, *Mass of the Higgs Boson*, Phys. Rev. Lett. **36** (1976) 294–296.

http://link.aps.org/doi/10.1103/PhysRevLett.36.294.

[36] B. W. Lee et al., *Weak interactions at very high energies: The role of the Higgs-boson mass*, Phys. Rev. D **16** (1977) 1519–1531. http://link.aps.org/doi/10.1103/PhysRevD.16.1519.

[37] M. Chanowitz et al., *Universal Scattering Theorems for Strongly Interacting W and Z*, Phys. Rev. Lett. **57** (1986) 2344–2347. http://link.aps.org/doi/10.1103/PhysRevLett.57.2344.

[38] D. A. Dicus and V. S. Mathur, *Upper Bounds on the Values of Masses in Unified Gauge Theories*, Phys. Rev. D **7** (1973) 3111–3114. http://link.aps.org/doi/10.1103/PhysRevD.7.3111.

[39] H. A. Weldon, *Effects of multiple Higgs bosons on tree unitarity*, Phys. Rev. D **30** (1984) 1547–1558. http://link.aps.org/doi/10.1103/PhysRevD.30.1547.

[40] A. Wingerter, *Implications of the Stability and Triviality Bounds on the Standard Model with Three and Four Chiral Generations*, Phys.Rev. **D84** (2011) 095012, arXiv:1109.5140 [hep-ph].

[41] LHC Higgs Cross Section Working Group Collaboration, S. Dittmaier et al., *Handbook of LHC Higgs cross sections: 1. Inclusive observables*, CERN-2011-002 (CERN, Geneva, 2011) , arXiv:1101.0593 [hep-ph].

[42] LHC Cross Section Working Group Collaboration, S. Dittmaier et al., *Handbook of LHC Higgs Cross Sections: 2. Differential Distributions*, arXiv:1201.3084 [hep-ph].

[43] LHC Higgs Cross Section Working Group Collaboration, S. Heinemeyer et al., *Handbook of LHC Higgs Cross Sections: 3. Higgs Properties*, arXiv:1307.1347 [hep-ph].

[44] W. Stirling, *Standard Model cross sections as a function of collider energy, with 125 GeV Higgs*, private communication (2012) .

[45] R. Frederix et al., *W and Z/γ^* boson production in association with a bottom-antibottom pair*, JHEP **1109** (2011) 061, arXiv:1106.6019 [hep-ph].

[46] CDF Collaboration, D0 Collaboration, A. Heinson, *Observation of Single Top Quark Production at the Tevatron Collider*, Mod.Phys.Lett. **A25** (2010) 309–339, arXiv:1002.4167 [hep-ex].

[47] L. Evans and P. Bryant, *LHC Machine*, JINST **3** (2008) S08001.

[48] ALICE Collaboration, K. Aamodt et al., *The ALICE experiment at the CERN LHC*, JINST **3** (2008) S08002.

[49] LHCb Collaboration, A. A. J. Alves et al., *The LHCb Detector at the LHC*, JINST **3** (2008) S08005.

[50] LHCf Collaboration, O. Adriani et al., *The LHCf detector at the CERN Large Hadron Collider*, JINST **3** (2008) S08006.

[51] TOTEM Collaboration, G. Anelli et al., *The TOTEM experiment at the CERN Large Hadron Collider*, JINST **3** (2008) S08007.

[52] M. Capeans et al., *ATLAS Insertable B-Layer Technical Design Report*, Tech. Rep. CERN-LHCC-2010-013. ATLAS-TDR-19, CERN, Geneva, Sep, 2010.

[53] L. Moneta et al., *The RooStats Project*, PoS **ACAT2010** (2010) 057, `arXiv:1009.1003 [physics.data-an]`.

[54] W. Verkerke and D. P. Kirkby, *The RooFit toolkit for data modeling*, eConf **C0303241** (2003) MOLT007, `arXiv:physics/0306116 [physics]`.

[55] R. Brun and F. Rademakers, {*ROOT*} *An object oriented data analysis framework*, Nuclear Instruments and Methods in Physics Research Section A: Accelerators, Spectrometers, Detectors and Associated Equipment **389** (1997) no. 12, 81 – 86. `http://www.sciencedirect.com/science/article/pii/S016890029700048X`. New Computing Techniques in Physics Research V.

[56] G. Cowan et al., *Asymptotic formulae for likelihood-based tests of new physics*, Eur.Phys.J. **C71** (2011) 1554, `arXiv:1007.1727 [physics.data-an]`.

[57] A. Wald, *Tests of Statistical Hypotheses Concerning Several Parameters When the Number of Observations is Large*, Transactions of the American Mathematical Society **54** (1943) 426–482.

[58] ATLAS Collaboration, *Procedure for the LHC Higgs boson search combination in summer 2011*, Tech. Rep. ATL-PHYS-PUB-2011-011, CERN, Geneva, Aug, 2011.

[59] GEANT4 Collaboration, S. Agostinelli et al., *GEANT4: A Simulation toolkit*, Nucl.Instrum.Meth. **A506** (2003) 250–303.

[60] E. Richter-Was et al., *ATLFAST 2.0 a fast simulation package for ATLAS*, Tech.

Rep. ATL-PHYS-98-131, CERN, Geneva, Nov, 1998.

[61] T. Sjostrand et al., *PYTHIA 6.4 Physics and Manual*, JHEP **0605** (2006) 026, arXiv:hep-ph/0603175 [hep-ph].

[62] T. Sjostrand et al., *A Brief Introduction to PYTHIA 8.1*, Comput.Phys.Commun. **178** (2008) 852–867, arXiv:0710.3820 [hep-ph].

[63] P. M. Nadolsky et al., *Implications of CTEQ global analysis for collider observables*, Phys.Rev. **D78** (2008) 013004, arXiv:0802.0007 [hep-ph].

[64] ATLAS Collaboration, *ATLAS tunes of PYTHIA 6 and Pythia 8 for MC11*, .

[65] G. Ferrera et al., *Associated WH production at hadron colliders: a fully exclusive QCD calculation at NNLO*, Phys.Rev.Lett. **107** (2011) 152003, arXiv:1107.1164 [hep-ph].

[66] A. Djouadi et al., *HDECAY: A program for Higgs boson decays in the Standard Model and its supersymmetric extension*, Comput. Phys. Commun. **108** (1998) 56–74.

[67] A. Sherstnev and R. Thorne, *Parton Distributions for LO Generators*, Eur.Phys.J. **C55** (2008) 553–575, arXiv:0711.2473 [hep-ph].

[68] ATLAS Collaboration, *New ATLAS event generator tunes to 2010 data*, Tech. Rep. ATL-PHYS-PUB-2011-008, CERN, Geneva, Apr, 2011.

[69] Corcella, G. and others, *HERWIG 6: an event generator for hadron emission reactions with interfering gluons (including super-symmetric processes)*, JHEP **01** (2001) 010.

[70] J. M. Campbell and R. Ellis, *MCFM for the Tevatron and the LHC*, Nucl.Phys.Proc.Suppl. **205-206** (2010) 10–15, arXiv:1007.3492 [hep-ph].

[71] A. D. Martin et al., *Parton distributions for the LHC*, **63** (2009) 189.

[72] T. Gleisberg et al., *Event generation with SHERPA 1.1*, JHEP **02** (2009) 007, arXiv:0811.4622 [hep-ph].

[73] S. Catani et al., *QCD Matrix Elements + Parton Showers*, JHEP (2001) 22, arXiv:hep-ph/0109231 [hep-ph].

[74] H.-L. Lai et al., *New parton distributions for collider physics*, **82** (2010) 074024.

[75] K. Melnikov and F. Petriello, *Electroweak gauge boson production at hadron colliders through $\mathcal{O}(\alpha_s^2)$*, Phys.Rev. **D74** (2006) 114017, arXiv:hep-ph/0609070 [hep-ph].

[76] S. Alioli and others, *NLO Higgs boson production via gluon fusion matched with shower in POWHEG*, JHEP **0904** (2009) 002, arXiv:0812.0578 [hep-ph].

[77] P. Nason and C. Oleari, *NLO Higgs boson production via vector-boson fusion matched with shower in POWHEG*, JHEP **1002** (2010) 037, arXiv:0911.5299 [hep-ph].

[78] C. Oleari and L. Reina, *$W^{\pm}b\bar{b}$ production in POWHEG*, JHEP **1108** (2011) 061, arXiv:1105.4488 [hep-ph].

[79] M. Aliev et al., *HATHOR: HAdronic Top and Heavy quarks crOss section calculatoR*, Comput.Phys.Commun. **182** (2011) 1034–1046, arXiv:1007.1327 [hep-ph].

[80] B. P. Kersevan and R.-W. E., *The Monte Carlo Event Generator AcerMC version 3.5 with interfaces to* Pythia *6.4,* Herwig *6.5 and* Ariadne *4.1*, April, 2008.

[81] N. Kidonakis, *Next-to-next-to-leading-order collinear and soft gluon corrections for t-channel single top quark production*, Phys.Rev. **D83** (2011) 091503, arXiv:1103.2792 [hep-ph].

[82] N. Kidonakis, *NNLL resummation for s-channel single top quark production*, Phys.Rev. **D81** (2010) 054028, arXiv:1001.5034 [hep-ph].

[83] N. Kidonakis, *Two-loop soft anomalous dimensions for single top quark associated production with a W- or H-*, Phys.Rev. **D82** (2010) 054018, arXiv:1005.4451 [hep-ph].

[84] S. Badger et al., *QCD corrections to the hadronic production of a heavy quark pair and a W-boson including decay correlations*, JHEP **1103** (2011) 027, arXiv:1011.6647 [hep-ph].

[85] V. Hirschi et al., *Automation of one-loop QCD corrections*, JHEP **1105** (2011) 044, arXiv:1103.0621 [hep-ph].

[86] G. Ossola et al., *Reducing full one-loop amplitudes to scalar integrals at the integrand level*, Nucl.Phys. **B763** (2007) 147–169, arXiv:hep-ph/0609007 [hep-ph].

[87] G. Ossola et al., *CutTools: A Program implementing the OPP reduction method to compute one-loop amplitudes*, JHEP **0803** (2008) 042, arXiv:0711.3596 [hep-ph].

[88] R. Frederix et al., *Automation of next-to-leading order computations in QCD: The FKS subtraction*, JHEP **0910** (2009) 003, arXiv:0908.4272 [hep-ph].

[89] S. Frixione et al., *Three jet cross-sections to next-to-leading order*, Nucl.Phys. **B467** (1996) 399–442, arXiv:hep-ph/9512328 [hep-ph].

[90] S. Gieseke et al., *Colour reconnections in Herwig++*, Eur.Phys.J. **C72** (2012) 2225, arXiv:1206.0041 [hep-ph].

[91] M. Cacciari et al., *The Anti-k_T jet clustering algorithm*, JHEP **0804** (2008) 063, arXiv:0802.1189 [hep-ph].

[92] ATLAS Collaboration, G. Aad et al., *Jet energy measurement with the ATLAS detector in proton-proton collisions at $\sqrt{s} = 7$ TeV*, Eur.Phys.J. **C73** (2013) 2304, arXiv:1112.6426 [hep-ex].

[93] M. Cacciari and G. P. Salam, *Pileup subtraction using jet areas*, Phys.Lett. **B659** (2008) 119–126, arXiv:0707.1378 [hep-ph].

[94] ATLAS Collaboration, *b-jet tagging calibration on c-jets containing D^{*+} mesons*, .

[95] ATLAS Collaboration, *Measurement of the Mistag Rate with 5 fb^{-1} of Data Collected by the ATLAS Detector*, .

[96] ATLAS Collaboration, *Measurement of the b-tag Efficiency in a Sample of Jets Containing Muons with 5 fb^{-1} of Data from the ATLAS Detector*, .

[97] ATLAS Collaboration, *Measuring the b-tag efficiency in a top-pair sample with 4.7 fb^{-1} of data from the ATLAS detector*, Tech. Rep. ATLAS-CONF-2012-097, CERN, Geneva, Jul, 2012.

[98] ATLAS Collaboration, G. Aad et al., *Performance of Missing Transverse Momentum Reconstruction in Proton-Proton Collisions at 7 TeV with ATLAS*, Eur.Phys.J. **C72** (2012) 1844, arXiv:1108.5602 [hep-ex].

[99] ATLAS Collaboration, *Search for the Standard Model Higgs boson in produced in association with a vector boson and decaying to bottom quarks with the ATLAS detector*, Tech. Rep. ATLAS-CONF-2012-161, CERN, Geneva, Nov, 2012.

[100] W. Verkerke and D. Kirkby, *The RooFit toolkit for data modeling*, in *2003 Computing in High Energy and Nuclear Physics, CHEP03*. 2003. arXiv:physics:0306116.

[101] S. Hoeche et al., *QCD matrix elements + parton showers: The NLO case*, JHEP **1304** (2013) 027, arXiv:1207.5030 [hep-ph].

[102] ATLAS Collaboration, *Jet energy scale and its systematic uncertainty in proton-proton collisions at $\sqrt{s} = 7$ TeV with ATLAS 2011 data*, Tech. Rep. ATLAS-CONF-2013-004, CERN, Geneva, Jan, 2013.

[103] S. Dittmaier et al., *Higgs radiation off bottom quarks at the Tevatron and the CERN LHC*, Phys.Rev. **D70** (2004) 074010, arXiv:hep-ph/0309204 [hep-ph].

[104] A. Denner et al., *EW corrections to Higgs strahlung at the Tevatron and the LHC with HAWK*, PoS **EPS-HEP2011** (2011) 235, arXiv:1112.5258 [hep-ph].

[105] M. Ciccolini et al., *Strong and electroweak corrections to the production of Higgs + 2 jets via weak interactions at the LHC*, Phys. Rev. Lett. **99** (2007) 161803.

[106] N. Kidonakis, *Differential and total cross sections for top pair and single top production*, arXiv:1205.3453 [hep-ph].

[107] A. Buckley et al., *Rivet user manual*, arXiv:1003.0694 [hep-ph].

[108] R. D. Ball et al., *Parton distributions with LHC data*, Nucl.Phys. **B867** (2013) 244–289, arXiv:1207.1303 [hep-ph].

[109] ATLAS Collaboration, G. Aad et al., *Search for the Standard Model Higgs boson produced in association with a vector boson and decaying to a b-quark pair with the ATLAS detector*, Phys.Lett. **B718** (2012) 369–390, arXiv:1207.0210 [hep-ex].

[110] G. Piacquadio, *Identification of b-jets and investigation of the discovery potential of a Higgs boson in the $WH \to l\nu b\bar{b}$ channel with the ATLAS experiment*. PhD thesis.

[111] A. R. Davison and J. Butterworth, *Exploring Electroweak Symmetry Breaking with Jet Substructure at the ATLAS Experiment*. PhD thesis, U. Coll. London, London, UK, 2010. Presented 2010.

[112] Y. L. Dokshitzer et al., *Better jet clustering algorithms*, JHEP **9708** (1997) 001, arXiv:hep-ph/9707323 [hep-ph].

[113] M. Wobisch and T. Wengler, *Hadronization corrections to jet cross-sections in deep inelastic scattering*, arXiv:hep-ph/9907280 [hep-ph].

[114] J. M. Butterworth et al., *Jet substructure as a new Higgs search channel at the LHC*, Phys.Rev.Lett. **100** (2008) 242001, arXiv:0802.2470 [hep-ph].

[115] M. Bahr et al., *Herwig++ Physics and Manual*, Eur.Phys.J. **C58** (2008) 639–707, arXiv:0803.0883 [hep-ph].

[116] G. Luisoni et al., *$HW^{\pm}/HZ$+ 0 and 1 jet at NLO with the POWHEG BOX interfaced to GoSam and their merging within MiNLO*, JHEP **1310** (2013) 083, arXiv:1306.2542 [hep-ph].

[117] M. L. Mangano et al., ALPGEN*, a generator for hard multi-parton processes in hadronic collisions*, JHEP **07** (2003) 001.

[118] S. Frixione et al., *The MC@NLO 4.0 event generator*, arXiv:1010.0819 [hep-ph].

[119] ATLAS Collaboration, G. Aad et al., *Performance of jet substructure techniques for large-R jets in proton-proton collisions at $\sqrt{s} = 7$ TeV using the ATLAS detector*, JHEP **1309** (2013) 076, arXiv:1306.4945 [hep-ex].

[120] ATLAS Collaboration, P. Clark, *The search for the Standard Model Higgs boson produced in association with a vector boson and decaying to bottom quarks with the ATLAS detector*, EPJ Web Conf. **49** (2013) 12011.

[121] Read, A. L., *Presentation of search results: the CL_s technique*, J. Phys. G **28** (2002) 2693–2704.

[122] ATLAS Collaboration, T. A. Collaboration, *Measurements of the properties of the Higgs-like boson in the two photon decay channel with the ATLAS detector using 25* fb^{-1} *of proton-proton collision data*, Tech. Rep. ATLAS-CONF-2013-012, CERN, Geneva, Mar, 2013.

[123] ATLAS Collaboration, T. A. Collaboration, *Study of the spin of the Higgs-like boson in the two photon decay channel using 20.7 fb^{-1} of pp collisions collected at $\sqrt{s} = 8$ TeV with the ATLAS detector*, Tech. Rep. ATLAS-CONF-2013-029, CERN, Geneva, Mar, 2013.

[124] ATLAS Collaboration, T. A. Collaboration, *Search for $t\bar{t}H$ production in the $H \to \gamma\gamma$ channel at $\sqrt{s} = 8$ TeV with the ATLAS detector*, Tech. Rep.

ATLAS-CONF-2013-080, CERN, Geneva, Jul, 2013.

[125] ATLAS Collaboration, T. A. Collaboration, *Differential cross sections of the Higgs boson measured in the diphoton decay channel using 8 TeV pp collisions*, Tech. Rep. ATLAS-CONF-2013-072, CERN, Geneva, Jul, 2013.

[126] ATLAS Collaboration, *Measurements of the properties of the Higgs-like boson in the four lepton decay channel with the ATLAS detector using 25 fb^{-1} of proton-proton collision data*, Tech. Rep. ATLAS-CONF-2013-013, CERN, Geneva, Mar, 2013.

[127] ATLAS Collaboration, *Search for a Standard Model Higgs in the $H \to ZZ \to \ell\ell\nu\nu$ decay channel with 4.7 fb^{-1} with the ATLAS detector*, Tech. Rep. ATLAS-CONF-2012-016, CERN, Geneva, Mar, 2012.

[128] ATLAS Collaboration, *Search for a Standard Model Higgs in the mass range 200-600 GeV in the channel $H \to ZZ \to llqq$ with with the ATLAS detector*, Tech. Rep. ATLAS-CONF-2012-017, CERN, Geneva, Mar, 2012.

[129] ATLAS Collaboration, *Study of the channel $H \to Z^*Z \to \ell^+\ell^- q\bar{q}$ in the mass range 120-180 GeV with the ATLAS Detector at $\sqrt{s}$=7 TeV*, Tech. Rep. ATLAS-CONF-2012-163, CERN, Geneva, Nov, 2012.

[130] ATLAS Collaboration, *Measurements of the properties of the Higgs-like boson in the $WW^{(*)} \to \ell\nu\ell\nu$ decay channel with the ATLAS detector using 25 fb^{-1} of proton-proton collision data*, Tech. Rep. ATLAS-CONF-2013-030, CERN, Geneva, Mar, 2013.

[131] ATLAS Collaboration, *Study of the spin properties of the Higgs-like particle in the $H \to WW^{(*)} \to e\nu\mu\nu$ channel with 21 fb^{-1} of $\sqrt{s} = 8$ TeV data collected with the ATLAS detector.*, Tech. Rep. ATLAS-CONF-2013-031, CERN, Geneva, Mar, 2013.

[132] ATLAS Collaboration, *Search for associated production of the Higgs boson in the $WH \to WWW \to \ell\nu\ell\nu\ell\nu$ and $ZH \to ZWW \to \ell\ell\ell\nu\ell\nu$ channels with the ATLAS detector at the LHC*, Tech. Rep. ATLAS-CONF-2013-075, CERN, Geneva, Jul, 2013.

[133] ATLAS Collaboration, *Search for a high-mass Higgs boson in the $H \to WW \to l\nu l\nu$ decay channel with the ATLAS detector using 21 fb^{-1} of proton-proton collision data*, Tech. Rep. ATLAS-CONF-2013-067, CERN, Geneva, Jul, 2013.

[134] ATLAS Collaboration, *Search for the Higgs boson in the $H \to WW \to \ell\nu jj$ decay channel using 4.7 fb^{-1} of pp collisions at $\sqrt{s} = 7$ TeV with the ATLAS detector*, Tech. Rep. ATLAS-CONF-2012-018, CERN, Geneva, Mar, 2012.

[135] ATLAS Collaboration, *Search for the Standard Model Higgs boson in the $H \to Z\gamma$ decay mode with pp collisions at $\sqrt{s} =$ 7 and 8 TeV*, Tech. Rep. ATLAS-CONF-2013-009, CERN, Geneva, Mar, 2013.

[136] ATLAS Collaboration, *Search for a Standard Model Higgs boson in $H \to \mu\mu$ decays with the ATLAS detector.*, Tech. Rep. ATLAS-CONF-2013-010, CERN, Geneva, Mar, 2013.

[137] ATLAS Collaboration, T. A. Collaboration, *Search for the Standard Model Higgs boson produced in association with top quarks in proton-proton collisions at $\sqrt{s} = 7$ TeV using the ATLAS detector*, Tech. Rep. ATLAS-CONF-2012-135, CERN, Geneva, Sep, 2012.

[138] CMS Collaboration Collaboration, *Combination of standard model Higgs boson searches and measurements of the properties of the new boson with a mass near 125 GeV*, Tech. Rep. CMS-PAS-HIG-13-005, CERN, Geneva, 2013.

[139] LEP Working Group for Higgs boson searches, ALEPH Collaboration, DELPHI Collaboration, L3 Collaboration, OPAL Collaboration, R. Barate et al., *Search for the standard model Higgs boson at LEP*, Phys.Lett. **B565** (2003) 61–75, arXiv:hep-ex/0306033 [hep-ex].

[140] CMS Collaboration, *Search for Higgs Boson Production in Association with a Top-Quark Pair and Decaying to Bottom Quarks or Tau Leptons*, Tech. Rep. CMS-PAS-HIG-13-019, CERN, Geneva, 2013.

[141] CMS Collaboration, S. Chatrchyan et al., *Identification of b-quark jets with the CMS experiment*, JINST **8** (2013) P04013, arXiv:1211.4462 [hep-ex].

[142] CMS Collaboration, S. Chatrchyan et al., *Search for the standard model Higgs boson produced in association with a W or a Z boson and decaying to bottom quarks*, arXiv:1310.3687 [hep-ex].

[143] CMS Collaboration, *Higgs to $b\bar{b}$ in the VBF channel*, Tech. Rep. CMS-PAS-HIG-13-011, CERN, Geneva, 2013.

List of Figures

List of Tables